The University Of Sheffield.

Resource efficient development of combinatorial materials for future Multilayer Ceramic Capacitor applications

By

George William Kerridge

A thesis submitted in partial fulfilment of the requirements for the degree of Doctor of Philosophy.

Thesis Supervisors

Dr. Julian S. Dean

&

Prof. Derek C. Sinclair

The University of Sheffield
Faculty of Engineering
Department of Material Science and Engineering

October 2021

Table of Contents

Abstract

This thesis investigates the permittivity-temperature (ε_r-T) profiles of individual dielectric materials through simulation led experiments. The results are used to assess the capability of using layered ceramic systems to meet the Temperature Coefficient of Capacitance (TCC) requirements of Multi-Layer Ceramic Capacitors. The layered ceramics exceed the performance of existing $BaTiO_3$ (BT) based materials, especially at high temperatures (>125°C). The application of simulations reduces the need for experimental research, accelerating the discovery of new material combinations of interest.

Combining dielectric layers in a series combination has the following benefits over materials currently used commercially:

(a) Literature reported ε_r-T data can be used directly as input data.
(b) Individual materials can exhibit highly temperature dependent ε_r-T data.
(c) Materials do not require heterogeneous microstructures to be viable.
(d) New material combinations do not require extensive and iterative experimental research.
(e) Simulations can effectively predict novel material combinations of interest.
(f) Changes to performance criteria demands (operating temperature range, TCC_{abs}(%), ε_{RT}) are easily accommodated.
(g) The electrical connectivity of the material layers is controlled by the user and not dependent on processing conditions.

Ternary layer systems using 9 $NaNbO_3$-$BaTiO_3$ (NNBT) ε_r-T profiles as input data can be optimised to meet X9P classification (-55 to 200°C, TCC_{abs}< ±10%). This performance is beyond the capability of existing commercial BT-based materials and required a high T_{max} (peak in ε_r-T profile) material layer which is only achieved at high NN contents.

Tetragonal Tungsten Bronze $(Ca,Sr,Ba)Nb_2O_6$ materials were investigated as high T_{max} materials, with selected compositions displaying a T_{max} range from 62 to 382°C achieved by altering the A-site cations. The large temperature range of TCC stability from 25 to 400°C (TCC_{abs}< ±22%), demonstrates the potential of these layered ceramic systems to significantly progress the performance of MLCC devices.

Acknowledgements

I would first like to thank my supervisors, Dr. Julian S. Dean and Prof. Derek C. Sinclair. Their combined expertise in functional ceramic materials, plus their unwavering supervision and support, have been critical in the success of my studies.

I am grateful to the EPSRC, for the 4 year DTP scholarship funding, which enabled my PhD studies and financed the ability to present my work internationally.

My thanks to Dr. Philip Foeller for his guidance at the start of my PhD studies, and for providing his data on the $NaNbO_3$-$BaTiO_3$ system, which provided a great starting point for my simulation and experimental work.

I would also like to thank my fellow PhD colleagues in the H7 office, and to all those in the Sheffield Functional Materials Group, for their support over the last 4 years.

I would like to give particular thanks to Senior Technician Kerry Mclaughlin and Dr. Jess Andrews. Their friendship and positive attitude were particularly valuable on the many days when experiments did not go to plan.

Finally, I would like to thank my Fiancée Rachel and my family. Their kind words, endless support and unrelenting love has been critical in the completion of this work. My full appreciation to those I love cannot be described in words.

1. Introduction

1.1. Background

Multilayer ceramic capacitors (MLCCs) are a fundamental component in modern electrical circuit design [1]. They are used in a wide range of technology sectors with extensive use in devices ranging from personal mobile devices, through to orbiting satellites. One key application of MLCCs is in the smoothing out of spikes from direct current that can cause performance issues in sensitive electrical systems. This ubiquity of usage, and the development of more complex electrical circuits, has resulted in a continuous increase in global demand for MLCC components. In 2018, the global production of MLCCs was 3.6 trillion units, with predictions of global production exceeding 4.5 trillion units by 2024 [2].

An MLCC is a passive electrical component consisting of an alternating stack of dielectric materials and internal electrode plates, Figure 1.1. The electrodes are terminated alternately, with the dielectric layer acting as an electrical insulator. The total capacitance of the MLCC is directly related to the permittivity of the dielectric material, presuming all else is constant, e.g. number of layers, electrode area etc.

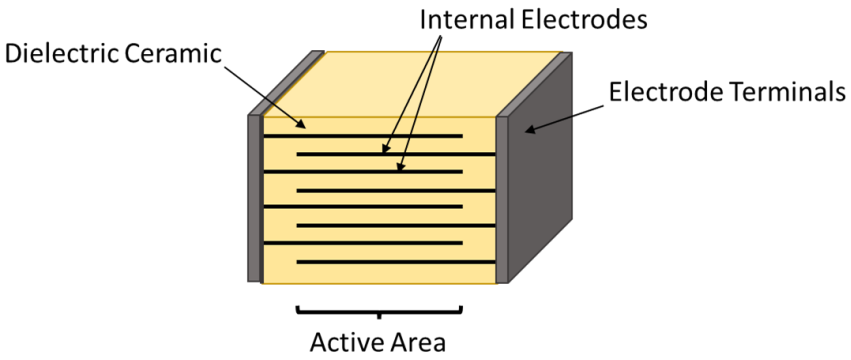

Figure 1.1 Schematic of a multilayer ceramic capacitor (MLCC).

Since the 1940s, many ceramic capacitors have been based upon Barium Titanate (BT) based ceramic materials [3]. Undoped BT has a high permittivity (ε_r ~ 2000) at a room temperature; however, the permittivity of undoped BT is very temperature sensitive, rising to ε_r >10,000 at ~ 120°C, before sharply falling again. To stabilise the permittivity response, BT is chemically doped. A significant proportion of chemical elements in the periodic table can be introduced into the crystal structure, either as a single dopant or in combination with other elements [4]. This variety in potential combinations is further expanded by the dependence of the amounts of dopants used and how the ceramics are synthesised.

From over 50 years of development, research has led to BT based materials with significantly improved temperature stability. This stability is often quantified using the figure of merit called the Temperature Coefficient of Capacitance (TCC), calculated as:

$$TCC(\%) = \frac{\varepsilon_T - \varepsilon_{25}}{\varepsilon_{25}} * 100 \quad (1.1)$$

where ε_{25} is the permittivity of the material at 25°C and ε_T is the permittivity at temperature T.

Using BT materials, MLCCs with the X7R classification (TCC = ±15%, for -55 to 125°C) are mass produced. BT based MLCCs struggle to stabilise permittivity beyond 150°C, incurring significant reduction in TCC performance.

Technological developments such as electric vehicles are leading to electrical circuits being in closer proximity to mechanical systems. During operation, these mechanical systems are generating significant amounts of heat, and thus there is need for electrical devices that can operate at temperatures greater than 150°C. Therefore, there is demand to find new material systems that maintain their TCC rating to these elevated temperatures [5]. However, the choice of material system(s) to replace BT is challenging. A significant amount of experimental work is required to investigate a single material system and its interactions with chemical dopants. This task becomes exponentially more difficult when heterogeneous ceramic systems (like core and shell grains) are considered. To allow a fair comparison, significant effort in optimising each system would be necessary.

The iterative approach of developing materials is very inefficient due to the large number of parameters that need to be explored. This often results in a great deal of data being generated, to achieve a single result that meets the desired requirements.

1.2. Aim & Scope

This thesis investigates the development of new composite material systems for MLCC applications, with operating temperature ranges beyond those currently achieved with BT based materials. This work looks to utilise simulations to expedite the material selection process. Although this work is not directly sponsored by industry, it does continue a collaboration with AVX Ltd. This collaboration, and previous work by Phil Foeller [6], motivated the choice of the $NaNbO_3$-$BaTiO_3$ (NNBT) material system. The $Ca_xSr_yBa_{1-x-y}Nb_2O_5$ (CSBN) materials were chosen due to the A-site dependency on varying the high temperature response.

The work focuses on the optimisation of composite systems with simple geometric designs. This limitation is to allow simulations to be effectively run on a standard desktop computer. As such, expensive supercomputer facilities are not required to predict and optimise the dielectric properties of the composite ceramic systems. For input data, published material data is heavily utilised in predicting materials with the desired dielectric properties. This approach aims to minimise the number of materials that need to be produced experimentally, allowing efficient use of laboratory access.

Finally, this thesis demonstrates experimental verification of the simulation results, with the results enabling improvements to the simulation models to be made.

1.3. Overview of the Study

The structure of the thesis and content of each chapter are as follows.

A review of the literature related to this thesis is covered in chapter 2. This includes the fundamentals of MLCC devices and of dielectric ceramic materials. Previously published work on specific material systems used in this work are summarised with a focus on results from various crystalline ceramics.

The experimental methodologies used are described in Chapter 3. This includes the conditions used to synthesis the bulk ceramics and the characterisation techniques used.

The simulation approach is detailed in Chapter 4. Starting with the foundation equations, the chapter outlines the approach used to simulate the permittivity values of a ternary layered composite system. This leads onto how each ternary combination is simulated for a range of different layer thickness ratios. The approaches used to compare the performance of different material combinations are discussed, and how the results are displayed and analysed.

Chapter 5 Contains the following publication where I am the first author:

Kerridge, G., Sinclair, D.C., Dean, J.S., 2021. *Resource efficient exploration of ternary phase space to develop multi-layer ceramic capacitors*. Acta Materialia 207, 116690. doi:10.1016/j.actamat.2021.116690

The paper applies the simulation methods discussed in Chapter 4 to simulate every ternary material combination possible for a given number of input materials. The publication uses a dataset of 9 different $NaNbO_3$-$BaTiO_3$ (NNBT) materials as initial inputs that were previously reported by Dr Philip Foeller [6]. Further experimental work was undertaken to verify the simulation results. This chapter demonstrates the potential of the simulation approach in rapidly identifying potential material combinations of interest, and the relative thicknesses required to optimise TCC.

Chapter 6 expands the work of the previous chapter, by considering the impact of co-sintering of dielectric material layers. Two NNBT materials with compatible sintering requirements were selected and optimised for the X8 temperature range (-55 to 150°C). The successful co-sintering of these two materials allowed the permittivity profile of this bilayer to be compared to those simulated.

Chapter 7 moves away from BT containing materials, to consider those with a Tetragonal Tungsten Bronze (TTB) structure. The $(Ca_xSr_yBa_{1-x-y})Nb_2O_6$ material system was selected, with various A-site compositions selected to produce materials with a range of T_{max} values. Layered systems were simulated, with temperature ranges that greatly exceed those achievable with BT based materials (>300°C).

Finally, conclusions and future work are discussed in Chapter 8.

1.4. References

[1] M. J. Pan and C. A. Randall, "A brief introduction to ceramic capacitors," IEEE Electrical Insulation Magazine, vol. 26, no. 3, pp. 44-50, 2010, doi: 10.1109/mei.2010.5482787.

[2] "Global Multilayer Ceramic Capacitor (MLCC) Market, by Type (Class I (NP0/C0G, U2J, others), Class II (X7R, X5R, Y5V, Z5U), by Application (Consumer Electronics, Automotive, Manufacturing, Telecommunication, Transportation, Healthcare). Forecast till 2024",ID: MRFR/SEM/6269-HCR. Market research future, Available from https://www.marketresearchfuture.com/reports/multilayer-ceramic-capacitor-market-7738 (last accessed September 2021)

[3] H. Kishi, Y. Mizuno, and H. Chazono, "Base-metal electrode-multilayer ceramic capacitors: Past, present and future perspectives," (in English), Jpn. J. Appl. Phys. Part 1 - Regul. Pap. Short Notes Rev. Pap., Review vol. 42, no. 1, pp. 1-15, Jan 2003, doi: 10.1143/jjap.42.1.

[4] V. Veerapandiyan, F. Benes, T. Gindel, and M. Deluca, "Strategies to Improve the Energy Storage Properties of Perovskite Lead-Free Relaxor Ferroelectrics: A Review," Materials, vol. 13, no. 24, p. 5742, 2020, doi: 10.3390/ma13245742.

[5] A. Zeb and S. J. Milne, "High temperature dielectric ceramics: a review of temperature-stable high-permittivity perovskites," (in English), J. Mater. Sci.-Mater. Electron., Review vol. 26, no. 12, pp. 9243-9255, Dec 2015, doi: 10.1007/s10854-015-3707-7.

[6] P. Foeller, "Novel materials and routes for rare-earth-free BaTiO3-based ceramics for MLCC applications.," Materials Science and Engineering, University of Sheffield, 2017. [Online]. Available: http://etheses.whiterose.ac.uk/18954/

2. Literature Review

2.1. Introduction

This literature review covers the fundamentals of ferroelectric materials for MLCC applications and the approaches used industrially to make the permittivity response stable across a required temperature range. The current materials are discussed, as well as their limitations in maintaining performance at high temperature. This invariably makes use of core-shell microstructures. A concluding discussion on composite MLCCs reported in the literature is provided which use layers of different ferroelectric materials that may offer an alternative architecture in the design of future MLCCs.

2.2. Dielectric materials

The term 'dielectric material' is broad, describing any material that has the properties of being both an electrical insulator and polarisable when exposed to an external electric field [1]. A dielectric material is not restricted to solids with liquids and gases also being dielectric materials. This thesis focuses on ceramic dielectrics with the focus on materials with potential applications in MLCC devices.

The relative permittivity ε_r, is used to quantify a materials ability to store electric charge, by comparing the permittivity of the material to that of a vacuum:

$$\varepsilon_r = \frac{\varepsilon}{\varepsilon_0} \tag{2.1}$$

where ε_r is relative permittivity of the material, ε is the permittivity of the material (units of F/m) and ε_o is the permittivity of free space (8.85 x 10^{-12} F/m). ε_r is a unitless value.

A schematic of a simple plate capacitor is shown in Figure 2.1. The relative capacitance is directly proportional to the material used to separate the electrode plates as compared to a vacuum, as:

$$C = \frac{\varepsilon_0 \varepsilon_r A}{d} \tag{2.2}$$

where C is capacitance, A is surface area overlap of the electric plates and d is the distance of separation between the electrode plates. The separation distance is also equivalent to the thickness

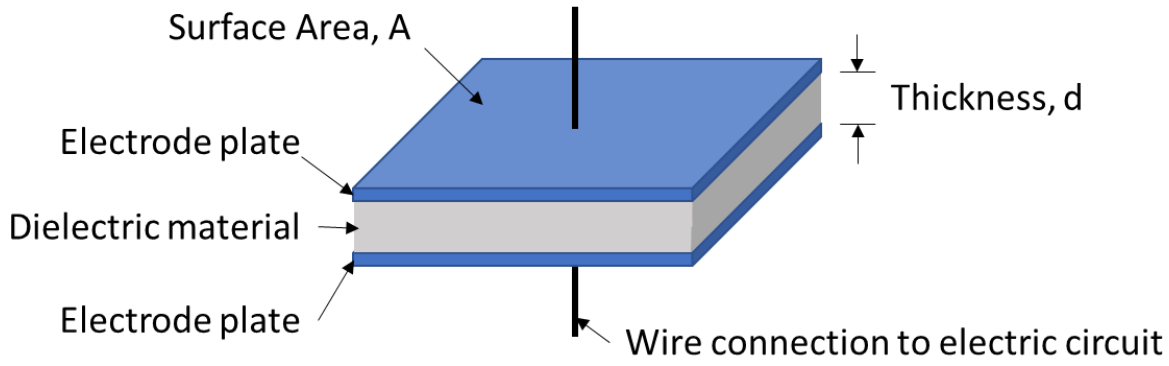

Figure 2.1 Schematic of a simple plate capacitor.

of the dielectric material.

Although decreasing the thickness of the dielectric layer increases the capacitance it also increases the electric field the material experiences based on a fixed applied voltage:

$$E = \frac{V}{d} \tag{2.3}$$

where E is the electrical field experienced by the dielectric, V is the applied voltage and d is the thickness of the dielectric layer.

The dielectric breakdown strength (DBS) of a material relates to the maximum E value the material can experience whilst retaining its insulating and capacitive properties. Whilst avoiding DBS, commercial MLCCs regularly contain dielectric layer thicknesses of ≤10 µm.

2.2.1. Dielectric loss (tan δ)

In an Alternating Current (AC), the electric field direction is changing at the frequency of the applied AC. In a resistive circuit, the resistance is independent of frequency and as V=IR, the changes in voltage and current are in-phase and proportional. This can be seen by the waveforms of AC voltage and current being in-phase, Figure 2.2 (a).

In an ideal capacitor, the current is related to voltage by:

$$I = C\frac{dV}{dt} \tag{2.4}$$

where I is current, C is capacitance, V is voltage and t is time.

From equation (2.4) the current across a capacitor is largest when there is the greatest change in voltage. This relationship results in a 90° phase shift between the AC voltage and current, as shown in Figure 2.2 (b).

Real dielectric materials do not behave ideally and contain a resistive component. This resistance results in losses of electrical energy, due to some conversion to heat energy during the AC cycles. The δ value is the difference in phase shift between the ideal and real capacitor, Figure 2.2 (c). The larger the δ shift, the lower efficiency in electrical storage.

The tangent of the δ, tan δ, quantifies the dielectric loss of a dielectric material. A low tan δ is desired for capacitor applications, to minimise the energy losses (as heat) per cycle and thus increasing the efficiency of the capacitor in storing electrical energy.

The real capacitance can be modelled as an ideal Capacitor element in series with an Equivalent Series Resistor (ESR), Figure 2.2 (d). tan δ is the ratio of these components ESR to C_{ideal}:

$$\tan \delta = 2\pi f \, C_{ideal} * ESR \tag{2.5}$$

where f is frequency.

For the purposes of this thesis, the dielectric material needs to attain tan δ < 0.04 for the material to be considered for MLCC applications. More stringent limits, such as tan δ <0.02, are often quoted in the literature [2].

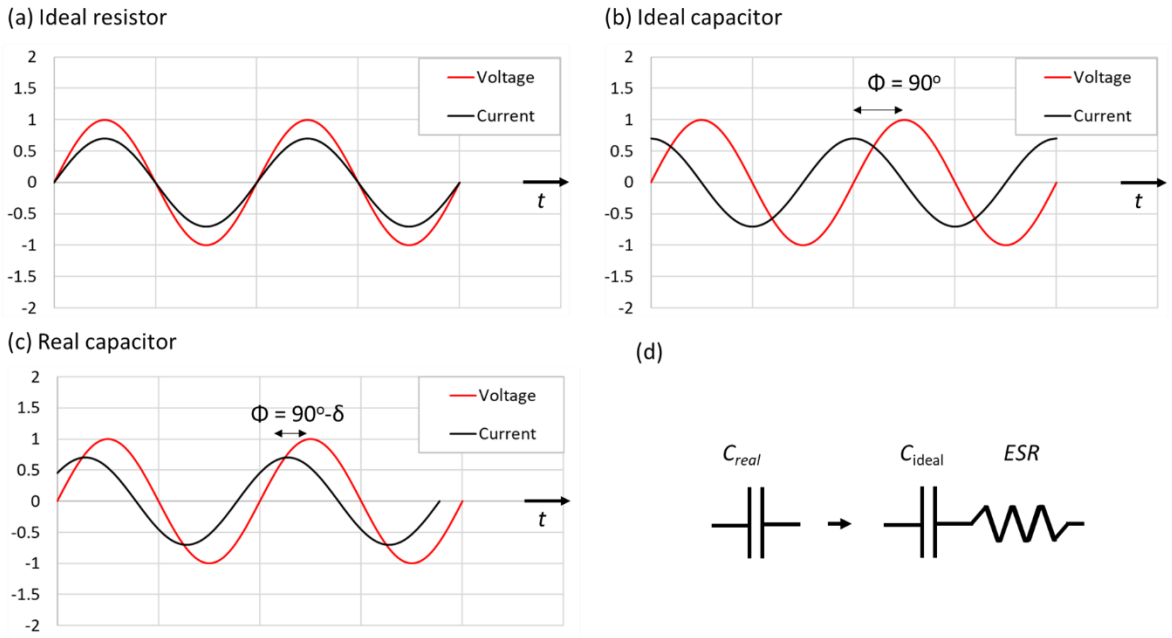

Figure 2.2 Waveforms of voltage and current. (a) A purely resistive response and (b) a purely capacitive response. The capacitive element has a phase shift, Φ = 90°. A real dielectric material contains both a resistive and capacitive component, resulting in 0 < Φ < 90°.

2.3. Ferroelectricity

Having first been observed in Rochelle salt ($KNaC_4H_4O_6 \cdot 4H_2O$) [3] ferroelectricity was observed in $BaTiO_3$ in ~ 1940 [4, 5]. Ferroelectric materials possess a spontaneous polarisation, the direction of which can be reversed under an external electric field [5, 6]. In an MLCC, the high polarisation behaviour can store useful electrical energy in the material, improving the capacitance (or reducing the size) of the MLCC.

2.3.1. Ferroelectric domain walls

Although ferroelectric materials have spontaneous polarisation, it is energetically unfavourable for all the dipoles to align in the same orientation, due to the large depolarisation field generated to maintain electroneutrality [7]. Instead, ferroelectric materials consist of ferroelectric domains with each region having a localised dipole alignment. Neighbouring domains have a different alignment direction (e.g. 90° or 180° in tetragonal $BaTiO_3$), minimising the macroscopic polarisation and the depolarisation forces. The region(s) separating these domains are referred to as domain walls.

Under an external electric field, a net polarisation is induced in the ferroelectric material in the direction of the electric field. This polarisation evolves through the growth of domains in the field direction. This domain growth results in the movement in the domain walls, and involves the 'flipping' of misaligned dipoles (and domains) to the field direction [8].

In an alternating current, the field direction is continuously changing, involving the constant movement of these domain walls as the field direction changes. The energy required to move the domain walls is lost to the system as heat, with domain wall motion being a main contributor to tan δ for many ferroelectric materials.

2.3.2. Curie Weiss Law

At the Curie Temperature (T_c), a phase transition occurs in which the material transitions from being a polar ferroelectric to a non-polar paraelectric. Above T_c, the permittivity decays according to the Curie-Weiss law:

$$\varepsilon_r - 1 = \frac{C}{T - T_O} \tag{2.6}$$

where C is the Curie constant, T is the specified temperature ($T>T_C$) and T_o is the extrapolated Curie Weiss temperature. In many ferroelectric ceramics, $\varepsilon_r >> 1$, and thus the left hand side simplifies to:

$$\varepsilon_r - 1 \approx \varepsilon_r \tag{2.7}$$

An example permittivity profile of a first order phase transition from a ferro- to para-electric transition is shown in Figure 2.3 (a), with the permittivity response sharply increasing as temperatures approach the phase transition. The permittivity peak occurs at the temperature T_{max}, before decreasing with increasing temperature. The linear response observed in the inverse permittivity plot ($T>T_{max}$), demonstrates the decrease in permittivity follows the Curie Weiss law ($\varepsilon_r \propto T^{-1}$). The T_O value can be obtained by extrapolating this gradient to the x axis. In 1st order phase transition ferroelectrics, $T_O < T_C$, whilst for 2nd order transitions $T_O = T_c$ [6, 7].

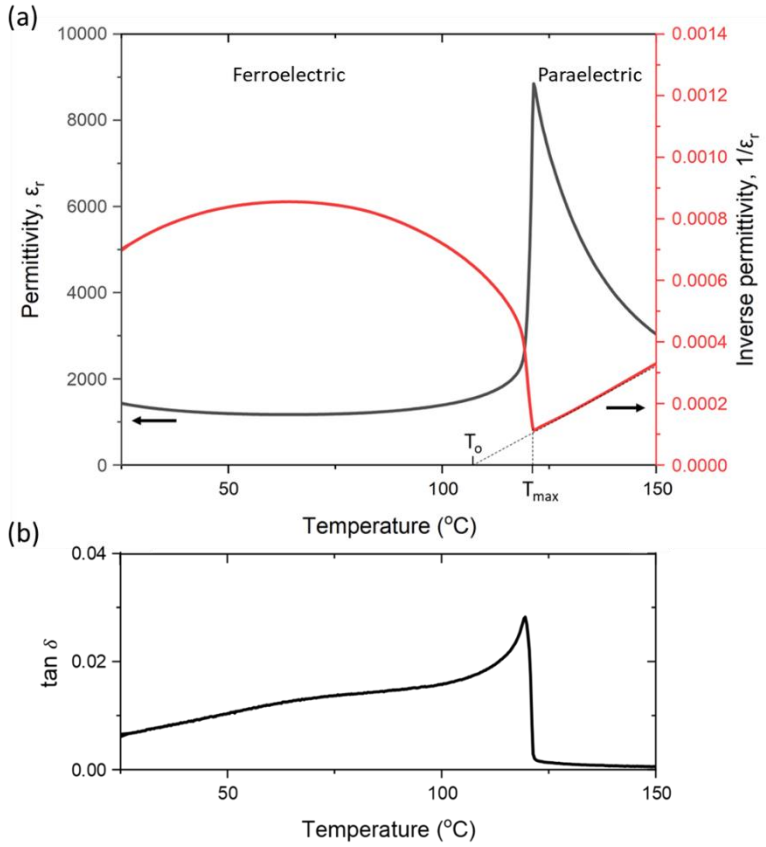

Figure 2.3 The dielectric behaviour of a typical ferroelectric material approaching a first order ferroelectric to paraelectric phase transition. (a) The sharp permittivity peak of a ferroelectric transitioning to a paraelectric (black line), whilst the red line shows the inverse permittivity profile (red line). The temperature of maximum permittivity, T_{max}, is also shown in the inverse permittivity response. The tan δ response, (b), shows a maximum as T_{max} is approached. Figure based on BT data reported by Foeller [9].

The tan δ response is shown in Figure 2.3 (b), with high dielectric losses occurring as the temperature approaches T_{max}.

2.3.3. Ferroelectric Materials

This increase in dielectric loss with temperature is attributed to the increased mobility of the domain walls. This occurs due to the decrease on internal stress in the crystal structure, as the lattice distortion decreases [7]. Beyond T_{max}, the tan δ suddenly declines, as domains no longer form and thus no dielectric losses due to domain wall occur. Ferroelectric Materials

Ferroelectric oxides have 4 general groups: Tungsten Bronze, Oxygen Octahedral ABO_3 Perovskites, Pyrochlore and Bismuth containing layered structures [6]. Ferroelectric materials are a subset of pyroelectric materials, which in turn are a subset of piezoelectric materials, Figure 2.4. For piezoelectric materials, a mechanical stress on the material generates an internal electric polarisation. Piezoelectric usages include stress sensors [10] and microelectromechanical systems (MEMS) [11]. Pyroelectric materials induce electric polarisation through a temperature gradient and have potential in harvesting waste heat [12].

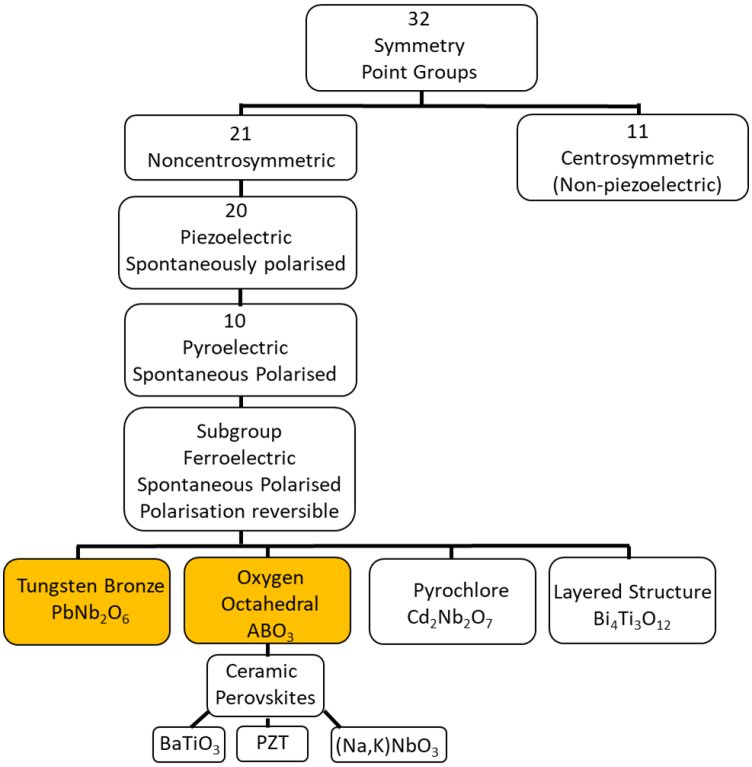

Figure 2.4 Diagram showing how ferroelectric materials are also pyroelectric and piezoelectric materials, and the four groups of ferroelectric materials [5].

2.3.4. Anti-Ferroelectric

In anti-ferroelectric materials (AFE), the electric dipoles align in an antiparallel formation, with adjacent dipoles having opposite directions [13]. Figure 2.5 shows the same direction of dipoles achieved in FE materials (a), compared to the chequerboard type formation of AFE materials (b).

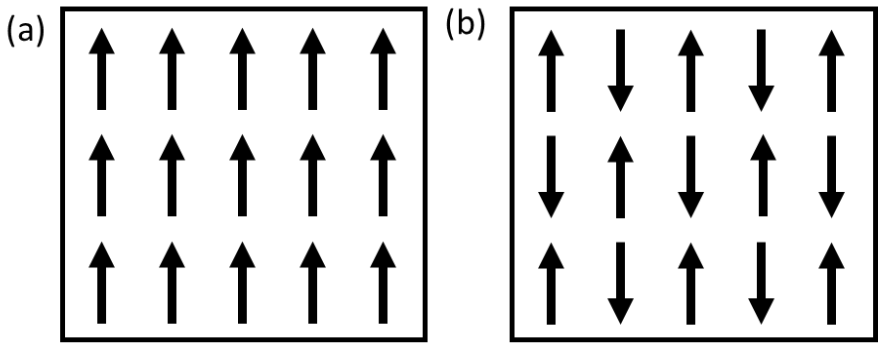

Figure 2.5 Schematic of dipole alignment in (a) ferroelectric and (b) anti-ferroelectric materials.

This preference of an antiparallel orientation results in no macroscopic spontaneous polarisation occurring in AFE materials, as the dipole directions average to zero. For an AFE material to be polarised, a large external field is required to force a bias in dipole direction to that of the external field, and thus inducing behaviour similar to a FE [5]. AFE behaviour is lost at temperatures above T_c as the material becomes paraelectric. With the exception of high electric fields, the permittivity values achieved for AFE materials are usually significantly lower than for FE materials. AFE materials are therefore only considered for high voltage circuits, such as high energy capacitor applications [14].

Some materials can undergo phase transitions, where the material transitions from FE to AFE behaviour. An example of this is Sodium Niobate, ($NaNbO_3$), which is discussed in section 0.

2.3.5. Relaxor-Ferroelectric

Under an alternating current (AC), there is momentary delay in the creation of the permittivity response of a material, as the dipoles orientate to the new field direction. If the field changes direction faster than the dipoles can reorientate the net polarisation of the material is reduced. This dielectric relaxation issue results in the permittivity magnitude of the material being frequency dependent, with lower permittivity achieved when measured at higher AC frequencies.

In classical ferroelectric materials, AC frequencies up to 1 MHz have little effect on the permittivity response, other than a slight suppression in maximum permittivity (ε_{max}) at the ferro- to para-electric phase transition. The temperature which the peak in permittivity occurs (T_{max}) is unaffected by frequency.

Relaxor-ferroelectric materials display significant dependency on frequency, often affecting the permittivity response over large temperature regions [15]. For brevity, these materials are referred to as relaxors in this thesis. Relaxor materials often display broad permittivity profiles, regardless of the frequency of the external field [16]. A higher frequency results in a lower ε_{max}, with T_{max} shifting to higher temperatures, as shown in Figure 2.6 (a). A different response is observed in the tan δ

response of many relaxor materials, with larger losses at higher frequencies, Figure 2.6 (b). However, like permittivity, an increase in T_{max} with frequency also occurs in the tan δ response.

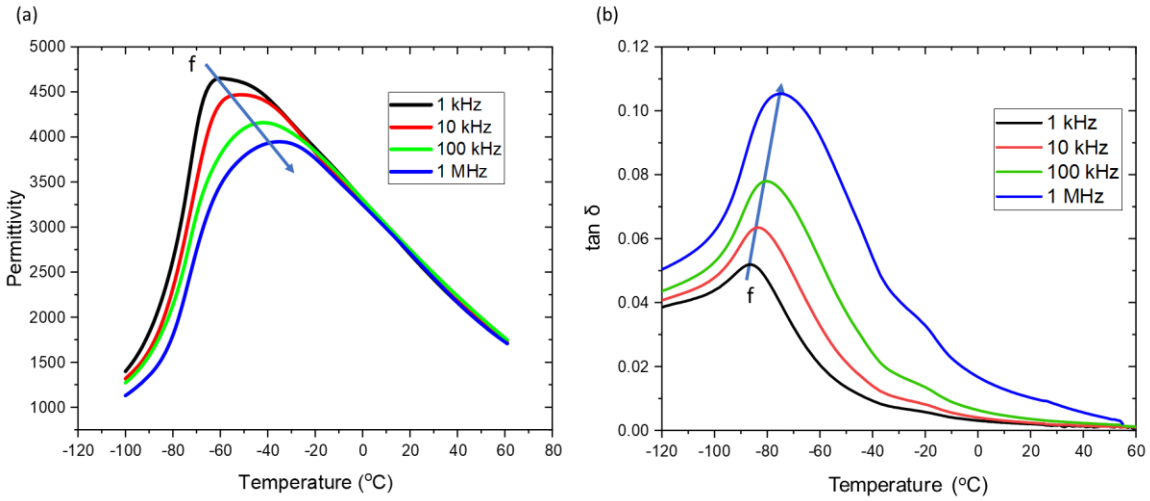

Figure 2.6 Typical dielectric behaviour of a relaxor material. (a) Typical permittivity-temperature profiles, showing frequency dependent permittivity behaviour. (b) Corresponding tan δ - temperature profiles, also demonstrating frequency dependency.

The frequency dependency of relaxor materials is often explained on the basis of the presence of polar nano regions (PNR). These regions have relaxation times that increase as temperature decreases [17]. This is attributed to the increased size of PNRs at lower temperatures which requires more time to reorient to the field direction.

At lower temperatures, the PNRs have a greater potential to contribute to the permittivity response of the material. However, the PNRs are also more susceptible to being 'frozen' at a specific frequency, suppressing their contribution to the magnitude of the permittivity. This makes the permittivity response highly frequency dependent at low temperatures. As temperature increases, the PNRs become less susceptible to being frozen, however their contribution is also reduced. This inter-relationship results in T_{max} increasing with frequency and ε_r decreasing with temperature. This response is shown in Figure 2.6. The exact origins and physics of PNRs are contested in the literature [16] and are beyond the scope of this work.

2.4. Multilayer Ceramic Capacitors (MLCC) types and classifications

Historically there are several classes of ceramic capacitors; however, these have been simplified to two distinct classes (Class 1 and Class 2) [1]. This thesis focuses on dielectric materials for Class 2 MLCCs, however a comparison to Class 1 is included for completeness.

Table 2.1 compares the relative performance of the two classes. The dielectric materials used for Class 1 applications are usually paraelectric resulting in a low permittivity response, and thus struggle to achieve high capacitance without the need for a large device. This permittivity response

is designed to be independent of temperature, frequency, and voltage. TiO_2 is a commonly used material, with various doping elements used to circumvent the reducing permittivity response that occurs for a paraelectric material with increasing temperature. The voltage independence is limited to relatively low voltages (< 50 V), due to issues with material damage when subjected to high electric fields.

Table 2.1 Summary of the performance differences between Class 1 and Class 2 MLCCs.

	Class 1 ceramics	**Class 2 ceramics**
Material	Paraelectric (e.g TiO_2)	Ferroelectric (e.g $BaTiO_3$)
Permittivity	10 – 500	500 – 10000
Voltage limits	< 50V	< 100V
Temperature Dependence	No	Yes
Frequency Dependence	Yes	Yes
Voltage Dependence	No	Yes
Ageing	No	Yes

The TCC performance of an MLCC over a specific temperature range is classified using a letter-number-letter code, Table 2.2. The first letter represents the lowest temperature of the range, whereas the number is the highest number of the temperature range. The last letter is the maximum TCC value allowed for the designated temperature range.

Table 2.2 Classification codes for Class 2 MLCCs.

Low temperature code (°C)	High temperature code (°C)	Allowed Capacitance change (TCC, %)
X = −55	4 = +65	P = ±10%
Y = −30	5 = +85	R = ±15%
Z = +10	6 = +105	S = ±22%
	7 = +125	T = +22/−33%
	8 = +150	U = +22/−56%
	9 = +200	V = +22/−82%

The TCC performance of two common classifications (X7R and Y5V), are shown in Figure 2.7. The P, R and S code letters are symmetrical in TCC%, with identical requirements in stability for both positive and negative % changes. The T, U and V codes all limit positive TCC% to less than +22%, however a greater negative % change is allowed. The V code is most asymmetric, with TCC limits of +22% and -82%.

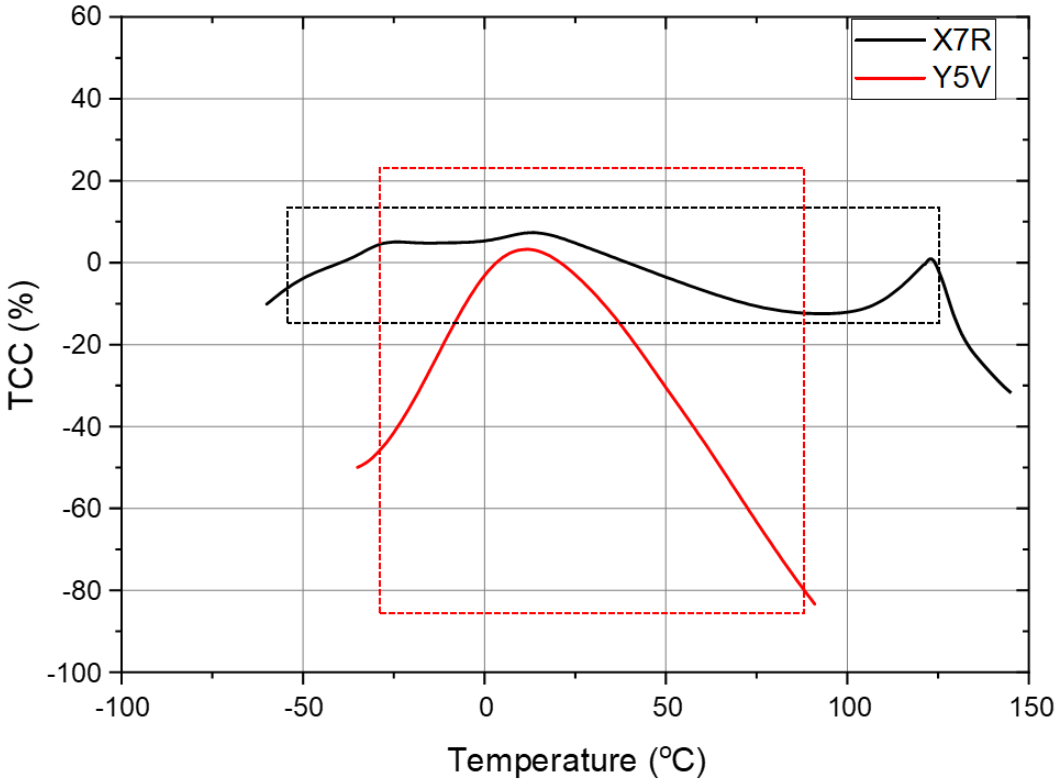

Figure 2.7 Example TCC profiles that meet the X7R (-55 to 125°C, TCC= ±15%) and Y5V classification (-30 to 85°C, TCC = +22/-82%). Dashed boxes indicate the deviation in TCC allowed for these two classifications and the respective temperature ranges.

2.4.1. Voltage Dependence

The voltage dependence of MLCC devices is often quantified as Voltage Coefficient of Capacitance (VCC), calculated as:

$$VCC\ (\%) = \frac{\varepsilon_r(V) - \varepsilon_r(0)}{\varepsilon_r(0)} * 100 \tag{2.8}$$

where $\varepsilon_r(0)$ is the relative permittivity at zero DC bias and $\varepsilon_r(V)$ is the relative permittivity at applied DC voltage V.

For Class 2 MLCCs, an AC voltage between 0.5 and 1 is typically applied when measuring the capacitance of a device. This AC voltage is enough to induce domain wall motion, generating a net polarisation in the ferroelectric material. The schematic in Figure 2.8 (a) has a cyclic AC voltage, with zero DC bias. The vertical arrow directions demonstrate the polarisation direction changes (+/-) that this field induces in the ferroelectric materials. Plot (c) discretises the waveform into positive direction (blue) and negative direction (yellow) boxes, also indicated by the arrow directions. These boxes represent equivalent time periods, demonstrating no preference in polarisation direction.

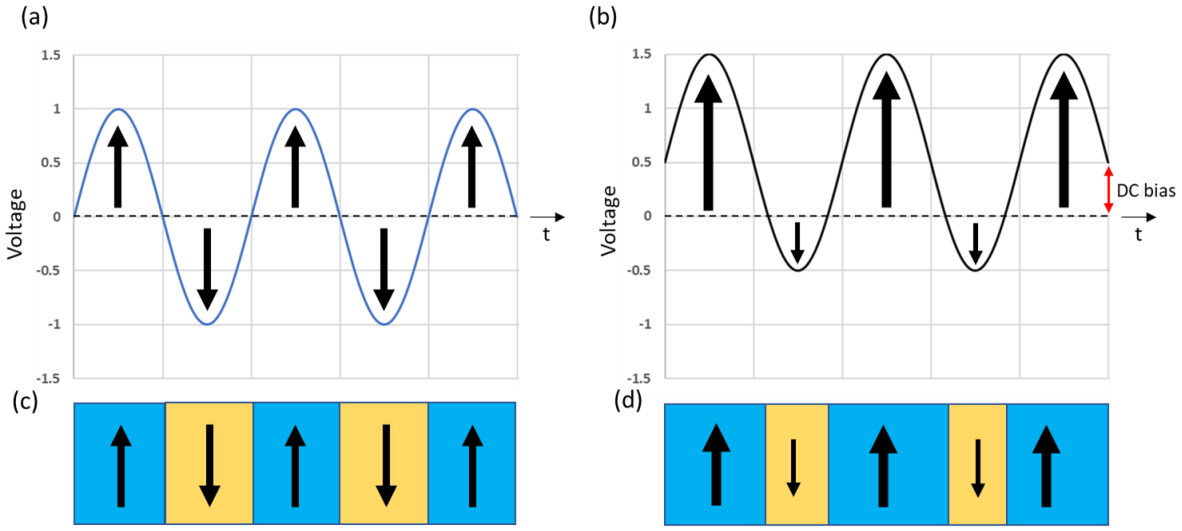

Figure 2.8 Voltage sine wave produced in Alternating Current, without (a) and without (b) DC Bias. (c) and (d) demonstrate the distribution of time in polarisation direction, of (a) and (b) respectively.

However many MLCC applications occur in electrical systems with a DC bias, an example of this voltage waveform is shown in Figure 2.8 (b). The waveform has a larger magnitude in the positive direction, than in the negative direction. The voltage is also positive for a greater proportion of the alternating cycle, as shown by the enlarged blue regions of part (c). If DC bias is substantial, the negative voltage will not be sufficient to completely reverse the polarisation direction of the ferroelectric material, resulting in some domains having a static polarisation direction.

This situation reduces the capacitance magnitude of the ferroelectric material, as only a proportion is responding to the AC field direction. This decrease in capacitance with DC Bias is observed in Class 2 MLCCs, Figure 2.9. As a greater DC Bias is applied, the capacitance magnitude is further reduced.

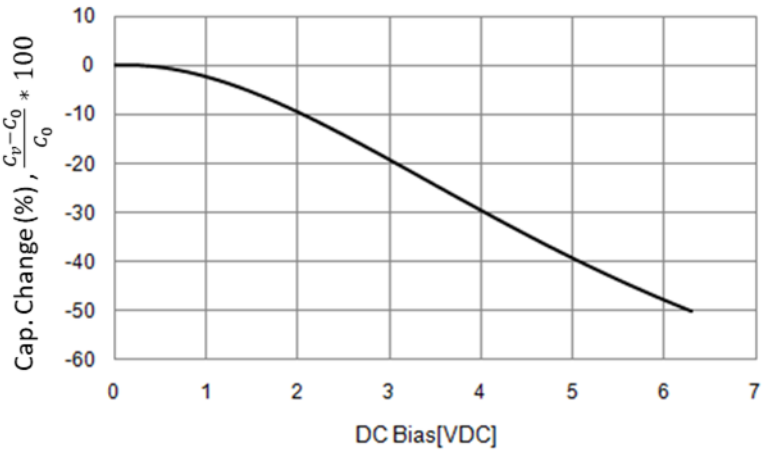

Figure 2.9 VCC response of a typical class 2 MLCC material, demonstrating the decrease in capacitance as the DC bias applied is increased. VCC values are often given on MLCCs at 25°C.

One of the earliest approaches to model the VCC response was reported by Johnson et al. [18], using the following semi-empirical formula:

$$\varepsilon_r(E) = \frac{\varepsilon_r(0)}{[1 + 3\beta(\varepsilon_r(O) * \varepsilon_o)^3 * E^2]^{1/3}} \tag{2.9}$$

Where $\varepsilon_r(0)$ is the relative permittivity at zero applied field, E is the external applied field, ε_o is the permittivity of vacuum and β is a coefficient of ferroelectric nonlinearality. The β coefficient of a ceramic sample is determined through fitting to the experimental measurements. The modelled response to experimental data is shown in Figure 2.10, reported by Johnson et al. on $Ba_{0.6}Sr_{0.4}TiO_3$ material.

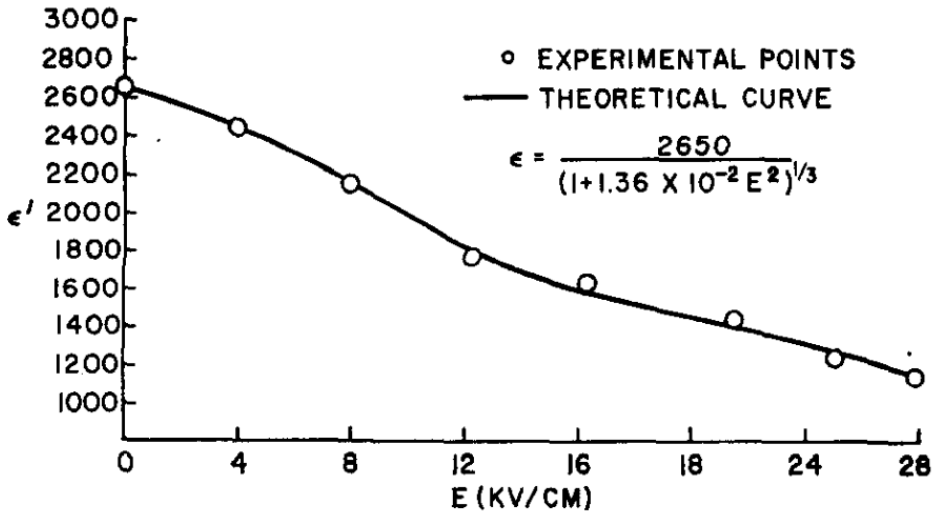

Figure 2.10 Change in Permittivity response with increasing electric field strength. The theoretical curve, obtained from Johnson Equation, fitting closely to the experimental points. Figure by Johnson et al. [18], with permission of AIP Publishing.

This model has been reported to be particularly effective for ceramics of large grain size [19], which have relatively uniform electric field strength. However localised regions of high electric field can be produced due the microstructure of the ceramic [20], or the roughness of the electrode surface [21], which Johnson's equation cannot properly consider. These simulations require Finite Element Methods (FEM) approaches, which allow non-uniform electric fields to be simulated, at the cost of simulation complexity. However the demand for ultrafine grains industrially [22], makes FEM and other approaches necessary to model dielectric layers in MLCC devices.

2.5. Perovskite Structure

When calcium titanate ($CaTiO_3$) was discovered in 1839, it was named Perovskite, after the mineralogist Count Lev Perovski. The term perovskite structure is used for a group compounds of similar crystal structure, ABX_3. This thesis mainly focuses on perovskites with oxygen (O^{2-}) as X, however other anions do form perovskite structures, such as the fluoride materials $NaMgF_3$ [23] and $AgCuF_3$ [24].

The ideal perovskite structure has a cubic unit cell, as shown in Figure 2.11 (a). The repeating unit cell has A-sites at the corners, with oxygen atoms at each face centre, creating an oxygen octahedron. The B-site is at the centre of the cube, within the oxygen octahedron.

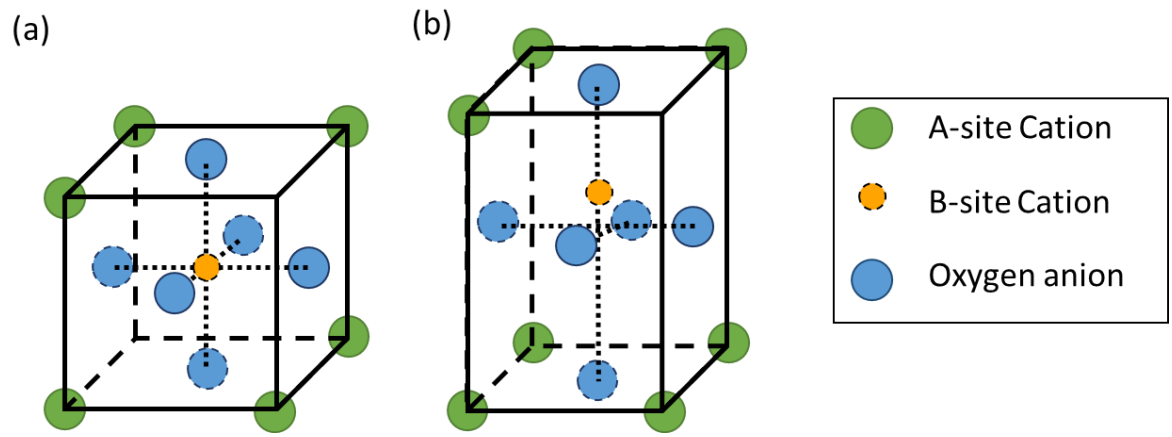

Figure 2.11 Schematic of the perovskite structure, with A-site cations at the corners and oxygen anions at the face centres. The oxygen formation produces an octahedron, at the centre of which is the B-site cation. (b) A c axis elongation, with the B-site not central to the unit cell.

2.5.1. Tolerance Factor

The stability of the perovskite structure is largely dependent on the relative atomic radii of the A-site cations (r_A), B-site cations (r_B) and oxygen anion (r_O). For an ideal cube, the face-diagonal distance is the face-length value multiplied by √2, as shown in Figure 2.12 (a). The oxygen octahedra and B-site cation proximity are shown in (b), whereas (c) shows the A-site cations and oxygen anion contacts.

From (b) and (c) the ideal perovskite structure is achieved when the atomic radii satisfy both x = 2 (r_A + r_O) and √2 x = 2(r_B +r_O), for the same value of x.

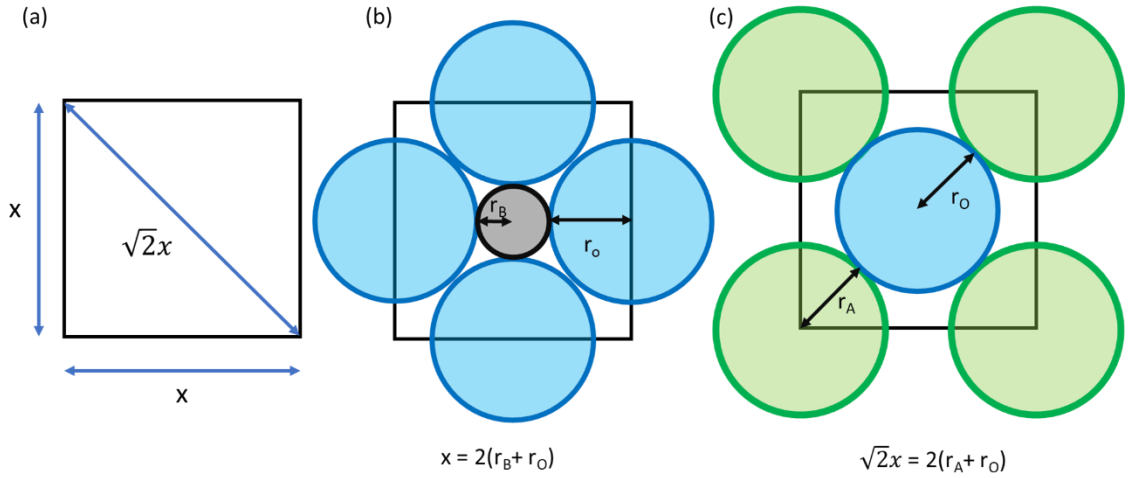

Figure 2.12 The face dimensions of an ideal cube (a), and how this relationship is applied to ideal cubic perovskites. (b) The (200) plane cutting through 4 of the face centre oxygen atoms, showing the small B cation at the centre. (c) The face of the unit cell (100) plane, with anions at the corners and oxygen at the face centre.

The Goldschmidt tolerance factor uses this interrelationship of an ideal cube to quantify the degree of distortion that occurs in the perovskite structure:

$$t = \frac{r_A + r_O}{\sqrt{2}(r_B + r_O)} \tag{2.10}$$

with an ideal cubic perovskite occurring for t=1. The perovskite structure occurs for compounds with a range of t = 0.77 to 1.06 [25]. An A cation size mismatch often results in a distortion of the unit cell from a perfect cube. If the A site cation is too small, then t < 1, with oxygen octahedral tilting occurring to minimise the A-O distance [26]. An oversized A site cation, t>1, causes distortion to the oxygen octahedra, inducing a displacement of the B site cation from the centre of the unit cell. Perovskites with t > 1, are frequently associated with ferroelectric materials with high permittivity values [25].

Larger cations usually occupy the A-site, with smaller cations occupying the B-site. To achieve stoichiometry, the A and B-site cations often have 1 of 3 cation charge ratios, Table 2.3.

Table 2.3 Cation and charge ratios of perovskite structures.

Cation ratio	Charge Formula	Example	Tolerance factor	Ref.
1:2	$A^{2+}B^{4+}O^{2-}_3$	$BaTiO_3$	1.06	[27]
1:1	$A^{3+}B^{3+}O^{2-}_3$	$LaAlO_3$	1.009	[28]
1:5	$A^{1+}B^{5+}O^{2-}_3$	$NaNbO_3$	0.967	[29]

2.6. $BaTiO_3$ (BT)

In the case of $BaTiO_3$, the A-site cation is oversized, with *t*=1.06. The phase transitions and the resulting effect on the permittivity response with temperature is shown in Figure 2.13. At high temperatures (T > 120°C), the B-site cation (Ti^{4+}) sits at the centre of the BO_6 octahedron, resulting in BT being cubic and paraelectric. At T ~120°C, BT transitions from a cubic to tetragonal structure with an elongation along the [001] direction. This distortion causes a displacement of the B-site cation (Ti^{4+}) from the centre of the unit cell (with creation of a dipole moment), making BT ferroelectric. The spontaneous polarisation, P_s, direction is [001], i.e in the same direction as the elongated c axis of the unit cell.

The tetragonal structure is stable until ~5°C, below which BT becomes orthorhombic (T_{O-T} = 5°C). The final distortion occurs at -90°C, with a transition to a rhombohedral structure (T_{R-O} = -90°C). As shown in Figure 2.13, there is an increase in permittivity at each phase transition which is due to the internal distortions created as the structure undergoes the phase transition [6]. However, the responses at T_{R-O} and T_{O-C} are minor compared to the permittivity peak resulting at T_c, with ε_{max} often exceeding ~ 10,000. This increase in permittivity results in TCC > 500% which is significantly above the requirements for MLCC applications, Table 2.2. Undoped BT is therefore unsuitable for Class 2 MLCC applications.

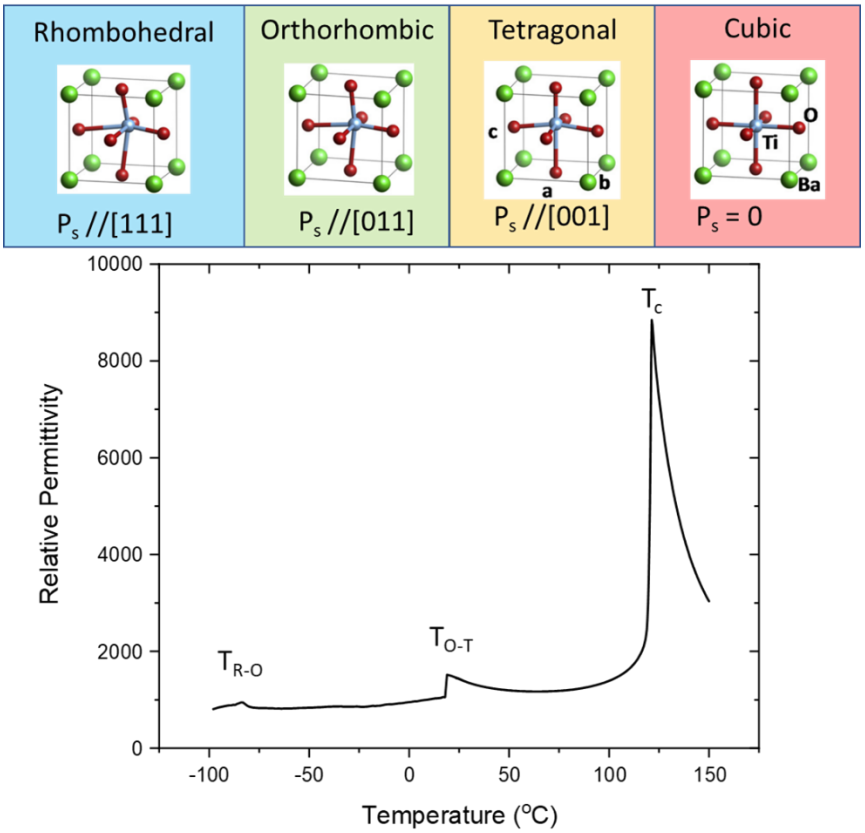

Figure 2.13 Dielectric response of $BaTiO_3$ (BT), for the temperature range -100 to 150 °C. The abrupt changes in permittivity are attributed to the various polymorphic phase transitions. The temperature ranges of stability for each polymorph are shown above the plot, with rhombohedral and cubic responses continuing beyond the plotted temperature range.

2.7. Core Shell Microstructures

To make $BaTiO_3$ a viable material for MLCC applications, it is often chemically doped to produce a heterogenous ceramic microstructure. As shown in Figure 2.14, there are many cations that can be substituted onto either the A or B sites of BT. Except for the small increase in T_c with particular Ca^{2+} doping concentrations [30], these cation substitutions result in a decrease in T_c compared to undoped BT. A much more rigorous review of doped BT has recently been published by Veerapandiyan et al. [31].

For isovalent doping (Ba^{2+} or Ti^{4+} substituted with cations of the same charge), the decrease in T_c can be explained by the reduction of the Goldschmidt tolerance value towards the ideal value (t = 1). t = 1.06 of undoped BT is due to a mismatch of the Ba^{2+} and Ti^{4+} cation sizes. To improve towards t = 1, either the A-site cation size needs to decrease or the B-site cation size needs to increase.

t values are more sensitive to changes in the B site radii due to the √2 on the denominator ($\sqrt{2}(r_B + r_O)$). This simple relationship allows a general explanation as to why B site substitution has a greater effect on T_c, when substitutions are limited to isovalent cations [1]. However, as shown by the sharp

decrease in T_c with A-site doped La^{3+} (based on the composition $Ba_{1-x}La_xTi_{1-x/4}O_3$) this Goldschmidt relationship of ionic radii readily applies to aliovalent substitutions (where cations are not of the same charge number). In this case, the decrease in T_c is related to the creation of Ti vacancies in the crystal structure that greatly disrupt the formation of the ferroelectric domains [32].

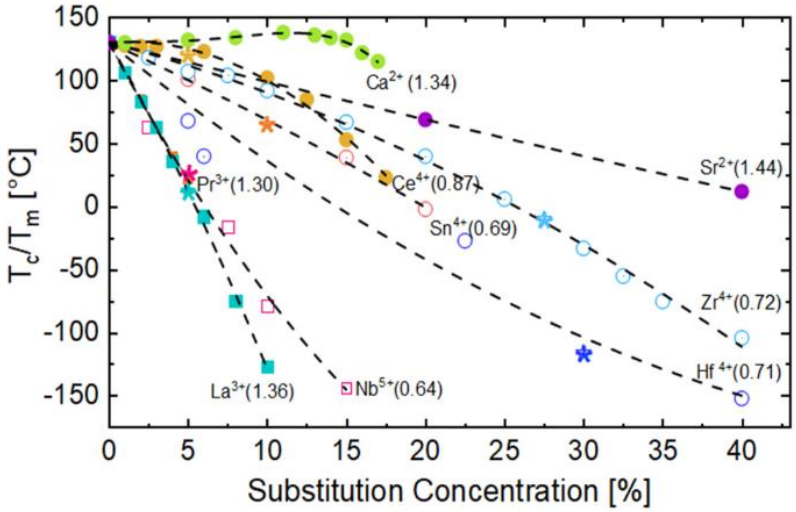

Figure 2.14 BT can be doped on the A-sites (filled symbols) or B-sites (open symbols) by many elements. Except for Ca^{2+}, all result in a decrease in T_c, with increased concentration. Figure from Veerapandiyan et al. 31], with permission from MDPI.

A core and shell microstructure is often produced by first forming undoped BT grains and then milling in a liquid containing the chemical dopants [33, 34]. When dried, this approach results in a thin layer of dopants on the surface of the BT grains. During the sintering step, the high temperature induces mass transport of the dopants into the BT grains with the dopants replacing the Ba^{2+} or Ti^{4+} cations from their respective lattice sites. The sintering time is restricted to limit the diffusion process, resulting in a 'shell' region consisting of a doped gradient, and a 'core' region of undoped BT.

This microstructure for a Y-doped BT ceramic is shown in Figure 2.15 (a), with the core and shell regions of a grain labelled, whereas (b) shows the gradient of Yttrium doping towards the centre of the grain. The doping concentration of the shell produces a broadened permittivity response with T_{max} that is lower than undoped BT.

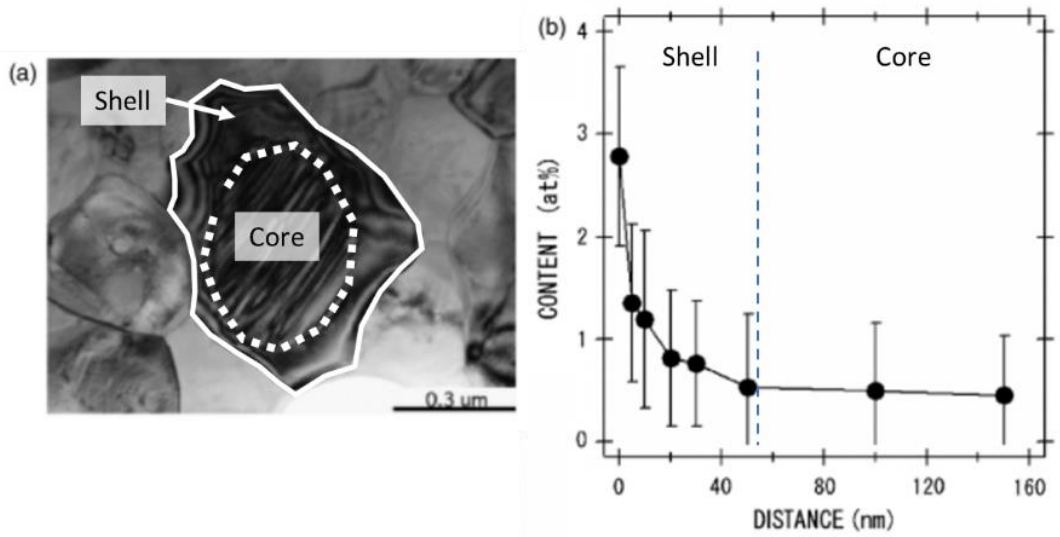

Figure 2.15 TEM image of a core and shell microstructure created with Yttrium doped BT. (b) Y doping gradient from 0 to ~50 nm into the grains, which is the shell region. Deeper than 50 nm is labelled as the core region, with little Y content. Adapted from Yasukawa et al. [35].

An example permittivity profile achieved by the creation of a core and shell microstructure is shown in Figure 2.16. The permittivity response at low temperature is improved by the gradient of T_{max} produced by the shell. At T ~120°C, the permittivity of the shell region is low due to it being paraelectric. The sharp peak at T_{max} ~120°C of undoped BT is therefore suppressed by the shell material.

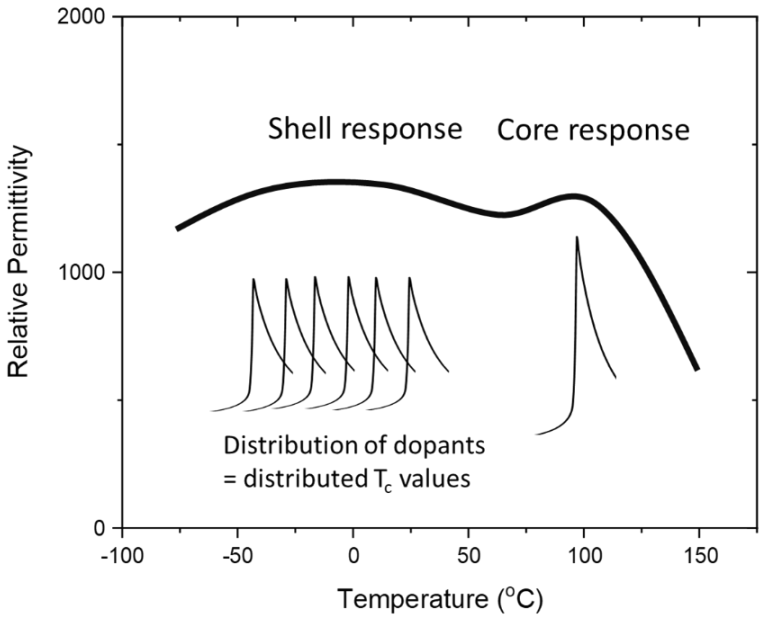

Figure 2.16 Typical permittivity response of a core and shell microstructured ceramic, showing T_{max} of both the shell and core. The shell response increases the low temperature permittivity, whereas it suppresses the high temperature permittivity peak of the undoped BT core.

2.7.1. BT limitations

One issue with the core and shell model is the impact of the core to shell ratio on the stability of the permittivity response. This ratio can be challenging to quantify due to the 3D geometry of the grains in the ceramics. Transmission Electron Microscopy (TEM) is often used to produce a 2D image that allows the core and shell regions to be distinguished. This approach can underestimate the size of the grains, as the 'slice' is unlikely to cut through the absolute middle of a grain. Therefore, many grains are assessed in a single image, with the core to shell average ratio being extracted. However, as reported by Morshead et al. [36], the simplest averaging approach can lead to large errors in extracted ratios compared to the actual core to shell ratio.

This approach of quantifying the core to shell ratio is also destructive, often preventing the sample being electrically tested after being prepared for TEM. Although the permittivity response of a core to shell ratio can be simulated [37-39], producing a specific core to shell ratio requires fine tuning of multiple interacting factors [40].

An example of the dependence on the processing conditions of producing a TCC profile for core-shell BT ceramics is seen in the work by Jeon et al. [41], Figure 2.17. For ceramics sintered at 1300°C for 0.5 hours, the TCC profile displays a significant peak that is due to the presence of a large core (undoped BT). As the sintering time is increased, the core response is suppressed, as seen by the decrease in TCC(%) at 120°C, and the increase at low temperature. For ceramics sintered for 0.5 hours, X8R (-55 to 150°C) is just achieved. However, with 1 hour of dwell time X8R is not achieved, degrading to X7R (max temperature being 125°C). If the sintering time exceeds 4 hours there is significant deterioration of the TCC profile.

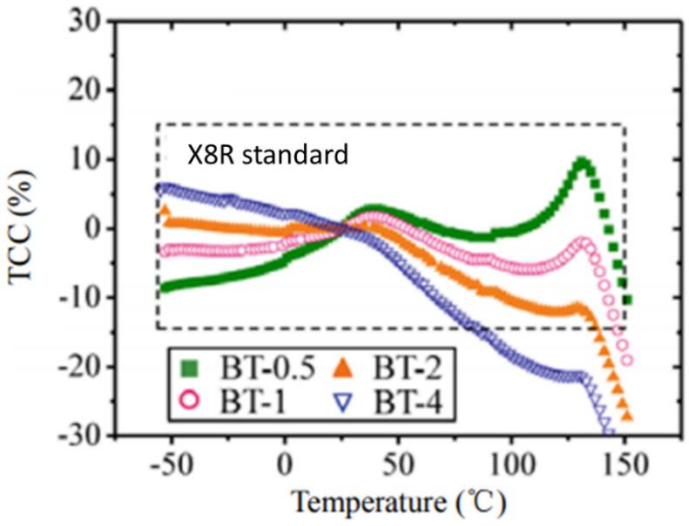

Figure 2.17 Sintering time dependence on the TCC (%) profile of BT based core shell materials. The numbers in the legend are the number of hours of the dwell time (at 1300°C). Figure by Jeon et al. [41], with permission of Springer.

Another issue with core and shell materials is the dependence of the TCC response on the geometry/dimensions of the sample. Wang et al. [40] produced tape cast ceramics with core shell microstructures, with thicknesses ranging from 5 to 17.8 µm. As seen in Figure 2.18, the thinnest layers have a TCC-temperature profile that is dominated by the shell region of the core shell microstructure, with a low temperature peak in TCC(%). As the layer becomes thicker, the contribution of the core region increases, resulting in a TCC-temperature profile containing equal responses from both the shell and core regions. The plot also shows the TCC response for the material as a bulk ceramic pellet (red line). The peak at ~125°C shows a further increase in the contribution of the core region to the permittivity response. The low temperature peak (around -30°C) that is observed in the micron scale layers is not present in the bulk ceramic pellet.

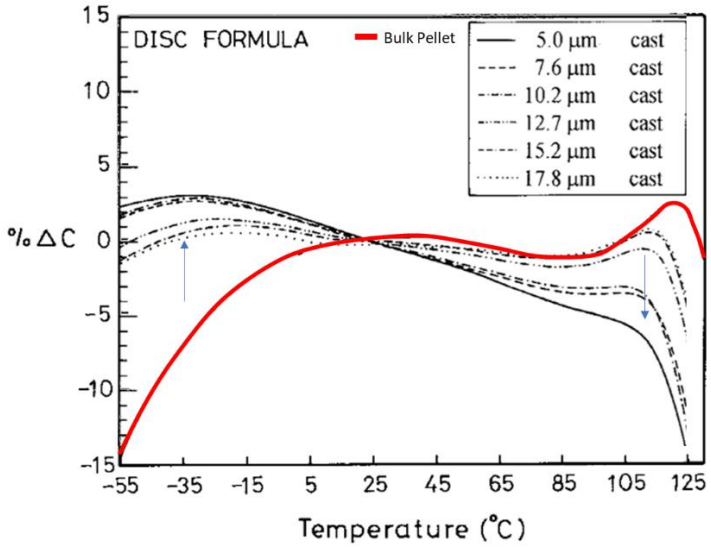

Figure 2.18 Comparison of the dielectric profile of a BT ceramic with a core shell microstructure. Adapted from Wang et al. [40]

These differences indicate that analysis of bulk ceramic samples would not be sufficient to properly optimise the sintering conditions of the core shell microstructure in tape cast materials. The reliance on producing MLCC scaled layers results in additional cost and time in researching these materials.

2.8. $NaNbO_3$ (NN)

Sodium Niobate, $NaNbO_3$, is a perovskite material, with a Goldschmidt tolerance t = 0.967 [29]. The 7 polymorphs of $NaNbO_3$ (NN) were first reported by Megaw et al in [42]. The exact crystal structures that occur have been debated over the last few decades. Initial work relied upon X-ray Diffraction (XRD) for symmetry identification, with NN reported as being orthorhombic at ambient temperatures up to 360°C [43]. The orthorhombic unit cell is shown in Figure 2.19.

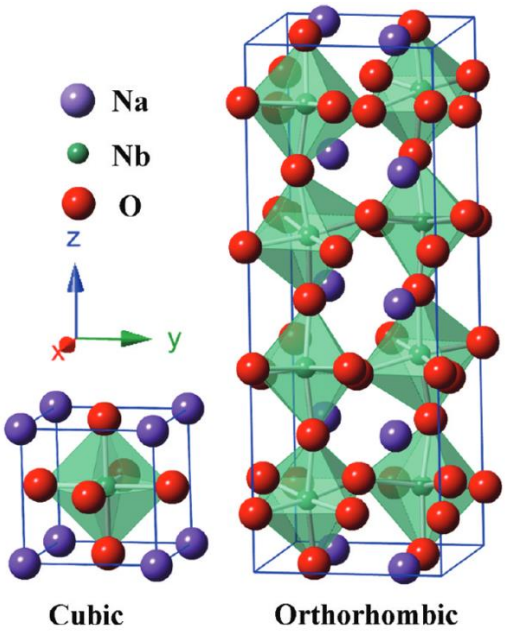

Figure 2.19 Orthorhombic crystal structure of $NaNbO_3$. Figure used with permission from Li et al. © 2012 American Chemical Society [44].

However, development of techniques such as neutron scattering have allowed for further analysis. Darlington et al. [45] reported that a monoclinic symmetry is produced at ambient temperatures. These findings are summarised in Table 2.4. The multiplicity column describes the number of oxygen octahedral units per unit cell.

Table 2.4 Phases of Sodium Niobate (NN), adapted from Darlington et al. [45]. Phases identified using Neutron Scattering.

Phase	Temp. range (°C)	Symmetry	Lattice constants	Unit cell angles	Multiplicity
N	<-80	Rhombohedral	$a'=b'=c'$	α=β =γ<90°	2×2×2
P	-80 ~ 370	Monoclinic	$a'\neq b'>c'$	α=β =90°, γ<90°	2×2×4
R	370 ~ 480	Orthorhombic	$a'\neq b'\neq c'$	α=β =γ=90°	2×4×6
S	480 ~ 520	Orthorhombic	$a'\sim b'\sim c'$	α=β =γ=90°	2×4×6
T1	520 ~ 575	Orthorhombic	$a'<b'<c'$	α=β =γ=90°	2×2×2
T2	575 ~ 640	Tetragonal	$a'=b'<c'$	α=β =γ=90°	2×2×1
U	> 640	Cubic	a=b=c	α=β=γ =90°	1×1×1

The work by Yuzyuk et al. [46] applied a host of different characterisation techniques (i.e Raman scattering, synchrotron x-ray diffraction and dielectric measurements), to further define the symmetry changes, Figure 2.20. This work reported the monoclinic P phase reported by Darlington et al [43] to be three polytypes; monoclinic (P_o), incommensurate (INC) and orthorhombic (P_m).

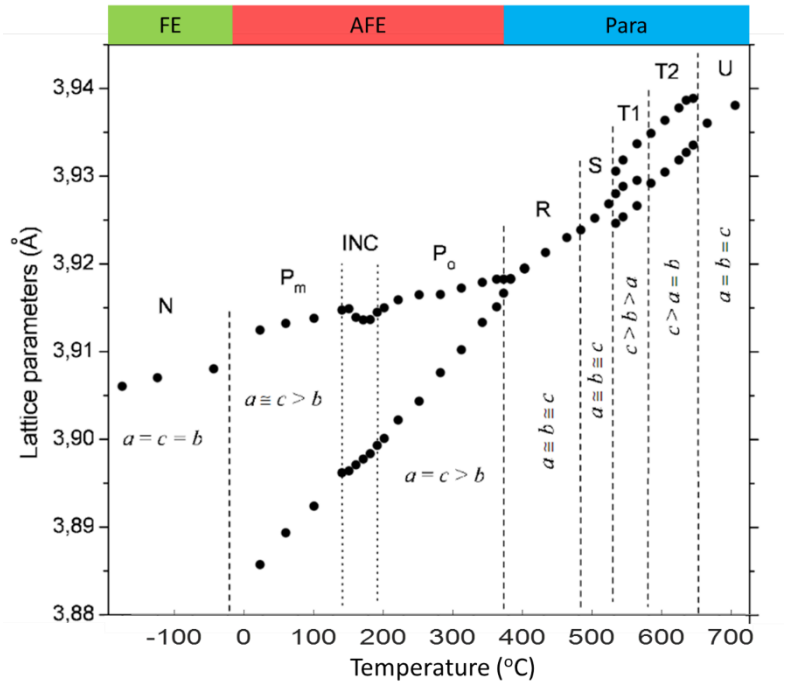

Figure 2.20 Summary of the NN polymorphic phase transitions adapted from Yuzyuk et al. [44]. The division into Ferroelectric (FE), Antiferroelectric (AFE) and Paraelectric (Para) phases are included above the plot.

The incommensurate phase produces a small response in permittivity at ~165°C, as reported by Guo et al. [47], Figure 2.21. Guo et al. report that through the use of in-situ hot-stage Transmission Electron Microscopy (TEM), the presence of an incommensurate phase at ~165°C in NN was directly observed.

As shown in Figure 2.21, the permittivity response at ambient temperature is low ($\varepsilon_{RT} < 250$), which is attributed to the antiferroelectric (AFE) behaviour. The permittivity increases at ~360°C, with the system undergoing a phase transition from AFE to paraelectric. The high temperature of this phase transition is well above most working conditions of MLCC devices, again making undoped NN unsuitable for MLCC applications.

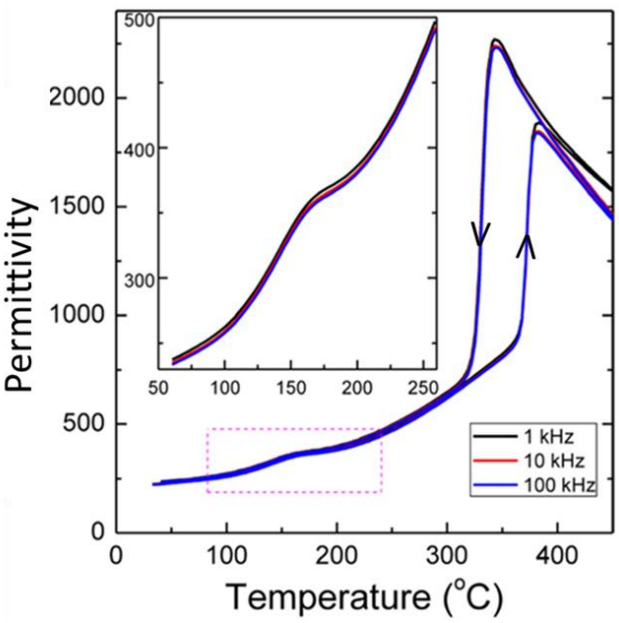

Figure 2.21 Permittivity-Temperature profile of NN, from 25°C to 450°C. Sub plot focusing on the dielectric anomaly at ~165°C, which the authors confirm is due to an incommensurate phase. The measurement direction (heating or cooling) of the permittivity profiles is labelled with arrows. Plot adapted from Guo et al. [47].

Potassium doping, $K_xNa_{1-x}NbO_3$ (KNN), has been found to stabilise the ferroelectric phase to higher temperatures [48], resulting in a permittivity profile more suitable for capacitor applications. The permittivity profiles of NN and two KNN compositions are compared in Figure 2.22, by Singh et al. [49]. The higher ε_{RT} achieved with K doping demonstrates the potential for NN with appropriate chemical substitutions to be used as a high T_{max} material.

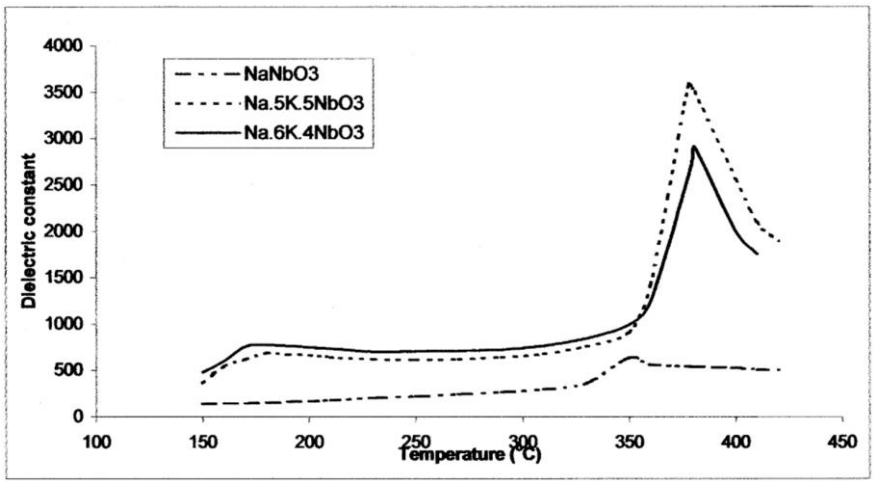

Figure 2.22 Dielectric properties of antiferroelectric $NaNbO_3$ (NN) and with K do*pi*ng (KNN). Figure by Singh et al. [49], with permission of Elsevier.

2.9. Solid Solution perovskites with high temperature stability

To achieve materials with high permittivity and T_c>150°C, many different BT based solid solutions have been investigated.

A review paper by Zeb and Milne [2] summarised potential perovskite-based solid solutions that have temperature stable permittivity at high temperatures. Relatively simple binary solid solutions, such as $BaTiO_3$ – $BiScO_3$ have rapidly progressed to more complex systems, such as 0.5 $BaTiO_3$ – 0.25$BiZrTO_3$ –0.25$BiScO_3$, in the pursuit of improved high temperature stability of the permittivity response.

The relaxor type profile of 50$BaTiO_3$–25$Bi(Zn_{0.5}Ti_{0.5})O_3$–25$BiScO_3$ is shown in Figure 2.23. Due to the relaxor behaviour, the broad permittivity peak shifts to higher temperatures with increasing frequency. The bars above the plot in Figure 2.23 show the temperature ranges that meet TCC < ±15%. If just considering the 1 kHz frequency, the temperature range extends to a lower temperature than if all the frequencies were considered. This frequency dependency is also seen in the tan δ response, with higher frequencies showing significantly higher losses than low frequencies.

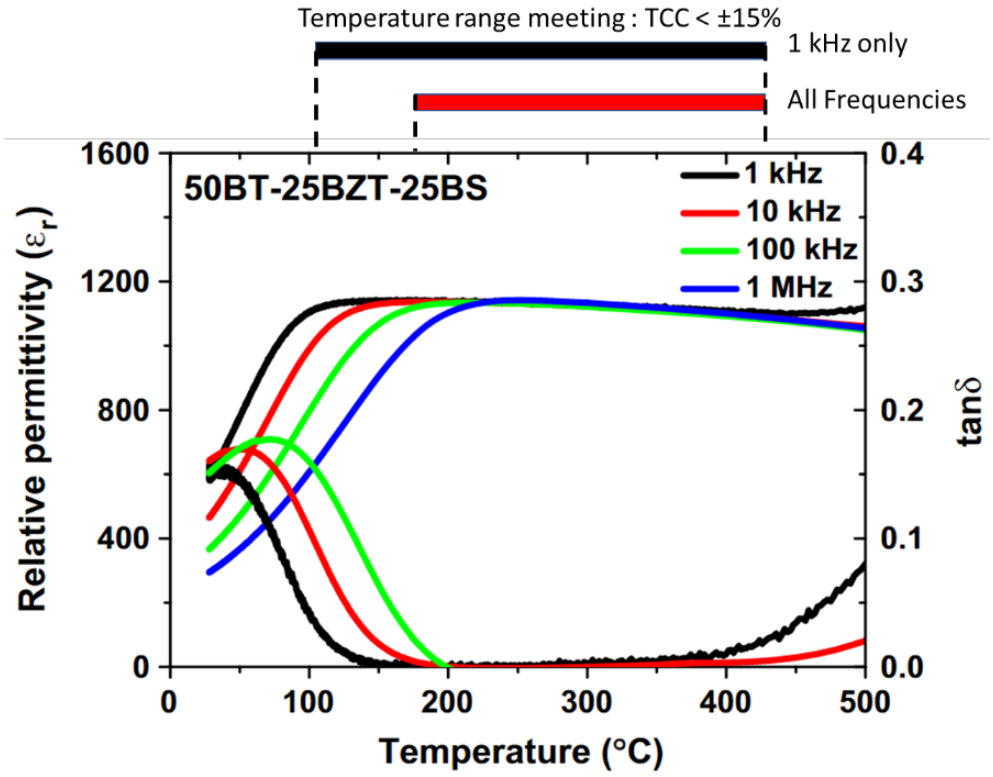

Figure 2.23 Permittivity response of 50$BaTiO_3$–25$Bi(Zn_{0.5}Ti_{0.5})O_3$–25$BiScO_3$ material, showing a broad permittivity peak at high temperatures. The temperature ranges that TCC < ±15% is achieved with tan δ < 0.02, is included above the plot. Figure adapted from a review by Zeb and Milne [2], with permission of Springer.

A summary of other promising solid solutions reported in the review are shown in Figure 2.24. As all these materials are compared at 1 kHz, the temperature ranges that achieve the desired performance, TCC <±15% and tan δ < 0.02, will be smaller if operated at a higher AC frequency. The temperature ranges that overlap for both these performance requirements gives the 'usable' temperature range. Although materials have been produced to meet the current temperature ranges used for most MLCCs (-55 to 125°C), a permittivity of ~ 600 is about half of those achieved in low doped BT materials with core shell microstructures [49, 50].

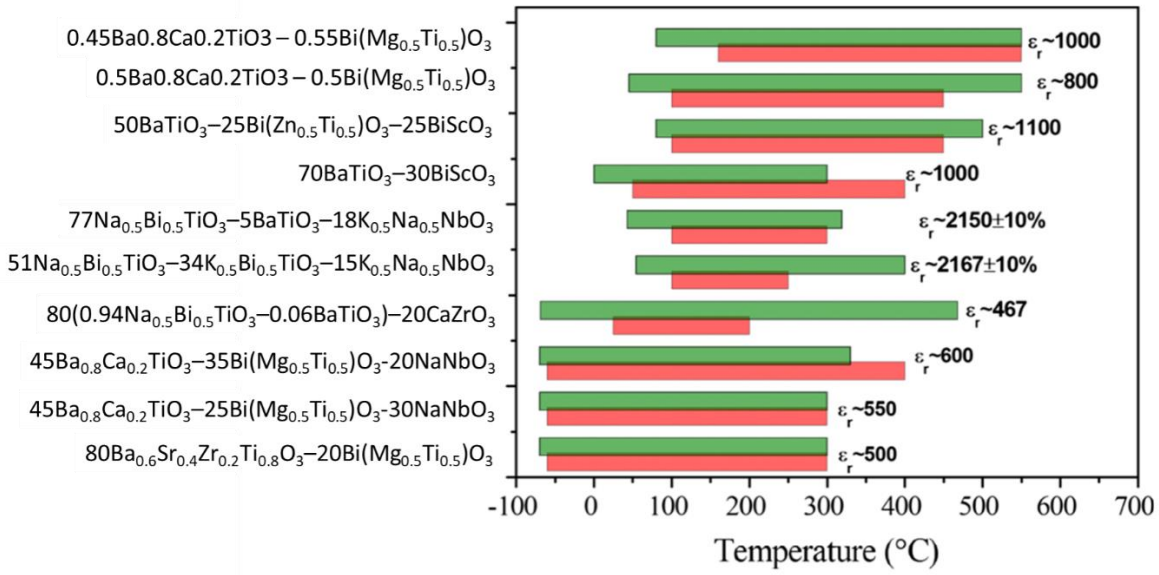

Figure 2.24 Summary of high temperature stability for the permittivity of several different solid solutions. Figure adapted from Zeb and Milne [2],with permission of Springer.

Unfortunately, the current use of base metal electrodes would likely be incompatible with many bismuth containing materials, due to chemical interactions during the high temperature sintering step. Many research laboratories produce MLCCs using platinum electrodes, which avoids these issues, although they are unlikely to be economically viable for mass production.

2.10. $NaNbO_3$-$BaTiO_3$ (NNBT)

The $NaNbO_3$:$BaTiO_3$ (NNBT) solid solution was first comprehensively reported in 1978 by Raevskii et al. [52], demonstrating a continuous solid solution of NNBT for all NN compositions. Across the solid solution, T_c follows a parabolic shape, Figure 2.25. Taking the temperature of maximum permittivity (T_{max}), the plot also contains data from several other authors. From the frequency dependency, the solid solution can be divided into 3 broad regions.

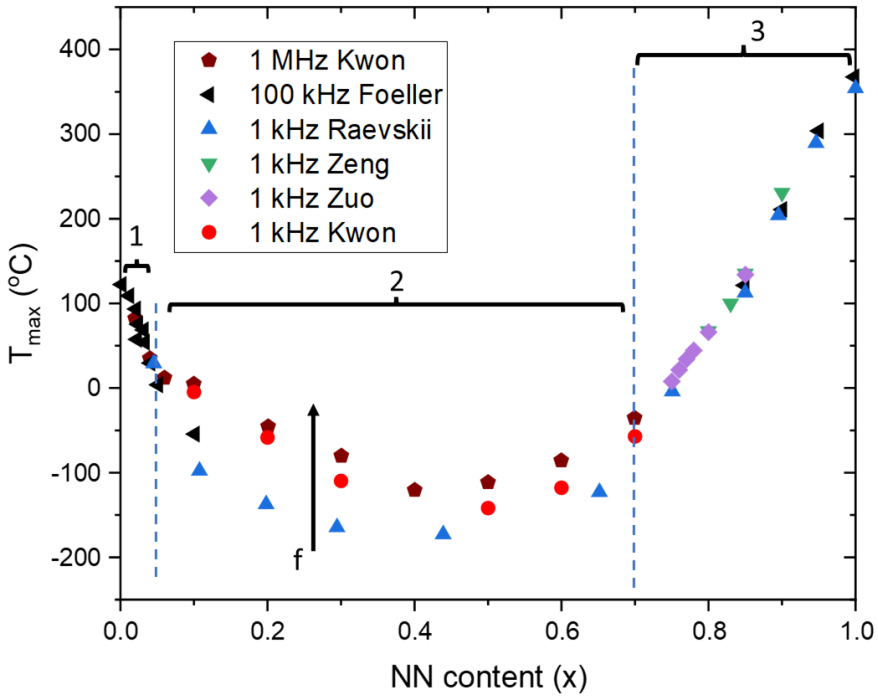

Figure 2.25 Dependence of T_{max} on NN content (%) in the NNBT solid solution. Figure contains work by Foeller [9], Kwon et al. [53], Raevskii et al. [52] and Zeng et al. [54], Zho et al. [55]. Frequency dependency of T_{max} occurs between 6% and 70% of NN content, with frequency increasing in the direction of the arrow.

In region 1, (x = 0 to 0.06), a classical ferroelectric response is observed with T_{max} decreasing with NN content at a near linear rate. This relationship is for a homogeneous distribution of NN, however Benlahrache et al. report the formation of core and shell materials in this compositional window [56], Figure 2.26. The plot shows that sintering x = 0.03 for 120 minutes, a core and shell microstructure was produced with a T_{max} that is due to the presence of the undoped BT core (T_{max} ~ 130°C) and is not representative of the T_{max} expected if the doping was homogeneous.

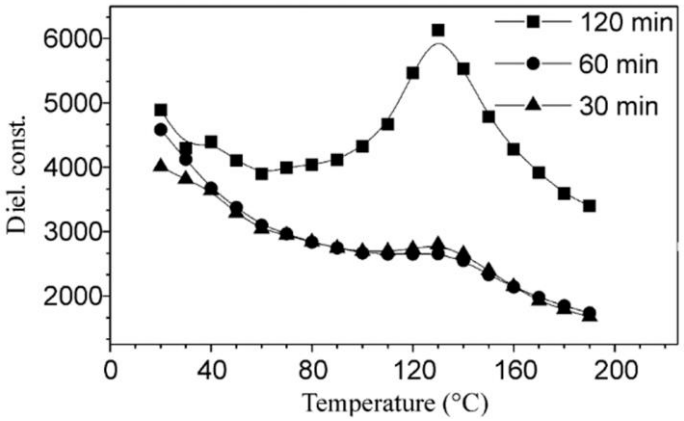

Figure 2.26 Production of a core and shell microstructure with 3% NN content. A dwell of 120 mins fully densified the materials, without significant homogenisation. Figure from Benlahrache et al. [56], with permission of Elsevier.

For Region 2 in Figure 2.25, (x = 0.06 to 0.7), these compositions display relaxor-type behaviour with a T_{max} that is frequency dependent. The difference in frequency used in the measurement of permittivity by Raevskii (1 MHz) and Kwon (1 kHz and 1 MHz) shows a consistently lower T_{max} when a lower frequency is used.

Applying the Goldschmidt tolerance values of NN (0.94) and BT (1.06), a perovskite with ideal average A and B site cations is achieved at x=0.5. The predicted stability of the cubic structure at x=0.5 matches with the experimental measurements, as x=0.4-0.5 have the lowest T_{max} of the solid solution (~ -175°C).

Above x=0.5, the relaxor behaviour begins to diminish until x=0.7. From x=0.7 to 1, a near linear increase in T_{max} with NN content is matched with a transition from a broadened permittivity peak to a sharp ferroelectric-type response at x=0.9. Above x=0.9, the AFE behaviour of pure NN begins to dictate the dielectric response, resulting in a significant decrease in the permittivity maximum.

The range in T_{max} (-100 to ~220°C) that is achievable, whilst maintaining ε_{RT} >1000, makes the NNBT system of potential interest for high temperature MLCC devices. To achieve a higher T_{max} than undoped BT, NN rich compositions (NN>0.7) are required and thus BT becomes the minor phase.

2.11. Tetragonal Tungsten Bronze materials

The Tetragonal Tungsten Bronze (TTB) structure is similar to the perovskite structure in containing connected BO_6 octahedra. However as shown in Figure 2.4, TTBs are a unique subgroup of ferroelectric materials. Unlike the 2 sites of a perovskite, there are 5 unique cation sites in the TTB structure, the generic formula of TTBs being $(A1)_2(A2)_4(B1)_2(B2)_8(C)_4(X)_{30}$.

Due to the similarity of the B1 and B2 sites, these sites are usually universal to a cation, often leading to simplification. This was the case for $PbNb_2O_6$, observed by Goodman in 1953 to have distinct differences from the ABO_3 of perovskites [57].

The TTB unit cell is shown in **Error! Reference source not found.** (a). There are 10 octahedra in the (100) plane, but only 1 octahedron in the (001) plane. These unit cell dimensions of a TTB are compared to $BaTiO_3$ and $NaNbO_3$ in **Error! Reference source not found.** (b).

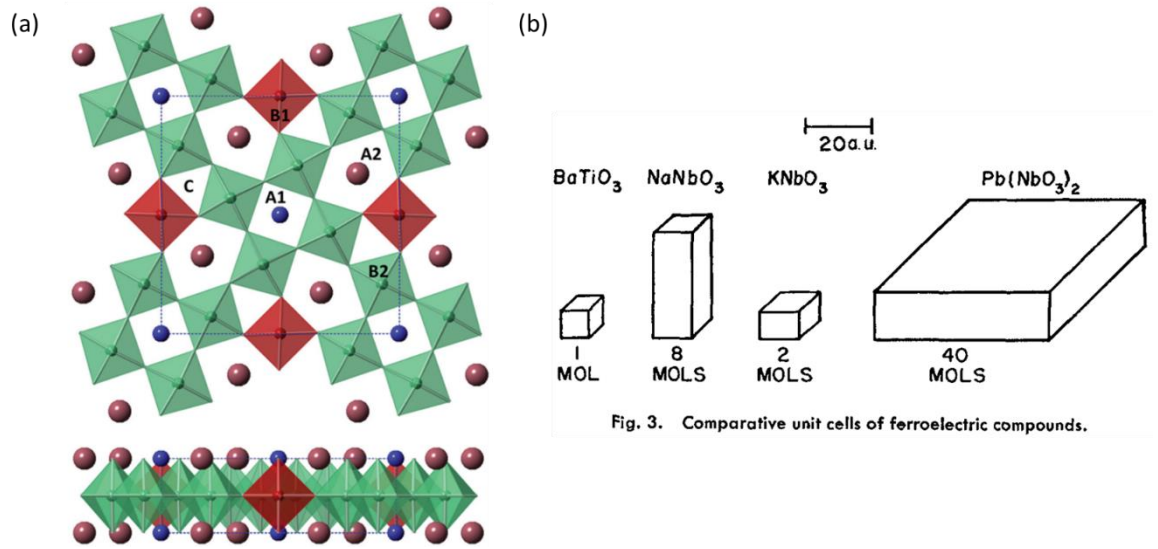

Figure 2.27 (a) TTB structure in the (001) and (100) planes, figure from Gardner et al. [58]. (b) Comparison of the size of the TTB unit cell to those of $BaTiO_3$ and $NaNbO_3$, figure from Goodman et al. [57], with permission of Wiley-Blackwell.

Due to the different coordination numbers of the A_1, A_2 and C sites, the size of sites is ordered as $C<A_1<A_2$.

TTBs are commonly referred to as 'stuffed', 'filled', 'unfilled' and 'empty', depending upon the proportion of A and C sites that are vacant, Table 2.5. Stuffed (no vacancies) require single charge cations on the A and C sites. Filled and unfilled refer to the occupancy of the A-sites, with both having unfilled C sites. Filled materials contain a mix of +1 and +2 charged cations, whilst unfilled usually contain only +2 cations. Finally, 'empty' TTBs can be created with trivalent cations, such as rare earth elements, and contain <50% occupied A-sites.

Table 2.5 Types of TTBs based upon A site vacancies.

	Occupancy			
Name	A sites	C sites	Example Composition	References
Stuffed	$A_1+A_2 = {}^{6}/_{6}$	${}^{4}/_{4}$	$K_6Li_4Nb_{10}O_{30}$	[59]
Filled	$A_1+A_2 = {}^{6}/_{6}$	${}^{0}/_{4}$	$Ba_4Na_2Nb_{10}O_{30}$	[60]
Unfilled	$A_1+A_2 < {}^{6}/_{6}$	${}^{0}/_{4}$	$Sr_xBa_{1-x}Nb_2O_6$	[61]
Empty	$A_1 < {}^{1}/_{2}$	${}^{0}/_{4}$	$Ba_4La_{0.67}Nb_{10}O_{30}$	[58]

In this thesis, 'unfilled' TTBs with divalent cations (Ba^{2+},Sr^{2+}, Ca^{2+}) were focused upon, with the B sites containing Nb^{5+}. These compositions do not contain rare earth elements, which suffer from particular global demand issues, or monovalent cations that have compatibility issues with base metal electrodes in MLCCs. The following sections discuss $(Sr,Ba)Nb_2O_6$ and $(Ca,Ba)Nb_2O_6$, before discussing systems with all 3 A-site cations, $(Ca,Sr,Ba)Nb_2O_6$.

2.12. $Sr_xBa_{1-x}Nb_2O_6$ (SBN)

In 1970, Carruthers and Grasso [62] reported on the ternary system of BaO- SrO – Nb_2O_5, finding the binary phase diagram $SrNb_2O_6$: $BaNb_2O_6$ produces materials with the TTB structure, Figure 2.28 (a). The $(Sr_x,Ba_{1-x})Nb_2O_6$ region (labelled SBN), was phase pure for the range x = 0.2 – 0.8. However, they report that x = 0.8 is achieved only if the composition is first melted, with x = 0.65 being the highest Sr content that could be produced in a bulk ceramic sample (1400°C), [63]. The T_{max} dependence on Sr^{2+} content, reported by several authors is included in Figure 2.28 (b). The work by Vandamme et al. and Kang et al. report the same linear relationship of decreasing T_{max} with increasing Sr^{2+} content. The T_{max} data reported by Said et al. [63] have some agreement until x = 0.55, where the decrease in T_{max} stops. This is likely due to the sintering conditions preventing further incorporation of Sr^{2+} into the TTB structure.

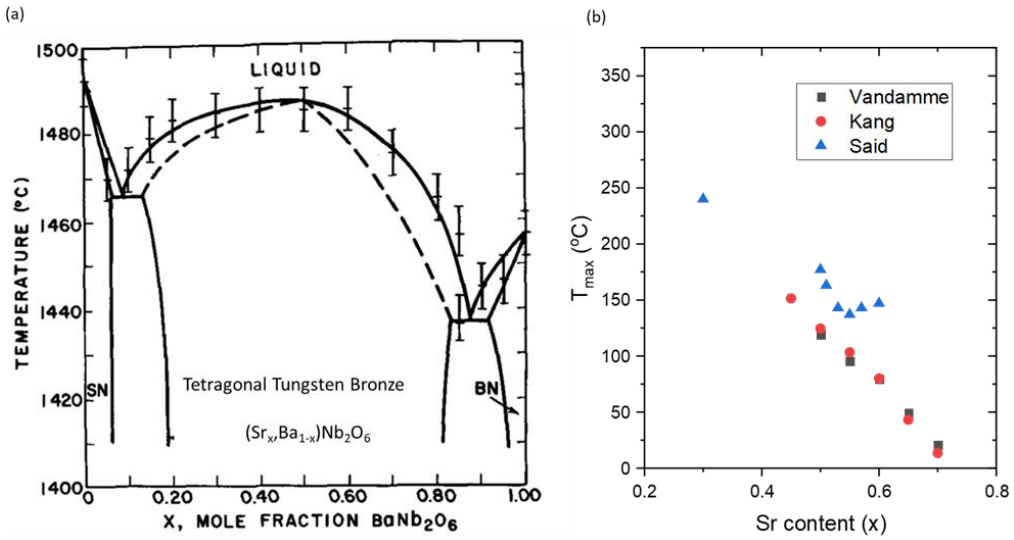

Figure 2.28 Phase Diagram of $SrNb_2O_6$ – $BaNb_2O_6$. Compositions were first melted and then freeze cooled to maximise the TTB stability range, adapted from Carruthers and Grasso [62]. (b) T_{max} relationship with Sr^{2+} content reported by Vandamme et al. [64], Kang et al. [61] and Said et al. [63].

In single crystals, the lattice parameters and site occupancy of SBN has been reported by Podlozhenov et al [65], Figure 2.29. In (a), the lattice parameters decrease with increasing Sr^{2+} content, reducing the unit cell volume. As shown in **Error! Reference source not found.** (a), the *a* axis consists of 10 oxygen octahedra, the tilting of which has a greater effect on the size of *a* than a small change in A-site cation size. This results in the *a* axis having a smaller % change than occurs in the *c* axis, which is more sensitive to the A-site cation radii.

In Figure 2.29 (b), Podlozhenov et al. report a preference of site occupancy for Sr^{2+} and Ba^{2+}. Due to the larger cation size of Ba^{2+}, it is restricted to occupy only the A_2 site [66]; however, Sr^{2+} can occupy either A_1 or A_2. As shown in Figure 2.29 (b), Sr^{2+} first occupies the A_1 sites, before filling the A_2 sites, leading to the vacancy ratio of A_1 and A_2 being Sr^{2+} content dependent [67].

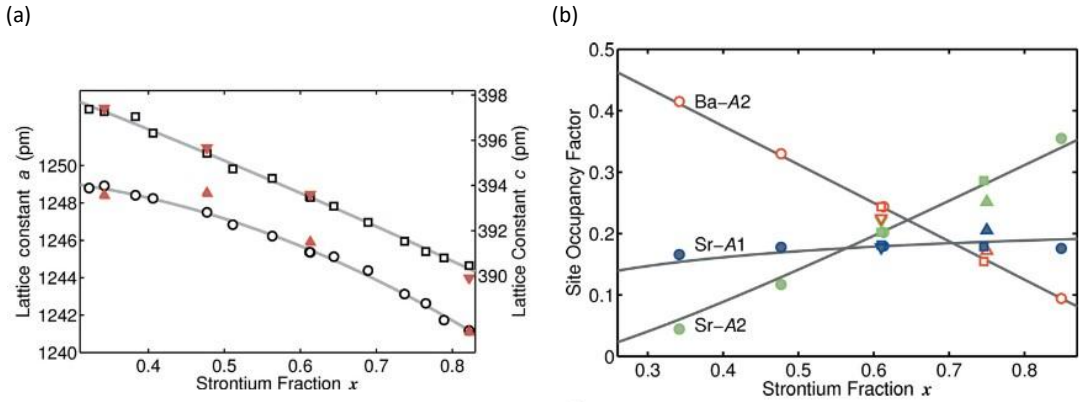

Figure 2.29 (a) Lattice parameters and (b) A site occupancy dependence on the Sr:Ba ratio in SBN. Figure reproduced from Podlozhenov et al. [65], with permission of Wiley-Blackwell.

2.13. $Ca_xBa_{1-x}Nb_2O_6$ (CBN)

$Ca_xBa_{1-x}Nb_2O_6$ was first reported by Ismailzade in 1960 [68], with Esser the first to grow single crystals of CBN [68, 69]. Unlike SBN, the relatively small Ca^{2+} is restricted to occupying only the A_1 cation sites, with Ba^{2+} only occupying the A_2 sites [70]. A_1 sites are only 1/3 of the A sites in a TTB structure, $(A1)_2(A2)_4(B1)_2(B2)_8(C)_4(X)_{30}$, and thus CBN is restricted to a theoretical limit of x = 0.4. Experimentally a range of x=0.15 to 0.40 has been reported, when annealed at high temperatures (~90% of melting temperature) [71]. However as shown in Figure 2.30 (a), this compositional region regresses as the annealing temperature decreases. At 1200°C, the composition region decreases to x= 0.17 to 0.33.

In Figure 2.30 (b), several different reports on the synthesis of CBN materials are combined to show the trend in T_{max}. The increase in Ca content results in a linear decrease in T_{max} (marked with a black dashed line) until $x \sim 0.32$ where T_{max} becomes constant. This discontinuation is due to the limit of Ca^{2+} incorporation in the TTB structure with additional Ca^{2+} forming a secondary phase of $CaNb_2O_6$.

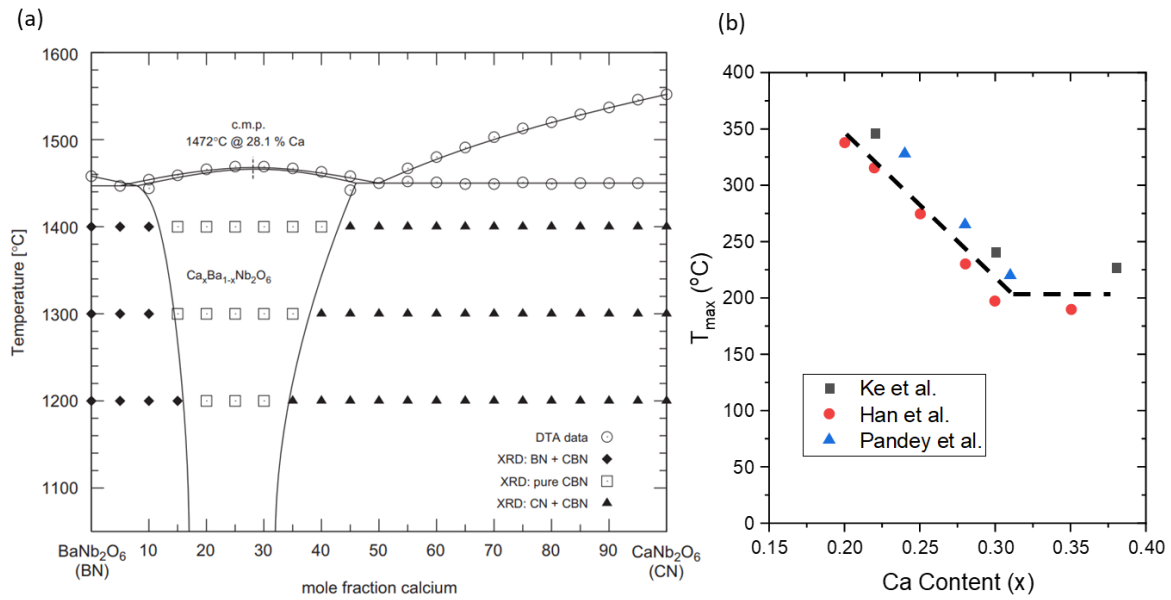

Figure 2.30 Stability of the CBN phase. (a) $BaNb_2O_6$: $CaNb_2O_6$ binary phase diagram, adapted from Burianek et al. [72]. (b) A collection of CBN data reported in the literature [73-74], showing a relationship between the Ca content and T_{max} observed from the permittivity-temperature profile. The black dashed line shows where this trend stops, with a Ca content above 0.32 not inducing any further decrease in T_{max}.

The difficulty in achieving phase pure ceramics with x>0.35 has been reported by Ke et al. [73] with the secondary phase of $CaNb_2O_6$ being present for all sintering temperatures. However, the higher temperature reduced the presence of $CaNb_2O_6$ with more Ca^{2+} entering the TTB structure. This affects the T_{max} of the composition, as shown in Figure 2.31 by Ke et al. [73]. A higher sintering temperature results in a lower T_{max} of the permittivity response, which is attributed to more Ca^{2+} ions in the TTB structure.

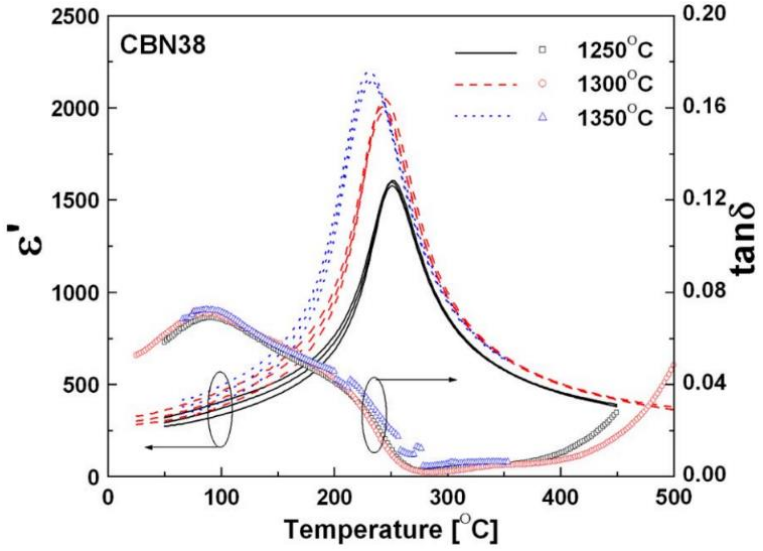

Figure 2.31 Dielectric response of CBN x=0.4, demonstrating the dependence of sintering temperature on the phase transition temperature. Figure reproduced from Ke et al. [73], with permission of AIP Publishing.

Due to Ca^{2+} being a smaller cation than Ba^{2+}, the c_o lattice parameter decreases with increasing Ca^{2+} content, Figure 2.32. The a_o parameter shows no noticeable dependence with Ca^{2+} which is a similar result to that of SBN and again related to the oxygen octahedra being the dominant determinate of the a_o parameter.

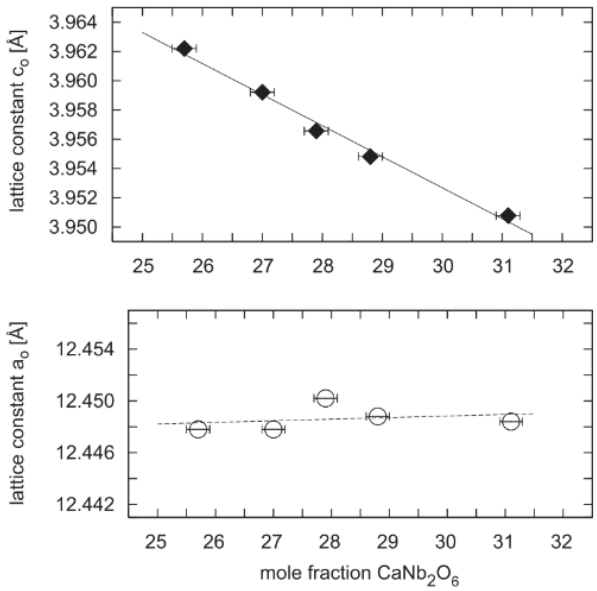

Figure 2.32 Dependence of Ca^{2+} content in CBN on the lattice constants. Figure reproduced from Burianek et al. [72], with permission of Elsevier.

2.14. $(Ca_xSr_yBa_{1-x-y})Nb_2O_6$ (CSBN)

The ternary phase diagram of $CaNb_2O_6$-$SrNb_2O_6$-$BaNb_2O_6$ is reported by Muehlberg et al. [71], the greyed region resulting in the phase pure formation of $(Ca_xSr_yBa_{1-x-y})Nb_2O_6$ (CSBN) in Figure 2.33. The left and right sides of the ternary diagram represent the binary CBN and SBN systems. The solubility limits of CBN and SBN are connected with red lines, showing the TTB structured CSBN is predicted for any composition produced from combining phase pure CBN and SBN materials. The CSBN region extends beyond these limits, as shown by the grey regions that occur outside of the two red lines in Figure 2.33.

The ternary plot is overlaid by different CSBN compositions reported in the literature. The individual points are colour coded by T_{max}, with the right hand colour bar showing the relationship between colour and T_{max}. The CBN and SBN data are included, which populate the left and right edges of the ternary diagram, respectively. Additional data from Chen et al. [76], Malyshkina et al. [77] and Zhang et al. [78] are included to populate the CSBN region. The T_{max} in the CSBN region appears to follow the trends observed in CBN and SBN, with CSBN materials with compositions close to SBN having low T_{max} values and CSBN materials more similar to CBN having higher T_{max} values.

However, there are some compositions reported which do not behave in this manner. Chen et al. report T_{max} of $Ca_{0.1}Sr_{0.2}Ba_{0.7}Nb_2O_6$ has a higher T_{max} than either $Ca_{0.3}Ba_{0.7}Nb_2O_6$ or $Sr_{0.3}Ba_{0.7}Nb_2O_6$ (218°C, compared to 197°C and 162°C, respectively). Therefore, mixing an CBN and SBN together may produce an CSBN material with a T_{max} that is above either of the component T_{max} values.

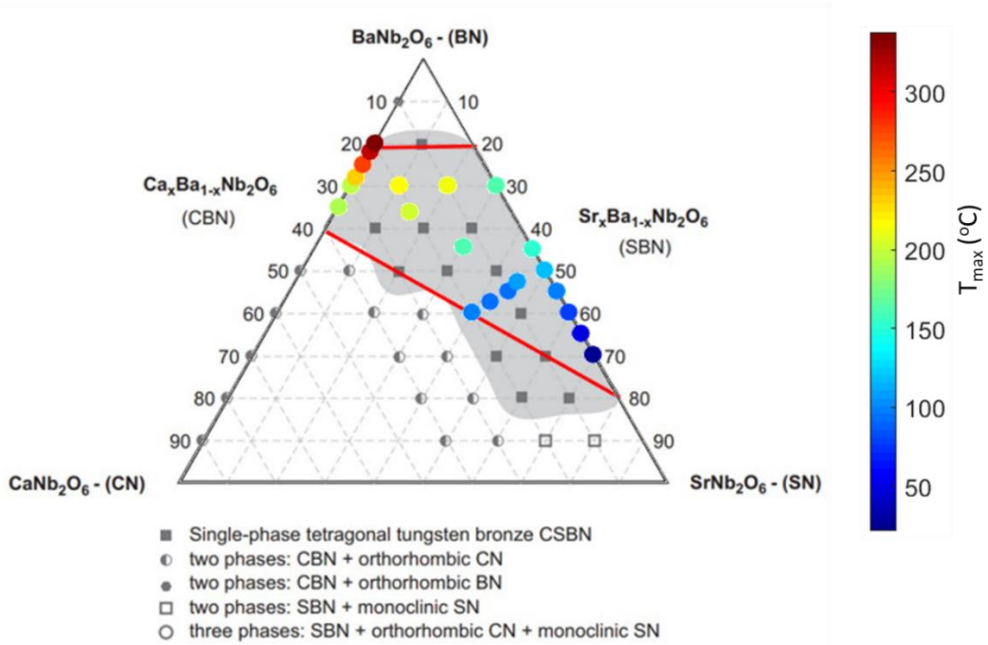

Figure 2.33 Ternary diagram of $CaNb_2O_6$ – $BaNb_2O_6$ – $SrNb_2O_6$ demonstrating the TTB stability region. Red tie lines superimposed to simplify the CSBN region of stability. Figure adapted from Muehlberg et al. [71].

2.15. Composite Dielectric Layers in MLCCs

As discussed in the BT section, the temperature dependence of a material can be improved by doping to produce heterogeneous microstructures, such as core shell. However, many of these systems are based on BT materials which, as previously discussed, struggle to be temperature independent above ~150°C. Although heterogeneous materials based on alternative systems are possible, the iterative process of optimising the processing conditions are expensive, especially when considering the effects of doping elements and their concentrations.

An alternative is to have MLCCs of two or more different dielectric layer materials. In 1991, Tashiro et al. [79] reported a $PbTiO_3$ based composite MLCC, with layers with a high and low T_{max} (labelled H and L, respectively in Figure 2.34). In Figure 2.34 (a), issues with the electrodes allowed interdiffusion between the material layers, resulting in the low T_{max} material becoming thicker and denser, whereas the high T_{max} layer became thinner and more porous. However, Figure 2.34 (b) demonstrates a more successful composite system. This was also due to changing the two materials to be more chemically similar, minimising the driving force for inter layer diffusion.

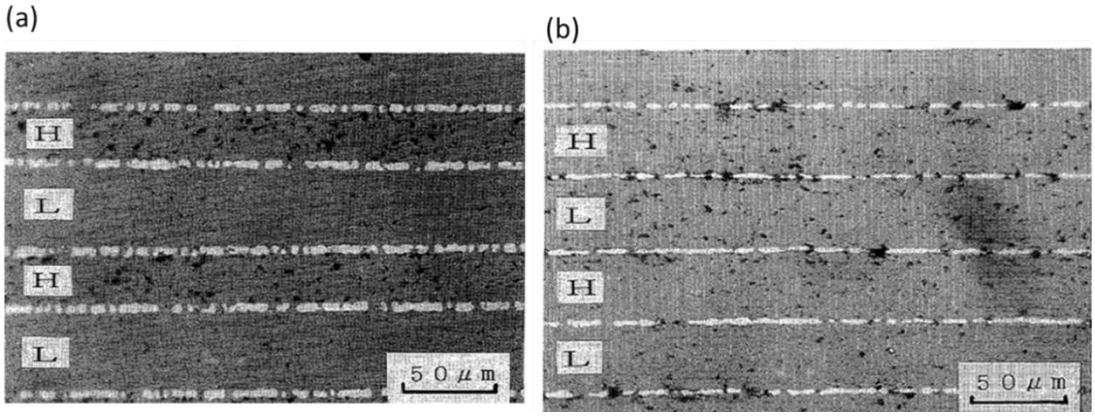

Figure 2.34 SEM of a composite MLCC by Tashiro et al. [79]. Two materials with high and low T_c values were stacked (labels L and H). Sintering caused the L layers to thicken and densify, whereas the H layer become thinner and more porous. Figure reproduced from Tashiro et al. [79], with permission of IOP Publishing.

They also report the effect that the stacking sequence has on the amount of interdiffusion observed. Figure 2.35 shows the change in capacitance with temperature when the L and H layers are stacked in different ways. (a) is alternating, with each electrode dividing the L and H layers. The amount of interdiffusion results in a single broad peak. (b) and (c) have stacks of 3 and 5 of the same layers (e.g. L-L-L-H-H-H-L-L-L). These stacking sequences result in less diffusion, resulting in a profile that demonstrates responses from the low T_{max} material (-30°C) and high T_{max} material (120°C).

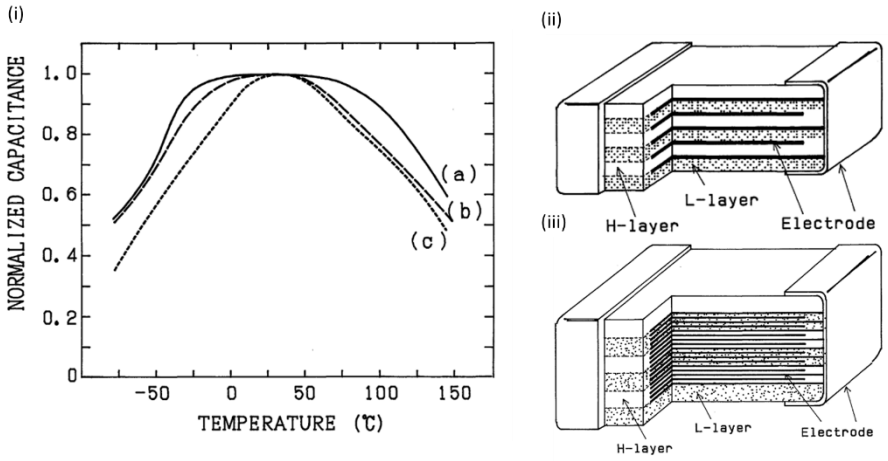

Figure 2.35 Normalised capacitance of composite MLCC by Tashiro et al showing how the layer stacking arrangement affects the permittivity response. In plot (i), (c) alternating layers, (b) groups of 3 similar layers repeating, and (a) 5 similar layers repeating. The schematics of (ii) and (iii) demonstrate the differences of (a) and (c) stacking sequences. Figure reproduced from Tashiro et al. [79], with permission of IOP Publishing.

2.15.1. Sn doped BT Composite MLCC

In 2017, Song et al. reported on a compositionally graded MLCC, with Sn doped BT ($BaTi_{1-x}Sn_xO_3$) [80]. The Sn^{4+} content was varied from 0.01 to 0.08, in intervals of 0.01, therefore, compositionally different layers were produced. The dependence of the permittivity response on the Sn content is shown in Figure 2.36 (a), with a T_c range of -10 to 75°C.

The capacitance profile of the MLCC produced is shown in Figure 2.36 (b). The profile has a broad peak at around 25°C. Although the MLCC has less temperature stability than the individual components, the capacitance at -50 and 125°C is significantly below the 25°C peak, resulting in a -45% and -50% decrease in capacitance at these extreme temperatures. Figure 2.36 (c) shows a schematic of how the layers were combined. By sorting the layers by Sn content, the difference in composition between neighbouring layers is minimised. This limits the chemical potential, reducing the drive of diffusion between the layers. Any induced diffusion of Sn content between layers will result in little change in T_c, again due to the x=0.01 difference between layers.

From this work, composite MLCCs are plausible for BT based materials. However, unless the component layers have significantly different T_c values, the MLCC is unlikely to stabilise the capacitance response at the temperature extremes.

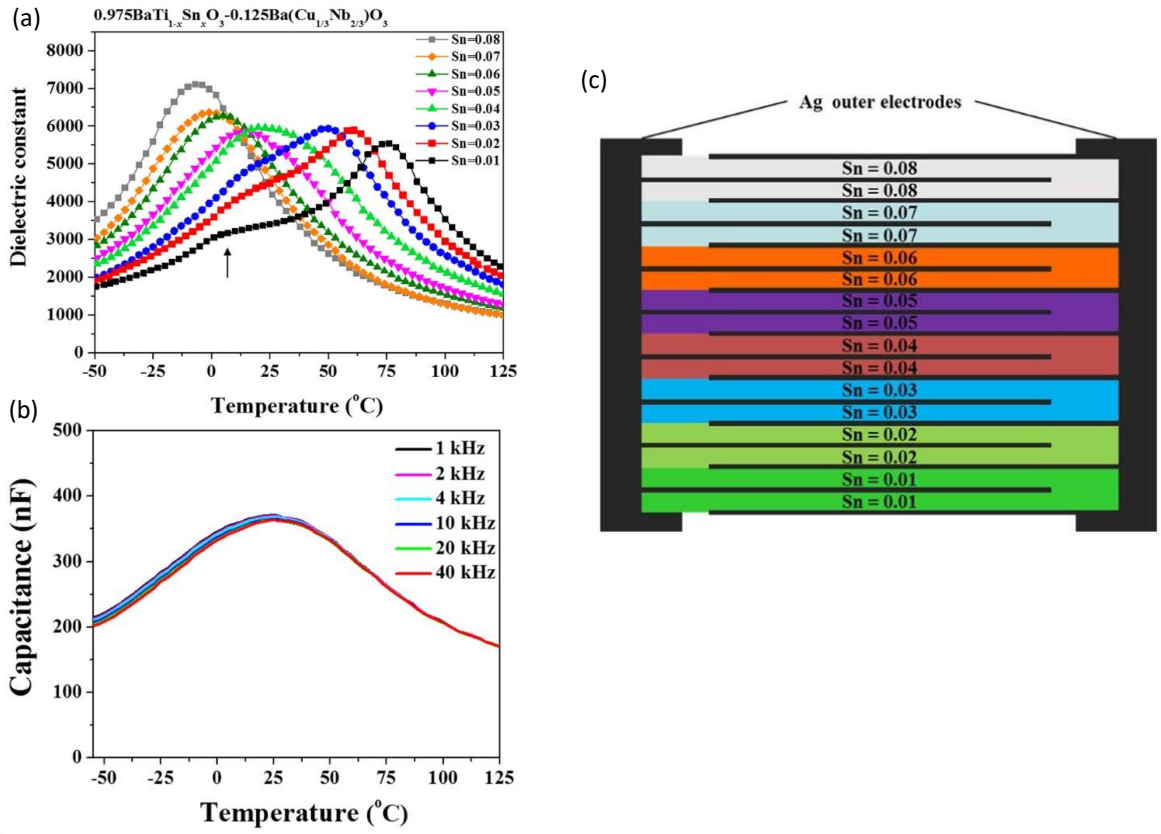

Figure 2.36 MLCC with layers of gradient of Sn doped materials. (a) The permittivity (1 kHz) profiles of the 8 component materials. (b) The capacitance response for the same temperature range, and (c) is a schematic of the layer stacking used. Figure adapted from Song et al. [80], with permission of Springer.

2.15.2. BST composite MLCC

Recently, Choi et al. [81] reported on the production of a strontium doped barium titanate ($Ba_{1-x}Sr_xTiO_3$) based composite MLCC. The permittivity responses of the component materials are shown in Figure 2.37 (a). In this work, the x= 0.20 to 0.35 range results in a T_c change from 73 to 26°C. This 47°C change is significantly smaller than the Sn doped work by Song et al. [80].

Although there are fewer components (4 vs 7) and a smaller Tc range (47 vs 75°C) compared to the work by Song et al. [80], the composite MLCC has a similar stability for the permittivity profile. This is partly due to the presence of an orthorhombic to tetragonal phase transition (T_{O-T}) in the perovskite BST, that supports the permittivity at lower temperatures.

The permittivity and capacitance profiles reported in the work by Choi et al. [81], was extracted and converted to TCC profiles, Figure 2.37 (b). The simulated response of the four components in series agrees well with the measured response from the composite MLCC. Unlike the Pb based work of Tashiro et al. [79], there does not seem to be inter-diffusion between different ceramic layers. One reason may be the use of B_2O_3 and Li_2O sintering aids, to achieve a low sintering temperature

(920°C) compared to the ~1350°C for BST without sintering aids [82]. This low temperature sintering approach therefore inhibits any significant and detrimental diffusion between layers.

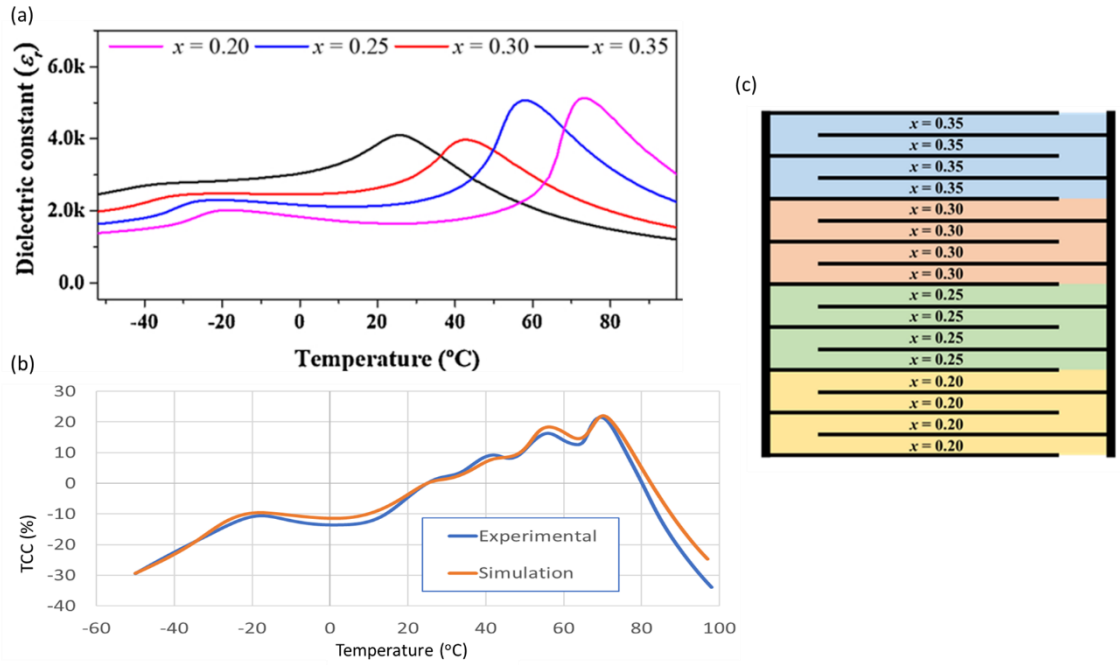

Figure 2.37 Composite MLCC based on BST materials, by Choi et al. [81]. The permittivity profiles (1 MHz) of the component layers (a) were combined in equal layer numbers to produce an MLCC with the TCC profile shown in (b). The simulation profile was calculated from the component data, showing excellent agreement with the experimental data. (c) A schematic of the layer configuration showing each component is grouped as 4 layer stacks. Figure adapted from Choi et al. [81]

For the composite MLCCs discussed, each contains an equal number of each material layer type. As seen in materials with core and shell microstructure, the relative ratios of the materials can have a substantial effect on the resulting composites performance.

With the BT based composite MLCCs, the material layers selected have had T_{max} ranges that are too narrow. Taking Figure 2.37 (a) as an example, above 80°C every material layer is paraelectric and thus has a decreasing permittivity response. This results in the composite device having poor temperature stability above 80°C. Although the reported composite MLCCs show excellent potential, there appears to be a lack of understanding as to what materials should be combined, and how systems can be optimised.

The NNBT system, with a T_{max} range from ~ -100 to 220°C offers great potential to be combined to produce composite MLCCs, with the added potential of stabilising over wider temperature ranges than those currently achieved with BT based systems.

2.16. Summary

Monolithic composite materials, such as BT based ceramics with core & shell microstructures, have been optimised over many years to meet stringent dielectric properties and TCC% criteria for the X7 (-55 to 125°C) temperature range. The industry commonly expects dielectric properties of $\varepsilon_r > 1000$, $\tan \delta < 0.04$ and TCC% of at least R classification (±15%). This high competition makes composite MLCCs for this temperature range unlikely to be commercially feasible, due to their disadvantage of being more complex to manufacture than monolithic materials.

However beyond 125°C the performance of BT materials begins to struggle, making alternative solutions appealing. As shown in Figure 2.21, there is significant research into finding new material compositions suitable for high temperature MLCC applications [2]. These systems are often complex in their elemental composition, and often do not retain their temperature stability range down to room temperature.

Due to the difficulty in producing a monolithic material with an extended high temperature performance (-55 to >200°C), composite MLCCs could be a potential solution. Although several composite MLCCs have been reported in the literature [79-82], the temperature stability of the capacitance response is yet to be competitive with monolithic approaches.

To stabilise the capacitance response of composite MLCCs across wider temperatures, material combinations of greater T_{max} differences should likely be considered. Low T_{max} (<25°C) or high T_{max} (>125°C) materials would counter the decline in permittivity in these temperature regions, which is often reported in composite MLCCs (e.g. Figure 2.36 and Figure 2.37). Some material systems can achieve this T_{max} range through changing elemental compositions, such as NNBT shown in Figure 2.25. With a T_{max} range of -100°C to ~220°C, NNBT appears an interesting system for composite MLCCs with X9 capabilities (-55 to 200°C).

A reported issue with combining dielectric layers of different chemical composition is the potential for interdiffusion, especially during the sintering process. Discontinuities in the electrode layers can provide ceramic-ceramic interfaces and can promote substantial diffusion, as shown in Figure 2.34. Although time limited interdiffusion is used to produce heterogeneous ceramics with core and shell microstructures, it is often difficult to predict the resulting dielectric properties. Composite MLCCs without interdiffusion effects have been reported, with a dielectric performance that can be directly simulated from the dielectric properties of the individual material layers, as shown in Figure 2.37.

The CSBN material system has been reported to have a wide T_{max} range of 60 to ~300°C. This T_{max} range could be potential as a high T_{max} component material for composite MLCCs, especially for specialised high temperature (>200°C) applications.

2.17. References

[1] A. J. Moulson and J. M. Herbert, "Electroceramics : materials, properties, applications," Second ed. Chichester: Wiley, 2003, pp. 310-311.

[2] A. Zeb and S. J. Milne, "High temperature dielectric ceramics: a review of temperature-stable high-permittivity perovskites," (in English), J. Mater. Sci.-Mater. Electron., Review vol. 26, no. 12, pp. 9243-9255, Dec 2015, doi: 10.1007/s10854-015-3707-7.

[3] J. Valasek, "Piezo-Electric and Allied Phenomena in Rochelle Salt," Physical Review, vol. 17, no. 4, pp. 475-481, 1921, doi: 10.1103/physrev.17.475.

[4] C.A. Randall and R.E. Newnham, "History of the First Ferroelectric Oxide, BaTiO3," ed. Mater. Res. Inst. Pennsylvania State Univ. Univ. Park. PA 16802 USA, 2004.

[5] G. H. Haertling, "Ferroelectric Ceramics: History and Technology," Journal of the American Ceramic Society, vol. 82, no. 4, pp. 797-818, 1999, doi: 10.1111/j.1151-2916.1999.tb01840.x.

[6] R. Whatmore, "Ferroelectric Materials," Springer International Publishing, 2017, pp. 1-1.

[7] D. Damjanovic, "Ferroelectric, dielectric and piezoelectric properties of ferroelectric thin films and ceramics," (in English), Rep. Prog. Phys., Review vol. 61, no. 9, pp. 1267-1324, Sep 1998, doi: 10.1088/0034-4885/61/9/002.

[8] V. Y. Shur and E. L. Rumyantsev, "Kinetics of ferroelectric domain structure: Retardation effects," Ferroelectrics, vol. 191, no. 1, pp. 319-333, 1997, doi: 10.1080/00150199708015657.

[9] P. Foeller, "Novel materials and routes for rare-earth-free BaTiO3-based ceramics for MLCC applications.," Materials Science and Engineering, University of Sheffield, 2017. [Online]. Available: http://etheses.whiterose.ac.uk/18954/

[10] A. Petritz et al., "Imperceptible energy harvesting device and biomedical sensor based on ultraflexible ferroelectric transducers and organic diodes," Nature Communications, vol. 12, no. 1, 2021, doi: 10.1038/s41467-021-22663-6.

[11] I. Kanno, "Piezoelectric MEMS: Ferroelectric thin films for MEMS applications," Japanese Journal of Applied Physics, vol. 57, no. 4, p. 040101, 2018, doi: 10.7567/jjap.57.040101.

[12] S. Pandya et al., "Pyroelectric energy conversion with large energy and power density in relaxor ferroelectric thin films," Nat. Mater., vol. 17, no. 5, pp. 432-438, 2018, doi: 10.1038/s41563-018-0059-8.

[13] B. Jaffe, "Antiferroelectric Ceramics with Field-Enforced Transitions: A New Nonlinear Circuit Element," Proceedings of the IRE, vol. 49, no. 8, pp. 1264-1267, 1961, doi: 10.1109/jrproc.1961.287917.

[14] A. Chauhan, S. Patel, R. Vaish, and C. Bowen, "Anti-Ferroelectric Ceramics for High Energy Density Capacitors," Materials, vol. 8, no. 12, pp. 8009-8031, 2015, doi: 10.3390/ma8125439.

[15] A. A. Bokov and Z. G. Ye, "Recent progress in relaxor ferroelectrics with perovskite structure," (in English), Journal of Materials Science, Review vol. 41, no. 1, pp. 31-52, Jan 2006, doi: 10.1007/s10853-005-5915-7.

[16] A. Peliz-Barranco, F. Caldern-Piar, O. Garca-Zaldvar, and Y. Gonzlez-Abreu, "Relaxor Behaviour in Ferroelectric Ceramics," InTech, 2012.

[17] Z. Y. Cheng, R. S. Katiyar, X. Yao, and A. S. Bhalla, "Temperature dependence of the dielectric constant of relaxor ferroelectrics," Physical Review B, vol. 57, no. 14, pp. 8166-8177, 1998, doi: 10.1103/physrevb.57.8166.

[18] K. M. Johnson, "Variation of Dielectric Constant with Voltage in Ferroelectrics and Its Application to Parametric Devices," Journal of Applied Physics, vol. 33, no. 9, pp. 2826-2831, 1962, doi: 10.1063/1.1702558.

[19] J.-W. Liou and B.-S. Chiou, "Effect of Direct-Current Biasing on the Dielectric Properties of Barium Strontium Titanate," Journal of the American Ceramic Society, vol. 80, no. 12, pp. 3093-3099, 2005, doi: 10.1111/j.1151-2916.1997.tb03237.x.
[20] L. Padurariu, L. Curecheriu, V. Buscaglia, and L. Mitoseriu, "Field-dependent permittivity in nanostructured BaTiO3ceramics: Modeling and experimental verification," Physical Review B, vol. 85, no. 22, 2012, doi: 10.1103/physrevb.85.224111.
[21] M. M. Samantaray, A. Gurav, E. C. Dickey, and C. A. Randall, "Electrode Defects in Multilayer Capacitors Part II: Finite Element Analysis of Local Field Enhancement and Leakage Current in Three-Dimensional Microstructures," Journal of the American Ceramic Society, vol. 95, no. 1, pp. 264-268, Jan 2012, doi: 10.1111/j.1551-2916.2011.04768.x.
[22] V. Buscaglia and C. A. Randall, "Size and scaling effects in barium titanate. An overview," J. Eur. Ceram. Soc., vol. 40, no. 11, pp. 3744-3758, 2020, doi: 10.1016/j.jeurceramsoc.2020.01.021.
[23] C. D. Martin, W. A. Crichton, H. Liu, V. Prakapenka, J. Chen, and J. B. Parise, "Phase transitions and compressibility of NaMgF3 (Neighborite) in perovskite- and post-perovskite-related structures," Geophysical Research Letters, vol. 33, no. 11, 2006, doi: 10.1029/2006gl026150.
[24] W. Tong and G. G. Amatucci, "Silver copper fluoride: A novel perovskite cathode for lithium batteries," (in English), Journal of Power Sources, Article vol. 362, pp. 86-91, Sep 2017, doi: 10.1016/j.jpowsour.2017.07.008.
[25] F. S. Galasso, Structure, properties, and preparation of perovskite-type compounds. London: Pergamon Press, 1969.
[26] A. Glazer, "The classification of tilted octahedra in perovskites," Acta Crystallographica Section B, vol. 28, no. 11, pp. 3384-3392, 1972, doi: doi:10.1107/S0567740872007976.
[27] V. Buscaglia and C. A. Randall, "Size and scaling effects in barium titanate. An overview," J. Eur. Ceram. Soc., vol. 40, no. 11, pp. 3744-3758, 2020, doi: 10.1016/j.jeurceramsoc.2020.01.021.
[28] I. Yamada, A. Takamatsu, and H. Ikeno, "Complementary evaluation of structure stability of perovskite oxides using bond-valence and density-functional-theory calculations," Science and Technology of Advanced Materials, vol. 19, no. 1, pp. 101-107, 2018, doi: 10.1080/14686996.2018.1430449.
[29] L. Gao, H. Guo, S. Zhang, and C. A. Randall, "A perovskite lead-free antiferroelectric xCaHfO3-(1-x) NaNbO3 with induced double hysteresis loops at room temperature," Journal of Applied Physics, vol. 120, no. 20, p. 204102, 2016, doi: 10.1063/1.4968790.
[30] L. Zhang et al., "Comment on the use of calcium as a dopant in X8R BaTiO3-based ceramics," (in English), Applied Physics Letters, Article vol. 90, no. 14, p. 3, Apr 2007, Art no. 142914, doi: 10.1063/1.2720305.
[31] V. Veerapandiyan, F. Benes, T. Gindel, and M. Deluca, "Strategies to Improve the Energy Storage Properties of Perovskite Lead-Free Relaxor Ferroelectrics: A Review," Materials, vol. 13, no. 24, p. 5742, 2020, doi: 10.3390/ma13245742.
[32] F. D. Morrison, D. C. Sinclair, and A. R. West, "Electrical and structural characteristics of lanthanum-doped barium titanate ceramics," (in English), Journal of Applied Physics, Article vol. 86, no. 11, pp. 6355-6366, Dec 1999, doi: 10.1063/1.371698.
[33] C. H. Kim, K. J. Park, Y. J. Yoon, D. S. Sinn, Y. T. Kim, and K. H. Hur, "Effects of milling condition on the formation of core-shell structure in BaTiO3 grains," (in English), J. Eur. Ceram. Soc., Article vol. 28, no. 13, pp. 2589-2596, Sep 2008, doi: 10.1016/j.jeurceramsoc.2008.03.030.
[34] C. H. Kim, K. J. Park, Y. J. Yoon, M. H. Hong, J. O. Hong, and K. H. Hur, "Role of yttrium and magnesium in the formation of core-shell structure of BaTiO3 grains in MLCC," (in English), J.

Eur. Ceram. Soc., Article vol. 28, no. 6, pp. 1213-1219, 2008, doi: 10.1016/j.jeurceramsoc.2007.09.042.
[35] K. Yasukawa, M. Nishimura, Y. Nishihata, and J. Mizuki, "Core-shell structure analysis of BaTiO3 ceramics by synchrotron X-ray diffraction," (in English), Journal of the American Ceramic Society, Article vol. 90, no. 4, pp. 1107-1111, Apr 2007, doi: 10.1111/j.1551-2916.2007.01537.x.
[36] F. H. Morshead et al., "How to extract reliable core-volume fractions from core-shell polycrystalline microstructures using cross sectional TEM micrographs," (in English), J. Eur. Ceram. Soc., Article vol. 37, no. 8, pp. 2795-2801, Jul 2017, doi: 10.1016/j.jeurceramsoc.2017.03.006.
[37] J. S. Dean, J. H. Harding, and D. C. Sinclair, "Simulation of Impedance Spectra for a Full Three-Dimensional Ceramic Microstructure Using a Finite Element Model," (in English), Journal of the American Ceramic Society, Article vol. 97, no. 3, pp. 885-891, Mar 2014, doi: 10.1111/jace.12750.
[38] J. P. Heath, J. S. Dean, J. H. Harding, and D. C. Sinclair, "Simulation of Impedance Spectra for Core-Shell Grain Structures Using Finite Element Modeling," (in English), Journal of the American Ceramic Society, Article vol. 98, no. 6, pp. 1925-1931, Jun 2015, doi: 10.1111/jace.13533.
[39] J. P. Heath, J. H. Harding, D. C. Sinclair, and J. S. Dean, "The Analysis of Impedance Spectra for Core–Shell Microstructures: Why a Multiformalism Approach is Essential," Advanced Functional Materials, vol. 29, no. 38, p. 1904036, 2019, doi: 10.1002/adfm.201904036.
[40] S.-F. Wang and G. O. Dayton, "Dielectric Properties of Fine-Grained Barium Titanate Based X7R Materials," Journal of the American Ceramic Society, vol. 82, no. 10, pp. 2677-2682, 2004, doi: 10.1111/j.1151-2916.1999.tb02141.x.
[41] S.-C. Jeon, B.-K. Yoon, K.-H. Kim, and S.-J. L. Kang, "Effects of core/shell volumetric ratio on the dielectric-temperature behavior of BaTiO3," Journal of Advanced Ceramics, vol. 3, no. 1, pp. 76-82, 2014, doi: 10.1007/s40145-014-0096-y.
[42] H. D. Megaw, Ferroelectrics 7, 87 (1974).
[43] G. Shirane, R. Newnham, and R. Pepinsky, "DIELECTRIC PROPERTIES AND PHASE TRANSITIONS OF NANBO3 AND (NA,K)NBO3," (in English), Physical Review, Article vol. 96, no. 3, pp. 581-588, 1954, doi: 10.1103/PhysRev.96.581.
[44] P. Li, S. Ouyang, G. Xi, T. Kako, and J. Ye, "The Effects of Crystal Structure and Electronic Structure on Photocatalytic H2 Evolution and CO2 Reduction over Two Phases of Perovskite-Structured NaNbO3," The Journal of Physical Chemistry C, vol. 116, no. 14, pp. 7621-7628, 2012, doi: 10.1021/jp210106b.
[45] C. N. W. Darlington and K. S. Knight, "On the lattice parameters of sodium niobate at room temperature and above," Physica B: Condensed Matter, vol. 266, no. 4, pp. 368-372, 1999, doi: 10.1016/s0921-4526(99)00043-5.
[46] Yuzyuk, "Unknown article," J. Phys.: Condens., vol. 17, 2005, doi: 10.1088/0953-8984/17.
[47] H. Guo, H. Shimizu, and C. A. Randall, "Direct evidence of an incommensurate phase in NaNbO3 and its implication in NaNbO3-based lead-free antiferroelectrics," Applied Physics Letters, vol. 107, no. 11, p. 112904, 2015, doi: 10.1063/1.4930067.
[48] D. Wang, G. Wang, Z. Lu, Z. Al-Jlaihawi, and A. Feteira, "Crystal Structure, Phase Transitions and Photoferroelectric Properties of KNbO3-Based Lead-Free Ferroelectric Ceramics: A Brief Review," Frontiers in Materials, vol. 7, 2020, doi: 10.3389/fmats.2020.00091.
[49] K. Singh, V. Lingwal, S. C. Bhatt, N. S. Panwar, and B. S. Semwal, "Dielectric properties of potassium sodium niobate mixed system," Mater. Res. Bull., vol. 36, no. 13-14, pp. 2365-2374, 2001, doi: 10.1016/s0025-5408(01)00711-5.

[50] S. F. Wang and G. O. Dayton, "Dielectric properties of fine-grained barium titanate based X7R materials," (in English), Journal of the American Ceramic Society, Article vol. 82, no. 10, pp. 2677-2682, Oct 1999. [Online]. Available: <Go to ISI>://WOS:000085763700017.

[51] L. Gong, X. H. Wang, S. P. Zhang, H. Wen, and L. T. Li, "Grain size effect on electrical and reliability characteristics of modified fine-grained BaTiO3 ceramics for MLCCs," (in English), J. Eur. Ceram. Soc., Article vol. 34, no. 7, pp. 1733-1739, Jul 2014, doi: 10.1016/j.jeurceramsoc.2013.12.028.

[52] I. P. Raevskii, L. M. Proskuryakova, L. A. Reznichenko, E. K. Zvorykina, and L. A. Shilkina, "Obtaining solid solutions in the NaNbO3-BaTiO3 system and investigation of its properties," Soviet Physics Journal, vol. 21, no. 2, pp. 259-261, 1978, doi: 10.1007/bf00898503.

[53] D. K. Kwon et al., "Temperature- and Frequency-Dependent Dielectric Properties of Sol-Gel-Derived BaTiO3-NaNbO3 Solid Solutions," (in English), J. Electron. Mater., Article vol. 45, no. 1, pp. 631-638, Jan 2016, doi: 10.1007/s11664-015-4162-1.

[54] J. T. Zeng, K. W. Kwok, and H. L. W. Chan, "Ferroelectric and piezoelectric properties of Na1-xBaxNb1-xTixO3 ceramics," (in English), Journal of the American Ceramic Society, Article vol. 89, no. 9, pp. 2828-2832, Sep 2006, doi: 10.1111/j.1551-2916.2006.01172.x.

[55] R. Zuo, H. Qi, J. Fu, J. Li, M. Shi, and Y. Xu, "Giant electrostrictive effects of NaNbO3-BaTiO3 lead-free relaxor ferroelectrics," Applied Physics Letters, vol. 108, no. 23, p. 232904, 2016, doi: 10.1063/1.4953457.

[56] M. T. Benlahrache, N. Benhamla, and S. Achour, "Dielectric properties of BaTiO3-NaNbO3 composites," (in English), J. Eur. Ceram. Soc., Article; Proceedings Paper vol. 24, no. 6, pp. 1493-1496, 2004, doi: 10.1016/s0955-2219(03)00577-6.

[57] G. Goodman, "Ferroelectric Properties of Lead Metaniobate," Journal of the American Ceramic Society, vol. 36, no. 11, pp. 368-372, 1953, doi: 10.1111/j.1151-2916.1953.tb12820.x.

[58] J. Gardner and F. D. Morrison, "A-site size effect in a family of unfilled ferroelectric tetragonal tungsten bronzes: Ba4R0.67Nb10O30 (R = La, Nd, Sm, Gd, Dy and Y)," (in English), Dalton Trans., Article vol. 43, no. 30, pp. 11687-11695, Aug 2014, doi: 10.1039/c4dt00126e.

[59] S. C. Abrahams, P. B. Jamieson, and J. L. Bernstein, "Ferroelectric Tungsten Bronze-Type Crystal Structures. III. Potassium Lithium Niobate K(6−x−y)Li(4+x)Nb(10+y)O30," The Journal of Chemical Physics, vol. 54, no. 6, pp. 2355-2364, 1971, doi: 10.1063/1.1675186.

[60] X. L. Zhu, K. Li, and X. M. Chen, "Ferroelectric Transition and Low-Temperature Dielectric Relaxations in Filled Tungsten Bronzes," (in English), Journal of the American Ceramic Society, Article vol. 97, no. 2, pp. 329-338, Feb 2014, doi: 10.1111/jace.12790.

[61] B. H. Kang and G. T. Joo, "Dielectric properties of SrxBa1-xNb2O6 ceramics and single crystals," (in English), Jpn. J. Appl. Phys. Part 2 - Lett. Express Lett., Article vol. 45, no. 8-11, pp. L245-L246, Mar 2006, doi: 10.1143/jjap.45.l245.

[62] J. R. Carruthers and M. Grasso, "Phase Equilibria Relations in the Ternary System BaO-SrO-Nb[sub 2]O[sub 5]," Journal of The Electrochemical Society, vol. 117, no. 11, p. 1426, 1970, doi: 10.1149/1.2407336.

[63] M. Said, T. S. Velayutham, W. C. Gan, and W. H. Abd Majid, "The structural and electrical properties of SrxBa(1-x)Nb2O6 (SBN) ceramic with varied composition," (in English), Ceram. Int., Article vol. 41, no. 5, pp. 7119-7124, Jun 2015, doi: 10.1016/j.ceramint.2015.02.023.

[64] N. S. Vandamme, A. E. Sutherland, L. Jones, K. Bridger, and S. R. Winzer, "Fabrication of optically transparent and electrooptic strontium barium niobate ceramics," (in English), Journal of the American Ceramic Society, Article vol. 74, no. 8, pp. 1785-1792, Aug 1991, doi: 10.1111/j.1151-2916.1991.tb07789.x.

[65] S. Podlozhenov, H. A. Graetsch, J. Schneider, M. Ulex, M. Wöhlecke, and K. Betzler, "Structure of strontium barium niobate Sr x Ba1 − x Nb2O6 (SBN) in the composition range

0.32 ≤ x ≤ 0.82," Acta Crystallographica Section B Structural Science, vol. 62, no. 6, pp. 960-965, 2006, doi: 10.1107/s0108768106038869.
[66] J. G. Carrio, Y. P. Mascarenhas, W. Yelon, I. A. Santos, D. Garcia, and J. A. Eiras, "Structure Refinement of (Sr,Ba)Nb2O6 Ceramic Powder from Neutron and X-Rays Diffraction Data," Materials Research, vol. 5, no. 1, pp. 57-62, 2002, doi: 10.1590/s1516-14392002000100010.
[67] S. S. Aamlid, S. M. Selbach, and T. Grande, "The Effect of Cation Disorder on Ferroelectric Properties of SrxBa1-xNb2O6 Tungsten Bronzes," (in English), Materials, Article vol. 12, no. 7, p. 11, Apr 2019, Art no. 1156, doi: 10.3390/ma12071156.
[68] I. Ismailzade, "An X-ray study of the BaNb2O6-CaNb2O6 and BaNb2O6-SrNb2O6 systems," Sov. Phys. Crystallogr, vol. 5, p. 268, 1960.
[69] M. Esser, M. Burianek, D. Klimm, and M. Muhlberg, "Single crystal growth of the tetragonal tungsten bronze CaxBa1-xNb2O6 (x=0.28; CBN-28)," (in English), J. Cryst. Growth, Article vol. 240, no. 1-2, pp. 1-5, Apr 2002, Art no. Pii s0022-0248(02)00868-0, doi: 10.1016/s0022-0248(02)00868-0.
[70] M. Esser et al., "Optical characterization and crystal structure of the novel bronze type CaxBa1-xNb2O6 (x=0.28; CBN-28)," Crystal Research and Technology, vol. 38, no. 6, pp. 457-464, 2003, doi: 10.1002/crat.200310057.
[71] M. Muehlberg et al., "Phase equilibria, crystal growth and characterization of the novel ferroelectric tungsten bronzes (CBN) and (CSBN)," J. Cryst. Growth, vol. 310, no. 7-9, pp. 2288-2294, 2008, doi: 10.1016/j.jcrysgro.2007.12.023.
[72] M. Burianek, B. Joschko, I. Kerkamm, T. Schoenbeck, D. Klimm, and M. Muehlberg, "Crystal growth and characterization of CaxBa1-xNb2O6 (CBN) in the composition range of 0.22 <= x(Ca) <= 0.35," (in English), J. Cryst. Growth, Article vol. 299, no. 2, pp. 413-417, Feb 2007, doi: 10.1016/j.jcrysgro.2006.10.269.
[73] S. M. Ke, H. Q. Fan, H. T. Huang, H. L. W. Chan, and S. H. Yu, "Dielectric, ferroelectric properties, and grain growth of CaxBa1-xNb2O6 ceramics with tungsten-bronzes structure," (in English), Journal of Applied Physics, Article vol. 104, no. 2, p. 6, Jul 2008, Art no. 024101, doi: 10.1063/1.2956615.
[74] X. K. Han, L. L. Wei, Z. P. Yang, and T. Zhang, "Phase formation, dielectric and ferroelectric properties of CaxBa1-xNb2O6 ceramics," (in English), Ceram. Int., Article vol. 39, no. 5, pp. 4853-4860, Jul 2013, doi: 10.1016/j.ceramint.2012.11.078.
[75] C. S. Pandey, J. Schreuer, M. Burianek, and M. Muhlberg, "Relaxor behavior of CaxBa1-xNb2O6 (0.18 <= x <= 0.35) tuned by Ca/Ba ratio and investigated by resonant ultrasound spectroscopy," (in English), Physical Review B, Article vol. 87, no. 9, p. 7, Mar 2013, Art no. 094101, doi: 10.1103/PhysRevB.87.094101.
[76] H. Chen, S. B. Guo, X. L. Dong, F. Cao, C. L. Mao, and G. S. Wang, "CaxSr0.3-xBa0.7Nb2O6 lead-free pyroelectric ceramics with high depoling temperature," (in English), Journal of Alloys and Compounds, Article vol. 695, pp. 2723-2729, Feb 2017, doi: 10.1016/j.jallcom.2016.11.192.
[77] O. Malyshkina, A. Ivanova, Y. Malyshkin, A. Folomeeva, M. Shashkov, and J. Dec, "Effect of Ca, Sr and Ba distribution on the relaxor properties of CSBN single crystals," Ferroelectrics, vol. 511, no. 1, pp. 76-81, 2017, doi: 10.1080/00150193.2017.1334183.
[78] J. Zhang, X. Dong, F. Cao, S. Guo, and G. Wang, "Enhanced pyroelectric properties of Cax(Sr0.5Ba0.5)1−xNb2O6 lead-free ceramics," Applied Physics Letters, vol. 102, no. 10, p. 102908, 2013, doi: 10.1063/1.4795795.
[79] S. Tashiro, Y. Mizukami, and H. Igarashi, "Fabrication of Composite MLC's and Their Dielectric Properties," (in English), Japanese Journal of Applied Physics, Article vol. 30, no. Part 1, No. 9B, pp. 2311-2314, Sep 1991, doi: 10.1143/jjap.30.2311.

[80] H. C. Song, J. E. Zhou, D. Maurya, Y. Yan, Y. U. Wang, and S. Priya, "Compositionally Graded Multilayer Ceramic Capacitors," (in English), Sci Rep, Article vol. 7, no. 1, p. 12353, Sep 27 2017, Art no. 12353, doi: 10.1038/s41598-017-12402-7.

[81] H.-J. Choi, J.-U. Woo, H.-G. Hwang, D.-S. Kim, M. Sanghadasa, and S. Nahm, "Microstructure and dielectric properties of compositionally graded Ba Sr TiO3 multilayer tunable capacitors," J. Eur. Ceram. Soc., vol. 41, no. 4, pp. 2559-2567, 2021, doi: 10.1016/j.jeurceramsoc.2020.12.027.

[82] W.-H. Lee et al., "Structural and dielectric properties of B2O3/Li2O-added Ba0.6Sr0.4TiO3 multilayer ceramics for tunable devices," Ceram. Int., vol. 46, no. 3, pp. 2640-2647, 2020, doi: 10.1016/j.ceramint.2019.09.248.

3. Experimental Methodology

3.1. Overview

This chapter describes the fabrication and characterisation techniques used in this work. The solid-state approach is described, as well as the stages to ensure correct synthesis and finally the measurement and characterisation of the materials in bulk ceramic form.

3.2. Fabrication

To fabricate the $(x)NaNbO_3(1-x)BaTiO_3$ (NNBT) and $(Ca_xSr_yBa_{1-x})Nb_2O_6$ (CSBN) at the various compositions, the conventional solid-state synthesis approach was followed. This approach mixes and reacts different reagent powders to achieve the desired composition, enabling the material to be characterised for purity, crystal structure and property measurements.

The reagents used were Na_2CO_3 (99.5%, Fisher Scientific, Loughborough, UK), Nb_2O_5 (99.99% Sigma-Aldrich, Gillingham, UK), $BaCO_3$ (≥99%, Sigma-Aldrich, Gillingham, UK), TiO_2 (≥99.9%, Sigma-Aldrich, Gillingham, UK), $SrCO_3$ (99.5%, Fisher Scientific, Loughborough, UK) and $CaCO_3$ (99.5%, Fisher Scientific, Loughborough, UK).

At the temperatures given in Table 3.1, the reagents were dried for at least 6 hours, then held at 200°C. The hot reagents were then transferred to a sealed desiccator, and allowed to cool to RT.

Table 3.1 Drying Temperatures of Reagents.

Reagent Material	Drying Temperature (°C)
Na_2CO_3	180
Nb_2O_5	900
$BaCO_3$	180
TiO_2	900
$SrCO_3$	180
$CaCO_3$	180

The reagents were then batched out for each composition at their respective stoichiometric ratios to achieve 0.25 mols of product, with ~50 g reagent batches producing ~30 g of product per composition.

The weighed reagent powders were transferred into a 500ml High Density Polyethylene (HDPE) milling bottle, that contains 300 g of yttria-stabilized zirconia milling media. Enough isopropanol is added to wet the powder before the reagents are milled for 6 hours. The slurry was then dried at 80^{o}C overnight. The dried powder was then passed through a 250 μm sieve to separate the powder from the milling media.

In an alumina crucible, the mixed reagent powders were calcined at 1000^{o}C for 6 hours, before cooling to RT. The heating and cooling rates of the chamber furnace were set to +5 ^{o}C/min and -5 ^{o}C/min, respectively to prevent any thermal shock effects. Post calcination, the milling, drying and sieving steps were repeated to produce the product in powder form.

To achieve green body pellets, ~0.2 g of powder was loaded into a 10 mm diameter die and pressed at 0.2 Tonnes in a uniaxial press for 2 minutes. Some green pellets were further compacted using a Cold Isostatic Press (CIP), pressing at 30 MPa for 2 minutes.

Diphasic ceramic composite pellets were also produced, containing two different calcined powders, either as a mix or as a layered system. Different molar ratios of the two powders were batched out, with the mixing occurring by grinding with a pestle and mortar.

To achieve a layered pellet, the 1st powder is first loaded into a uniaxial die and lightly pressed to achieve a flat surface. The 2nd powder can then be added, and the composite. As a green body these layers are distinct, with a mechanical contact.

The pellets were transferred into a platinum foil lined alumina boat and loaded into a box furnace for sintering. The single and dual step sintering profiles used are shown in Figure 3.1 (a) and (b). Both profiles start with the pellet at room temperature and heated at a ramp rate of 5^{o}C min^{-1} to the dwell temperature. The NNBT materials were sintered with a single step for 6 hours, at a maximum temperature of 1250^{o}C, to avoid the lowest melting point reported by Raevskii et al. [1], (1270^{o}C at x = 0.75).

The CSBN pellets were predominantly sintered following the procedure in Figure 3.1 (b). The first dwell encourages chemical homogenisation, whilst the higher temperature of the 2nd dwell induces densification. This approach minimises the formation of an intermediate liquid phase forming during the sintering, which has been previously reported to cause substantial grain growth [2]. The box furnaces were then allowed to cool, with the furnace preventing a cooling rate beyond -5^{o}C min^{-1}.

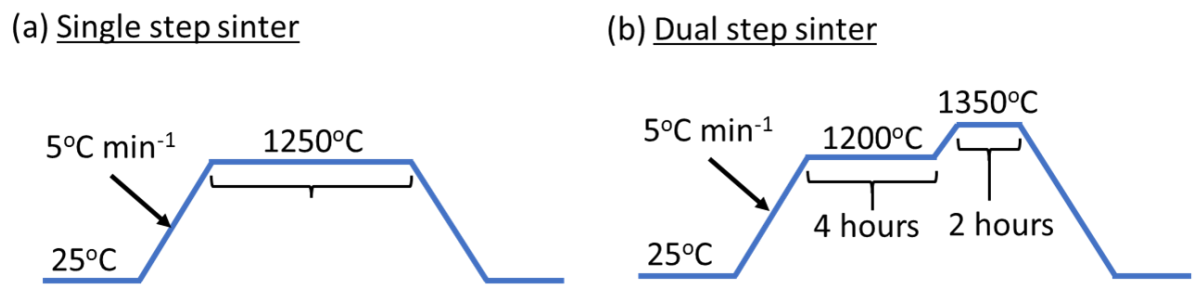

Figure 3.1 Sintering profiles for a single step (a) and a dual step (b) sinter.

3.3. Characterisation

3.3.1. Preparation & Dimensions

To prepare the pellets for density and electrical measurements, the pellets surfaces were polished. Pellets were hand polished with wet sandpaper, from 120 to 1200 grit, and rinsed with distilled water before being dried at 80°C.

The diameter and thickness of the pellets were measured using digital callipers, taking the average from 3 measurements on each sample.

3.3.2. Archimedes' Density

The density of the sintered pellets was measured using an Archimedes' balance (MS-DNY-43, Mettler Toledo, Greifensee, Switzerland). By comparing the mass of the pellet in air and when being submerged in distilled H_2O the density of the pellet was calculated by:

$$\rho = \frac{A}{A - B}\left(\rho_{liquid} + \rho_{air}\right) + p_{air} \tag{3.1}$$

where ρ is the density of the pellet, A is the mass of the pellet in air, B is the mass when measured submerged in a liquid (H_2O), ρ_{liquid} and ρ_{air} are the density of the H_2O and air, respectively. The apparatus uses an internal look up table to determine the H_2O density from the temperature of the distilled water.

3.3.3. Theoretical Density

The theoretical density of a ceramic composition depends upon the volume of its unit cell and the sum of the atomic weights of the elements:

$$\rho_{th} = \frac{MW * n}{V_{cell} * N_A} \tag{3.2}$$

where ρ_{th} is the theoretical density (g/cm^3) , MW is the molecular weight of a unit cell, n is the number of atoms per unit cell, V_{cell} is the volume of the unit cell and N_A is the constant Avogadro's number (6.02214 x 10^{23} mol^{-1}). Using the lattice parameters of the ceramics obtained from X-Ray Diffraction data, V_{cell} for the composition can be extracted.

3.3.4. Dilatometry Measurements

Dilatometry measures the change in length or volume of a sample as a function of temperature. Often it is used to measure the coefficient of thermal expansion (CTE) of a material, measuring the length change as the sample is heated at a constant rate. This work uses dilatometry to quantify the densification process as a green-body sample is heated towards a suitable sintering temperature. The densification process results in the sintered pellet having a smaller volume than the green body pellet.

To measure the temperature dependence of this densification process, a DIL 402C (Netzsch, Selb, Germany) dilatometer was used. Green body pellets of >25mm length were loaded and heated at 5°C/min from 25 to 1250°C, in an N_2 atmosphere . The in-situ measurement of the length of the sample during the heating process allows the % linear change of the sample to be established, Figure 3.2.

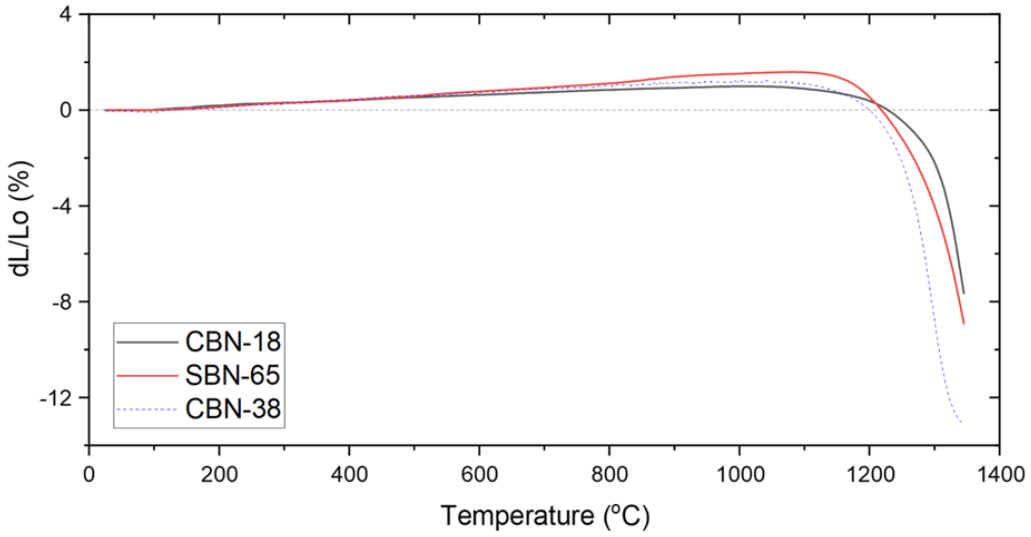

Figure 3.2 Dilatometry measurements of green-body pellets being heated towards a sintering temperature. The temperature where densification begins can be determined from the negative length change %.

3.3.5. X-Ray Diffraction

X-Ray diffraction (XRD) was performed throughout the fabrication process from the raw reagent powders to the sintered ceramics. The Bruker D2 Phaser (Karlsruhe, Germany) was used for initial phase identification. Powdered samples were loaded into Bruker PMMA holders, ensuring a flat and consistent surface by using a glass slide. Using Cu K-alpha ($K\alpha_1$ and $K\alpha_2$) radiation at 30 kV and 10 mA, data were collected for the 2θ range of 20 to 100°. The phase libraries in the 'DIFFRAC.EVA' software (Bruker, Karlsruhe, Germany) were used to aid identification.

Lattice parameters were determined using the STADI P PSD diffractometer from STOE (Darmstadt, Germany). The beam monochromator filters the Cu K-alpha radiation to be only Cu $K\alpha_1$ radiation. A small amount of finely ground powdered sample is mixed with PVA at the centre of a transparent plastic disc and dried in place with an electric drier. The disc is then loaded into the transmission sample holder. Operating in transmission mode, data were collected for the 2θ angle range of 20 to 100°, with a step size of 0.2° and a scan rate of 80 s/step. An external silicon sample was used as a standard to calibrate the angle measurements recorded.

Bragg's law relates the 2θ of the peak positions to the lattice spacing:

$$n\lambda = 2\, d_{hkl} \sin\theta_{hkl} \tag{3.3}$$

where n is a positive integer, λ is the wavelength of the incident beam (Cu $K\alpha_1$ = 1.5408 Å), d_{hkl} is the lattice spacing (Å) and θ_{hkl} is the glancing angle, which is the angle between the incident beam and the detector.

The geometry of a unit cell can be defined by the 3 edge lengths of the cell (a,b,c) and the 3 angles (α, β, γ) between them.

For a cubic unit cell, the lattice parameters simplify to a = b = c, and α = β = γ = 90. The Miller indices of the lattice plane relate the lattice parameter a, to d_{hkl} by:

$$\frac{1}{{d_{hkl}}^2} = \frac{h^2 + k^2 + l^2}{a^2} \tag{3.4}$$

For a tetragonal unit cell, a = b ≠ c, and these can be found by:

$$\frac{1}{{d_{hkl}}^2} = \frac{h^2 + k^2}{a^2} + \frac{l^2}{c^2} \tag{3.5}$$

For an orthorhombic unit cell, a ≠ b ≠ c, and these can be found by:

$$\frac{1}{{d_{hkl}}^2} = \frac{h^2}{a^2} + \frac{k^2}{b^2} + \frac{l^2}{c^2} \quad (3.6)$$

3.3.6. Scanning Electron Microscopy

Scanning electron Microscopy (SEM) was used to investigate the microstructure of powders and sintered pellets. A narrow beam of electrons is fired at a sample which produces elastic (back scatter) or inelastic collisions (secondary electron) that are then detected. By scanning the electron beam across the sample, high resolution images are produced.

To prepare powdered samples, a small amount of powder is stuck to carbon tape which is then adhered to an aluminium stub. For pellets, the internal fracture surface was imaged. The pellet fragments were mounted to the aluminium SEM sample holder with silver paste and dried at 120°C. To prevent surface charging effects, a thin gold film is sputtered onto both sample types electrically connecting the fracture surface to the aluminium sample holder.

An FEI inspect F50 scanning electron microscope, (FEI, Oregon, USA) , using a spot size of 3 nm and acceleration voltage of 20kV was used to obtain secondary electron imaging. Energy Dispersive Spectroscopy (EDS) was also implemented to perform compositional analysis of the ceramic pellets. An X-Ray beam induces atoms to ionise and eject an inner electron of a characteristic energy, the emitted X-Ray is detected and intensity of each energy peak is used to determine the atomic composition [3].

3.3.7. Inductance-Capacitance-Resistance Measurements

Inductance- Capacitance-Resistance (LCR) techniques were used to characterise the capacitance and dielectric loss of ceramic pellets at a series of temperatures. The temperature dependence and magnitude of the capacitance and/or dielectric loss can often be associated with structural phase transitions in the ceramics.

Pellets were prepared for electrical measurements by first polishing the top and bottom faces of the pellet, before coating with a gold paste (T-10112, Metalor Technologies, Birmingham, UK). The Au paste was dried at 200°C for ~10 minutes, before coating the other side under the same conditions. The electrodes were then fired at 800°C for 2 hours.

To measure the electrical properties at high temperatures, the pellets were loaded into a custom jig. Pt wire contacts the pellet via the electrode faces, using spring tension to achieve a constant force regardless of furnace temperature. Electrical measurements were taken using an inductance/capacitance/resistance (LCR) meter (Agilent E4980 Precision LCR Meter, Agilent Technologies, USA). At an applied voltage of 100 mV, the instrument collected capacitance and tan δ

data at 5 set frequencies (1, 10, 100 and 250 kHz and 1 MHz) per minute. A non-inductively wound furnace was programmed to heat at 1°C/min, resulting in an average data collection of 1°C/min. A thermocouple near the loaded pellet recorded the local temperature inside the jig at each electrical measurement.

A cryo-cooler system (Cryodrive 1.5, Oxford Cryosystems, UK) was used to cool pellet samples to sub-ambient temperatures. The pellets were loaded into a vacuum chamber (Oxford Instruments), and a vacuum pump was used to decrease the pressure to 0.1 mbar, preventing ice forming in the chamber.

The cryocooler then removed thermal energy from the system, until the lowest desired temperature is achieved. The electrical properties of the pellets were measured on a heating cycle, at 2°C increments every 150 seconds.

The relative permittivity ε_r, of the material can be inferred from the capacitance data by:

$$\varepsilon_r = \frac{C \cdot d}{\varepsilon_o \cdot A} \qquad (3.7)$$

where ε_r is the relative permittivity of the material, C is the capacitance measured, d is the thickness of the pellet, ε_o is the permittivity of free space constant (8.854 x 10^{-12} F/m) and A is the surface area of the Au electrode pair.

LCR is also used to measure the capacitance response of two or three pellets, electrically connected in series. Pellets were first polished such that they had identical surface area A, and electrode coated individually. The pellets were then stacked, with the interfaces being electrode-electrode, preventing any mis-alignment issue affecting the geometry correction. The pellet stack was then loaded into the ambient LCR and subambient LCR in the same manner used for a single pellet, with care taken to ensure the pellets were aligned in the jig to maximise electrode contact surface area.

3.4. References

[1] I. P. Raevskii, L. M. Proskuryakova, L. A. Reznichenko, E. K. Zvorykina, and L. A. Shilkina, "Obtaining solid solutions in the NaNbO3-BaTiO3 system and investigation of its properties," Soviet Physics Journal, vol. 21, no. 2, pp. 259-261, 1978, doi: 10.1007/bf00898503.

[2] S. M. Ke, H. Q. Fan, H. T. Huang, H. L. W. Chan, and S. H. Yu, "Dielectric, ferroelectric properties, and grain growth of CaxBa1-xNb2O6 ceramics with tungsten-bronzes structure," (in English), Journal of Applied Physics, Article vol. 104, no. 2, p. 6, Jul 2008, Art no. 024101, doi: 10.1063/1.2956615.

[3] Handbook of Advanced Ceramics: Materials, Applications, Processing, and Properties, 2nd Edition (Handbook of Advanced Ceramics: Materials, Applications, Processing, and Properties, 2nd Edition). 2013, pp. 3-10.

4. Simulation methodology

4.1. Overview

The goal of this simulation approach is to predict the permittivity profile of a ternary layered composite system for different component materials. The component materials are selected by the user, enabling experimentally obtained permittivity profiles to be used as inputs. For a set temperature range, the code evaluates the TCC performance of a material combination across all feasible layer thickness fractions. By repeating for each possible combination of component materials, the code provides predictions to their relative TCC performance. The best material combinations can therefore be predicted, as well as the systems optimised thickness fractions. This approach can also be used as a screening process, to reduce a very large number of possible combinations to a few, enabling the user to focus their time and resources effectively.

Written in MATLAB, the code allows the user to control many of the simulation parameters through a user interface, without the need for any command line inputs. With reasonable settings, a standard desktop computer can process roughly 9 different ternary combinations per second. The code demonstrates commercial potential, due to the ability to rapidly assess pre-existing material dataset to find high performing material combinations for composite MLCCs.

4.2. Ternary layer simulation

To identify the best combination of materials and layer ratios to produce a TCC compliant MLCC, we systematically explore the range of thickness combinations for all possible material combinations. The number of combinations for a given number of input materials (without repetition) is given by

$$C(n,k) = \frac{n!}{k!\,(n-k)!} \tag{4.1}$$

where n represents the number of input materials and k is the number of materials in the system. Although k can be any integer, we limit the system complexity to a tri-layer, thus k = 3. For a dataset of 9 materials, n = 9, (4.1) therefore calculates 84 unique ternary combinations. Using an enumeration function included in the MATLAB software, the list of unique three material systems is established.

In a layered system, each layer is assumed to be an individual capacitor, electrically connected either in series or parallel, see Figure 4.1. Depending on the connectivity, the capacitance of the layered system is denoted as C_s or C_p. Each layer is assumed to be smooth and consistent layer thickness. The capacitance models assume the area of the electrode plates is significantly larger than the

thickness of the plates (equal to the total thickness of dielectric layers), and thus ignoring stray field effects. The capacitance data used was all measured at 100 kHz, which is a frequency commonly reported in the literature. However capacitance data at other frequencies can be used as inputs.

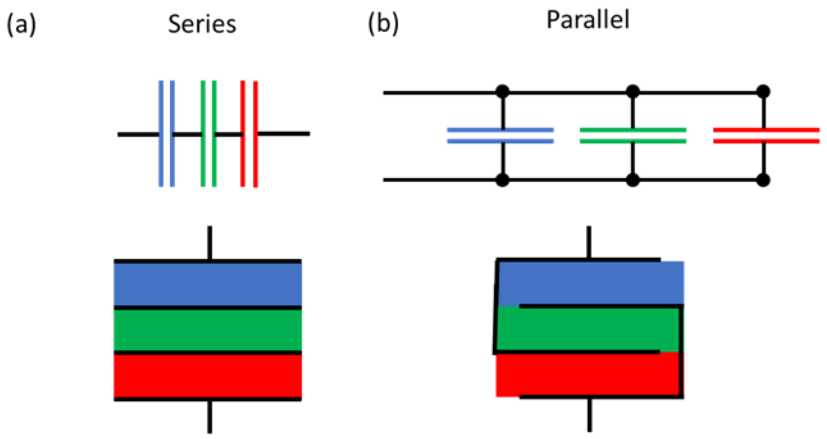

Figure 4.1 Schematic of capacitors in (a) series and (b) parallel, with a representation of how these are created with ceramic layers (below).

For a layer system in series, C_s as a function of temperature T is calculated with equation (4.2). The system depends on the individual capacitance C(T), from each layer and can be re-written as a combination of the permittivity of free space ε_0, the relative permittivity $\varepsilon_r(T)$ and the geometric dimensions of area (A) and thickness (d) of the individual layers. The area terms in the equation can be removed by setting $A_s = A_1 = A_2 = A_3$.

$$C_S(T) = \left[\frac{1}{C_1(T)} + \frac{1}{C_2(T)} + \frac{1}{C_3(T)}\right]^{-1} = \left[\frac{d_1}{\varepsilon_0 \varepsilon_{r_1}(T) A_1} + \frac{d_2}{\varepsilon_0 \varepsilon_{r_2}(T) A_2} + \frac{d_3}{\varepsilon_0 \varepsilon_{r_3}(T) A_3}\right]^{-1} \quad (4.2)$$

By converting the real thickness of the layers to that of a relative thickness fraction, the equation can be made dimensionless.

$$d_{f,1} = \frac{d_1}{d_1 + d_2 + d_3}, d_{f,2} = \frac{d_2}{d_1 + d_2 + d_3}, d_{f,3} = \frac{d_3}{d_1 + d_2 + d_3} \quad (4.3)$$

Therefore, the total series permittivity ε_s, can be written to be dependent only on the relative thickness fraction d_f, of the three individual dielectric layers (materials) and their ε(T) profiles.

$$\varepsilon_S(T) = \left[\frac{d_{f,1}}{\varepsilon_1(T)} + \frac{d_{f,2}}{\varepsilon_2(T)} + \frac{d_{f,3}}{\varepsilon_3(T)}\right]^{-1} \text{ where } d_{f,1} + d_{f,2} + d_{f,3} = 1 \quad (4.4)$$

The total parallel permittivity ε_p is derived with the same method, by starting with the equation for capacitors connected in parallel.

$$C_p(T) = C_1 + C_2 + C_3 = \frac{\varepsilon_0 \varepsilon_{r1}(T) A_1}{d_1} + \frac{\varepsilon_0 \varepsilon_{r2}(T) A_2}{d_2} + \frac{\varepsilon_0 \varepsilon_{r3}(T) A_3}{d_3} \quad (4.5)$$

$$\varepsilon_p(T) = \frac{\varepsilon_1(T)}{d_{f,1}} + \frac{\varepsilon_2(T)}{d_{f,2}} + \frac{\varepsilon_3(T)}{d_{f,3}} \quad ,where\ d_{f,1} + d_{f,2} + d_{f,3} = 1 \quad (4.6)$$

To expedite the process of optimisation these equations are employed in a computational algorithm using MATLAB. Experimentally measured Ɛ-T profiles are used as inputs for the component Ɛ(T).

As described in the experimental methodology section, the permittivity data for a material is rarely measured at regular temperature intervals. Therefore, the experimental data requires pre-processing in the form of an interpolated spline fitting process to allow for fast calculation of the complete temperature window. To avoid spline fit extrapolating outside of the experimentally measured range, which can generate significant error, the temperature window for all materials is limited to the common temperature range of all the materials, as shown in Figure 4.2.

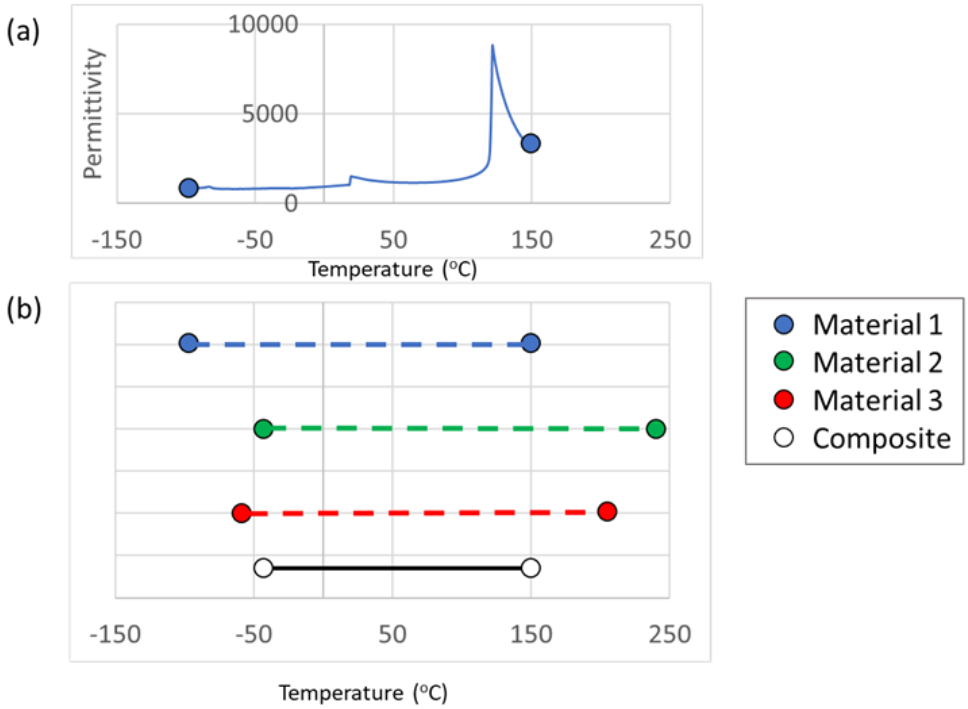

Figure 4.2 Finding the shared temperature range for all measured materials. The temperature limits for an example profile is shown in (a). (b) has 3 components, each with data for a specific temperature range. The composite system for these components is limited to the common (black line) temperature range.

This temperature range might be further reduced to align with the standard operating temperature ranges for MLCCs, as listed in Table 4.1. This temperature range is then discretised into an array of temperatures at a regular interval, ΔT. Setting ΔT = 1°C is commonly found to fit the data appropriately, as this matches the average increments of the experimental measurements. The cardinality (number of temperature points), T_{card}, for a temperature range is:

$$T_{card} = \frac{range\ (T)}{\Delta T} = \frac{\max(T) - \min\ (T)}{\Delta T} + 1 \tag{4.7}$$

As each input material is pre-processed for the same list of temperatures, the data becomes a matrix of the permittivity of n columns by T_{Points} rows. Therefore, matrix mathematics can be easily implemented into the code, expediting the ε_s or ε_p calculations.

Table 4.1 List of industrial standard temperature ranges and the code to grade temperature stability between the temperature limits.

Low temperature code (°C)	High temperature code (°C)	Allowed capacitance change (TCC, %)
X = −55	4 = +65	P = ±10
Y = −30	5 = +85	R = ±15
Z = +10	6 = +105	S = ±22
	7 = +125	T = +22/−33
	8 = +150	U = +22/−56
	9 = +200	V = +22/−82

For every ternary system, the relative thickness fraction, d_f , of each material can range between 0 and 1. If $d_f = 0$ for a specific layer, this material is not physically represented, and the system reduces to a binary system. Unary systems occur when one material has $d_f = 1$, as the other two have $d_f = 0$. In Figure 4.3, the left-hand ternary diagram demonstrates which layer ratios reduce to binary or unary systems.

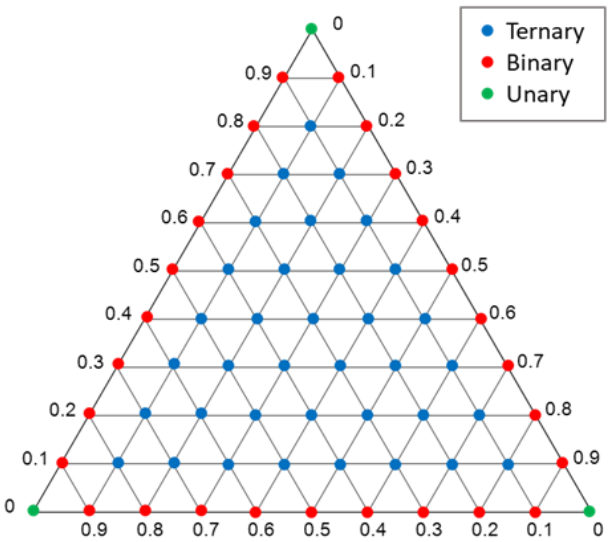

Figure 4.3 Example of a ternary diagram discretised into a triangular mesh of layer ratios. This example having a d_f interval of 0.1. The points are colour coded by the number of layers it represents.

The comparative thickness of the layers, r_n in a system can be calculated by:

$$r_n = \frac{\max\left(d_{f,1}, d_{f,2}, d_{f,3}\right)}{\min\left(d_{f,1}, d_{f,2}, d_{f,3}\right)}, \qquad \text{where } d_{f,(1,2,3)} > 0 \tag{4.8}$$

where r_n is the largest d_f value layer divided by the layer with the smallest d_f value. If a $d_{f1,2,3)} = 0$, then the equation simplifies to consider only those layers of a real thickness. As an example, r_n that occurs for the d_f range $d_{f,2} < d_{f,1}$ is shown in Figure 4.4. If $d_{f,2} << d_{f,1}$, then r_n approaches infinity. If $d_{f,2} = 0.5$, then $r_n = 1$, which is the smallest r_n value achievable.

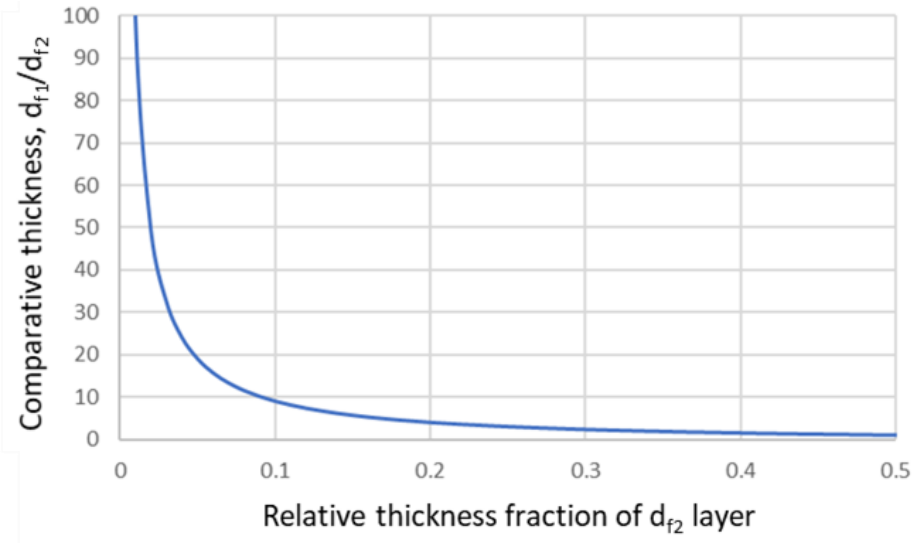

Figure 4.4 The comparative thickness of the two layers in a binary system can be plotted as a function of the relative thickness of one of the layers, d_{f2}. For $d_{f2} < 0.1$, the thickness of d_{f1} quickly becomes more than 10 times thicker than d_{f2}.

Due to layer fractions with a large r_n values being undesirable for MLCC applications, a minimum d_f limit of $d_{f,(1,2,3)} > x$ can be set. As seen in Figure 4.6, an $x > 0$ reduces the ternary diagram to only the regions that have feasible layer ratios. In consideration of practical applications employing tape casting, the minimum thickness of any one layer should not be less than 10% of the total thickness ($x = 0.1$), as layers more than 9 times thicker would be impractical to manufacture and affect the volumetric efficiency of the MLCC substantially. This limit does not restrict the system simplifying to a binary or unary, as a layer can still have $d_f = 0$.

There are 7 distinct sub-regions on a ternary diagram that meet these requirements, as seen in Figure 4.6 when $x > 0$. These can be grouped as 3 unary points, 3 binary lines, and a ternary 2D area. The $d_{f,(1,2,3)}$ ranges that are allowed in each sub-region are summarised in Figure 4.5.

Unary

$d_{f1} = 1\ ,\ d_{f(2,3)} = 0$

$d_{f2} = 1\ ,\ d_{f(1,3)} = 0$

$d_{f3} = 1\ ,\ d_{f(1,2)} = 0$

$$N_{Una} = 3$$

Binary

$x \leq d_{f(1,2)} \leq (1-x)\ ,\ d_{f3} = 0$

$x \leq d_{f(1,3)} \leq (1-x)\ ,\ d_{f2} = 0$

$x \leq d_{f(2,3)} \leq (1-x)\ ,\ d_{f1} = 0$

$$N_{Bin} = 3 * \left(\frac{1-2x}{\Delta d_f} + 1\right)$$

Ternary

$$x \leq d_{f(1,2,3)} \leq (1-2x)$$

$$N_{Tern} = \frac{k^2+k}{2}\ ,where\ k = \frac{1-3x}{\Delta d_f}$$

Total $\quad N_{Total} = N_{Una} + N_{Bin} + N_{Tern}$

Figure 4.5 The d_f ranges that define the regions of a ternary diagram that are feasible for a layer minimum thickness fraction x. The number of discretised $d_{f(1,2,3)}$ simulations is dependent on x and the interval of points, Δd_f.

The three unary points have only a single material, with $d_f = 1$, with each material in the combination being simulated as the unary material. Similarly, there are 3 different ways from three potential materials to achieve a binary system. Each binary region has 1 dimension on the ternary diagram, with the general form (d_f , 1-d_f , 0). The range of d_f is converted into an array of points with an interval of Δd_f, resulting in d_f = [x : Δd_f : 1-x]. Using these values, each binary region can be discretised, by repeating for the 3 different permutations of the general form.

The 2D ternary region is discretised as a triangular lattice with the same Δd_f as for the binary. The lattice has points at the three corners of the area (1-2x, x, x), ensuring the outer perimeter of the triangular area is included in the lattice. The number of points required to populate a ternary diagram, for specified x and Δdf values, is calculated using the equations also included in Figure 4.5.

Figure 4.3 is an example of the unary, binary, and ternary system points that are produced when x = 0.1 and Δdf = 0.1. The reduction in points to be simulated, whilst retaining Δdf, can be significant if x is set to be > 0. For Δdf = 0.01 and x = 0.1, N_{Total} = 2803, a 45% reduction in the 5151 points required if x = 0.

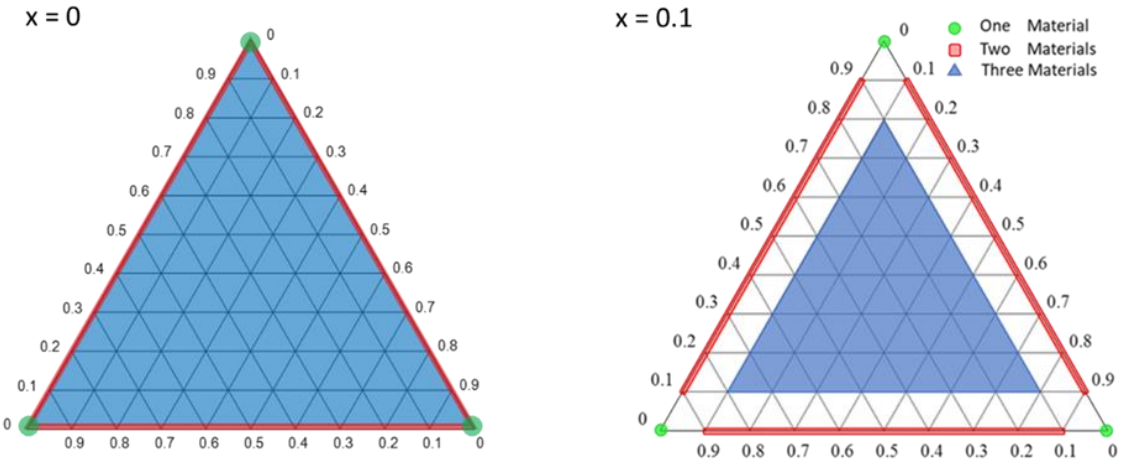

Figure 4.6 The df rules that divide a ternary diagram into regions of ternary, binary and unary layered systems. The minimum thickness fraction x, limits the minimum thickness of df. i.e x = 0 has no minimum limits on df, whilst x = 0.1 results in df > 0.1. However binary and unary regions are maintained for x > 0, as df = 0 is allowed regardless of x value. A more comprehensive breakdown of the regions are described in Figure 4.5.

For a layer system in series, $\varepsilon_s(T)$ can be calculated using equation(4.4), whilst the parallel version $\varepsilon_p(T)$ is found using (4.6). By repeating either step for the N_{Total} points, the dependence of $\varepsilon(T)$ on the layer thickness fraction of the material combinations can be simulated. As each $\varepsilon(T)$ profile consists of T_R temperature points, each material combination involves $T_R * N_{Total}$ permittivity values.

For a dataset of n> 3 materials, this approach is repeated for each material combination possible, (4.1). Therefore, a simulation involves $C * T_{card} * N_{Total}$ number of ε values calculated. For 9 materials (84 combinations), simulated for an X9 temperature range at 1°C, with x = 0.1 and Δdf = 0.01, there are over 60 million permittivity values calculated.

$$84 * 256 * 2802 \approx 60{,}018{,}840$$

This number of permittivity values is unfeasible to be analysed by hand, however there are several steps that can be taken to extract the information regarding which materials combine to achieve a good temperature stable permittivity response, and the corresponding layer thickness fractions.

The first step is to convert each $\varepsilon(T)$ profile to a TCC(T) profile, using equation (4.9). This equation normalises a $\varepsilon(T)$ profile to its magnitude at room temperature (25°C), and calculates the percentage deviation from this value for each temperature T. This normalisation process results in TCC(25°C) = 0 for every profile.

$$TCC(T) = 100 \times \frac{\varepsilon(T) - \varepsilon_{(T=25)}}{\varepsilon_{(T=25)}} \tag{4.9}$$

Although there are many approaches that could be used to assess the temperature stability of these TCC(T) profiles, it is the largest percentage change that is often considered to be the most important parameter to assess. One reason for this is that MLCCs are sold as having a certain capacitance value, and a large % change in the capacitance of an MLCC may affect the operation of other components in an electrical system. Therefore, a TCC(T) profile can be graded by the absolute maximum deviation:

$$TCC_{abs} = max|TCC(T)| \tag{4.10}$$

As seen in column 3 of Table 4.1, MLCCs with asymmetrical TCC codes also exist, which allow a larger negative % change than a positive one, with (4.11) including the scaling factor *f* to account for varying allowance of asymmetry. TCC_{asym} has limited use but is used in the analysis of the regions of a ternary diagram that meet different TCC codes for a certain temperature range.

$$TCC_{asym} = max\left|\max(TCC(T)), \frac{\min\,(TCC(T))}{f}\right| \tag{4.11}$$

The TCC_{abs} data for a material combination can be visualised on a single ternary diagram, by applying a colourmap to the data. This makes the data easier to evaluate, as it allows the user to quickly identify regions of layer thicknesses which have the best TCC performance.

The layer thickness ratio with the best TCC_{abs}, can be easily determined using (4.12) with TCC_{min} having the possibility of being a unary, binary or ternary layer thickness ratio:

$$TCC_{min} = \min\,(\,TCC_{abs}\,) \tag{4.12}$$

To compare the performance of the best binary and ternary layer ratios, the localised optimised layer ratio for each of the unary, binary and ternary sub-regions is found using (4.13).

$$TCC_{localmin} = \min\big(\,TCC_{abs}(y)\big), where\ y\ is\ either\ N_{una\,(1,2,3)}, N_{Bin\,(1,2,3)}\ or\ N_{Tern} \tag{4.13}$$

Example of these $TCC_{localmin}$ are overlayed on the ternary diagram of Figure 4.7. In this example, the TCC_{min} (★) is also the $TCC_{localmin}$ for just the ternary layer ratios, however this is not always the case.

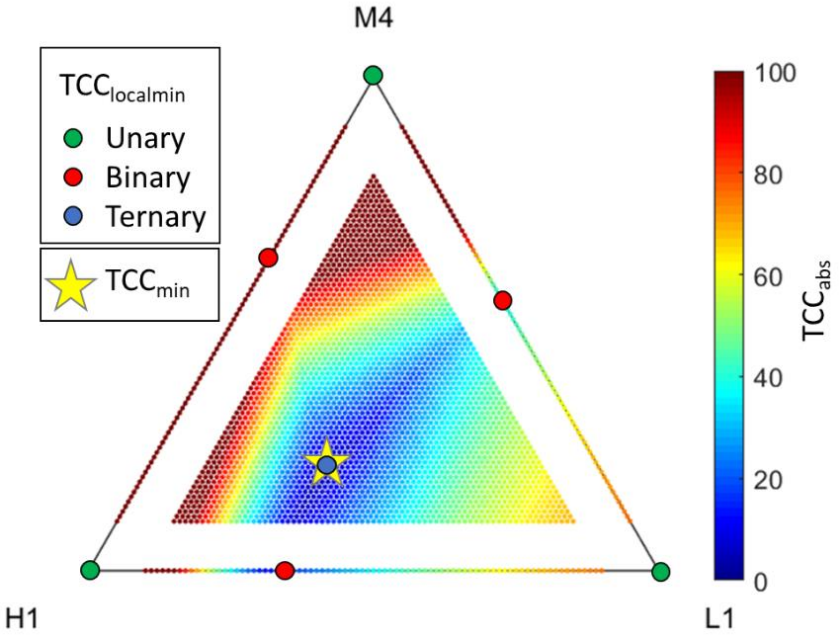

Figure 4.7 Ternary diagram, populated by the 2803 points simulated. The 7 $TCC_{localmin}$ values of the different sub regions of the ternary diagram are overlayed.

4.3. Permittivity filtering

Due to the permittivity at 25°C being an important performance parameter, layer ratios which have poor permittivity should not be considered, regardless of their TCC stability. The filter $\varepsilon_{RT} \geq \varepsilon_{min}$, ensures that the TCC_{min} of a combination has an ε_{RT} that exceeds the required ε_{min}:

$$TCC_{min} = \min\left(TCC_{abs}\left(\varepsilon_{RT} \geq \varepsilon_{min}\right)\right) \tag{4.14}$$

The effect of this filter can be seen in Figure 4.8, where (a) has no permittivity filter ($\varepsilon_{min} = 0$), and (b) has $\varepsilon_{min} = 1500$.

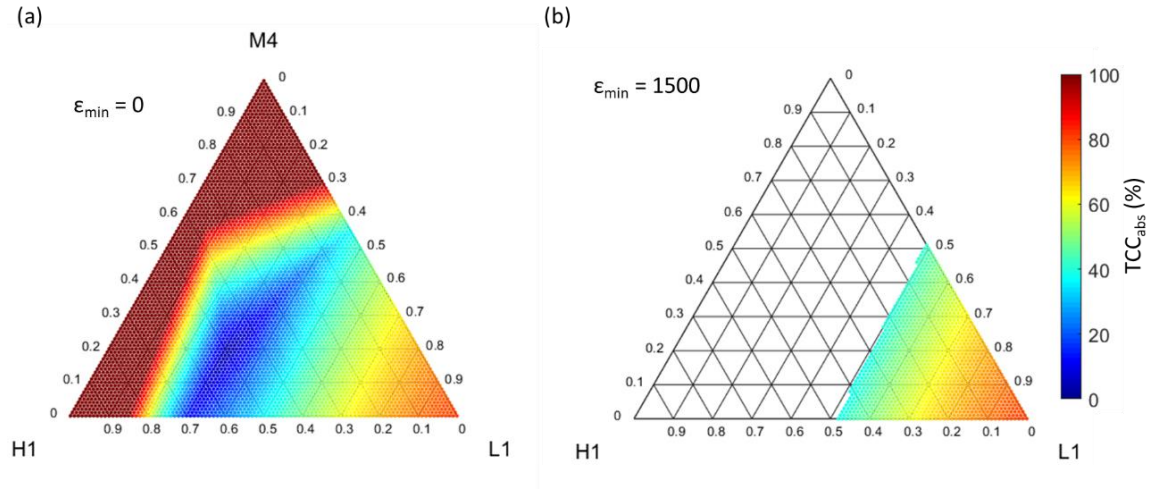

Figure 4.8 A permittivity minimum filters out under performing layer ratios, regardless of their TCC_{abs}. The TCC_{min} of a combination can be affected, as ε_{min} reduces the layer ratios that are considered for TCC_{min}. (a) has no filter (ε_{min} = 0), whereas (b) has ε_{min} = 1500.

4.4. Combinatorial Analysis

To evaluate the relative performance, the material combinations were ranked by their TCC_{min}. As each combination is compared at their optimised layer ratio, this approach compares the combinations by their best performance. Although the best TCC_{min} does not determine the most feasible material combination, it acts to roughly sort the relative performance of a potentially large number of combinations.

The sort function in MATLAB was used to rank the combinations by TCC_{min}, also generating the accompanying sort index. The sort index allows other information, such as the components in each combination, to remain associated to their correct combination.

The TCC_{min} values of the ranked combinations is plotted in Figure 4.9. The combinations are arranged worst to best, with the higher the ranking number being a worse ranking. By plotting left to right, the TCC_{min} improves towards ranked 1st. The use of the symbols ■, ●, ◆ represents whether the TCC_{min} of each combination occurs as a ternary, binary or unary system, respectively.

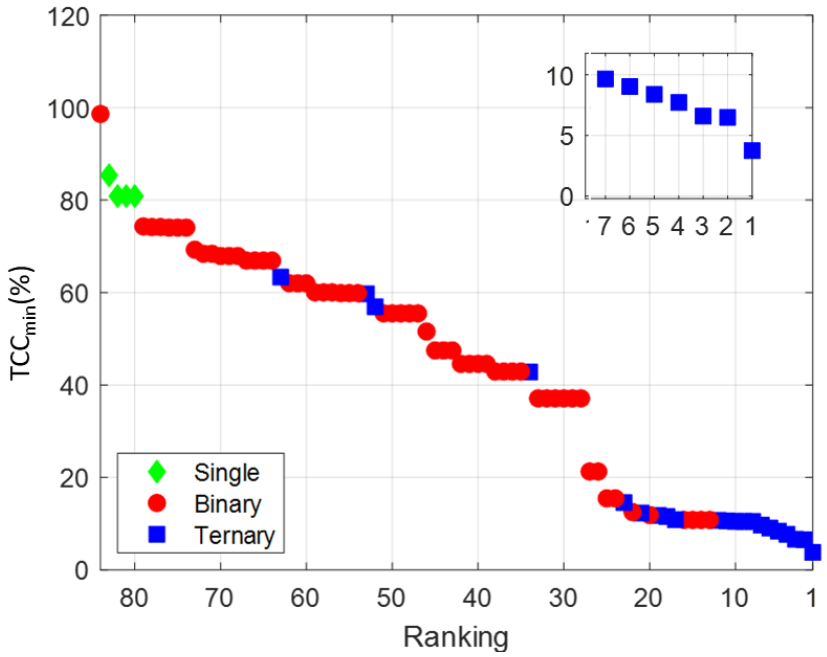

Figure 4.9 Ranked Optimised TCC of the 84 combinations (coloured symbols). 1st is the combination with the lowest TCC_{min}. The sub-plot of the top combinations allows better distinction of TCC_{min}.

Although each ternary combination is a unique set of materials, combinations can simplify to the same binary system, if they match for 2 of the 3 components. These combinations will therefore have identical TCC_{min} and ranked concurrently, producing plateaus in the TCC_{min} ranking.

With the combinations ranked by TCC_{min}, the trends in which components combine effectively can be extracted, Figure 4.10. From the permittivity profiles shown in Figure 4.10 (b), the components often have unique T_{max} values, but can also be roughly grouped with components of similar T_{max} values (L for low, M for middle and H for high T_{max}).

In Figure 4.10 (a), the components in each combination are plotted on the y axis according to their T_{max} value (left axis), with the right axis containing the name of each component (H1, M4, etc). For each x position, there are 3 components plotted. Similar to Figure 4.9, the ■, ●, ◆ symbols are used to denote whether the combination optimises as a ternary, binary or unary layer system. The T_{max} position and colour of the marker is unique for each component. An open symbol is used to represent if a material is in a combination, but not an active layer ($d_f = 0$) at the layer ratio of TCC_{min}.

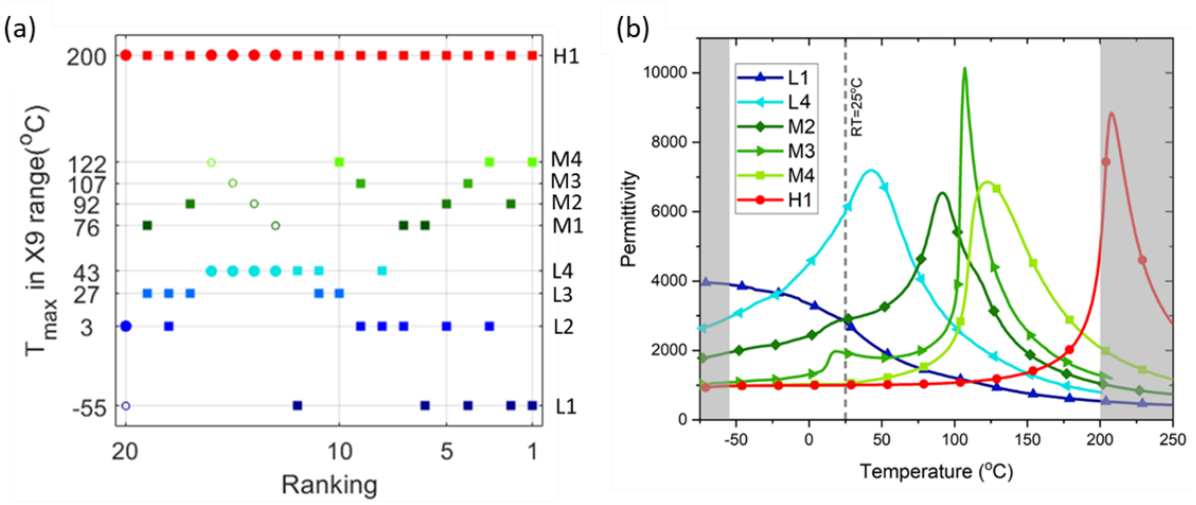

Figure 4.10 (a) A 'Fret' diagram displays the component materials that are in each combination. In this example, the components are distinguished by their respective T_{max} values. As these combinations are ranked by TCC_{min}, trends in which materials combine effectively can be observed. An open symbol represents components with $d_f = 0$. (b) is a selection of permittivity profiles used as input data (all 100 kHz), relating to the names on the right axis in (a).

By ordering the combinations by TCC_{min}, and the components (in this case T_{max}), it is possible to visualise the trends of which materials combine well, and those that do not improve TCC_{min}. In Figure 4.9, the binary plateau (red circles) of combinations ranked 13 to 16, can be found from Figure 4.10 (a) to be due to the L4 and H1 binary not being improved by any of the 'M' components (M1, M2, M3 or M4), with these 'M' components all being open circles.

Due to the added experimental complexity of going from a binary to a ternary, a ternary layer system will need to noticeably outperform the binary optimisations to be considered. Therefore, it is important to compare the relative performance of each combination, as a binary or ternary layer system, Figure 4.11. The plot shows the TCC_{abs} achieved when the combinations are restricted to optimise as a binary or ternary, with the best binary and best ternary values for each combination extracted from the $TCC_{localmin}$ values associated with each combination. If the best binary < best ternary, then this combination simplifies to a binary at TCC_{min}.

From Figure 4.11, rank 15 is an example where the binary TCC_{abs} is significantly better than when the system is forced to be a ternary layer system. Rank 8 is an example where although the system optimises as a ternary system, the benefit in performance over that achieved with only a binary system is negligible.

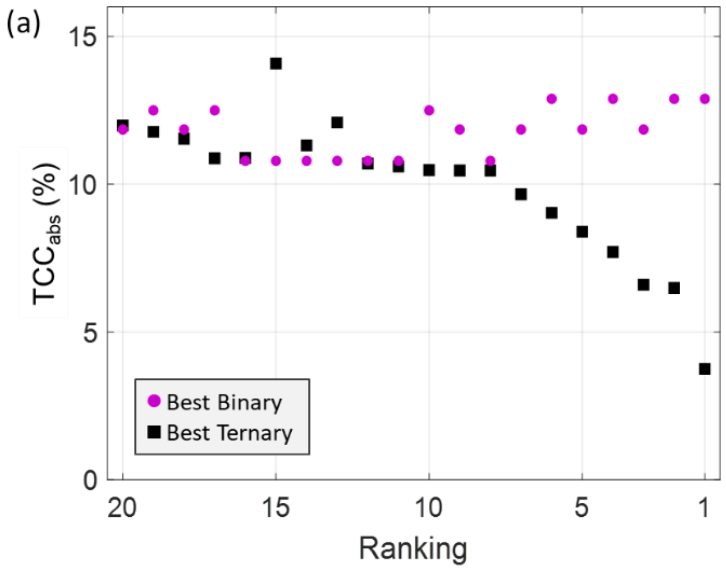

Figure 4.11 The best TCC_{abs} achievable for each 3-material combination, as a ternary and binary layered system. If the best binary point is below that of the best ternary, then the system optimises as a binary layer system. The performance benefit of using a ternary instead of a binary system, can be assessed.

4.5. Temperature Coefficient of Capacitance (TCC) Classification

Although the previous analysis has focused on the different optimised layer ratios, non-optimised layer ratios can still meet industrial specifications for TCC. A few examples of TCC codes are included in Table 4.1. The dependence on the layer ratio of the components, to the TCC classification achieved, is visualised in Figure 4.12.

For the symmetrical classifications (e.g. P, R, S), the allowed positive and negative TCC deviation is equivalent, allowing TCC_{abs} to be used to assess which class(es) a layer ratio achieves. TCC_{asym} is used to assess the asymmetrical classifications (T, U, V etc) in a similar manner, as the *f* factor accounts for the larger negative deviation allowed in TCC% for these classes.

Due to the hierarchical nature of the classifications, a layer ratio can achieve several codes, for example an X7R is also guaranteed to meet X7S.

The best classifications achieved for all layer ratios can be visualised in a ternary diagram, Figure 4.12 (a). For completion, Figure 4.12 (b) plots the asymmetric TCC classes individually, to demonstrate the overlapping of classes in the ternary diagram. The layer thickness tolerance to retain a certain TCC class can be determined, being the shortest distance from edge to centre.

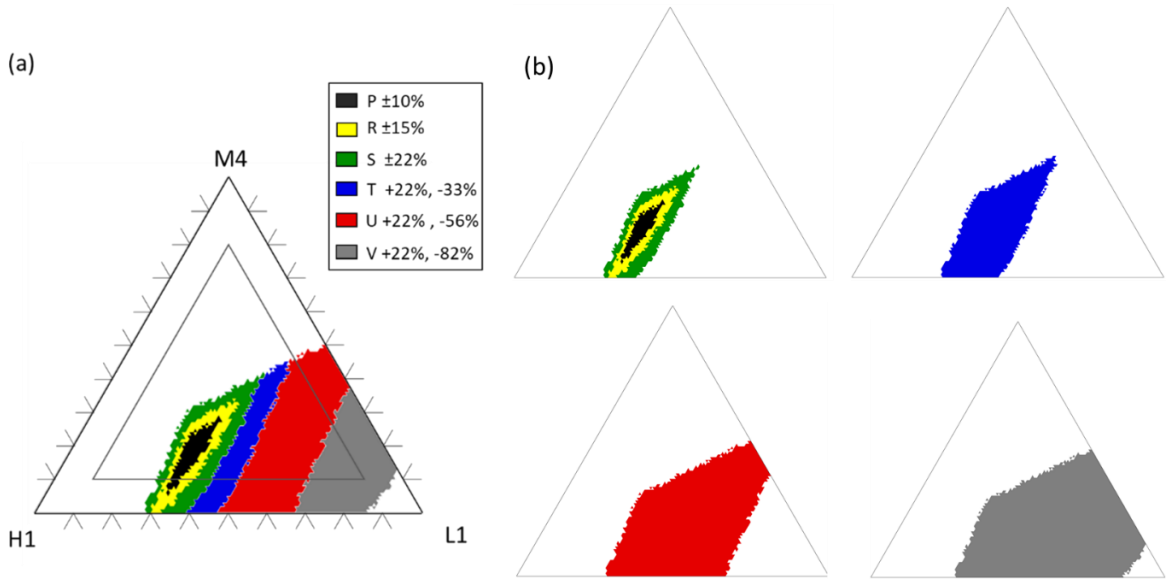

Figure 4.12 Ternary diagram of the layer thickness ratios that meet certain class-2 TCC classifications. The regions represent the tolerance of the layer ratio can deviate by, whilst still maintaining a certain TCC classification.

4.6. Appendix

During this PhD, an application in MATLAB was produced to make the simulation code easier to operate. This appendix summarises the order of operations undertaken by the code, referencing back to the equations included in this chapter. Figure 4.13 (a) contains a screenshot of the simulation application, with comments to the right. The *Load Data* button opens the file explorer for the user to then select the multiple files to be used. The user can then enter the parameters of the simulation. The comments to the right provides information on the variables that are set, and the equations they occur in. Once the data has been loaded and setting selected, the *Run Simulation* button will begin the simulation.

Figure 4.13 (b) demonstrates the order that the simulation equations are called in for each combination, and how the code simulates multiple combinations. As in (a), the code lines have equation numbers to link with the theory explained in this chapter. Part (c) provides the list of plots generated by the code. Many of these plots focus on the ranked performance of the combinations, which allow the user to quickly identify combinations of particular interest. Examples in this thesis of each plot outcome are also referenced. The application also has the capability of plotting the underlying ε_R-T and TCC-T profiles of a particular layer thickness fraction, allowing the user to study how these profiles are affected by changes in the layer dimensions.

(a) Importing data and settings options

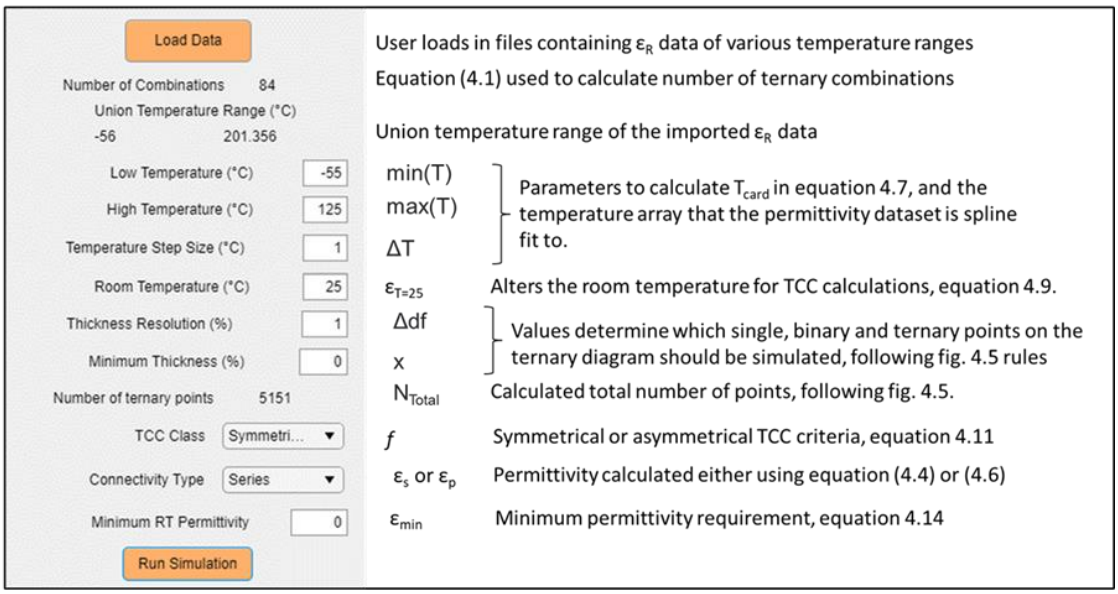

(b) Simplified simulation procedures

for all possible combinations : C(n,k)	(4.1)
for all thickness layer fractions : N_{Total}	Figure 4.5
ε_s profile	(4.4)
ε_s to TCC profile	(4.9)
TCC_{abs}	(4.10)
end	
TCC_{min}	(4.14)
$TCC_{localmin}$	(4.13)
end	

(c) Optimisation Results & Analysis

Sort combinations by their TCC_{min} performance	
Ranked performance plots:	
TCC_{min} vs combination ranking	Figure 4.9
Component T_{max} vs combination ranking	Figure 4.10 (a)
Specific combination plots:	
Ternary colourmap of TCC_{abs}	Figure 4.8
ε_R – T profiles of the best layer fraction	Figure 5.4
ε_R – T profile of a particular position of ternary diagram, enabling user to explore results.	Plots of ε_R – T from (4.4), for specified $d_{f(1,2,3)}$ values

Figure 4.13 Addition information on simulation application developed during this PhD work. (a) explains the various parameters that can be set by the user, whilst (b) is an overview of the order equations are performed in. (c) is a list of plot outputs, with referenced examples.

5. Peer Reviewed Publication

5.1. Publication information

Resource Efficient Exploration of Ternary Phase Space to Develop Multi-Layer Ceramic Capacitors

G. Kerridge, D. C. Sinclair and J. S. Dean

Department of Materials Science & Engineering, Sir Robert Hadfield Building, University of Sheffield, Mappin Street, UK, S1 3JD.

5.2. Abstract

We demonstrate a fast, efficient combinatorial method for the optimisation of materials for multi-layer ceramic capacitors (MLCCs). Experimentally gathered permittivity-temperature profiles for nine compositions spanning a solid solution are used as input, and with series mixing rules, binary and ternary permittivity contour maps are calculated based on individual layer thicknesses. These are converted into Temperature Coefficient of Capacitance (TCC) contour maps and an algorithm is then used to identify material combinations and individual thicknesses suitable for various MLCC classifications. These facilitate targeted experimentation and allowed experimental verification of the methodology. The approach highlights that binary systems can achieve X9(U, T, S and R) classification but the addition of a third complementary material can facilitate a tighter TCC classification (X9P) with a wider tolerance in layer thicknesses, providing a better strategy for mass production of MLCCs. The room temperature permittivity (ε_{RT}) for combinations with similar TCC values can also be evaluated to ensure adequate ε_{RT} is achieved for commercial applications.

5.3. Introduction

Multi-layer ceramic capacitors (MLCCs) based on ferroelectric $BaTiO_3$ (BT) are one of the most heavily produced passive components in electronic circuitry and have been a workhorse of the electronic components industry for more than 30 years [1].

The global MLCC market generated ~3.6 trillion $BaTiO_3$-based units last year and was valued at USD 5,6 billion in 2018. Until the advent of COVID 2019, the MLCC market was expected to reach USD 8.0 billion by the end of 2024 with a compound annual growth rate of 6.38% [2]. MLCCs are relied upon and used across multiple industries with significant demands coming from automotive and telecommunications, causing global supply shortage issues in 2018. An example of this is the recent iPhone X which requires over 1000 MLCCs compared to its predecessor the iPhone 6S with 700 pieces [3]. Another significant growth industry for MLCCs is the automotive sector due to the drive towards 'under-the-hood' electronics and increasing production of electric vehicles, where a modern

Tesla car requires over 10 times more MLCCs than a modern mobile phone [3]. These applications require MLCCs to operate at higher temperature and/or voltages to increase the driving range and charge/discharge times, thus requiring improvements in the temperature stability of the permittivity and/or dielectric breakdown of the ceramics.

To increase the capacitance of an MLCC, the material is required to possess a large permittivity or be fabricated with thinner layers and/or larger area. If the thickness of the dielectric layer is decreased, it brings not only manufacturing challenges but performance and reliability issues due to the increased electric field across the material. Increasing the area is also limited due to the physical case size of the device. By stacking thin layers of BT-based dielectric ceramics (ca 1 – 10 microns) between base metal electrodes (e.g. Ni), MLCCs can possess high capacitance with a temperature stability designed to be retained over designated temperature ranges. Ferroelectric BT is typically the base material as it possesses a high permittivity ~ 1000 - 2500 at room temperature, rising to a sharp maximum of ~ 12,000 at the Curie Temperature, T_c of ~ 120 ^{o}C; however, modification to the heavily temperature dependent permittivity through chemical doping is required to meet industrial requirements and specifications [4, 5]. This temperature stability is measured by a metric known as the Temperature Coefficient of Capacitance (TCC) which describes the maximum percentage change in capacitance over a specified temperature range using a reference room temperature of 25°C and calculated as:

$$TCC(T) = 100 \times \frac{\varepsilon_T - \varepsilon_{RT}}{\varepsilon_{RT}} \tag{5.1}$$

where ε_T is the permittivity at a temperature T, and ε_{RT} is the reference permittivity at a room temperature of 25^{o} C. Using a specified temperature range and TCC fluctuation, capacitors can be subdivided into categories using a letter-number-letter code. A selection of these codes is provided in Table 5.1. For example, a ± 15% temperature variation in TCC across a temperature window of -55 to +125 ^{o}C is known as X7R. TCC changes can also be asymmetric, such as Z5U, which allows TCC changes of +22 to -56% over a temperature from +10 to +85 ^{o}C.

Table 5.1 A list of class II capacitor codes that provides the operational temperature window and allowed changes in TCC.

Low temperature code (°C)	High temperature code (°C)	Allowed capacitance change (TCC, %)
X = −55	4 = +65	P = ±10
Y = −30	5 = +85	R = ±15
Z = +10	6 = +105	S = ±22
	7 = +125	T = +22/−33
	8 = +150	U = +22/−56
	9 = +200	V = +22/−82

The overall permittivity-temperature (ε-T) profile depends on many parameters, including but not limited to; BT grain size, B/T ratio, dopant concentration(s)/distribution(s), volume fraction of grain core and shell regions, thickness of the dielectric layers and the applied electric field [6-17]. Through an intensive trial and error process, various ceramic formulations [18] and device processing conditions (i.e. milling, heating/cooling rates, oxygen partial pressure(s), sintering temperatures and dwell times) [19, 20] are employed to create different volume fractions of core and shell regions to systematically modify the ε-T profile of BT-based ceramics. TCC can thus be controlled over a sufficiently wide temperature range to satisfy industrial standards *via* optimisation of appropriate core-shell volume fractions [10, 21].

It can take several years to develop and optimise a formulation to meet the required TCC. Unfortunately, many fail on other device requirements, such as the Voltage Coefficient of Capacitance (VCC), Electric field Breakdown Strength (EBS), Fatigue Resistance (Life-Time), dielectric loss (tan δ) or resistivity (RC constant). As such very few formulations succeed to commercial applications. Typically, this is done by using a traditional solid-state route. Powder processes such as selecting and drying reagents, calcination and sintering uses substantial energy and time for each step. Techniques such as Finite Element Modelling (FEM) have made it possible to simulate the permittivity response of core-shell microstructured ceramics (on the basis the shell is more resistive than the core) [22-24] and can provide insight and guidance into experimentation of the desired volume fractions of core and shell materials in the dielectric [25], the effects of electrode roughness [26] and the grain size effect on the electric field dependence of the permittivity [27].

Typically for BT-based MLCCs, the dielectric requires $\varepsilon_{RT} > 1000$. There have been investigations on other variations in the layering of materials to alter the way they combine their electrical properties. Instead of single-layer parallel combinations, bi-layer combinations of different materials in direct

contact have also been investigated. Amaral et al [28] combined undoped $BaTiO_3$ and $BaTi_{1-x}Zr_xO_3$, where x = 0.05 to 0.15. As the difference in Zr-content increased between adjacent layers, the permittivity profiles deviated from the prediction based on the ε-T profiles of the two individual materials. SEM results revealed Zr-diffusion at the interface where the Zr-content was intermediate between x = 0.00 and 0.15 of the respective layers. Consequently, the ε-T profile of the interface was not included in the model, leading to a disparity between the measured and calculated ε-T profiles.

Following the same concept, Song et al. [29] selected their materials to limit diffusion between the layers. The materials chosen were a series of $0.975BaTi_{1-x}Sn_xO_3$-$0.025Ba(Cu_{1/3}Nb_{2/3})O_3$, with the Sn doping level increasing in uniform steps from x = 0.01 to 0.08. The layers were separated by Pt electrodes and stacked in the MLCC to ensure the chemical composition difference between any layer and its neighbour was x = ±0.01. This restricted variation in composition was an attempt to limit inter layer diffusion; however, it also limited the variance in T_C which was in the range from -10 to 80 °C for the 8 materials investigated. When combined and co-sintered into an MLCC, the capacitance response was a broad peak with a maximum permittivity at ~25 °C and a TCC of -50% for the X7 temperature range. Although the TCC response improved compared to any of the individual materials, the lack of materials with high permittivity at the extremes of the temperature range (-55 and 125 °C, respectively) only improved stabilisation of the permittivity near 25 °C, rather than providing a significant improvement to the regions of relatively low permittivity. Although this work showed that a composite stack can be used to 'tune' the capacitance response, it also highlighted that materials selection is critical for optimisation.

One possible solution to impede diffusion is by the use of 'floating' electrodes between the materials to act as a physical barrier without being directly connected to the termination. Previously we have demonstrated the fabrication of a simple bilayer ceramic with an internal Au electrode to impede diffusion between sintered ceramics of undoped $BaTiO_3$ (BT) and $Ba_{0.975}Na_{0.025}Ti_{0.975}Nb_{0.025}O_3$ (2.5NNBT) [30]. TCC was optimised to ±6% over a ~ 100 °C temperature range from ~25 to 125 °C whilst maintaining $\varepsilon_r \sim 2000$ with low dielectric loss over the range using a ratio of 0.59:0.41. Although this demonstrated proof-of-concept for a binary layer system, the temperature range where TCC was suitably low was relatively modest and also required tight constraint on the volume fraction (thicknesses) of the two layers. For example, changing the BT:2.5NNBT ratio of the bilayer to 0.55:0.45 or 0.70:0.30 from the optimum 0.59:0.41 produced TCC values >15%.

TCC temperature ranges required for MLCCs are normally much larger, for example the X9 temperature range is 255 °C, from -55 to 200 °C. As BT forms a complete solid solution with $NaNbO_3$ (NN) selecting other NNBT compositions as one of the layers to produce a bi-layer with BT may achieve a larger temperature range with low TCC but may also sacrifice the magnitude of the permittivity. The use of internal electrodes themselves however needs to be considered with care, and can lead to local compositional changes in the ceramic. Wen et al. [31] studied the interface

between the dielectric and internal electrode layers in X7R-type MLCCs. A combination of SEM, EDX, and HRTEM revealed Ni from the electrode was able to diffuse into the BT perovskite lattice up to ~8 nm (via Ti-site substitution during the sintering process) and BT was able to penetrate into the electrode up to 3 nm, giving rise to a ~ 10 nm mixed region.

Conventional laboratory experiments on electroceramics are time and labour intensive and as a consequence they usually focus on in-depth characterisation of a select few 'promising' compositions from a wider series of materials. High-throughput approaches of synthesising materials have become an important approach to rapidly assess larger compositional ranges of material systems and are seen in all aspects of material science [32]. Combinatorial approaches have used atomic deposition processes to produce thin film samples with continuous or discrete compositional variations [33, 34]. There has been work in applying high-throughput methodologies to tape cast materials, which have a length scale similar to a dielectric ceramic layer in multi-layer ceramic capacitors [35].

Here we explore the potential of using such methods on a set of dielectric materials based on a perovskite solid solution. This approach can be used to rank combinations to meet TCC requirements (in the absence of electric field effects) for an extended operating temperature window whilst maintaining suitably high permittivity. The approach is resource efficient requiring only the fabrication and characterisation of the input materials, where many 100's already exist within available literature. This data can be used to generate the ε-T and TCC-T profiles for any combination of the available materials and to provide combinations that are suitable candidates for the various classifications of MLCCs. To illustrate this methodology, we have selected nine materials from the NNBT solid solution series as they exhibit a range of low electric field ε-T profiles normally explored for utilisation as dielectric materials in MLCCs.

5.4. Simulation methodology

To identify the best combination of materials and layer ratios to produce a TCC compliant MLCC, we systematically explore the range of thickness combinations for all possible material combinations. The number of combinations for a given number of input materials (without repetition) is given by

$$C(n,k) = \frac{n!}{k!\,(n-k)!} \tag{5.2}$$

where n represents the number of input materials and k is the number of materials in the system. In this article, we shall use 9 input materials, n = 9, and choose three to make up a tri-layer system, k=3. This generates a total 84 unique ternary combinations.

To calculate the permittivity of a layered system, each layer (material) is assumed to be an individual capacitor connected electrically in series with the others, see Supplementary Figure 1. Equation (5.3) describes the resulting series capacitance C_S as a function of temperature T for our ternary system. The system depends on the individual capacitance, C(T), from each layer and can be re-written as a combination of the permittivity of free space ε_0, the relative permittivity $\varepsilon_r(T)$ and the geometric dimensions of area (A) and thickness (d) of the individual layers.

$$C_S(T) = \left[\frac{1}{C_1(T)} + \frac{1}{C_2(T)} + \frac{1}{C_3(T)}\right]^{-1} = \left[\frac{d_1}{\varepsilon_0 \varepsilon_{r_1}(T) A_1} + \frac{d_2}{\varepsilon_0 \varepsilon_{r_2}(T) A_2} + \frac{d_3}{\varepsilon_0 \varepsilon_{r_3}(T) A_3}\right]^{-1} \quad (5.3)$$

Equation (5.3) can be simplified to a dimensionless equation, as shown in equation (5.4), where the total series permittivity is dependent on the relative thickness fractions, d_f of the three individual dielectric layers (materials) and their individual ε values.

$$\varepsilon_S(T) = \left[\frac{d_{f,1}}{\varepsilon_1(T)} + \frac{d_{f,2}}{\varepsilon_2(T)} + \frac{d_{f,3}}{\varepsilon_3(T)}\right]^{-1} \text{ where } d_{f,1} + d_{f,2} + d_{f,3} = 1 \quad (5.4)$$

To expediate the process of optimisation these equations are employed in a computational algorithm using MATLAB. We first input, from data files, the experimentally measured ε-T profiles for each material. We pre-process each input data set through spline fitting in 1°C steps across the desired temperature range. This is to ensure any noise in the experimental data does not significantly influence the optimisation process. The user then selects the required designed capacitor performance criteria, based on the codes in Table 5.1.

For every one of the 84 combinations, the relative thickness fraction, d_f, of each material will range between 0 and 1. We start the exploration for the optimised structure as a tri-layer system, but this can result in specific cases for the extreme values of d_f. If $d_f = 0$ is found for a specific layer, this material will then not be physically represented. This reduces the system from a ternary into a binary system of the other two materials. Unary systems can also be generated, where one material has $d_f = 1$ and the other two have $d_f = 0$. In consideration of practical applications employing tapecasting, the minimum thickness of any one layer is set at 10% of the total thickness. This corresponds to $d_f = 0.1$ on the basis that $d_f = 1.0$ (total available thickness) is of the magnitude of ~ 10 microns therefore restricting the thinnest layer to be ~ 1 micron. Beyond this limit we used increments of $d_f = 0.01$. The ternary map in Supplementary Figure 2 illustrates the 2802 unique thicknesses explored for an individual ternary combination. For each thickness value, a permittivity profile is calculated for the different material combinations within the ternary system using equation

(5.4). For our example of X9 classification we generated 256 permittivity values based on the temperature range of -55 to 200 °C with 1 °C increments. This generated 717,312 permittivity data points (2802 x 256) and 2802 ε-T profiles for each ternary combination.

Each of the 2802 ε-T profiles within a ternary combination is then converted into a corresponding TCC-T profile using equation (5.1) and the TCC-T profile performance is simplified to the maximum absolute deviation, i.e. $TCC_{abs} = \max|TCC|$. An example of a ternary TCC contour map of the 2802 TCC_{abs} values is given in Supplementary Figure 3. This process is repeated for all 84 ternary combinations. The MATLAB algorithm then identifies the lowest (optimised) TCC which we define as TCC_{min}, for each ternary combination and ranks these from lowest (84^{th}) to highest (1^{st}) in order of decreasing TCC_{min}. It is noteworthy that during this optimisation process many of the 84 ternary combinations reduce to binary systems. This allows us to identify the 84 TCC_{min} values (one from each of the 84 ternary combinations) and to create a TCC_{min} ranking list. Thus from 9 input materials to 84 ranked optimised TCC_{min}, we generate a total of ~60 M permittivity data points (714,510 x 84). This process (excluding the time to generate the input ε-T profiles for the 9 individual materials) takes under 10 seconds on a standard desktop machine.

5.5. Optimisation over a solid solution

We first choose our input materials, here nine input ε-T profiles were selected from a single solid solution. The ceramics were prepared via the conventional solid-state route; more details are given in [30]. The ε-T profiles were obtained using an LCR meter (Agilent E4980 Precision LCR Meter, Agilent Technologies) for a fixed frequency of 100 kHz with an applied ac voltage of 100 mV and corrected for sample geometry. A selection of the ε-T profiles from the series is shown in Figure 5.1 and pertinent details for the full input set are summarised in Table 5.2. The materials were selected on the basis of their permittivity maximum, ε_{max}, being within or close to the extreme limits of the X9 temperature window. For simplicity, the materials were divided into classifications of low (L, ε_{max} between -55 to 43 °C), medium (M, ε_{max} between 76 to 122 °C) or high (H, ε_{max} at 200 °C).

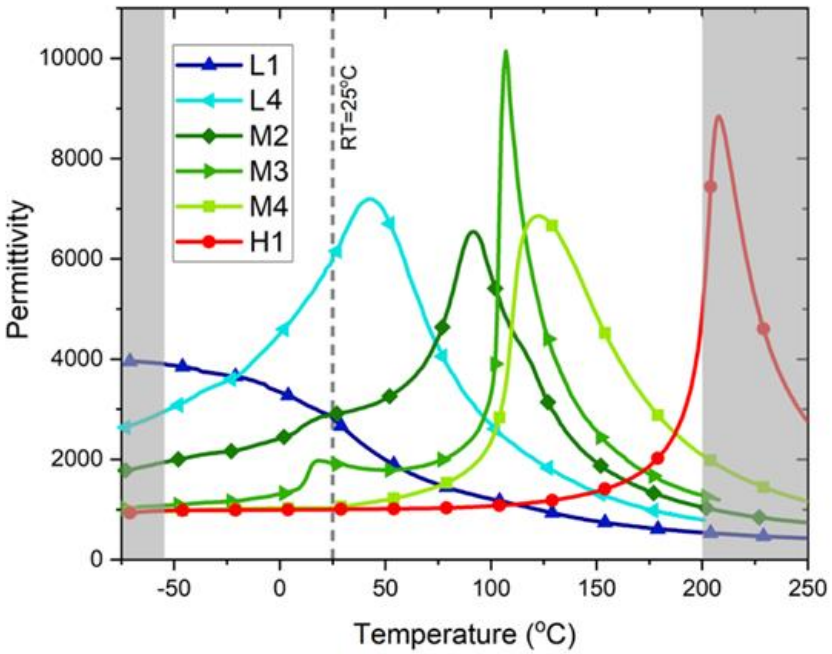

Figure 5.1 A selection of experimentally measured permittivity profiles (all 100 kHz) included in the materials database. Labelled L, M or H depending on where ε_{max} occurs in the X9 temperature range (-55 to 200 °C). The white background indicates the X9R temperature window.

The room temperature permittivity, maximum permittivity and the temperature at which the maximum occurs (ε_{RT}, ε_{max} and T_{max}, respectively) along with the upper and lower values of TCC and TCC_{abs} are shown in Table 5.2. No single material and therefore unary system meets the X9 classification for any capacitor type listed in Table 5.1. The largest TCC_{abs} values for the L- and H-type materials occur at the highest temperature, whereas for M-type materials, the largest TCC_{abs} values occur at lower temperatures. This can be attributed to the relative difference in ε_{RT} compared to ε_{max} at $T_{max.}$ as summarised below.

- **L-type** materials possess high ε_{RT} because ε_{max} and therefore T_{max} is in close proximity to RT. TCC therefore drops substantially at high temperature resulting in large values of TCC_{abs} at 200 °C.
- **M-type** materials have lower ε_{RT} but higher ε_{max} that are located within the X9 widow. These possess high TCC values with TCC_{abs} occurring within the middle of the X9 temperature range.
- **H-type** materials have high ε_{max} leading to poor TCC at high temperatures as the permittivity is always rising from ε_{RT}. TCC_{abs} therefore occurs at 200 °C.

Table 5.2 Classification and summary of the permittivity and temperature stability characteristics of the 9 materials used in the combinatorial simulations. TCC values are determined for the X9 temperature range (-55 to 200 °C).

		Ref	Maximum			Minimum			
	Material	ε_{RT}	ε_{max}	T_{max} (°C)	TCC_{upper} (%)	ε_{min}	T_{min} (°C)	TCC_{lower} (%)	TCC_{abs} (%)
	L1	2828	3905	-55	38	541	200	-81	81
	L2	5520	5770	3	5	808	200	-85	85
	L3	6710	6725	27	0	726	200	-89	89
	L4	6026	7192	43	19	799	200	-87	87
	M1	3036	5603	76	85	823	200	-73	85
	M2	2903	6540	92	125	1048	200	-64	125
	M3	1920	10140	107	428	1079	-55	-44	428
	M4	1038	6855	122	560	966	-55	-7	560
	H1	1002	4901	200	389	979	-55	-2	389

5.6. Optimisation: simulations.

For our example, each input material is considered in 28 of the possible 84 combinations. Any two of the materials considered together are present in 7 different ternary systems. The TCC_{min} for each ternary combination is shown in Figure 5.2 (a), and Figure 5.2 (b) shows the ranking in terms of the materials involved.

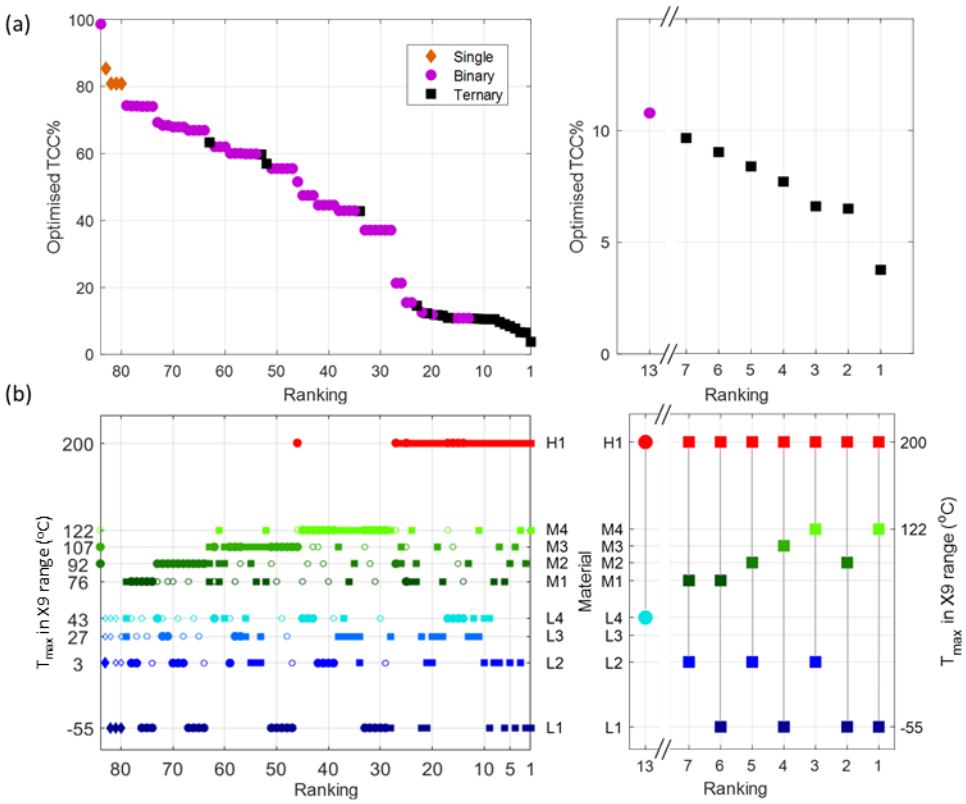

Figure 5.2. Output from the optimisation algorithm based on TCC_{min} for the 84 ternary material combinations. (a) TCC_{min} versus ranking for the 84 ternary combinations. (b) Variation in materials classifications for TCC_{min} optimisation. Note the best binary system (ranked 13) and seven best ternary systems (ranked 1-7). Aligned together, (a) and (b) show materials classification trends to achieve optimisation based on TCC_{min}. Note: in (b, left), filled diamonds, open circles and filled squares denote unary, binary and ternary combinations, respectively.

The right-hand side of each figure highlights optimised layer combinations for the top 7 best ranked systems and with rank 13, which represents the best bi-layer combination. The individual d_f values required to obtain TCC_{min} for each of these combinations is also given in Table 5.3.

Table 5.3 Selected TCC_{min} ranked ternary systems showing the materials involved and their d_f values. Rank 13 is the best bi-layer combination and ranks 7 to 1 are the top 7 tri-layer combinations.

	Material			d_f for each material		
Ranking	1	2	3	1	2	3
13	L4	-	H1	0.39	-	0.61
7	L2	M1	H1	0.27	0.14	0.59
6	L1	M1	H1	0.14	0.25	0.61
5	L2	M2	H1	0.28	0.16	0.56
4	L1	M3	H1	0.25	0.16	0.59
3	L2	M4	H1	0.39	0.10	0.51
2	L1	M2	H1	0.15	0.29	0.56
1	L1	M4	H1	0.31	0.19	0.50

Although these data capture TCC_{min} for each ternary system, Figure 5.3 compares the lowest TCC for the best bilayer and trilayer combinations for the top 20 ranked systems where TCC ≤ 15% and therefore within X9R classification. The ε-T and TCC-T profiles for the optimised bilayer (rank 13) and trilayer (rank 1) combinations are shown in Figure 5.4. The salient features from Figure 5.1 to Figure 5.4 are discussed below.

i. Of the 84 combinations, optimisation leads to 4 single, 59 binary and 21 ternary systems, Figure 5.2 (a).
ii. Between ranking 33 to 28, L1 and M4 combine 6 times within different ternary combinations where the third material is another L or M to produce a bilayer with a TCC_{min} of ~ 37%. Only with the addition of H1 to form a trilayer does the ternary combination outperform this. The optimised L1-M4-H1 trilayer outperforms all other combinations with TCC_{min} of 4%, Figure 5.2 (a) and (b).
iii. The best binary combination is a bilayer of L4-H1 (rank 13) with a ratio of 0.39:0.61, and TCC_{min} ~ 10.5%, Figure 5.2 (a), (b) and Table 5.3.
iv. The 7 highest ranking combinations based on TCC_{min} are trilayers that each contain a L, M and H material, see black squares in Figure 5.2 (a) and (b), can achieve X9P classification. The optimised trilayer (rank 1) achieves a 2.8 times improvement of TCC_{min} compared to the optimised bilayer (rank 13), Figure 5.3. Combinations that contain two L or two M materials rarely optimise as ternary systems with only one of them featuring in a final optimised

bilayer. The top 27 ranked combinations all contain H1 and perform noticeably better in TCC. This is due to the addition of a high temperature ε_{max} material that restricts the severe drop-off in TCC for all L and M1-3 materials at the upper temperature of the X9 range, Figure 5.1 and Table 5.2.

v. The significance of $T_{max.}$ is apparent from Figure 5.2 (b) where the highest ranked combinations are those with the largest spread in T_{max}. This is shown where L1 outperforms L2 when combined with the same M and H materials, ranked 1 and 3, respectively. The position of T_{max} is not the only significant factor, the shape of the ε–T profile is also important. The combination of L1-M2-H1 (rank 2) outperforms L1-M3-H1 (rank 4) in TCC_{min} by 3%, Figure 5.2 (b), despite M2 having a lower T_{max} and ε_{max} than M3, Figure 5.1 and Table 5.2. M2 has a broader and lower permittivity profile than M3, allowing better TCC stability in the middle of the X9 temperature window, Figure 5.1. Materials L3 and L4 do not appear in any of the L-M-H combinations that meet X9P.

vi. Bilayers of H1 combined with L1-4 can achieve TCC ~ 11-13%, red symbols in Figure 5.3 (a).

vii. Various trilayers based on L-L-H and L-M-H combinations have similar TCC values (blue symbols in Figure 5.3 (a) for rankings 20 to 8) to those of L-H bilayers highlighted in (v) by the red symbols in Figure 5.3 (a). Adding a third layer (either L or M) or replacing L4 with a combination of L and M materials for these rankings has very little (if any) improvement on TCC_{min} compared to the best bilayer combination of L4-H1 (rank 13).

viii. There is a distinct improvement in TCC for trilayers over bilayers for rankings 7 to 1, Figure 5.3, due to clear divergence in T_{max} for the L and M materials and the balanced combination of L-M-H materials.

To illustrate some of these features we discuss the ε-T and TCC-T profiles for the TCC_{min} optimised bilayer (rank 13) and trilayer (rank 1), Figure 5.4.

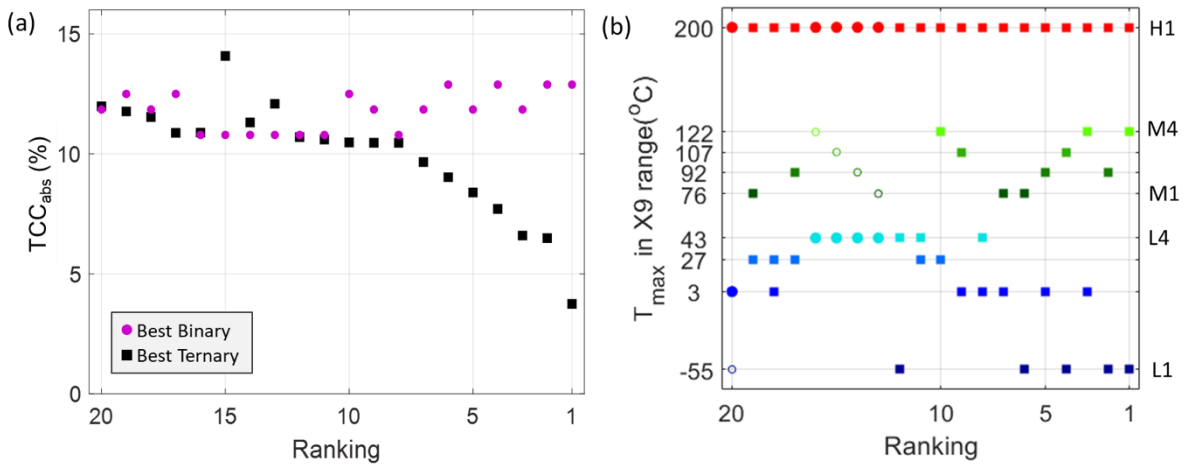

Figure 5.3 (a) The lowest TCC for the best bilayers and trilayers from the top 20 ranked combinations. (b) The Materials involved in the top twenty ranked combinations. In (b), open symbols in ranks 15-13 indicate the third starting material which optimised out of the system with $d_f = 0$.

The optimised bilayer has its TCC_{lower} at -55°C, and TCC_{upper} at 200°C. As the permittivity of the two materials combine in a reciprocal manner, equation (5.4), the permittivity of the bilayer tends towards the lower permittivity material (for similar values of d_f). L4 allows for suppression of the large TCC_{upper} of H1 at 200°C, and H1 suppresses TCC_{lower} of L4, Figure 5.4 (a), black line. At the optimised d_f ratio, the two turning points of the TCC profile are reasonably well balanced and allow TCC_{lower} and TCC_{upper} to be within X9R specification, Figure 5.4 (b), black line. This balancing, however, leads to this binary system being sensitive to changes in d_f, i.e X9R is met only for x = 0.38 – 0.44 with optimisation at x = 0.39.

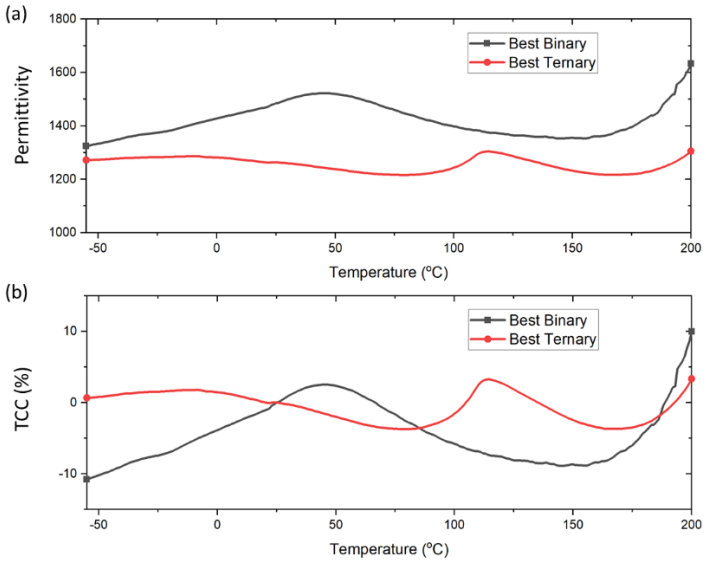

Figure 5.4 Comparison of the combinations that optimise as the best binary (L4-H1) and the best ternary (L1-M4-H1). (a) The e-T profiles at the optimised d_f values of 0.39:0.61 and 0.31:0.19:0.50, respectively, and (b) the corresponding TCC profiles. Simulation produced from experimental data of the materials, measured at 100 kHz.

The optimised trilayer (rank 1) can achieve X9P classification due to the flatter ε-T profile, Figure 5.4 (a) red line, due to the distribution of the three T_{max} values (i.e. -55, 122 and 200 °C, respectively) across the X9 window. The ε-peak of one material is suppressed by the other two leading to four turning points in the TCC-T profile, Figure 5.4 (b) red line, compared to the two turning points in the binary, Figure 5.4 (b) black line. The increased number of turning points allow TCC to be 'rotated' back into the X9P specification as successive turning points occur.

The importance of how the third material can influence the optimisation is illustrated in Figure 5.5 (a) for the TCC contour map of L1-M4-H1. Here we show the effect of (i) adding M4 into the best binary (L4-H1) and (ii) adding H1 into the L1-M4 binary. Both lead to the optimised TCC_{min} within the ternary system (rank 1) indicated by the yellow star in Figure 5.5 (a).

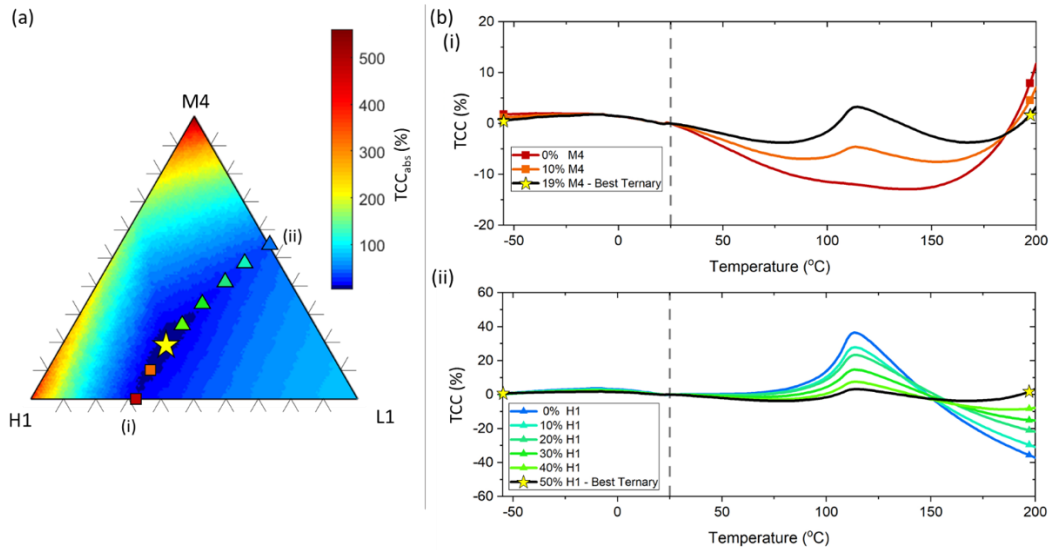

Figure 5.5 (a) The TCC contour map of the ternary system L1-M4-H1. The coloured symbols follow a lowering of TCC to obtain TCC_{min} (yellow star symbol) within the ternary system starting from the lowest TCC values associated with the H1-L1, point (i), and M4-H1, point (ii) binary systems. (b) (i) and (ii) are the TCC-T profiles that illustrate the influence of a third material (M4 and H1, respectively) on the binary systems of H1-L1 and L1-M4 to achieve TCC_{min}.

Starting on the L1-H1 binary system with the optimised d_f ratio of 0.39:0.61, point (i) in Figure 5.5 (a), there is a drop in TCC between 100-150 °C, whereas it rises steeply from ~ 175 to 200 °C, Figure 5.5 (b,i). As the M4 profile possesses a ε peak at 122 °C with decreasing ε at 200°C, it works well as an addition in this region of the X9 window. Increasing the d_f of M4 from 0.00 to 0.19, increases the overall ε at 100-150 °C whilst decreasing it at higher temperatures. This flattens the overall TCC profile and meets X9P specification, Figure 5.5 (b,i). The optimised d_f ratio on the L1-M4 binary system, point (ii) in Figure 5.5 (a), has a large peak in TCC at ~ 122 °C and a large and negative TCC at 200°C. These features are associated with the ε peak of M4 and the absence of the high ε of H1 at higher temperatures. Increasing the d_f of H1 from 0.00 to 0.50 suppresses the ε peak associated with M4 and increases the overall permittivity at higher temperatures thus suppressing both the TCC peak at ~122 °C and the large negative TCC at 200 °C to achieve X9P classification, Figure 5.5 (b,ii).

5.7. Optimisation: experimental verification

Identification of how to achieve TCC_{min} optimisation based on these material sets allows key ceramics to be combined in different thicknesses to validate the simulations and to replicate the TCC contour map and profiles shown in Figure 5.5. Ceramics of L1, M4 and H1 were prepared by the solid state method described previously [30] and their major faces coated with Au paste electrodes. The ceramics were stacked electrically in series to replicate bilayers or trilayers with the relative thicknesses of the ceramics representing their d_f. With initial thicknesses of 0.86, 0.83 and 4.51 mm for L1, M4 and H1 ceramics, respectively this allowed experimental ε-T profiles to be measured for

L1-M4, L1-H1 and M4-H1 bilayers at points 1, 2 and 3 and for an L1-M4-H1 trilayer at point 4 in the ternary system as shown in Figure 5.6.

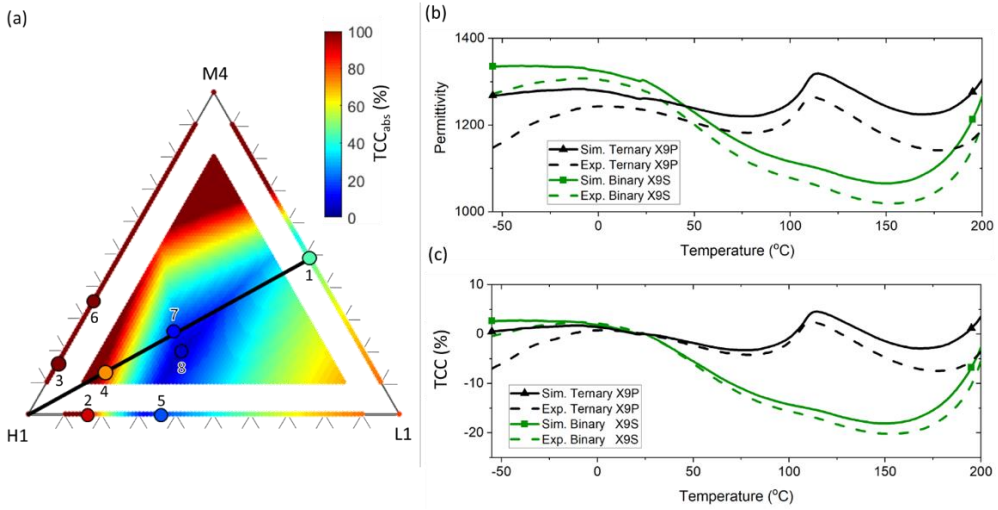

Figure 5.6 (a) The TCC contour map for the ternary system L1-M4-H1 with selected points (1-8) to indicate bilayer or trilayer combinations of ceramics used for experimental verification. (b) and (c) show the permittivity and TCC comparisons for simulated and experimentally measured samples of an X9S bilayer (point 5) and an X9P trilayer (point 8). The Internal triangle in (a) is the window where $d_f \geq 0.1$. Experimental data on pellets mechanically connected in series, such that electrode faces of each pellet is in direct contact.

Selective thinning of the ceramics created various d_f values, allowing other bilayers (points 5 and 6) and trilayers (7 and 8) to be investigated with samples 4, 7 and 1 being on a tie line between bilayer 1 (L1-M4) and H1 and sample 8 close to the 0.31:0.19:0.50 ratio required to obtain TCC_{min} based on the simulations. The list of pellet thicknesses and d_f values for the various bi- and tri-layers along with TCC (simulation) compared to TCC (experimental) are given in Table 5.4. The solid lines in Figure 5.7 (b) and (c) are the simulated profiles based on those d_f values, meeting the classifications of X9P (point 8) and X9S (point 5). The dashed lines are the experimental verification based on the results from the ceramics. The ε-T and TCC-T profiles obtained from the experimental results closely follow the simulated profiles but possess lower than predicted ε. The measured permittivity is ~2% lower than that simulated at room temperature, increasing to ~9% at both -55 and 200 °C for the trilayer. The bilayer behaves similarly, with the measured permittivity being ~ 4% lower at room temperature and rising to ~7% at the X9 temperature limits. This permittivity decrease affects TCC of the measured samples but not enough to cause them to fail the predicted specification. The lower ε values are attributed to contact interfaces between the ceramics in the bi- and tri-layer samples.

Table 5.4 Thickness and d_f values of ceramics along with TTC_{abs} values for simulations and experiments based on eight points (1-8) illustrated in Figure 5.6 (a).

No.	Pellet Thickness (mm)			Total Thickness (mm)	df of material			Simulation	Experimental
	L1	M4	H1		L1	M4	H1	TCC_{abs} (%)	TCC_{abs} (%)
1	0.86	0.83	-	1.69	0.51	0.49	-	44.5	44.9
2	0.86	-	4.51	5.37	0.16	-	0.84	91.4	91.6
3	-	0.83	4.51	5.34	-	0.16	0.84	302.2	264.1
4	0.84	0.83	4.51	6.18	0.14	0.13	0.73	95.0	72.4
5	0.84	-	1.52	2.36	0.36	-	0.64	18.1	20.2
6	-	0.83	1.52	2.35	-	0.35	0.65	227.3	164.1
7	0.84	0.83	1.52	3.19	0.26	0.26	0.48	15.9	11.4
8	0.84	0.55	1.34	2.73	0.31	0.20	0.49	4.6	7.5

5.8. Further Optimisations: (i) TCC classification and (ii) room temperature permittivity.

(i) Although optimisation for X9P provides a high specification capacitor based on trilayers it is not the only commercially viable option. With the use of this code, optimisation for TCC associated with other classifications is possible, as shown in Figure 5.7. Here the smallest (black) region highlights the tightest classification of X9P and this can only be obtained from ternary combinations. The optimised combination of 0.31:0.19:0.50 for L1-M4-H1 lies close to the centre of the black area and indicates there is a level of variation in d_f values within the ternary diagram where X9P can be achieved. This is potentially useful for any small variations in d_f values during processing of MLCCs. Relaxing the TCC classification from P=±10% to R=±15% generates additional sets of combinations, shown in the yellow region. Lowering the tolerance of TCC for the other classifications shown in Table 5.1 down to X9V (+22 to -82%) yields viable combinations as shown by the other coloured regions in Figure 5.7. TCC classification of P, R and S are symmetrical causing the optimised coloured region to maintain their shape; however, T, U and V classifications are asymmetrical and this permits greater negative deviation in TCC_{lower} than positive TCC_{upper} and results in these regions expanding towards combinations with increased d_f of L1. For these latter classifications it is clear that bilayers have a wide d_f tolerance window and offer a simpler practical solution as opposed to the use of trilayers.

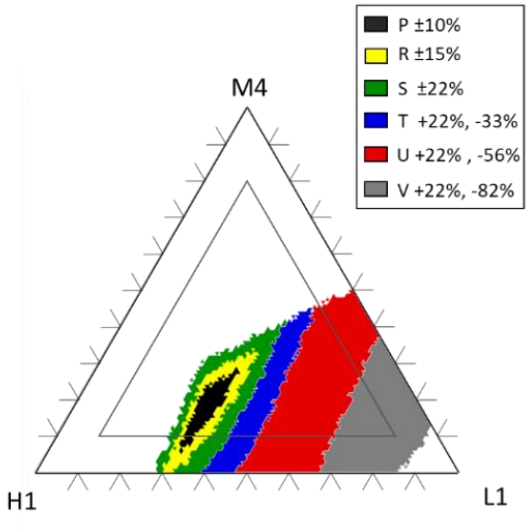

Figure 5.7 Simulated regions of the L1-M4-H1 ternary system that achieves different TCC classifications.

(ii) The main optimisation parameter in this script has been low electric field TCC; however, other parameters are important for MLCC manufactures, such as the room temperature permittivity, ε_{RT}. This is an output that our code can also generate in the TCC_{min} ranking process as shown in Figure 5.8. The general trend followed is that combinations that possess high ε_{RT} generally lead to a poor TCC_{min}.

As the permittivity tends to the lowest value (for a series type combination), materials with low $\varepsilon_{RT,}$ will reduce the overall permittivity of the device. In our example, the use of H1 provides the ability to increase the TCC operational temperature window (high T_{max} of 200 ^{o}C) but has the lowest ε_{RT} (1002) of the nine available materials, Table 5.1. 27 of the 28 combinations that include H1 result in TCC_{min} being < 22 %, Figure 5.2; however, there are significant variations in ε_{RT}, see inset in Figure 5.8. This may influence the final choice of material combinations for MLCC production.

Optimisation of TCC_{min} is favourable with T_{max} of the materials spread across the temperature range using a combination of L-M-H materials; however, ε_{RT} is enhanced by those with T_{max} near RT. From the 7 combinations in our example that optimise for X9P, the top ranked combination of L1-M4-H1 has both the lowest TCC_{min} and ε_{RT}, Figure 5.8. The 3rd ranked combination however of L2-M4-H1 offers an alternative option that comfortably achieves X9P specification (TCC_{min} ~ 6.5 %) but with an increase in ε_{RT} of ~1500. The higher ε_{RT} is attributed to the T_{max} values of L2 (3 ^{o}C) and M2 (92 ^{o}C) being closer to RT compared with L1 (-55 ^{o}C) and M4 (122 ^{o}C) in the top ranked combination, Figure 5.1 and Table 5.1.

As a consequence, the 3rd ranked combination of L2-M4-H1 based on TCC_{min} may be a better overall choice for MLCC production given the ~ 20% enhancement in ε_{RT}.

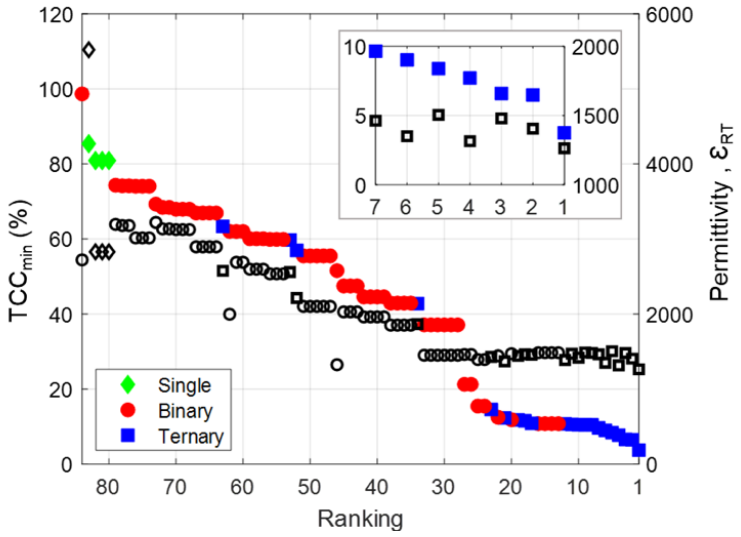

Figure 5.8 Ranked optimised TCC_{min} for the 84 combinations (coloured symbols), with an overlay of corresponding room temperature permittivity (open black squares). Inset shows TCC_{min} and room temperature permittivity for the top seven ranked ternary systems on an expanded scale.

5.9. Limitations and future directions

Although our approach does present a resource efficient starting point based on TCC it has several limitations and challenges. We outline three below.

(i) Availability of VCC data. Here we have focused on the low electric field dielectric properties of bulk ceramics to assist with materials selection and have based our criterion on optimising TCC first, and then ε_{RT}. In practice, the design of MLCCs requires dielectric layers of ~ 1- 10 microns. At such thicknesses there are several critical parameters that influence TCC and ε_{RT} based on size and scaling effects [16,18] that we have not considered, e.g. grain size, microstructure, the number of grain boundaries and voltage effects. Consideration of VCC is particularly important as it is known to influence TCC in thin dielectric layers of $BaTiO_3$-based formulations. To experimentally assess VCC requires ε-T measurements to be performed as a function of dielectric thickness (typically below ~ 10 microns) and under high electric fields (typically ~ 10's kV/cm). As a consequence, VCC data is not easily available for bulk ceramics and is rarely reported for proto-type MLCCs in the literature. This limits our present approach to consider TCC in the absence of electric field effects.

(ii) Interdiffusion, pO_2 stability and electrode effects. Our approach is based on dense ceramics being physically separated by Au electrodes prior to electrical characterisation. This avoids the interdiffusion effects that occur during processing of MLCCs based on layers with different composition and which lead to significant deviations between modelled and experimental TCC profiles [28, 29]. Such effects could be limited by selecting materials that have similar compositions or by the use of floating electrodes within MLCCs to restrict interdiffusion. Furthermore, the majority of MLCCs use Ni as internal electrodes and are processed under reducing conditions at high

temperatures. All potential materials identified would have to be tested for their ability to withstand these processing conditions and be compatible with Ni electrodes prior to MLCC development.

(iii) Resistivity. The calculations used in our approach are based only on permittivity and do not include the resistivity of the materials. Resistivity is an important parameter for bi- or tri-layered MLCCs as the potential difference across each material will be different. This will influence the electric field across each layer and therefore TCC.

Future work is currently underway to implement a description of the voltage effect into the prediction tool. A combination of VCC measurements with fitting from Johnson's approximation [27, 36] should allow some prediction on the influence of VCC on TCC. Further optimisation of voltage dependency to include features associated with grain size may be achieved by modifying the Johnson parameter [27]. Interdiffusion layers are being considered through linking to atomic scale simulations. By simulating the movement of cations in the interface region, the chemical composition variation of this region could be predicted. The permittivity response of the interface region could then be extrapolated from published solid-solution data, and included into the model as several layers. Electrode roughness is known to produce localised regions of high electric field, rather than a uniform electric field which Johnson's equations presume. The non-uniform electric fields would be predicted using FEM approaches, VCC approximations then simulating the variation in permittivity produced. A hybrid model that also includes layers simulated by FEM approaches etc, could allow micron length scale effects to be incorporated, improving the accuracy of the model.

In conclusion, we have presented and experimentally verified an efficient combinatorial method for the optimisation of materials for multi-layer ceramic capacitors (MLCCs) based on bilayer or trilayer combinations of materials. Experimental ε-T data from nine materials were used to generate ~ 60 M permittivity data points over the X9 classification temperature range for 84 unique ternary systems based on varying individual layer thicknesses. An algorithm was used to rank performance based on the low electric field TCC_{min} for each system; however, additional factors such as ε_{RT} and the justification for tri- as opposed to bi-layers were also considered in selecting the most appropriate combination of materials.

Our example demonstrated how to identify a subset of 7-8 ternary and a 'best binary' combination of materials with X9R classification. Although the example was based on experimental input from nine materials within a single solid solution phase there is (in principle) no limit to the number of input materials. A much wider range of materials can be explored; however, chemical compatibility, interdiffusion, microstructural control and the sintering characteristics of the individual materials remain practical issues that require investigation.

Finally, our method to assist with materials selection is based on TCC and ε_{RT} obtained from the low electric field dielectric properties of bulk ceramics. Future developments require consideration of the VCC and resistivity of the materials. These parameters are especially critical in the development

of high voltage and/or temperature X8R (and beyond) MLCCs. The approach is therefore a resource efficient *starting point* for the development cycle of engineered dielectrics for MLCC applications. It should be viewed as a prerequisite to the necessity of focusing on microstructural control, chemical and electrode compatibility and the development of critical MLCC characteristics (in addition to TCC and ε_{RT}) such as VCC, Life-time and EBS.

5.9.1. Acknowledgements.

We thank the Engineering and Physical Science Research Council (EPSRC) for a studentship (GK) and for financial support: EP/L017563/1; Substitution and Sustainability in Functional Materials and Device; DCS and JSD, and EP/P019919/1; Charging Ahead with Multi-Layer Ceramic Capacitor Materials; JSD.

5.10. References.

[1] H. Kishi, Y. Mizuno, and H. Chazono, "Base-metal electrode-multilayer ceramic capacitors: Past, present and future perspectives," *Japanese Journal of Applied Physics Part 1-Regular Papers Short Notes & Review Papers,* Review vol. 42, no. 1, pp. 1-15, Jan 2003, doi: 10.1143/jjap.42.1.

[2] "Global Multilayer Ceramic Capacitor (MLCC) Market, by Type (Class I (NP0/C0G, U2J, others), Class II (X7R, X5R, Y5V, Z5U), by Application (Consumer Electronics, Automotive, Manufacturing, Telecommunication, Transportation, Healthcare). Forecast till 2024", ID: MRFR/SEM/6269-HCR. Market research future, Available from https://www.marketresearchfuture.com/reports/multilayer-ceramic-capacitor-market-7738 (last accessed August 2020)

[3] D. Wolfe, "The global shortage of capacitors impacts all consumer electronics ",Quartz Media, March 2019.

[4] K. J. Park, C. H. Kim, Y. J. Yoon, S. M. Song, Y. T. Kim, and K. H. Hur, "Doping behaviors of dysprosium, yttrium and holmium in $BaTiO_3$ ceramics," *Journal of the European Ceramic Society,* Article vol. 29, no. 9, pp. 1735-1741, Jun 2009, doi: 10.1016/j.jeurceramsoc.2008.10.021.

[5] M. Y. Liu *et al.*, "Temperature stability of dielectric properties for $xBiAlO_3$-(1-x)$BaTiO_3$ ceramics," *Journal of the European Ceramic Society,* Article vol. 35, no. 8, pp. 2303-2311, Aug 2015, doi: 10.1016/j.jeurceramsoc.2015.02.015.

[6] L. Gong, X. H. Wang, S. P. Zhang, H. Wen, and L. T. Li, "Grain size effect on electrical and reliability characteristics of modified fine-grained $BaTiO_3$ ceramics for MLCCs," *Journal of the European Ceramic Society,* Article vol. 34, no. 7, pp. 1733-1739, Jul 2014, doi: 10.1016/j.jeurceramsoc.2013.12.028.

[7] T. R. Armstrong and R. C. Buchanan, "Influence of core shell grains on the internal-stress state and permittivity response of zirconia-modified barium-titanate," *Journal of the American Ceramic Society,* Article vol. 73, no. 5, pp. 1268-1273, May 1990, doi: 10.1111/j.1151-2916.1990.tb05190.x.

[8] F. D. Morrison, D. C. Sinclair, and A. R. West, "Electrical and structural characteristics of lanthanum-doped barium titanate ceramics," *Journal of Applied Physics,* Article vol. 86, no. 11, pp. 6355-6366, Dec 1999, doi: 10.1063/1.371698.

[9] K. Yasukawa, M. Nishimura, Y. Nishihata, and J. Mizuki, "Core-shell structure analysis of $BaTiO_3$ ceramics by synchrotron X-ray diffraction," *Journal of the American Ceramic Society,* Article vol. 90, no. 4, pp. 1107-1111, Apr 2007, doi: 10.1111/j.1551-2916.2007.01537.x.

[10] M. Y. Liu *et al.*, "Preparation and dielectric properties of X9R core-shell $BaTiO_3$ ceramics coated by $BiAlO_3$-$BaTiO_3$," *Ceramics International,* Article vol. 42, no. 1, pp. 379-387, Jan 2016, doi: 10.1016/j.ceramint.2015.08.120.
[11] C. A. Randall, S. F. Wang, D. Laubscher, J. P. Dougherty, and W. Huebner, "Structure property relationships in core-shell $BaTiO_3$-LiF ceramics," *Journal of Materials Research,* Article vol. 8, no. 4, pp. 871-879, Apr 1993, doi: 10.1557/jmr.1993.0871.
[12] Z. H. Yao, H. X. Liu, Y. Liu, Z. H. Wu, Z. Y. Shen, and M. H. Cao, "Structure and dielectric behavior of Nd-doped $BaTiO_3$ perovskites," *Materials Chemistry and Physics,* Article vol. 109, no. 2-3, pp. 475-481, Jun 2008, doi: 10.1016/j.matchemphys.2007.12.019.
[13] H. I. Hsiang, F. S. Yen, and C. Y. Huang, "Effects of porosity on dielectric-properties of $BaTiO_3$ ceramics," *Japanese Journal of Applied Physics Part 1-Regular Papers Short Notes & Review Papers,* Article vol. 34, no. 4A, pp. 1922-1925, Apr 1995, doi: 10.1143/jjap.34.1922.
[14] G. Arlt, D. Hennings, and G. Dewith, "Dielectric-properties of fine-grained barium-titanate ceramics," *Journal of Applied Physics,* Article vol. 58, no. 4, pp. 1619-1625, 1985, doi: 10.1063/1.336051.
[15] V. Buscaglia and C. A. Randall, “Size and scaling effects in barium titanate. An overview,” *Journal of the European Ceramic Society*, Article vol, 40, pp. 3744-3758, 2020, doi.org/10.1016/j.jeurceramsoc.2020.01.021.
[16] K. Hong, T. H. Lee, J. M. Suh, J. S. Park, H. S. Kwon, J. Choi and H. W. Jang, “Direct observation of surface potential distribution in insulation resistance degraded acceptor-doped $BaTiO_3$ multilayered ceramic capacitors”. *Electronic Materials Letters*, Article vol. 14, no. 5, pp 629-635, 2018, https://doi.org/10.1007/s13391-018-0066-6.
[17] K. Hong, T. H. Lee, J. M. Suh, S. H. Yoon and H. W. Jang, “Perspectives and challenges in multilayer ceramic capacitors for next generation electronics”. *Journal of Materials Chemistry C*, Article vol 7, no 32, pp 9782-9802, 2019, doi: 10.1039/c9tc02921d.
[18] M. T. Buscaglia, M. Viviani, Z. Zhao, V. Buscaglia, and P. Nanni, "Synthesis of $BaTiO_3$ core-shell particles and fabrication of dielectric ceramics with local graded structure," *Chemistry of Materials,* Article vol. 18, no. 17, pp. 4002-4010, Aug 2006, doi: 10.1021/cm060403j.
[19] C. H. Kim, K. J. Park, Y. J. Yoon, D. S. Sinn, Y. T. Kim, and K. H. Hur, "Effects of milling condition on the formation of core-shell structure in $BaTiO_3$ grains," *Journal of the European Ceramic Society,* Article vol. 28, no. 13, pp. 2589-2596, Sep 2008, doi: 10.1016/j.jeurceramsoc.2008.03.030.
[20] M. T. Benlahrache, N. Benhamla, and S. Achour, "Dielectric properties of $BaTiO_3$-$NaNbO_3$ composites," *Journal of the European Ceramic Society,* Article; Proceedings Paper vol. 24, no. 6, pp. 1493-1496, 2004, doi: 10.1016/s0955-2219(03)00577-6.
[21] Y. Sun, H. X. Liu, H. Hao, Z. Song, and S. J. Zhang, "Structure Property Relationship in $BaTiO_3$-$Na_{0.5}Bi_{0.5}TiO_3$-Nb_2O_5-NiO X8R System," *Journal of the American Ceramic Society,* Article vol. 98, no. 5, pp. 1574-1579, May 2015, doi: 10.1111/jace.13517.
[22] J. S. Dean, J. H. Harding, and D. C. Sinclair, "Simulation of Impedance Spectra for a Full Three-Dimensional Ceramic Microstructure Using a Finite Element Model," *Journal of the American Ceramic Society,* Article vol. 97, no. 3, pp. 885-891, Mar 2014, doi: 10.1111/jace.12750.
[23] J. P. Heath, J. S. Dean, J. H. Harding, and D. C. Sinclair, "Simulation of Impedance Spectra for Core-Shell Grain Structures Using FiniteElement Modeling,", *Journal of the American Ceramic Society,* Article vol. 98, no. 6, pp. 1925-1931, Jun 2015, doi: 10.1111/jace.13533.
[24] J. P. Heath, J. H. Harding, D. C. Sinclair, J. S. Dean, The Analysis of Impedance Spectra for Core–Shell Microstructures: Why a Multiformalism Approach is Essential. Advanced Function Materials, Article vol. 29, pp. 1904036- 1904036, 2019. doi: 10.1002/adfm.201904036
[25] J. S. Dean, P. Y. Foeller, I. M. Reaney, and D. C. Sinclair, "A resource efficient design strategy to optimise the temperature coefficient of capacitance of $BaTiO_3$-based ceramics using finite element modelling," *Journal of Materials Chemistry A,* Article vol. 4, no. 18, pp. 6896-6901, 2016. doi: 10.1039/c5ta09573e

[26] J. P. Heath, J. H. Harding, D. C. Sinclair, and J. S. Dean, "Electric field enhancement in ceramic capacitors due to interface amplitude roughness,", *Journal of the European Ceramic Society,* Article vol. 39, no. 4, pp. 1170-1177, Apr 2019, doi: 10.1016/j.jeurceramsoc.2018.10.033.
[27] L. Padurariu, L. Curecheriu, V. Buscaglia and L. Mitoseriu, "Field-dependent permittivity in nanostructured $BaTiO_3$ ceramics:Modeling and experimental verification," *Physical Review B*, Article vol. 85, 224111, 2012, doi: 10.1103/PhysRevB.85.224111.
[28] T. M. Amaral, E. Antonelli, D. A. Ochoa, J. E. Garcia, and A. C. Hernandes, "Microstructural Features and Functional Properties of Bilayered $BaTiO_3/BaTi_{1-x}Zr_xO_3$ Ceramics," *Journal of the American Ceramic Society,* Article vol. 98, no. 4, pp. 1169-1174, Apr 2015, doi: 10.1111/jace.13417.
[29] H. C. Song, J. E. Zhou, D. Maurya, Y. K. Yan, Y. U. Wang, and S. Priya, "Compositionally Graded Multilayer Ceramic Capacitors," *Scientific Reports,* Article vol. 7, p. 12, Sep 2017, Art no. 12353, doi: 10.1038/s41598-017-12402-7.
[30] P. Y. Foeller, J. S. Dean, I. M. Reaney, and D. C. Sinclair, "Design of a bilayer ceramic capacitor with low temperature coefficient of capacitance," *Applied Physics Letters,* Article vol. 109, no. 8, p. 4, Aug 2016, Art no. 082904, doi: 10.1063/1.4961616.
[31] H. Wen, X. H. Wang, and L. T. Li, "Observation on the interdiffusion in multilayer ceramic capacitors," *Japanese Journal of Applied Physics Part 1-Regular Papers Brief Communications & Review Papers,* Article vol. 45, no. 3A, pp. 1768-1770, Mar 2006, doi: 10.1143/jjap.45.1768.
[32] R. Potyrailo, K. Rajan, K. Stoewe, I. Takeuchi, B. Chisholm, and H. Lam, "Combinatorial and High-Throughput Screening of Materials Libraries: Review of State of the Art," *Acs Combinatorial Science,* Review vol. 13, no. 6, pp. 579-633, Nov-Dec 2011, doi: 10.1021/co200007w.
[33] S. Guerin and B. E. Hayden, "ABO_3 and $A_{1-x}C_xB_{1-y}D_y(O_{1-z}E_z)_3$: review of experimental optimisation of thin film perovskites by high-throughput evaporative physical vapour deposition," *Chemical Communications,* Review vol. 55, no. 68, pp. 10047-10055, Sep 2019, doi: 10.1039/c9cc03518d.
[34] P. J. McGinn, "Thin-Film Processing Routes for Combinatorial Materials Investigations-A Review," *Acs Combinatorial Science,* Review vol. 21, no. 7, pp. 501-515, Jul 2019, doi: 10.1021/acscombsci.9b00032.
[35] R. C. Pullar, "Combinatorial Bulk Ceramic Magnetoelectric Composite Libraries of Strontium Hexaferrite and Barium Titanate," *Acs Combinatorial Science,* Article vol. 14, no. 7, pp. 425-433, Jul 2012, doi: 10.1021/co300036m.
[36] K. M. Johnson, "Variation of Dielectric Constant with Voltage in Ferroelectrics and Its Application to Parametric Devices", *Journal of Applied Physics* Article vol. 33, 2826-2831 (1962) doi.org/10.1063/1.1702558

5.11. Supplementary Information.

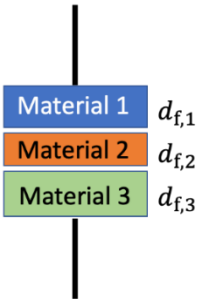

Supplementary Figure 1 Schematic diagram showing the trilayer arrangement of a capacitor with three different materials connected (electrically) in series.

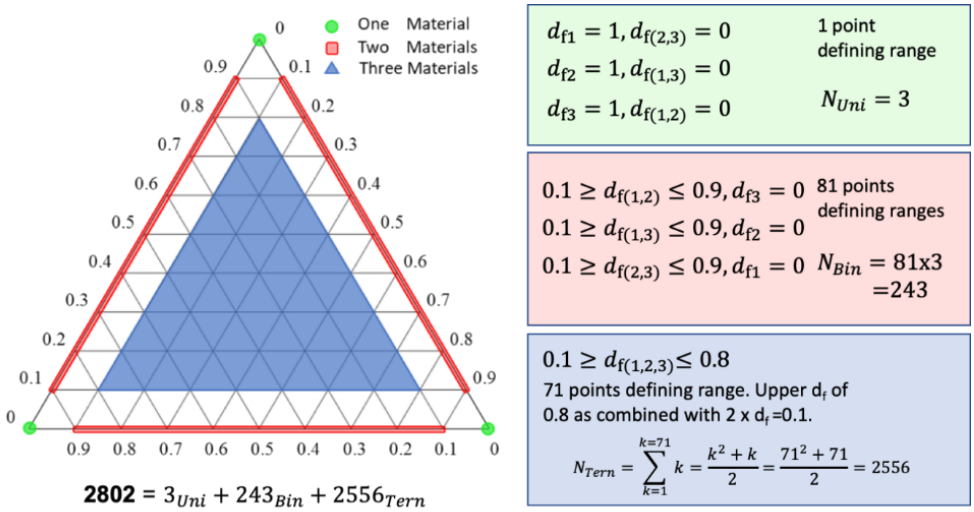

Supplementary Figure 2 Schematic of a ternary map that illustrates how 2802 unique thicknesses are generated and explored for an individual ternary combination of three different materials. Green symbols represent the 3 unary systems, the red symbols represent the 243 data points associated with the three binary systems (81 points per system) and the shaded blue triangle represents the 2556 points within the ternary system. Total explored was 3 + 243 + 2556 = 2802.

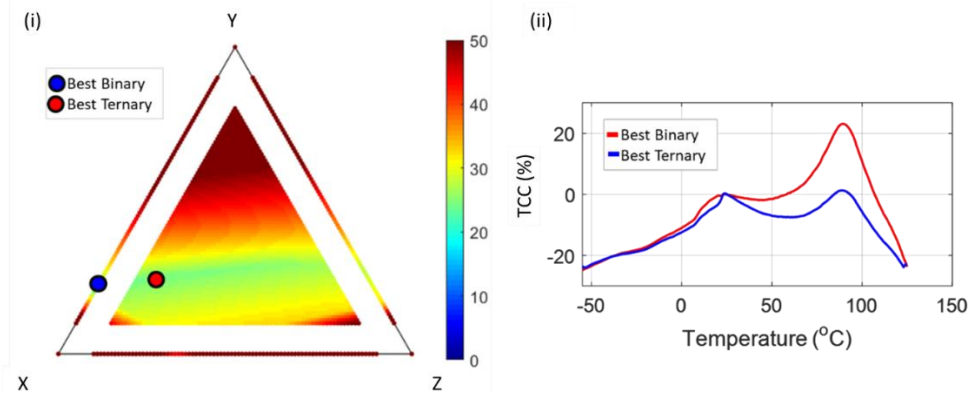

Supplementary Figure 3 (i) Example of a TCC contour map of a ternary system X-Y-Z. TCC_{min} for the best binary and ternary combinations are shown by the blue and red filled symbols in (i). (ii) Corresponding TCC profiles of the best binary and ternary combinations for X7 (-55 to 125 °C) classification. Simulations generated from permittivity data measured at 100 kHz.

6. NNBT bilayers with co-sintering

6.1. Introduction

As discussed in the previous chapter, layered systems of NNBT compositions have potential to stabilise permittivity over a wide temperature range [1, 2]. This is largely due to the wide range of T_{max} values achieved when altering the NN to BT ratio, as shown in Figure 6.1. However, this previous work did not investigate the impact of co-sintering the different NNBT compositions.

In commercial MLCCs, the layers of dielectric material and electrode plates are assembled prior to the sintering step [3, 4]. In composite MLCCs, with different dielectric material layers, this approach means the material layers are sintered at the same temperature [5, 6].

The previous chapter used NNBT input data produced by Foeller [7]. The low T_{max} (low NN) materials were sintered at 1400°C, whilst the high T_{max} (high NN) materials were sintered at 1250°C. If these materials are to be co-sintered, a common sintering temperature needs to be established. To prevent melting, the sintering temperature of a composition needs to be below that of the component with the lowest melting point. The melting point profile of the NNBT system by Raevskii et al. [1] is included in Figure 6.1. The melting issue prevents many materials with NN content above ~20% (>20 NNBT), from being sintered at or above 1250°C.

Kwon et al. reports that 10NNBT can be sintered at 1300°C for 2 hours, however these conditions result in undesirable grain growth in 70NNBT materials [2]. This incompatibility in sintering conditions suggests combining low NN and high NN materials is undesirable, as the sintering temperature is likely to result in a reduction in performance from one or both of the layers. However, low T_{max} materials can also be produced with higher NN content materials (15 to 70 NNBT), as shown in Figure 6.1. This chapter focuses on 70NNBT as the low T_{max}, for several reasons. From Figure 6.1, the T_{max} of 70 NNBT is expected to be around -50°C. As shown in Chapter 5, the L1 material (T_{max} = -55°C) was a useful material in countering the permittivity response of high T_{max} materials. This similarity in T_{max} suggests 70NNBT could replace low NN materials, whilst the lower sintering temperature required should improve the co-sintering compatibility when combined with high T_{max} NN materials.

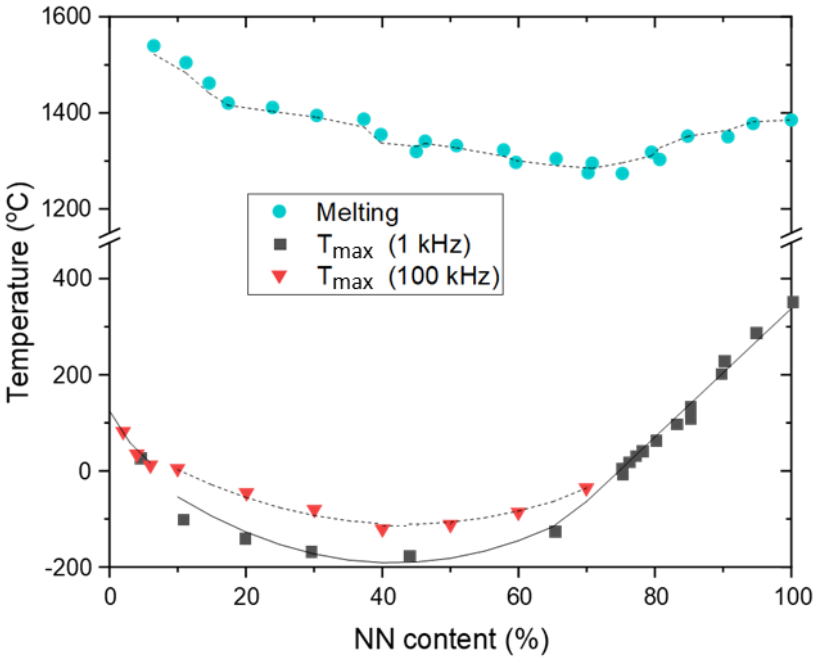

Figure 6.1 The dependence of NN dopant concentration in NNBT on the melting temperature and T_{max}. The melting temperature reported by Raevskii e al. [1], has a moving average trendline to aid the reader. The T_{max} plot contains 1 and 100 kHz data from literature [1, 2, 7] and trendlines for the reader.

A high T_{max} (>150°C) material can only be produced in the NNBT system if a high NN material is used (NN > 80 %). Previously, the high NN materials used were 85NNBT and 90NNBT, with T_{max} = 122 and 209°C, respectively.

This chapter focuses on the optimisation of the X8 temperature range (-55 to 150°C), which is near the limits of what can be achieved with conventional MLCC approaches. Interpolation of T_{max} values reported in the literature for high NN content led to 87.5 NNBT being selected, due to a predicted T_{max} = 170°C. As the T_{max} of ~170°C is above the maximum X8 working temperature (150°C), the Curie-Weiss type decay ($T>T_{max}$) does not need to be stabilised. At 150°C, 87.5NNBT has a rising permittivity response, which has additional benefits over 90NNBT as it can more effectively counter the decaying permittivity of 70NNBT. Although minor, the 87.5NNBT is also slightly closer in composition to 70 NNBT which should further improve sintering compatibility.

In a composite layered MLCC, the presence of dielectric-dielectric interfaces of different composition are likely to allow interdiffusion between the layers. From the many core-shell systems developed, controlled interdiffusion can have substantial benefits in stabilising the permittivity response [8-10]. Between 70NNBT and 87.5NNBT, the NN difference is minimised at 17.5% whilst maximising the T_{max} range from -35 to 170°C. The impact of an interface layer is investigated in this chapter, along with the effectiveness of modelling this interface region as a distinct 3rd layer.

6.2. Experimental Results

6.2.1. Characterisation of 70NNBT and 85NNBT

The XRD patterns of 70NNBT and 87.5NNBT are shown in Figure 6.2 (a). The calcination step (1000°C for 6 hrs) was insufficient in producing phase-pure materials with additional peaks matched to orthorhombic $NaNbO_3$: JCPDF card (33-1270). The $NaNbO_3$ peak intensity is greater in the 87.5NNBT XRD data compared to that of 70NNBT suggesting the 87.5NNBT is less complete in reaction, as shown in Figure 6.2 (b). The sintering process (1250°C for 6 hrs) removes any significant presence of $NaNbO_3$ in both samples. The sintering step also results in a shift in the peak positions to higher angles. This shift is related to a decrease in unit cell parameters, which has been reported previously to be due to an increase in NN content of the NNBT phase.

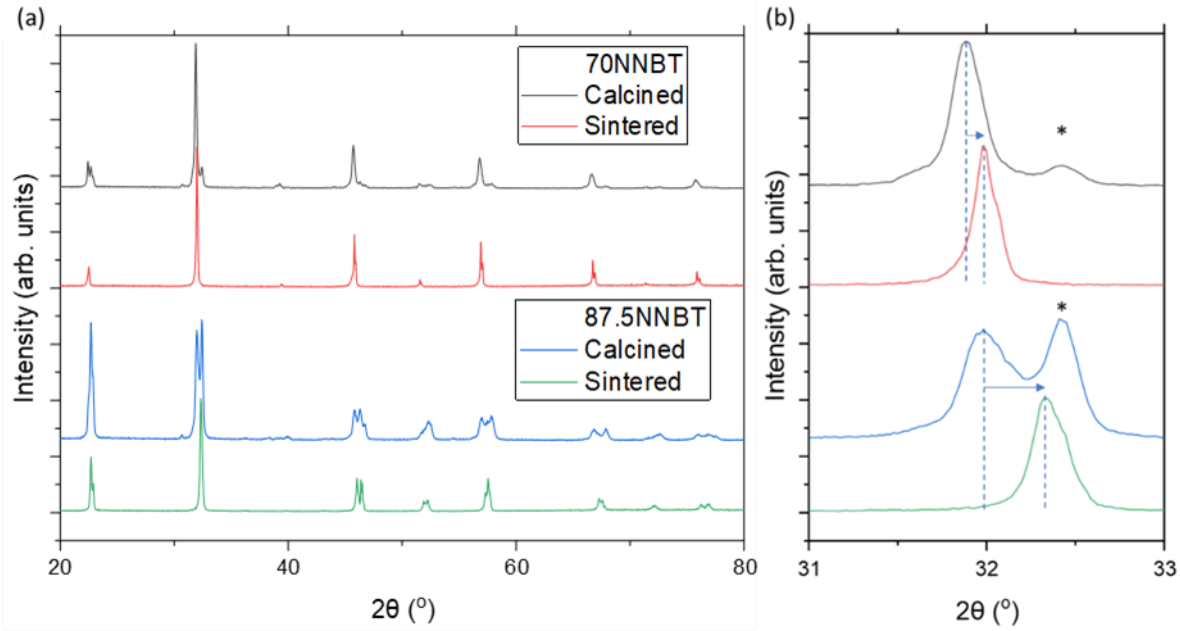

Figure 6.2 XRD patterns of 70NNBT and 87.5NNBT materials as calcined powders and sintered pellets. The synthesis is incomplete after the calcination step, with $NaNbO_3$ present (*). (a) shows the angle range of 2θ of 20 to 80°, whereas (b) focuses on 2θ of 31° to 33°. In (b), the dashed vertical lines indicate the NNBT peaks, with the arrows indicating the shift to high angle post sintering.

The RT lattice parameters and ceramic density of 70NNBT and 87.5NNBT are shown in Table 6.1. 70NNBT is identified as pseudo cubic, whilst 87.5NNBT is matched as orthorhombic (Pbcm space group). However, the similarity of the lattice values *a* and *c* makes the unit cell difficult to distinguish from that of a tetragonal structure. This has been reported previously, and is attributed to the addition of tetragonal BT to orthorhombic NN [11].

The effective cell volume allows a volume comparison of 70NNBT and 87.5NNBT. The unit cell of the pseudo-cubic 70NNBT contains 1 BO_6 octahedron, whilst the orthorhombic unit cell of 87.5NNBT contains 8 BO_6 octahedra. The effective cell volume allows these unit cell volumes to be compared, by comparing volume per BO_6 octahedron. The effective cell volume decreases with increased NN content, agreeing with previous reports [1].

Table 6.1 Summary of physical characteristics and lattice parameters of NNBT materials sintered at 1250 °C.

NN content	Theo. Density (g cm^{-1})	Rel. Density (%)	Crystal Structure	a (Å)	b (Å)	c (Å)	Effective Cell Volume ($Å^3$)
70	4.90	94.9 (5)	Pseudo-cubic	3.953 (4)	-	-	61.8 (1)
87.5	4.65	97.0 (4)	Orthorhombic	5.532 (5)	15.524(3)	5.543 (5)	59.5 (1)

The sintering profile produced dense pellets (ρ_{theo}>90%), with the permittivity profiles of 70NNBT and 87.5NNBT pellets (prepared with Au electrodes) are shown in Figure 6.3 (a) and (c), respectively. The corresponding tan δ profiles are shown in Figure 6.3 (b) and (d), respectively. Profiles measured at 1 and 100 kHz are included to highlight any frequency dependency.

The 70NNBT composition undergoes a broad permittivity response with a maximum around -50°C, with a declining permittivity profile above the maximum that supports the cubic structure observed from the XRD data, Figure 6.2. The permittivity peak is broad and frequency dependent, suggesting a relaxor type response. T_{max} is -56 and -46°C for 1 and 100 kHz, respectively. This frequency dependency is also observed in the tan δ response, Figure 6.3 (b), with the 100 kHz profile having a larger magnitude response at temperatures approaching the phase transition. Although the tan δ response has high losses, the peak occurs at temperatures <-55°C, and therefore below the operational temperatures of many MLCCs. tan δ <0.02 is achieved for -55 to 240°C, when measured at 1 kHz.

The permittivity response of 87.5NNBT, Figure 6.3 (c) is different to 70NNBT, instead displaying more classical ferroelectric behaviour. The sharp peak has ε_{max} ~ 10,900 at T_{max} = 173°C. The tan δ response of 87.5NNBT, Figure 6.3 (d), is relatively constant at ~ 0.02, until a sharp decline at the phase transition temperature. Above 200°C, both compositions have increased dielectric losses at 1 kHz, with tan δ > 0.02 above 250°C for both compositions.

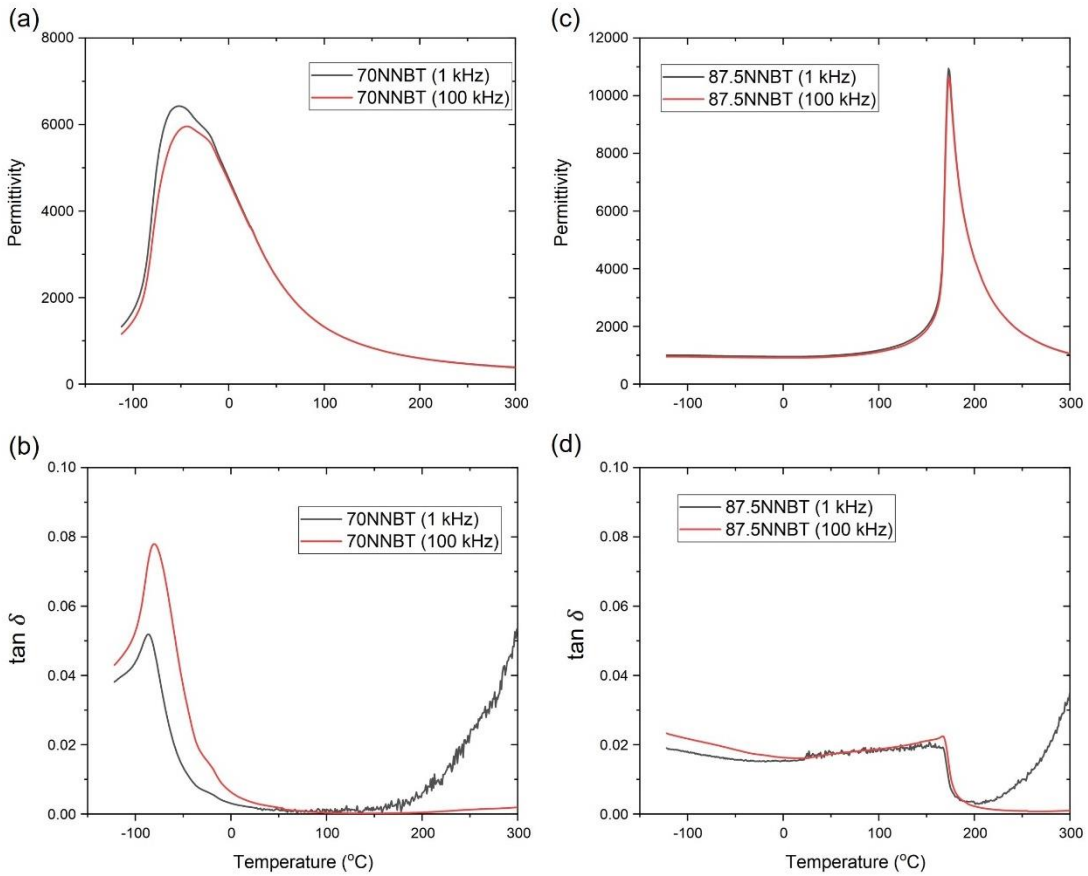

Figure 6.3 Permittivity and tan δ profiles of 70NNBT and 87.5NNBT at 1 and 100 kHz. 70NNBT in (a) and (b), respectively and 87.5NNBT in (c) and (d), respectively. Both samples were sintered at 1250°C for 6 hours.

6.3. Simulation : Bilayer 70NNBT : 87.5NNBT

The permittivity profiles of 70NNBT and 87.5NNBT (100 kHz) were used as inputs for the simulation optimisation code. The experimental data were first spline-fitted at 1°C steps, then simulated as layers in series, with full variation in the relative layer thicknesses, d_f = 0:0.01:1. The effect that relative layer thickness has on the permittivity response of the binary layer system is shown in Figure 6.4. At d_f = 0.0 and 1.0, the binary system simplifies to a single layer of 70NNBT and 87.5NNBT, respectively. Increasing the 87.5 NNBT layer thickness suppresses the low temperature peak of 70NNBT, whilst introducing the high temperature peak of 87.5NNBT. Due to the 70NNBT and 87.5NNBT permittivity profiles intersecting at 111°C, all binary combinations in series also share this intersection point with ε_{111} = 1179. The intersection point of the TCC(%) profiles is at 25°C, due to this being the temperature to which all permittivity profiles are normalised.

As shown in Figure 6.4 (b), the permittivity peak of 87.5NNBT results in a significant increase in TCC(%) above 150°C, which the slowly declining permittivity profile of 70NNBT struggles to counter. However, this temperature range is not included in the X8 temperature range (-55 to 150°C), and thus does not affect the optimisation results.

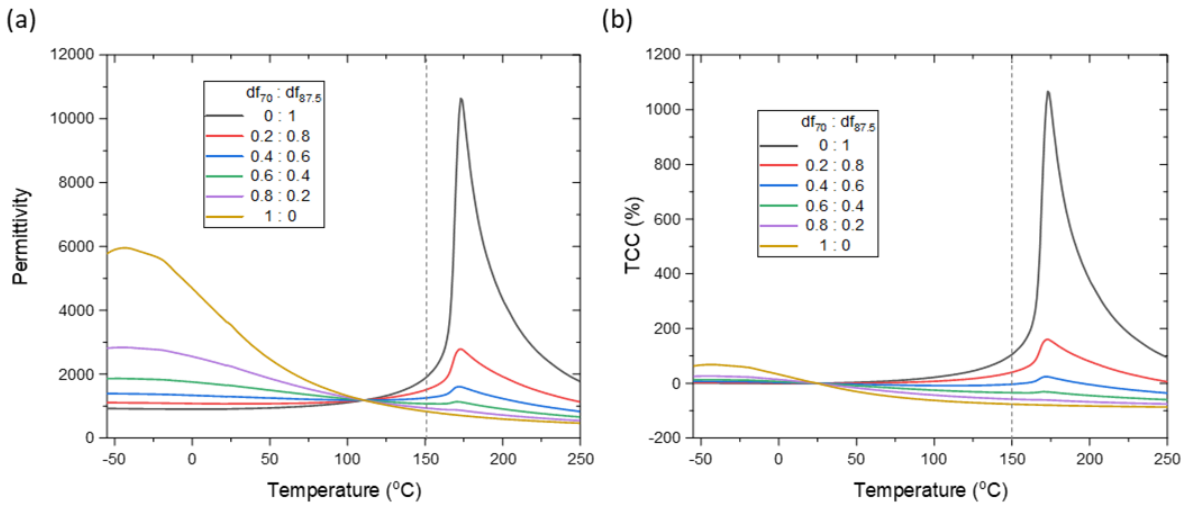

Figure 6.4 Permittivity-temperature (a) and TCC%-temperature profile (b) simulations of the 70NNBT and 87.5NNBT bilayer, for different relative thickness fraction ratios, where the ratio is defined as 70NNBT : 87.5NNBT. Input data of 70NNBT and 87.5NNBT were both measured at 100 kHz. The upper temperature of the X8 classification (150°C) is marked with the dashed line.

The TCC_{abs} relationship with the thickness fraction of the binary layer system is shown in Figure 6.5 (a). Starting with a single layer of 70NNBT, the addition of 87.5NNBT improves the TCC_{abs} performance by suppressing the low temperature permittivity peak of 70NNBT. The system optimises at $df_{87.5} = 0.63$, with $TCC_{abs} = 6\%$. Further increases in the 87.5NNBT layer thickness results in a deteriorating TCC_{abs} due to the development of a permittivity peak at high temperatures.

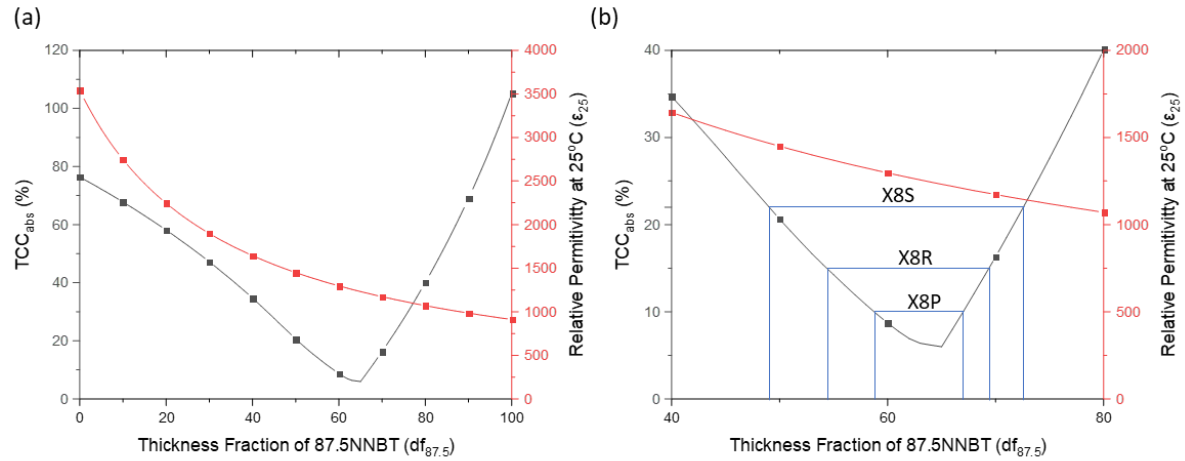

Figure 6.5 The dependence on the TCC_{abs} and ε_{25} simulated for the range of possible thickness fractions for 87.5NNBT:70NNBT bilayers. TCCabs calculated for the X8 temperature range (-55 to 150°C). (a) showing the full range of thickness fractions, whereas (b) focuses on the classifications achieved at the optimised thickness fractions.

ε_{RT} is also plotted in Figure 6.5 (a), showing a trade off in permittivity performance with the increased layer thickness of 87.5NNBT. The optimised layer fractions are shown in Figure 6.5 (b), with the fraction ranges that achieve several standard EIA classifications (X8S, R and P), and are

summarised in Table 6.2. X8S allows the largest deviation in TCC(%) profile (+22%), and therefore has the largest $df_{87.5}$ range to meet X8S. X8P is the strictest classification (+10%), and thus the smallest tolerance for layer thickness fractions. The ε_{RT} performance is greatest with the thinnest $df_{87.5}$ layer fraction possible. The minimum $df_{87.5}$ increases from 0.5 to 0.59 (X8S to X8P), and thus ε_{RT} decreases from ~ 1450 to 1310.

Table 6.2 Summary of the different TCC classifications predicted to be achievable for 70NNBT : 87.5NNBT bilayers in series with the range of $df_{87.5}$ expected to meet the classification and the resulting ε_{RT} range.

Class	TCC_{abs} (%)	$df_{87.5}$ fraction range	df range	ε_{RT} range
X8S	<22	0.50 - 0.72	0.22	1450 - 1151
X8R	<15	0.55 – 0.69	0.14	1369 - 1184
X8P	<10	0.59 – 0.66	0.07	1310 - 1219

6.4. Experimental : Bilayer 70NNBT:87.5NNBT

In chapter 5, the experimental measurements of binary or ternary layered systems were performed on stacks of ceramic pellets that had been individually sintered.

To investigate the effects of co-sintering ceramic layers of different compositions, ceramic composite pellets of 70NNBT and 87.5NNBT layers were produced. The 'green' bilayer pellet was produced following nearly the same procedure as described in the experimental methodology. However, after the first light press of the first powder in a uniaxial press, the second powder was loaded and a light press repeated. Out of the die, the bilayer pellet is treated the same as a monolithic pellet, with the green body density increased via Cold Isostatic Pressing. Finally, the pellets were sintered at 1250°C for 6 hours, at a ramp rate of 5°C min^{-1}, matching the conditions used to produce the individual pellets of 70NNBT and 87.5NNBT.

The bilayer pellets were sufficiently dense post sintering with ρ_{theo} = 93% and no delamination issues. The bilayer pellets were Au electroded for electrical measurements in an identical manner to individual pellets.

Using a light microscope, the thickness fraction of each material layer could be observed, Figure 6.6, as the two layers had slightly different hues. This assessment step was non-destructive, as the side of the bilayer pellet could be used. The 70NNBT layer was ~ 25% of the pellets thickness, therefore df_{70}=0.25 and $df_{87.5}$ = 0.75.

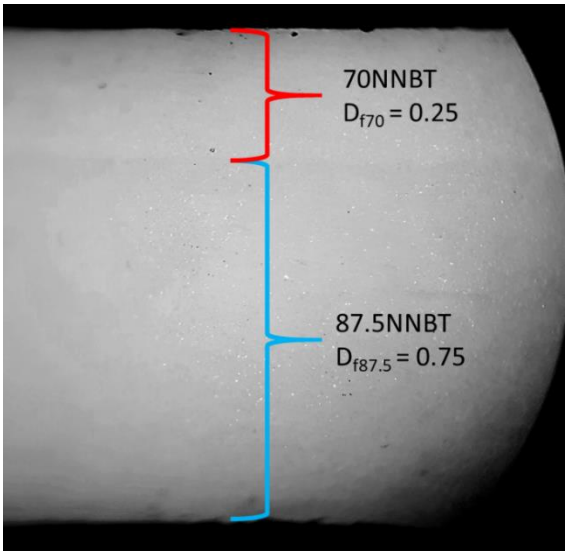

Figure 6.6 Side-on profile of the co-sintered bilayer of 70NNBT and 87.5NNBT, imaged with an optical microscope. Processing the image allowed the relative thickness values of the two materials to be estimated.

The permittivity and tan δ profiles of the binary co-sintered pellet are shown in Figure 6.7 (a) and (b), respectively. The permittivity profile has a significant peak associated with the thicker 87.5NNBT layer, with a minor peak at low temperatures from the 70NNBT layer. The permittivity profile has some frequency dependency at low temperatures due to the relaxor behaviour of 70NNBT. The tan δ profile is similar to that of 87.5NNBT, Figure 6.3 (d), however with a low temperature response due to the relaxor-type behaviour of the 70NNBT component.

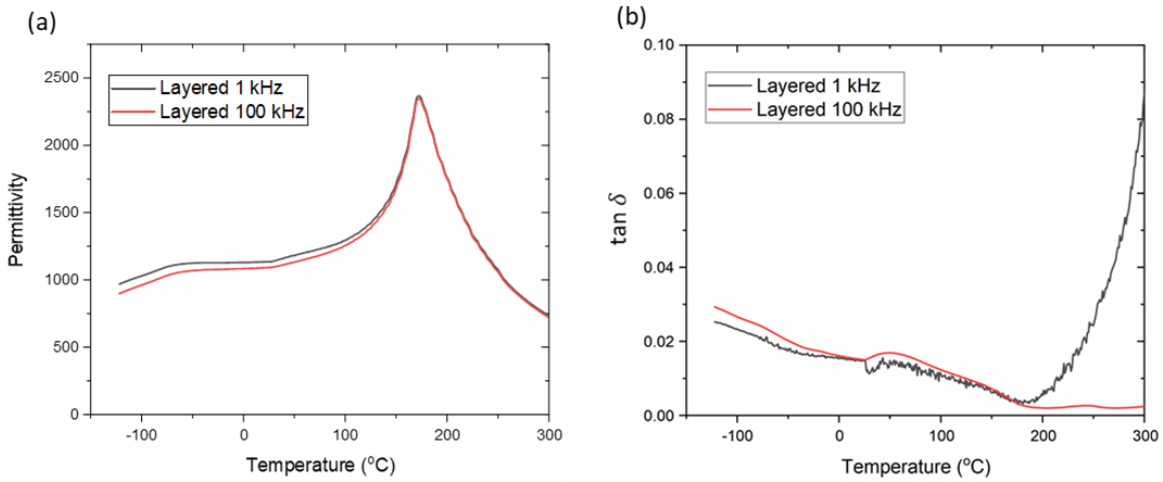

Figure 6.7 Experimental data for the co-sintered bilayer sample showing (a) permittivity, (b) tan δ at both 1 and 100 kHz.

The permittivity profile of the binary pellet was compared to the simulated response of the binary system for $df_{87.5}$= 0.75, Figure 6.8 The permittivity (a) and TCC profile (b) of the co-sintered bilayer ceramic pellet, compared to the simulated profile when df87.5= 0.75 and df70= 0.25. Simulation produced using 70NNBT and 87.5NNBT when measured at 100 kHz.. The magnitude of the measured

permittivity is very similar to the simulated profile with the values of ε_{RT} and ε_{max} being within the error bounds. There is no shift in T_{max} between experimental and simulation data, with the Curie-Weiss type decay of the permittivity (at $T>T_{max}$) being nearly identical. These similarities can also be observed in the TCC(%) profiles, Figure 6.8 The permittivity (a) and TCC profile (b) of the co-sintered bilayer ceramic pellet, compared to the simulated profile when df87.5= 0.75 and df70= 0.25. Simulation produced using 70NNBT and 87.5NNBT when measured at 100 kHz. (b).

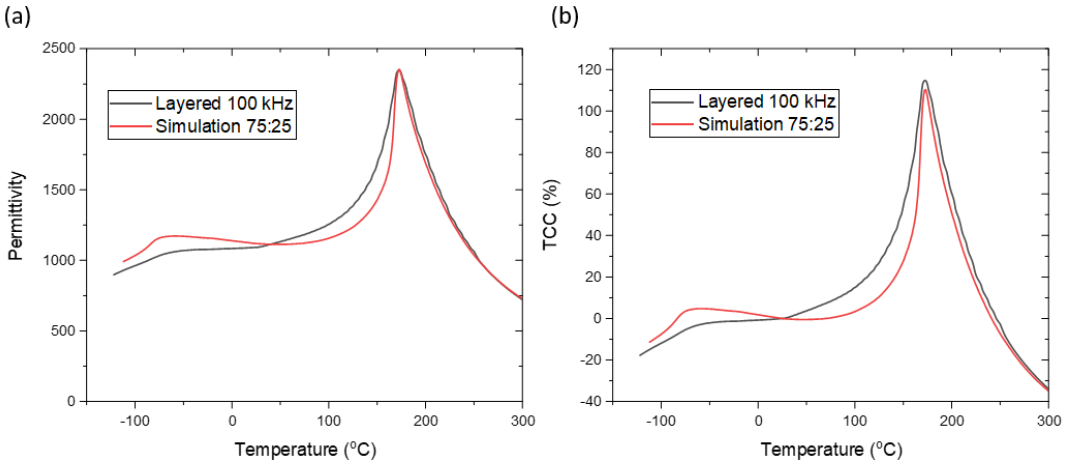

Figure 6.8 The permittivity (a) and TCC profile (b) of the co-sintered bilayer ceramic pellet, compared to the simulated profile when $df_{87.5}$= 0.75 and df_{70}= 0.25. Simulation produced using 70NNBT and 87.5NNBT when measured at 100 kHz.

As temperature approaches T_{max}, the simulation profile predicts a sharp rise in permittivity due to the classical ferroelectric behaviour of the 87.5NNBT component. The permittivity profile of the bilayer pellet is broader with the permittivity increasing at a lower temperature than simulated.

The low temperature response is also modified with the minor peak response of the 70NNBT component being more significant in the simulation than is observed in the co-sintered sample. Without the low temperature peak, the permittivity response is less temperature-stable at sub ambient temperatures than predicted, as observed by the poorer TCC(%) deviation in Figure 6.8 The permittivity (a) and TCC profile (b) of the co-sintered bilayer ceramic pellet, compared to the simulated profile when df87.5= 0.75 and df70= 0.25. Simulation produced using 70NNBT and 87.5NNBT when measured at 100 kHz. (b).

These minor differences in the permittivity profile are attributed to the co-sintered nature of the layers in the binary pellet. The simulation does not consider the effects of any interdiffusion between the two layers, or other interface effects, e.g. roughness or porosity.

6.5. Experimental Mixed comparison

In a layered structure, the direct contact of 70NNBT and 87.5NNBT is restricted to occur only at the interface, and therefore limits the potential interdiffusion. To maximise potential interdiffusion, pellets were produced containing a random mix of the two calcined powders.

The powders were batched at a 60:40 ratio of the 87.5NNBT and 70NNBT components, which as a binary layer in series achieves the X8P classification. The mix resulted in having an equivalent composition of 80.5NNBT. The resulting powder was mixed with a pestle and mortar. This resulted in a single batch of calcined powder, and thus pellets could be pressed as described in the experimental methodology. The mixed pellets were sintered at 1250°C for 6 hours at 5°C min^{-1}, matching the conditions used for all pellets produced in this chapter.

The XRD pattern of the mixed powder pellets is compared to those of 70NNBT and 87.5NNBT, Figure 6.9, with the peaks occurring at an angle between these two end members. Some peak splitting is observed, implying the material is not cubic at room temperature like 70NNBT.

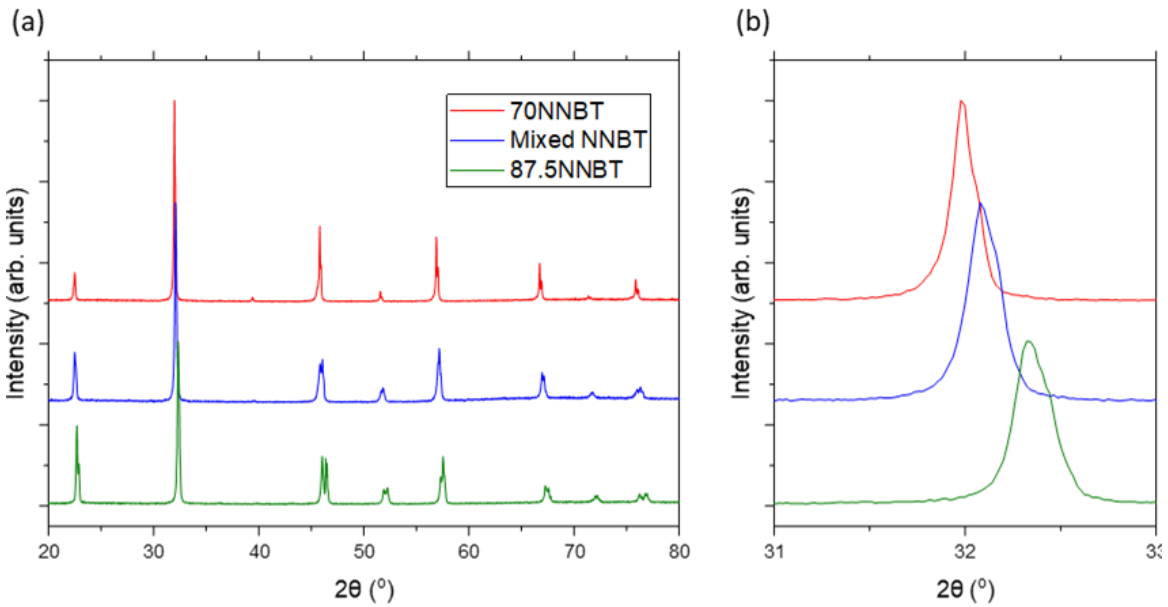

Figure 6.9 XRD pattern of the mixed powder NNBT ceramics, with comparison to 70NNBT and 87.5NNBT, (2θ = 20° – 80°). All were sintered at 1250°C for 6 hours. The mixed sample was produced by mixing the 70NNBT and 87.5NNBT calcined powders, at a vol% 40:60 ratio respectively, using a pestle and mortar.

The lattice parameters of mixed NNBT are compared to its components in Table 6.3. Mixed NNBT has an orthorhombic structure, like 87.5NNBT, with an effective cell volume that is between its starting components. The effective cell volume follows the trend of a decreasing volume with increased NN content.

Table 6.3 Lattice parameters obtained from XRD.

NN content	Crystal Structure	a (Å)	b (Å)	c (Å)	Effective Cell Volume (Å^3)
70	Pseudo-cubic	3.953 (4)	-	-	61.8 (1)
Mixed (80.5)	Orthorhombic	5.576 (7)	15.772 (3)	5.525 (7)	60.7 (2)
87.5	Orthorhombic	5.532(5)	15.524(3)	5.543(5)	59.5(1)

The effect of interdiffusion on the dielectric properties of the mixed pellet is shown in Figure 6.10. In (a), the permittivity profile of mixed NNBT has a single broad peak, with T_{max} = 78ºC. The lack of frequency dependency in the T_{max} suggests the broadness of the peak may be associated with a compositional gradient, rather than the relaxor type behaviour observed for 70NNBT. The tan δ response Figure 6.10 (b) matches that expected for ferroelectric behaviour, however with some additional broadness at temperatures approaching T_{max}.

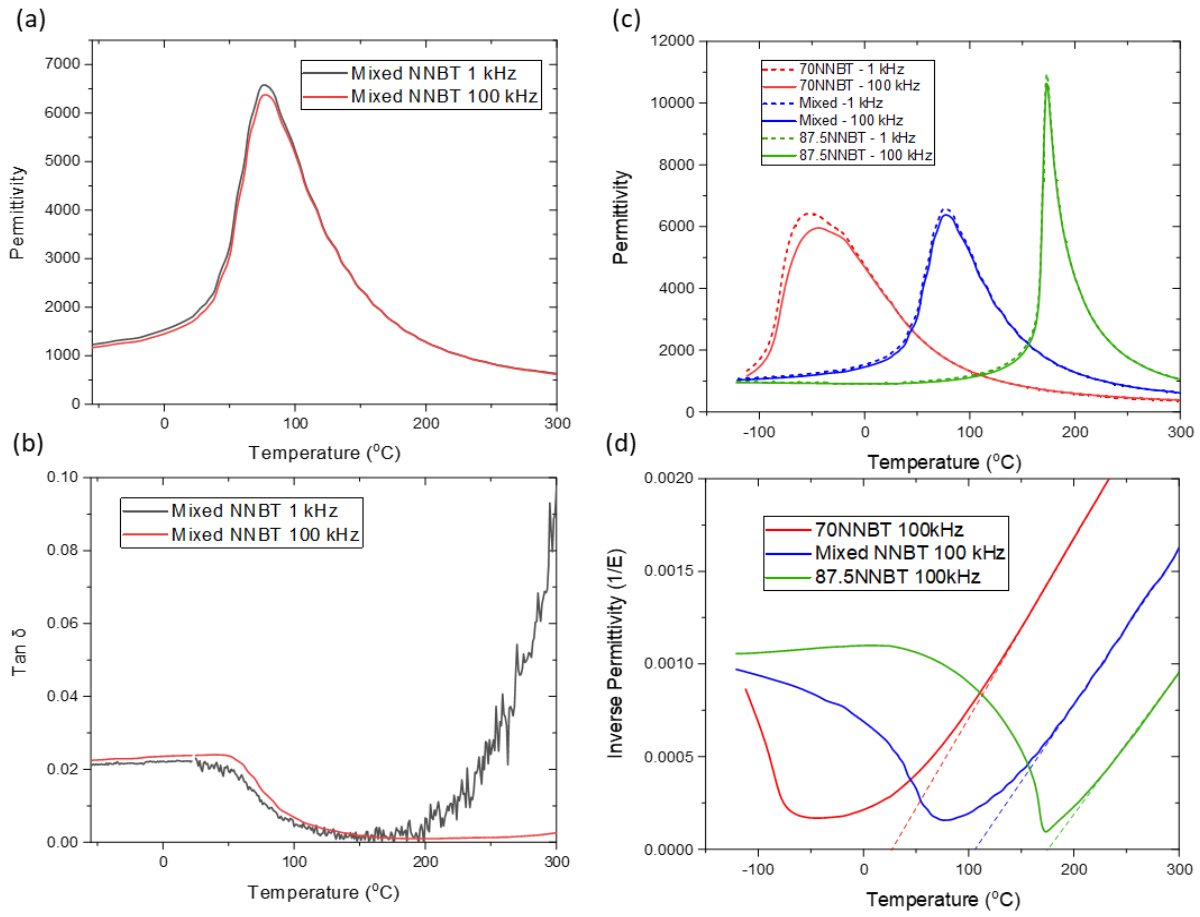

Figure 6.10 The permittivity-temperature (a) and tan δ-temperature (b) profiles of the NNBT sample produced from sintering a mixture of 70NNBT and 87.5NNBT calcined powders. A comparison of the mixed permittivity with its components is shown in (c). (d) is the inverse permittivity-temperature plot (100 kHz), with the temperature region obeying the Curie-Weiss law extrapolated as a dashed line.

The permittivity and inverse permittivity profiles of mixed NNBT and its component materials are compared in Figure 6.10 (c) and (d), respectively. The T_{max} of the mixed NNBT is between 70NNBT and 87.5NNBT, suggesting a resulting NNBT composition between these compositions. The broadened peak and permittivity magnitude is similar to the relaxor behaviour of 70NNBT, however the mixed NNBT does not exhibit the same frequency dependency expected for a relaxor material. The inverse permittivity plot (d) shows the Curie-Weiss law (extrapolated dashed lines) for 87.5NNBT intersects with the x axis near to T_{max}, indicating a classical ferroelectric response (2^{nd} Order). The mixed NNBT does not obey the CW law at T_{max}, however the difference between CW and T_{max} is smaller than observed for 70NNBT.

Similar permittivity profile characteristics for 80 NNBT (broad permittivity peak with negligible frequency dependency) has been reported previously for 80 NNBT [11]. This suggests the mixed NNBT is of nearly homogeneous composition, rather than containing a compositional gradient (such as in core and shell grains or functionally graded through the ceramic).

In Figure 6.11, the T_{max} values obtained in this work (▲ connected with a dashed line), are compared to those reported in the literature. Presuming mixed NNBT is homogeneous (i.e 80.5 NNBT), the T_{max} = 78°C is in close agreement with the linear trend observed by multiple authors [1, 7, 11, 12].

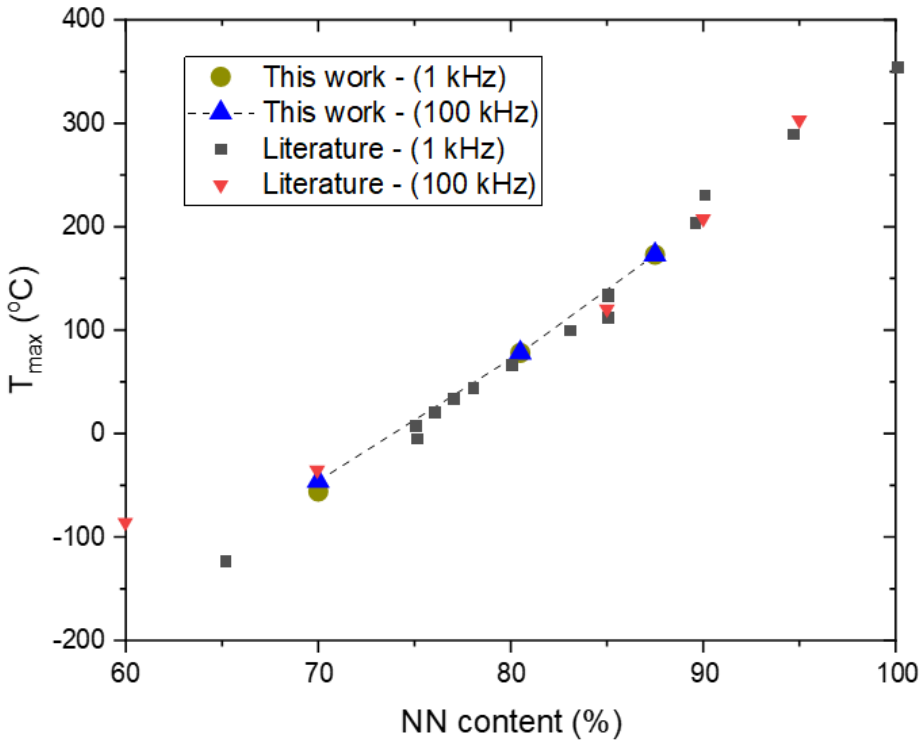

Figure 6.11 Plot of the T_{max} relationship for NNBT with high NN content (>60%), (1 kHz and 100 kHz). Data from the literature is included for comparison, [1, 7, 11, 12]. The T_{max} of mixed NNBT is plotted at the NN content equivalent (80.5 NNBT). Data from this work is connected with a dashed line to aid the reader to the near linear relationship with NN content.

6.6. Simulations to account for interface diffusion

Based upon the significant homogeneity that occurred in the mixed NNBT ceramics, there is potential for similar interdiffusion to occur when co-sintering the two NNBT compositions as a layered structure.

The permittivity response of mixed NNBT, with a T_{max} = 78°C, suggests that interdiffusion may explain why the co-sintered bilayer has a higher permittivity response for T = 75 to 125°C, than is predicted by the simulation results, Figure 6.8 The permittivity (a) and TCC profile (b) of the co-sintered bilayer ceramic pellet, compared to the simulated profile when df87.5= 0.75 and df70= 0.25. Simulation produced using 70NNBT and 87.5NNBT when measured at 100 kHz..

To account for the potential interdiffusion at the interface, an interface region is incorporated into the simulation, in the form of a 3rd distinct material layer. The permittivity profile of the mixed NNBT pellet was used as input data for this 3rd layer. The interface layer was set at 10% of the total height, or df_{int}=0.1. The interface layer is presumed to result in an equal reduction in the relative thickness of the 70NNBT and 87.5NNBT layers, as shown in Figure 6.12 (a).

The TCC(%) profile of the ceramic bilayer is compared to simulations with and without the interface layer considered in Figure 6.12 (b). Across the temperature range measured (-110 to 300°C), the fit of the simulation improved when the interface layer was included.

The low temperature response in the bilayer simulations, caused by the phase transition of the 70NNBT layer, is better suppressed when the interface layer is included. This is partially due to a reduction in the relative thickness of the 70NNBT layer but also the lower permittivity of the interface layer.

Above RT, the interface region (T_{max} = 78°C) causes the TCC(%) rate to increase at a similar rate with the experimental data. Although a better fit, there remains noticeable deviation from 100 to 150°C, implying the experimental bilayer contains compositions with T_c higher than those achieved from the mixed NNBT data.

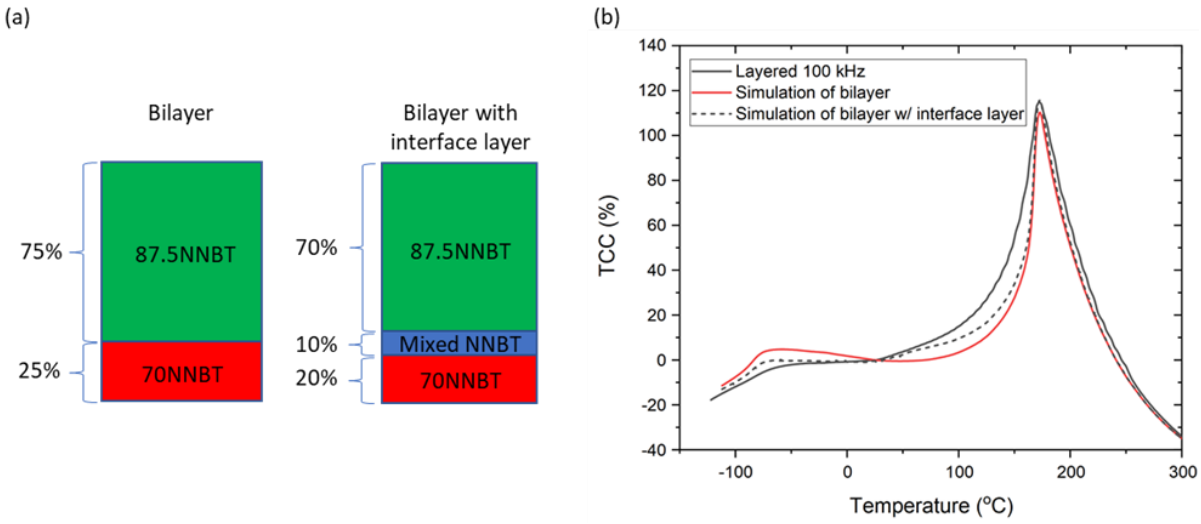

Figure 6.12 Comparison of the simulation when an interface layer is considered. (a) Schematic showing how the interface layer alters the relative thickness of the two starting layers. (b) Comparison of the TCC-temperature results of the simulations to the experimentally measured (co-sintered) bilayer pellet. Simulation produced using 70NNBT, 87.5NNBT and Mixed NNBT data, collected individually (all at 100 kHz).

The total thickness of the sintered bilayer pellet is 1.34 mm and thus $df_{int} = 0.1$ is equivalent to a thickness of 0.134 mm (134 microns). Other authors have reported interface thicknesses of ~30 microns in co-sintering BT based systems [13, 14], quantified via EDX techniques. However, these reports use a shorter sintering time of 2 hours, compared to 6 hours in this work. Considering the much longer sintering dwell, the simulated interface layer is of a realistic thickness.

With a dielectric thickness of 4-10 microns for most commercial MLCCs [3], any level of interdiffusion between co-sintered layers is likely to have a significant effect on the permittivity profile. At this scale the system is likely to behave as a single layer, rather than of two layers in series [5]. Therefore, direct ceramic-ceramic co-sintering is unlikely to be accurately simulated by the techniques used in this thesis, when applied to layers of micron thicknesses.

The simulations therefore require interdiffusion to be prevented between the dielectric layers in a composite MLCC. The use of internal electrodes have been reported to prevent interdiffusion [6]; however, the development of holes in these electrodes can still allow significant interdiffusion [5, 15] .

6.7. Conclusions

This chapter investigated the electrical properties of co-sintered NNBT materials for potential composite MLCC applications. The requirement for compatible materials during the sintering procedure resulted in 70NNBT and 87.5NNBT being selected for low and high T_{max} materials. The use of only high NN materials also meant a relatively low sintering temperature of 1250°C was possible, without the need for sintering aids.

The 70NNBT and 87.5NNBT materials were characterised to have T_{max} = -50 and 173°C, respectively with acceptable tan δ losses. These experimental profiles were used as inputs, with the simulations predicting an X8P classification could be achieved with $\varepsilon_{RT} \approx 1250$. This result exceeds those achieved by BT-based systems currently used commercially.

To investigate the effects of co-sintering, bilayer bulk ceramic pellets were pressed and sintered. With the relative thickness of the two layers obtained using a light microscope, the experimental results were compared to those of the simulations. A simple binary layer simulation modelled significant portions of the bilayer permittivity profile with only minor discrepancies.

When the two component materials were intimately mixed and sintered as a single pellet, significant homogenisation was observed. To account for potential interdiffusion occurring when a layered geometry is co-sintered, a thin interface layer (10% of total thickness with the properties of the mixed pellet) was added to the simulation. This additional 3rd layer resulted in the simulated permittivity profile having a much closer fit to the experimental data. However, with an equivalent real thickness of 134 microns, this interface layer is significantly larger than the current layer thicknesses used in commercial MLCC devices (4 – 10 microns). This demonstrates the need to prevent interdiffusion for the simulation to remain accurate at the micron length scale.

The use of published literature on the NN:BT relationship with T_{max} allowed lab time to be minimised, with only two compositions being produced and characterised. The interface region investigations were performed using calcined powders of these two compositions. Although this approach was particularly useful due to COVID-19, it also has potential to reduce the amount of iterative research that is currently required to develop new materials and formulations for future MLCCs.

6.8. Future Work

Future work should expand the NNBT compositions considered for binary and ternary layer simulations. To maintain sintering compatibility, NNBT compositions in the range x = 0.4 to 0.8 should be further characterised. Materials such as 40NNBT and 50NNBT are expected to have very low T_{max} values which may allow working temperatures below the -55°C currently used commercially.

In the current work, the component materials were selected and optimised without consideration of the creation of an interface region when co-sintering. This approach views the interface region as an uncertainty, and therefore a potential issue. However, interdiffusion is harnessed in core-shell materials, broadening permittivity-temperature profiles and stabilising the temperature coefficient of capacitance. Future work should investigate to actively predict the types of interface profiles that would form when co-sintering and use this as a 3rd layer to better assess the performance of

combining two materials. This approach is likely to lead to material combinations that have their performance improved when co-sintering occurs, than if interdiffusion was prevented.

Due to COVID-19 restrictions, scanning electron microscopy (SEM) techniques were not available to image the various ceramics. Future work should investigate the use of electron microscopy to assess the interface regions of co-sintered bilayer pellets. Energy-dispersive X-ray spectroscopy (EDX) across the layer interface has been previously successful in assessing the thickness of the interface region by measuring the change in content of the different cations [14]. This information would allow the interface region to be further sub-divided to better model the changes in NN:BT across the interface. Future work should therefore model the interface as several distinct layers, rather than a single layer as used in this work.

In this study, the sintering conditions (1250^{o}C for 6 hours), chosen to ensure densification that avoided open porosity. However, these hold times are significantly longer than those used commercially and therefore likely to encourage additional interdiffusion. Future work should therefore decrease the sintering time whilst maintaining adequately dense bilayer ceramics. A decrease in the sintering temperature with the use of sintering aids should also be investigated. Quantifying the change in interdiffusion with EDX should allow better assessment of the changes in the permittivity-temperature profiles.

Finally, future work should combine different material systems, for example perovskite and TTB dielectric materials, to investigate the impact of a combining materials with substantially different crystal structures and lattice parameters. At the interface this will lead to large mis-alignment between the crystal plane of the materials. This disorder at the interface may hinder the cation motion between materials, especially as the cation transfers from one lattice to the other. This may restrict the diffusion of cations between materials, which was observed when co-sintering NNBT materials together. The simulations developed in this thesis could then be used to screen the (potentially) many thousands of different combinations with the aim of improving the efficiency of developing new material combinations.

6.9. Appendix

As mentioned in section 6.8, Covid restrictions prevented electron microscopy being performed by the author of this thesis. SEM based techniques had therefore to be proposed as future work. Since writing this chapter, SEM analysis on the bilayer ceramic pellets has been performed by a fellow PhD student, James Killeen. His work included the preparation of samples for SEM and the collection of data (Backscatter (BS) images and Energy dispersive X-ray Spectroscopy (EDX) maps of the various elements). George Kerridge would like to acknowledge and thank James Killeen for the collection of this data.

A backscatter image of the interface region (250 x magnification) is shown in Figure 6.13. The left side of the image is the 70NNBT layer whereas the right side is 87.5NNBT. The small black dots in the image show porosity with 70NNBT having many fine pores compared to fewer but larger pores in the 87.5NNBT layer. Compared to the bulk porosity of the 70NNBT, the ~ 210 to 260 µm region has increased porosity. Beyond 260 µm, the level of porosity decreases dramatically with the 260 µm to 325 µm region having less porosity than either NNBT layers. Beyond 325 µm, the porosity of the 87.5NNBT remains relatively consistent.

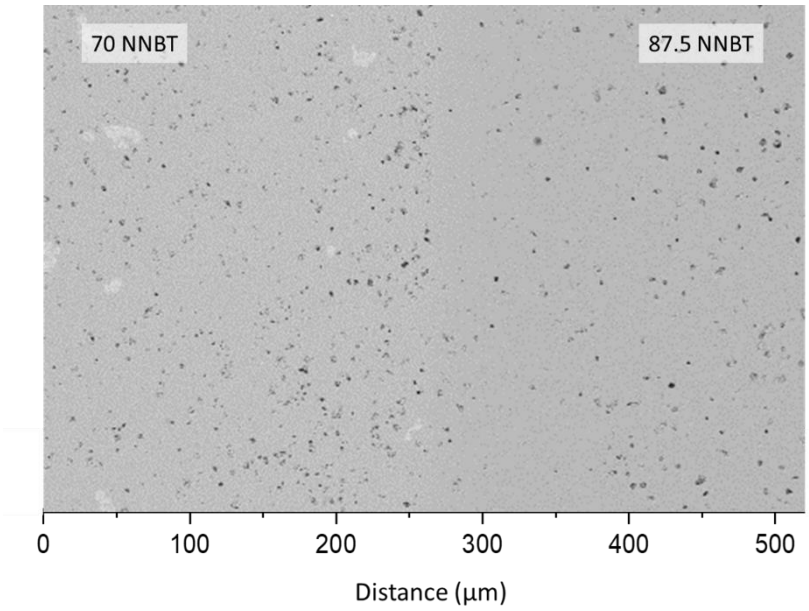

Figure 6.13 Back scatter image of the NNBT bilayer pellet with the interface of the two layers being at the centre of the image. The left side is 70NNBT and 87.5 NNBT is on the right (as labelled). Small black dots identify porosity in the ceramics.

The changes in porosity observed in Figure 6.13 are compared to changes of elemental composition in Figure 6.14. The interface region contains two sub-regions either side of the interface (250 um on x axis in Figure 6.13), the relatively high porosity region of 70NNBT and the relatively low porosity region of the 87.5NNBT layer. To the left of the interface region the elemental composition of the 70NNBT layer is relatively consistent; however, the small bright regions in the BS image suggest the presence of a secondary phase. The relative amounts of Na and Nb measured with EDX are lower in the 70NNBT than the 87.5NNBT regions, which is expected (x = 0.7 compared to x = 0.875). This increase in $NaNbO_3$ results in a reduction of $BaTiO_3$ which is also seen in the EDX data.

The transition from 70NNBT to 87.5NNBT results in a change in the elemental composition in the ~210 to 320 µm region, matching the interface region showing significant changes in porosity. It is not known whether the porosity changes are caused by a bias in mass transportation of elements between 70NNBT to 87.5NNBT or whether the porosity changes were induced by the method to produce the bilayer pellets in 'green' form. Away from the interface region, the elemental analyses

of both layers are relatively consistent, indicating these regions represent the bulk composition of both layers.

The increase in $NaNbO_3$ content from 70NNBT to 87.5NNBT leads to the Na and Nb concentration being highest in the bulk of 87.5NNBT. Similarly, the Ba and Ti content is highest in the bulk of the 70NNBT leading to a lower concentration of these elements in the bulk of 87.5 NNBT. Approaching the interface, the EDX data show a change in composition, with the transition from 70NNBT to 87.5NNBT completed in ~110 µm.

This measured value of ~110 µm for the interface region is close to the 137 µm predicted in section 6.6, which was made prior to this SEM work being conducted. This prediction was based upon the interface thickness that best accounted for the discrepancies between the simulated permittivity-temperature profiles and the experimentally measured data from the bilayer pellets. Although the SEM data reveal an apparent gradient in composition in the interface region (needs further investigation) the findings of section 6.6 indicate that it can be adequately modelled as a single material of average (intermediate) composition.

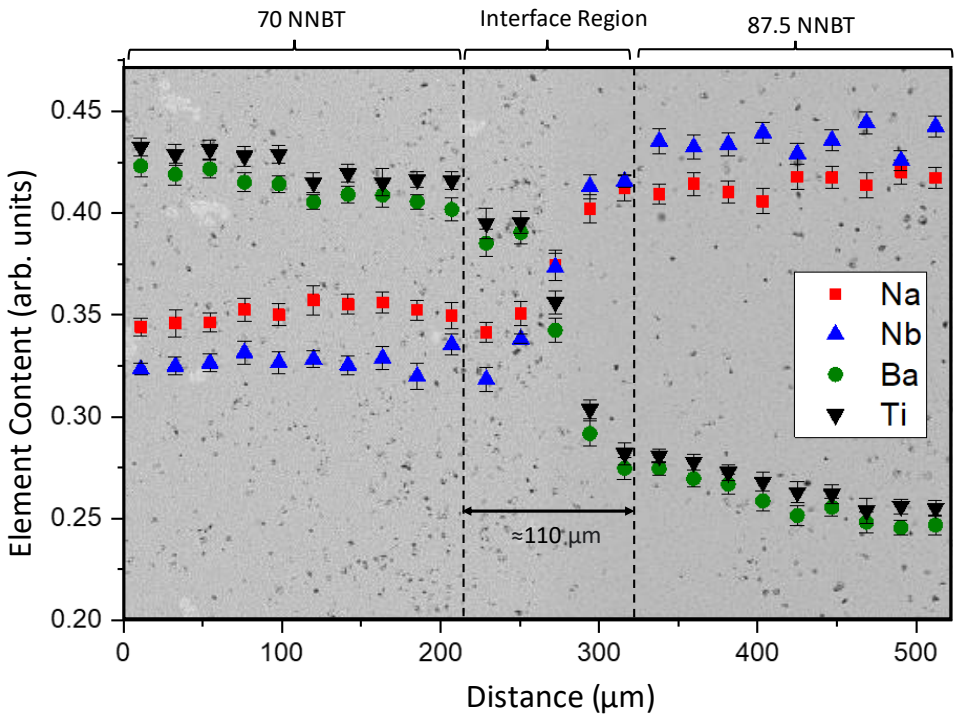

Figure 6.14 Electron Microscopy of the co-sintered bilayer pellet recorded at 250x magnification. BS image of the bilayer interface with bulk 70NNBT on the left and 87.5NNBT on the right. The overlaid plot is EDX data of the relative concentration of the elements (Na, Nb, Ba and Ti). The region displaying a transition in elemental concentration is labelled as the interface region.

6.10. References

[1] I. P. Raevskii, L. M. Proskuryakova, L. A. Reznichenko, E. K. Zvorykina, and L. A. Shilkina, "Obtaining solid solutions in the NaNbO3-BaTiO3 system and investigation of its properties," Soviet Physics Journal, vol. 21, no. 2, pp. 259-261, 1978, doi: 10.1007/bf00898503.

[2] D. K. Kwon et al., "Temperature- and Frequency-Dependent Dielectric Properties of Sol-Gel-Derived BaTiO3-NaNbO3 Solid Solutions," (in English), J. Electron. Mater., Article vol. 45, no. 1, pp. 631-638, Jan 2016, doi: 10.1007/s11664-015-4162-1.

[3] M. J. Pan and C. A. Randall, "A brief introduction to ceramic capacitors," IEEE Electrical Insulation Magazine, vol. 26, no. 3, pp. 44-50, 2010, doi: 10.1109/mei.2010.5482787.

[4] R. Whatmore, "Ferroelectric Materials," Springer International Publishing, 2017, pp. 1-1.

[5] S. Tashiro, Y. Mizukami, and H. Igarashi, "Fabrication of Composite MLC's and Their Dielectric Properties," (in English), Japanese Journal of Applied Physics, Article vol. 30, no. Part 1, No. 9B, pp. 2311-2314, Sep 1991, doi: 10.1143/jjap.30.2311.

[6] H. C. Song, J. E. Zhou, D. Maurya, Y. Yan, Y. U. Wang, and S. Priya, "Compositionally Graded Multilayer Ceramic Capacitors," (in English), Sci Rep, Article vol. 7, no. 1, p. 12353, Sep 27 2017, Art no. 12353, doi: 10.1038/s41598-017-12402-7.

[7] P. Foeller, "Novel materials and routes for rare-earth-free BaTiO3-based ceramics for MLCC applications.," Materials Science and Engineering, University of Sheffield, 2017. [Online]. Available: http://etheses.whiterose.ac.uk/18954/

[8] K. Yasukawa, M. Nishimura, Y. Nishihata, and J. Mizuki, "Core-shell structure analysis of BaTiO3 ceramics by synchrotron X-ray diffraction," (in English), Journal of the American Ceramic Society, Article vol. 90, no. 4, pp. 1107-1111, Apr 2007, doi: 10.1111/j.1551-2916.2007.01537.x.

[9] D. Hennings and G. Rosenstein, "Temperature-Stable Dielectrics Based on Chemically Inhomogeneous BaTiO3," Journal of the American Ceramic Society, vol. 67, no. 4, pp. 249-254, 2006, doi: 10.1111/j.1151-2916.1984.tb18841.x.

[10] Z. Tian, X. Wang, S. Lee, K. H. Hur, and L. Li, "Microstructure Evolution and Dielectric Properties of Ultrafine Grained BaTiO3-Based Ceramics by Two-Step Sintering," Journal of the American Ceramic Society, vol. 94, no. 4, pp. 1119-1124, 2011, doi: 10.1111/j.1551-2916.2010.04234.x.

[11] J. T. Zeng, K. W. Kwok, and H. L. W. Chan, "Ferroelectric and piezoelectric properties of Na1-xBaxNb1-xTixO3 ceramics," (in English), Journal of the American Ceramic Society, Article vol. 89, no. 9, pp. 2828-2832, Sep 2006, doi: 10.1111/j.1551-2916.2006.01172.x.

[12] R. Zuo, H. Qi, J. Fu, J. Li, M. Shi, and Y. Xu, "Giant electrostrictive effects of NaNbO3-BaTiO3 lead-free relaxor ferroelectrics," Applied Physics Letters, vol. 108, no. 23, p. 232904, 2016, doi: 10.1063/1.4953457.

[13] A. G. Serrano, A. L. Bonaventura, R. Boschilia, and E. Antonelli, "Microstructural, structural and electrical BaZr0.05Ti0.95O3/Ba0.75Sr0.25TiO3 ceramics properties of bilayered," (in English), Mater. Res. Bull., Article vol. 87, pp. 34-39, Mar 2017, doi: 10.1016/j.materresbull.2016.11.016.

[14] T. M. Amaral, E. Antonelli, D. A. Ochoa, J. E. Garcia, and A. C. Hernandes, "Microstructural Features and Functional Properties of Bilayered BaTiO3/BaTi1-xZrxO3 Ceramics," (in English), Journal of the American Ceramic Society, Article vol. 98, no. 4, pp. 1169-1174, Apr 2015, doi: 10.1111/jace.13417.

[15] Y. C. Lee, W. S. Lee, and F. S. Shieu, "Development of composite dielectrics with high specific capacitance and stable temperature characteristics," (in English), Journal of Materials Science, Article vol. 37, no. 13, pp. 2699-2705, Jul 2002, doi: 10.1023/a:1015817016268.

7. High Temperature materials based on $(Ca_xSr_yBa_{1-x-y})Nb_2O_6$

7.1. Introduction

The development of industries such as telecommunications and electric vehicles (EV) has led to a significant demand for MLCCs that have a stable capacitance response in high temperature environments. As previously discussed, chemically doped BT materials struggle to stabilise their permittivity response at temperatures above 150°C. Owing to the decades of experience with BT based materials, industry is reluctant to move away from BT-based systems unless substantially better performance or new markets can be achieved.

As seen in chapter 5, materials of the NNBT system can be combined to produce a layered system that stabilises permittivity from -55 to 200°C. However, this requires NNBT materials where BT is now the minor component of the system, at <15 mol%. Put another way, an NN-based material is required to achieve the high temperature stability. This example demonstrates the need for alternatives to BT-based materials to be considered when high temperature stability is required.

In this chapter, the Tetragonal Tungsten Bronze (TTB) structured materials of general formula $(Ca_xSr_yBa_{1-x-y})Nb_2O_6$, CSBN, were investigated, due to previous reports of very high T_{max} values [1-3]. This system simplifies as $(Ca_xBa_{1-x})Nb_2O_6$ (CBN) and the $Sr_yBa_{1-y}Nb_2O_6$ (SBN) materials, which have been thoroughly investigated over the last few decades [4-9].

CBN materials have high T_{max} values of between 228 and 350°C, for the TTB stable range of x=0.18 to 0.38. SBN materials, with the larger stability region of y= 0.25 to 0.75, have a T_{max} range of ~25 to 240°C. By combining CBN and SBN, the range of T_{max} achieved with the TTB structure is near continuous from 25°C to 350°C, as shown in Figure 7.1.

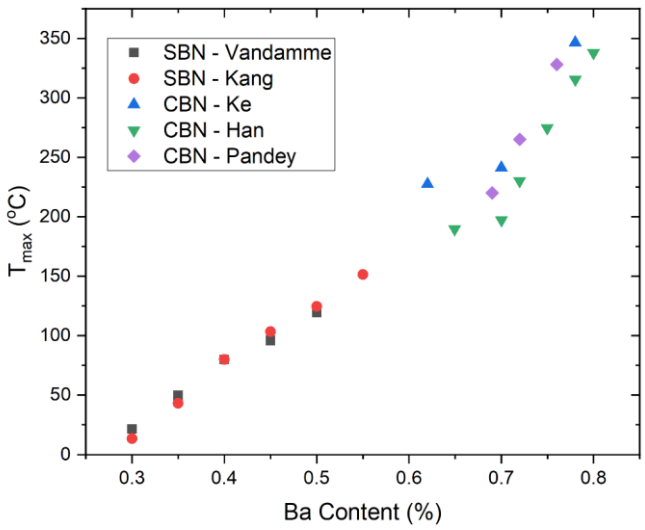

Figure 7.1 Range of T_{max} for the permittivity profile reported in the literature for SBN [2, 10] and CBN [1, 11, 12].

The stability of the TTB structure for CSBN materials has been reported by Muehlberg et al. [13], Figure 7.2, as the grey region of the ternary diagram. To aid the reader, red tie lines have been added, connecting CBN and SBN by their compositional limits. As the red lines are always within the grey region, the TTB structure is predicted to be maintained if a CSBN material is produced by combining CBN and SBN materials. This is likely to occur at the interface of a co-sintered system of CBN and SBN, suggesting a fully dense interface can be achieved when combining CBN and SBN materials.

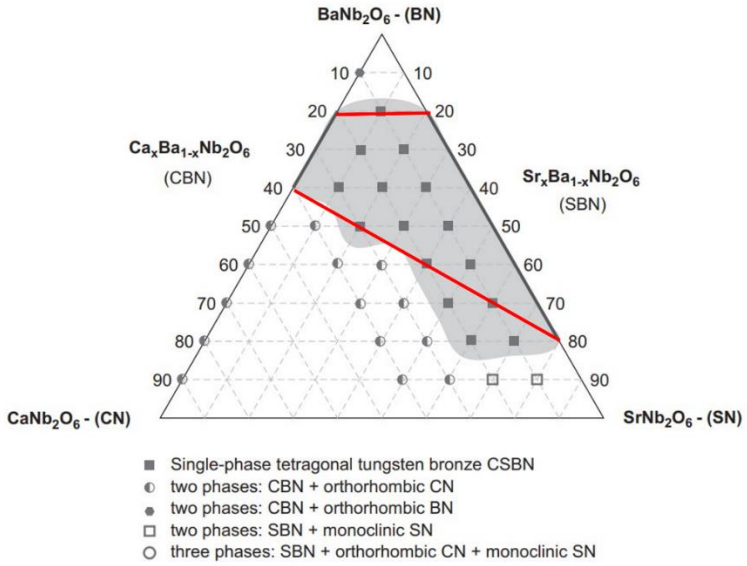

Figure 7.2 Ternary diagram of $CaNb_2O_6$ – $BaNb_2O_6$ – $SrNb_2O_6$, demonstrating the TTB stability region. Red tie lines superimposed to simplify the CSBN region of stability. Figure adapted from Muehlberg et al. [13].

By altering the Ca:Sr:Ba ratio, the CSBN system shows excellent promise in producing layered structures that have temperature stability in their permittivity response from 25°C to high temperatures. By using CBN and SBN materials, literature data can be used to predict compositions of interest, providing a strong starting base for experimental studies. The formation of CSBN materials, due to interdiffusion, may improve the stability of the permittivity response, in a similar manner to the limited interdiffusion used to produce core and shell microstructures in BT-based materials.

In this chapter, various CSBN materials were produced, targeting compositions that produce a set of permittivity profiles with a wide range of T_{max} values. The characterised materials were then used as inputs into the layered optimisation software, to simulate the permittivity profiles of different composite systems. The simulation results allowed further experimental research to focus on particular combinations. Finally, the interface material was considered, investigating the potential effect on the simulation results.

7.2. Experimental Methodology

The solid state processing and characterisation procedures are detailed in the experimental methods, chapter 3. Six (Ca,Sr,Ba)Nb_2O_6 materials were air sintered at 1200°C for 4 hours, followed by a 1350°C hold for 2 hours (so-called dual sintering). The resulting ceramics were characterised for their physical and electrical properties. Materials were labelled as CBN, SBN or CSBN, dependent on which A-site cations were present in the composition, and are shown on the ternary diagram of Figure 7.3.

To investigate co-sintering of these materials, mixed ceramic samples were produced. Calcined powders of two different starting compositions were batched and mixed in a pestle and mortar. The mixed samples were sintered with the same dual step procedure used on the starting (individual) six materials. Mixed samples were also sintered at 1350°C for 1 hour (so-called fast sintering), to investigate the effect of sintering time on the characterised materials.

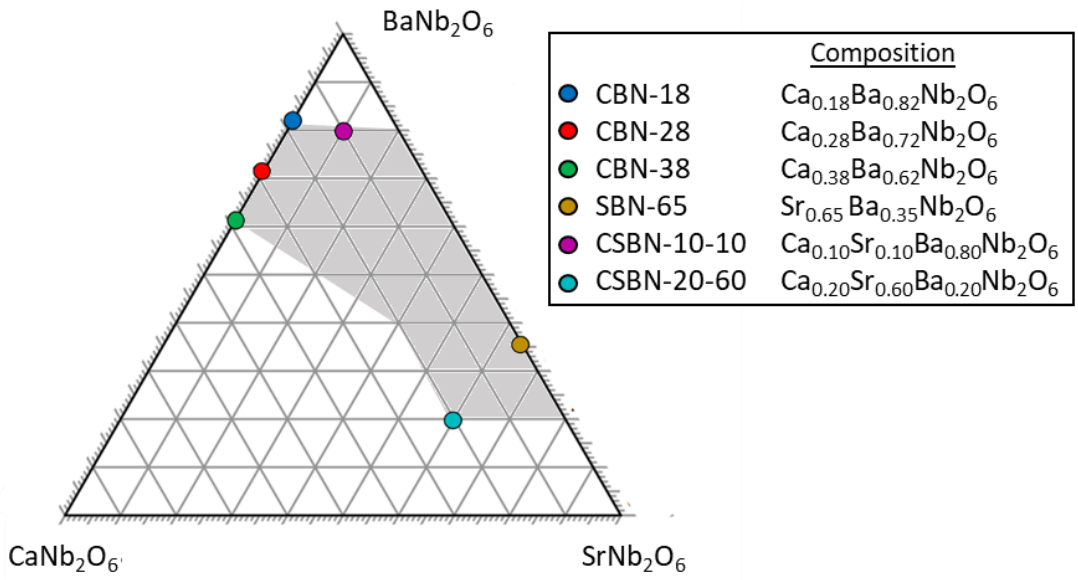

Figure 7.3 Ternary diagram of the CSBN compositions synthesised and characterised in this work. The TTB region reported by Muehlberg et al. [13], is included as a grey region

7.3. Experimental Results

Of the six materials, three simplify as CBN materials. To simplify comparison, these results are compared together with the Sr^{2+} containing materials also grouped together.

7.3.1. Phase Composition

For all six compositions, the XRD patterns matched the expected TTB structure and patterns; however, there were additional XRD peaks occurring for CBN-38 and CSBN-20-60, Figure 7.4 and Figure 7.5, respectively.

The additional peaks in CBN-38 were identified as $CaNb_2O_6$ (JCPDS 71-2406), with the intensity of the peaks suggesting a significant presence of this secondary phase. $CaNb_2O_6$ and $SrNb_2O_6$ were similarly identified as secondary phases in CSBN-20-60.

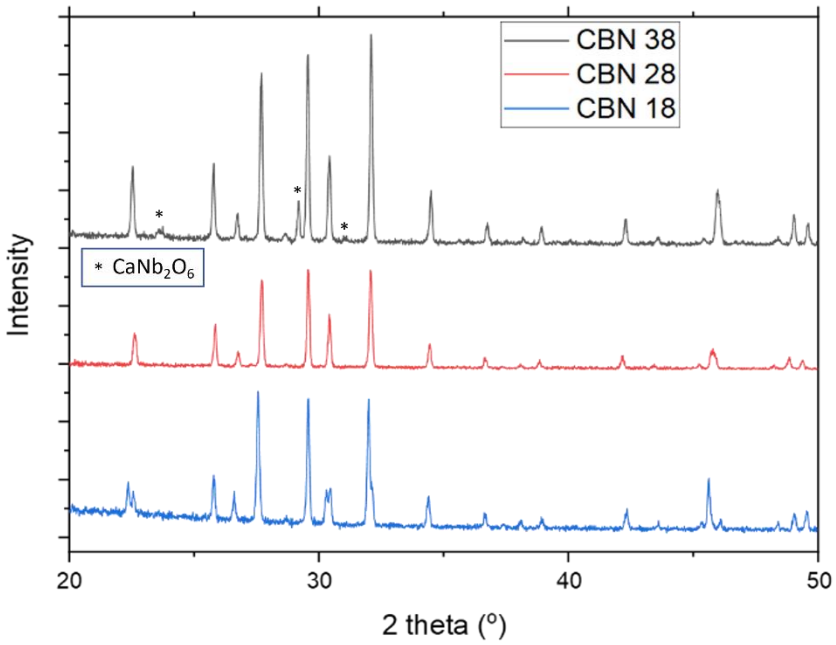

Figure 7.4 XRD patterns of $(Ca_xBa_{1-x})Nb_2O_6$ materials, sintered with the a two stage sinter (1200°C for 4H, 1350°C for 2H). Peaks not associated with the TTB structure, were identified as $CaNb_2O_6$, marked as *.

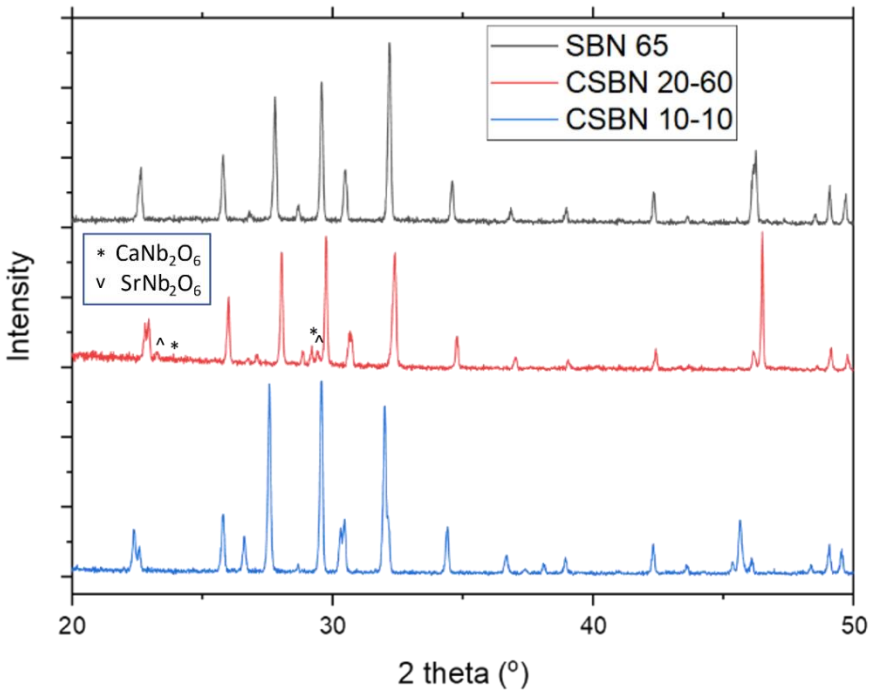

Figure 7.5 XRD patterns of (Ca,Sr,Ba)Nb_2O_6 materials, sintered with the two stage sinter (1200°C for 4H, 1350°C for 2H). Peaks not associated with the TTB structure, were identified as $CaNb_2O_6$ and $SrNb_2O_6$, marked as * and v respectively.

Scanning electron microscopy (SEM) was undertaken on the dual sintered CBN-38 material, Figure 7.6, to investigate the $CaNb_2O_6$ phase. The backscattered image of the microstructure (a) reveals a microstructure with two distinct compositions. Small, angular regions of low Z mass are distributed throughout the microstructure. The EDX imagery on the same area reveals these low Z mass regions are Ba-deficient, and Ca-rich. These Ca-rich regions reduce the CBN composition of the bulk, whilst retaining overall stoichiometry in the ceramic, equation (7.1).

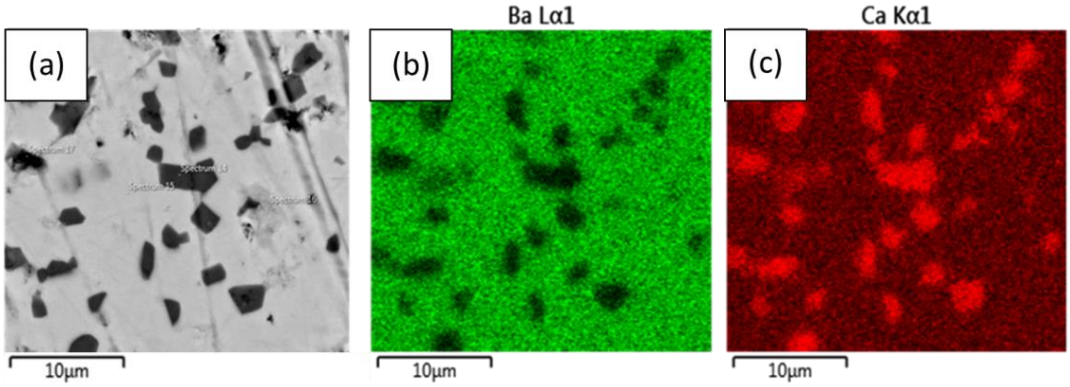

Figure 7.6 Electron Microscopy images of CBN-18, showing the presence of a secondary phase. (a) Back-scattered image, where brightness is relative to Z mass. The element mapped EDX images, (b) and (c), show the Ba and Ca content maps, respectively.

$$0.38CaCO_3 + 0.62BaCO_3 + Nb_2O_5 = \frac{0.62}{0.62+y}\left(Ca_{0.38-y}, Ba_{0.62+y}\right)Nb_2O_6 + \frac{y}{0.62+y}CaNb_2O_6 + CO_2 \quad (7.1)$$

7.3.2. Dielectric properties

The dielectric response of the materials from 25°C to above 400°C, are shown in Figure 7.7. In (a), the CBN materials demonstrate a ferroelectric to paraelectric phase transitions with T_{max} values that decrease with increasing Ca content. tan δ responses (b) contain responses due to these transitions, as well as additional responses at low temperatures, which have previously reported been attributed to incommensurate-commensurate transitions [1].

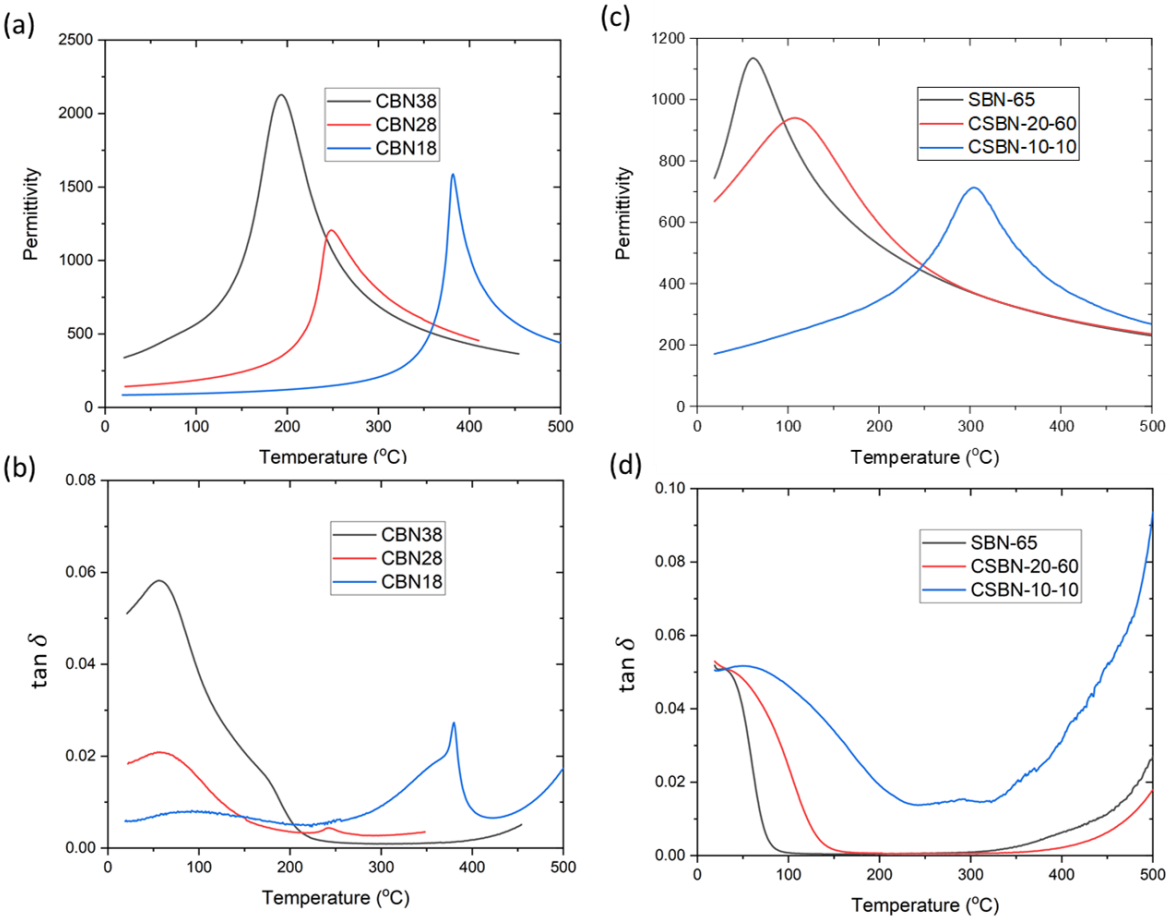

Figure 7.7 Dielectric data of six different TTB materials synthesised. (a) and (b) are the permittivity and tan δ response of the CBN materials (x = 0.18,0.28,0.38) respectively, whilst the response of Sr containing materials are shown in (c) and (d). All data measured at 100 kHz.

The Sr containing materials are grouped in (c) and (d). The Sr content in SBN affects T_{max} in the same manner as CBN. CSBN-20-60 has the highest content of Ca and Sr in the six materials, yet has the 2nd lowest T_{max}, beaten by SBN-65. Unlike the CBN materials, T_{max} of SBN-65 and CSBN-20-60 are frequency dependent. T_{max} of SBN-65 varies by 7°C, across the frequency range 1 kHz to 1 MHz. The frequency dependence of permittivity and tan δ in CSBN-20-60 is shown in Figure 7.8, with T_{max} having a variation of 15°C. In (b), the magnitude of tan δ is suppressed as the frequency increases. These frequency responses suggest a relaxor-ferroelectric type transition.

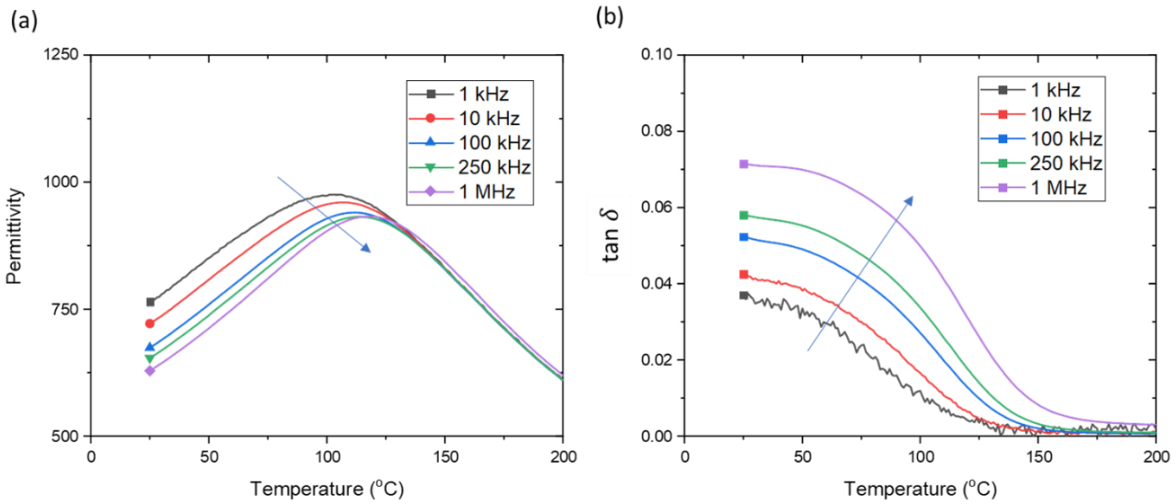

Figure 7.8 The frequency dependency of (a) permittivity and (b) tan δ for CSBN-20-60. The arrows highlight the response shift to higher temperatures with higher frequency.

7.3.3. Relationship of lattice parameters and dielectric response.

The relationships between T_{max} and the lattice parameters across the series are shown in Figure 7.9. The a_o lattice parameter displays only a weak relationship with T_{max}, indicating the A site composition has little or no effect on a_o. This is common in many TTB materials, with a_o often reported as being sensitive to the relative tilting of the oxygen octahedron sites and not of A-site cation radii [14].

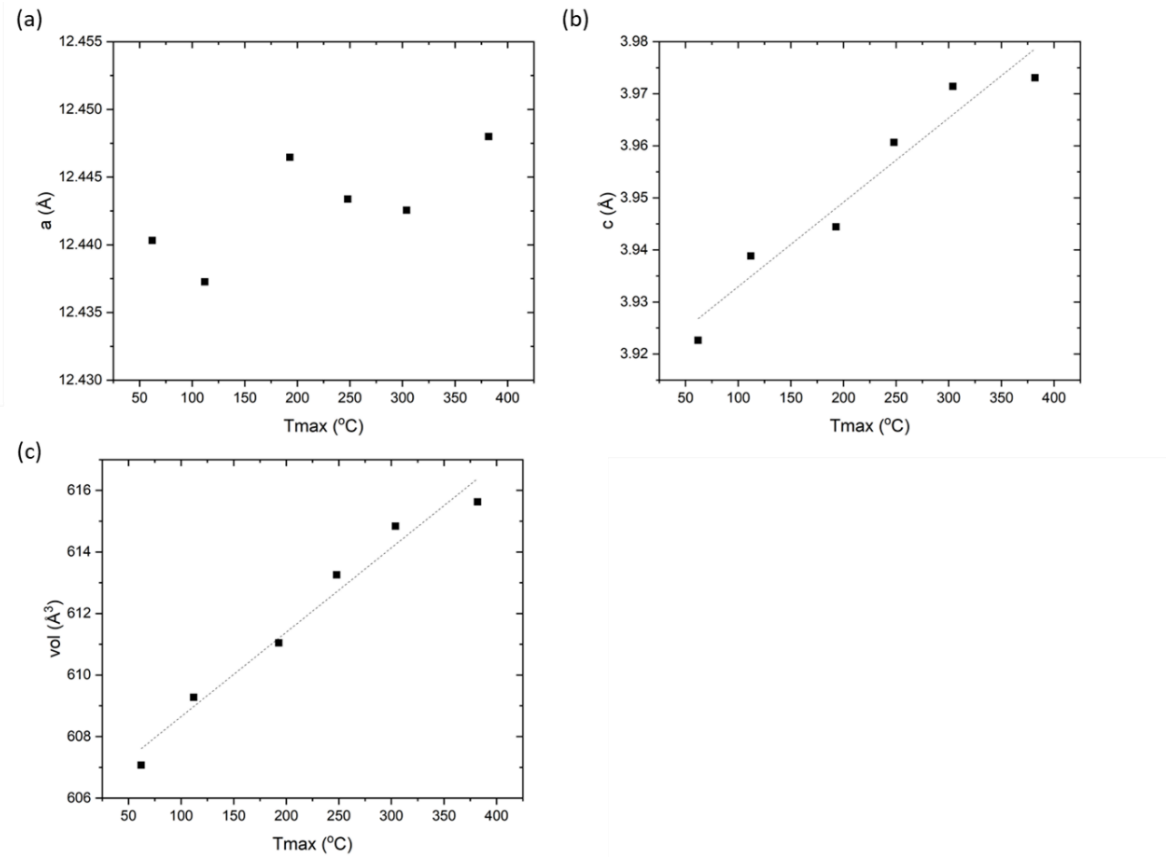

Figure 7.9 Relationship of the lattice parameters obtained from XRD, to T_{max} from LCR measurements for the six TTB materials produced. (a) Lattice parameter a, showing little deviation. (b) c axis lattice parameter, with a line to highlight the trend with T_{max}. (c) is the unit cell volume ($c*a^2$), also including a trend line.

For the c_o parameter and unit cell volume, both increase with T_{max}, with a line of best fit to act as a guide to the eye. Across the 325°C range of T_{max}, there was a change of 1.4% in the unit cell volume.

7.4. Simulation Results

A summary of the permittivity profiles for the six TTB materials synthesised are shown in Figure 7.10. All materials were processed and sintered in an identical manner, with the 100 kHz permittivity profile used. These were used as inputs to the MATLAB script, to simulate the permittivity profiles of layered composites, following the same process as described in the previous results chapter. Unlike the NNBT layered simulations, the temperature range was set from 25 to 400°C. This temperature range of 375°C is significantly larger than the 255°C of X9 class MLCCs.

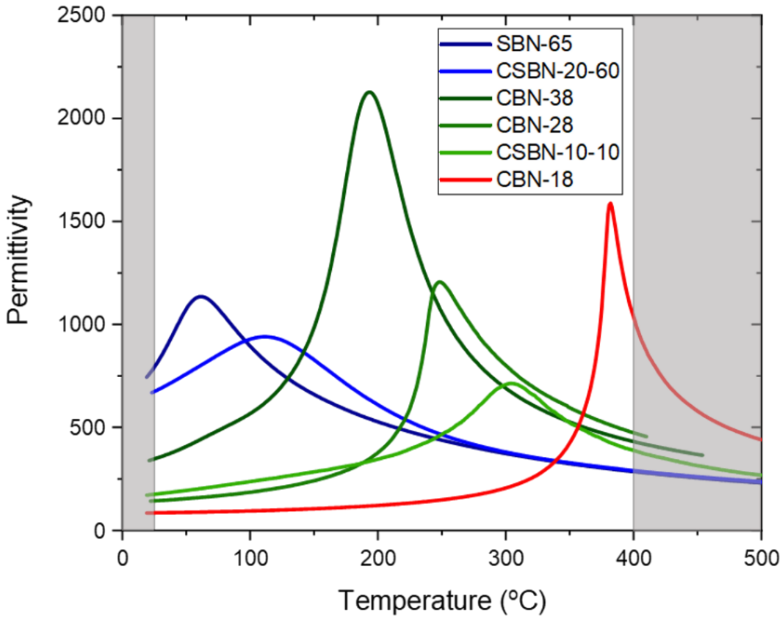

Figure 7.10 Permittivity profiles of the different materials characterised, measured at 100 kHz. The data collected from RT to 400°C being used in the optimisation simulations.

The performance of the 20 possible combinations is shown in Figure 7.11 (a), with the component materials in each combination provided in (b). Of the 20 starting combinations, 17 optimise as binary layered systems. As seen by the open circle symbols in (b), materials with a middle T_{max} are most likely to be inactive in the binary optimisation.

The worst 4 combinations, with TCC_{abs} > 100%, contain only medium and high T_{max} materials. Likewise, 16th to 8th rankings consist only of low and medium T_{max} materials. The combinations ranked 6th to 2nd all have low, medium and high T_{max} materials for optimisation. However, all optimise as binaries consisting of a low and high T_{max} material.

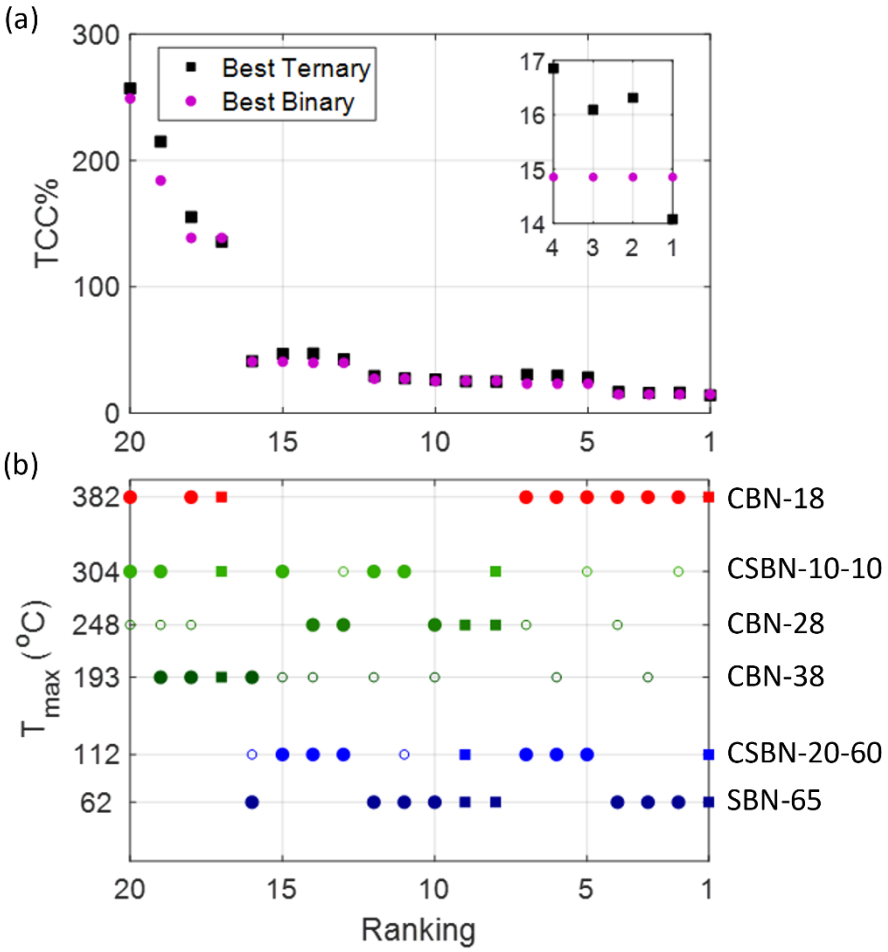

Figure 7.11 The 20 different combinations simulated as layers in series, ranked by TCC_{abs} performance. (a) TCC_{abs} values achieved for each combination as a binary and ternary layered system. The internal plot distinguishes the performance of the top four ranked combinations. (b) Component materials (filled symbols), with an empty circle indicating a material not used, as the combination optimises as a binary layer system.

This preference of combining low and high T_{max} materials is seen in the best ranked combination, which consists of the two low T_{max} materials (SBN-65 and CSBN-20-60) and the high T_{max} material (CBN-18), optimising as a ternary system.

As seen in Figure 7.11 (a), the TCC_{abs} of the best binary and best ternary of rank 1 is very similar, suggesting little performance benefit of using a ternary layered system. The permittivity and TCC profiles of both are compared in Figure 7.12. The best ternary ratio has slightly better suppression of the permittivity peak at ~60°C, which leads to a slight improvement in TCC_{abs} compared to the best binary profile.

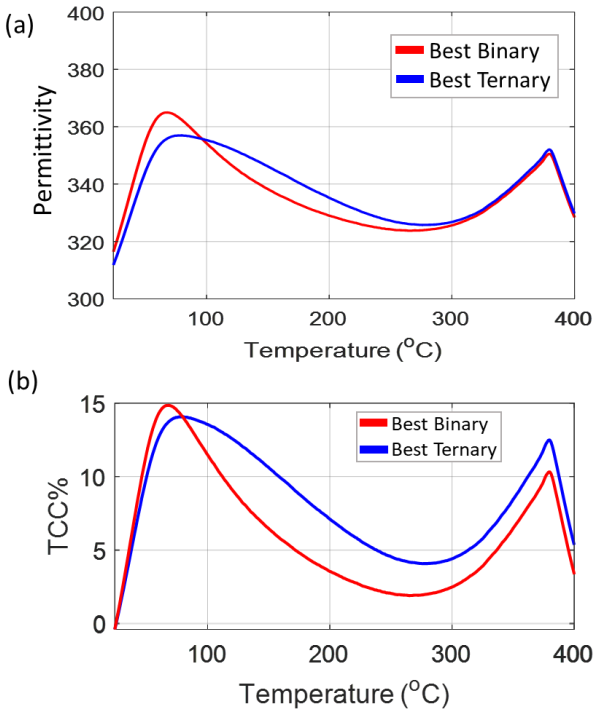

Figure 7.12 The permittivity profiles when the SBN-65, CSBN-20-60 and CBN-18 combination is optimised for layer thickness fractions. The best binary system and best ternary layered system are compared in terms of permittivity (a) and TCC% (b).

The ternary diagram for the dependence of relative layer ratio on the TCC performance for the best combination is shown in Figure 7.13 (a). The layer ratios of the best binary and best ternary are shown in Figure 7.13 (b). The best binary just meets the $TCC_{abs} < 15\%$ classification, with a $TCC_{abs} = 14.9\%$. However as seen in the ternary diagram, this classification is only achieved at one specific layer ratio (0.18:0.82).

As a ternary layer system, there are more layer ratios that achieve $TCC_{abs} < 15\%$. The SBN-65 layer ratio can alter from 0.10 to 0.37, and thus CSBN-20-60 by 0.72 to 0.45. This flexibility in SBN-65:CSBN-20-60 ratio requires the CBN-18 layer to be exactly 0.18 of the total thickness. This precision in layer thickness would be challenging to produce commercially.

(a)

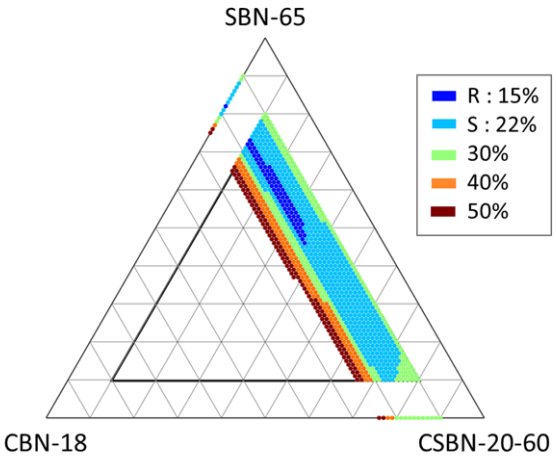

(b)

	Component layer content (%)				
	CBN-18	CSBN-20-60	SBN-65	ε_{RT}	TCC_{abs}
Best Binary	18	0	82	318	14.9
Best Ternary	18	20	62	313	14.1

Figure 7.13 (a) Ternary colourmap of the 1st ranked combination, showing the layer thickness ratios that achieve various TCC_{abs} values. The permittivity and TCC(%) profiles of the best binary and best ternary layer optimisation is shown in (b) and (c), respectively.

Relaxing the TCC classification requirements to $TCC_{abs} < 22\%$, allows a great range of layer thicknesses of CBN-18 of 0.12 to 0.20, for both binary and ternary layer systems. Therefore, this example shows that although the ternary system offers a slight TCC_{abs} improvement, it has little benefit otherwise over a binary system.

From the XRD pattern, the CSBN-20-60 contained secondary phases of $CaNb_2O_6$ and $SrNb_2O_6$, which may complicate attempts to investigate co-sintering characteristics. Therefore, the binary system of CBN-18 and SBN-65 was chosen for further focus.

7.4.1. Dilatometry of CBN-18 and SBN-65

To further investigate the suitability of CBN-18 and SBN-65 as a co-sintered system, dilatometry was performed on the individual materials. To aid the strength of the green body samples, 1 wt% Polyvinyl Alcohol (PVA) was added to the calcined powders before being uniaxial pressed. Green body pellets with length of >25mm were heated in a N_2 rich atmosphere at 10°C/min to 1350°C, with the change in sample length being continuously measured. To provide a comparison in densification rates, CBN-38 was also characterised.

The change in sample length due to this linear heating rate from RT to 1350°C, is shown in Figure 7.14. Starting at 25°C, the materials all have a slight increase in length due to thermal expansion. Densification begins about 1100°C, resulting in a decrease of sample length. CBN-38 demonstrates the most significant decrease in length with a >12% change at the end of the heating process. CBN-18 and SBN-65 have similar length change profiles with both experiencing an ~8% decrease in length. A mis-match in densification rates may prevent a layered structure from co-sintering due to mechanical strain causing layer de-lamination. The similarity in the results of CBN-18 and SBN-65 would limit this issue, suggesting compatible materials for co-sintering.

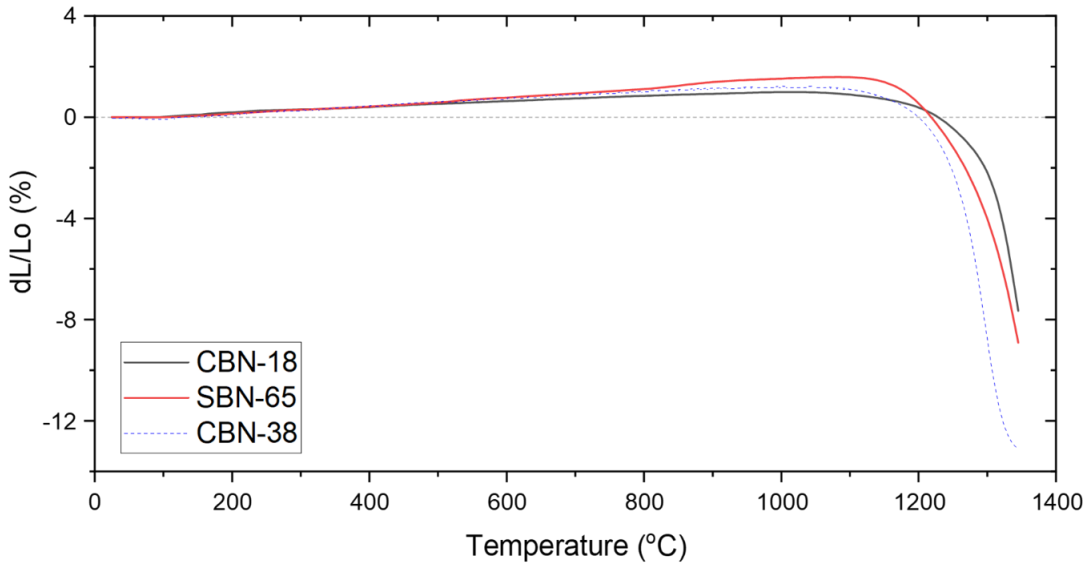

Figure 7.14 Dilatometry profiles for the sintering of CBN-18 and SBN-65 ceramics. Green samples heated at 10°C/min from 25 to 1350°C.

7.4.2. Series vs Parallel Optimisation

In previous chapters the focus has been on dielectric layers electrically connected in series. Figure 7.15, (a) shows a simplified structure of a current MLCC, with each monolayer electrically connected in parallel. An example of a binary layer in series is demonstrated in (b), with two dielectric materials between each pair of electrode plates. For both structures, the dielectric material(s) between each pair of electrodes are identical. Layers in parallel, (c), have only one dielectric material between electrode pairs but this material is not the same for each electrode pair.

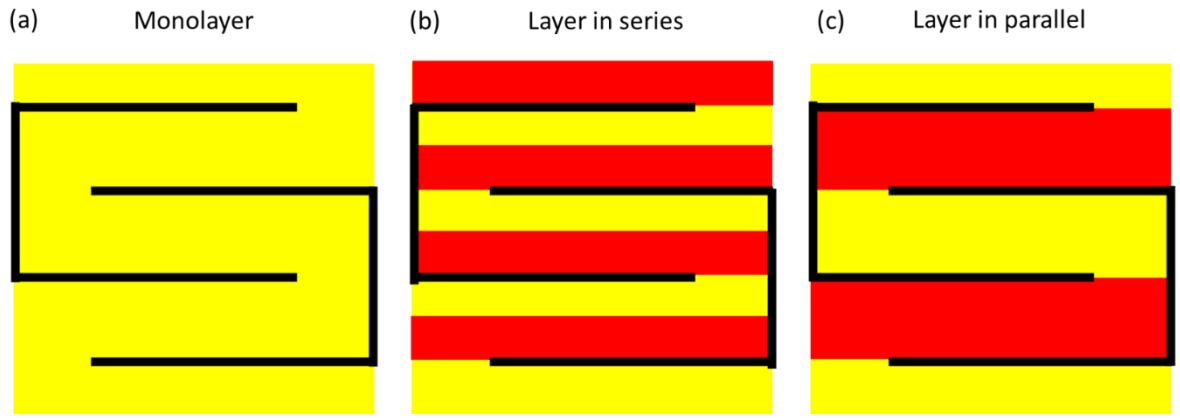

Figure 7.15 Schematics of layers with different electrical connectivity can be created in the geometry of an MLCC. (a) Monolayer, (b) bilayers in series, and (c) bilayers in parallel.

Assuming each material layer behaves as an ideal capacitor, the permittivity of a parallel layer system is:

$$\varepsilon_T = A_1\varepsilon_1 + A_2\varepsilon_2 + A_3\varepsilon_3 \quad , where\ A_1 + A_2 + A_3 = 1 \tag{7.2}$$

where A is the relative surface area of each of the materials in parallel. If each electrode pair has identical surface area, as in Figure 7.15 (c), different *A* values are created by how many layers of each material are stacked together. By simulating all possible A_1:A_2:A_3 combinations, the developed MATLAB code can simulate and optimise for parallel systems, in an identical way for layers in series.

Many heterogeneous composites, such as core and shell microstructures, can be modelled as a complex circuit of components in series and parallel. The range of responses from these circuits are between the upper and lower bounds of the system of pure series and pure parallel, respectively. Although the exact response of a particular microstructure is difficult to simulate accurately, the bounds are much easier to simulate.

The binary CBN-18 and SBN-65 were simulated in series and parallel for relative thickness fractions from 0 to 1 in steps of 0.01. The permittivity profiles were simulated for the temperature range of 25 to 400°C, and TCC_{abs} determined. The dependence of the relative thickness fraction on the TCC_{abs} is shown in Figure 7.16.

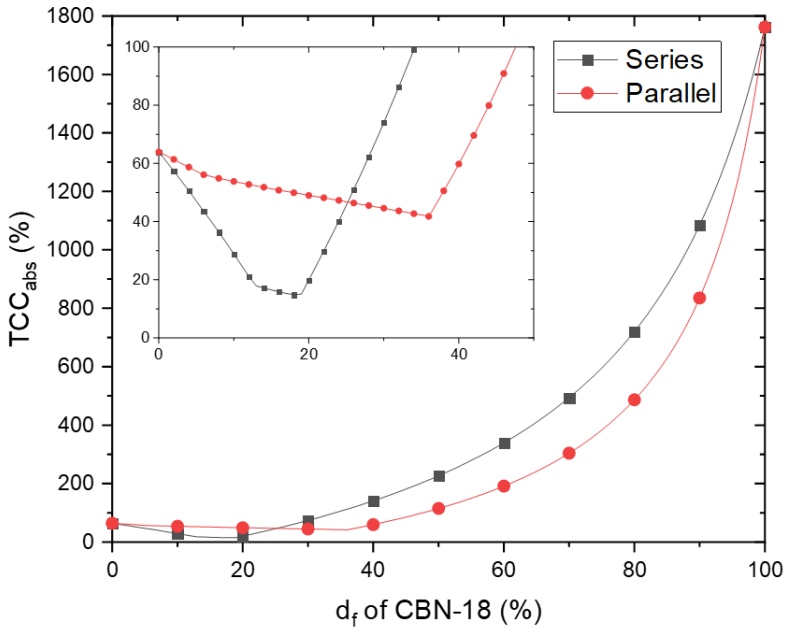

Figure 7.16 The dependence on the TCC_{abs} simulated for the range of possible thickness fractions for the SBN-65:CBN-18 bilayer when connected as either in series or in parallel. TCC_{abs} calculated for the temperature range (25°C to 400°C). The inset plot focuses on the d_f values that minimise TCC_{abs}, with symbols every 2%.

At 0 and 100%, both systems simplify as a monolayer, producing the same TCC_{abs} values. The series model optimises to the lowest TCC_{abs}, with TCC_{abs} = 14.9%. This occurs for the layer system at an 18:82 ratio of CBN-18:SBN-65. The parallel model optimises at a higher CBN-18 content, with TCC_{abs} = 41.8% at 0.36:0.64. As the monolayer of SBN-65 has a TCC_{abs}= 64%, the parallel model does not lead to much of an improvement for these materials. However, the parallel model does achieve a better TCC_{abs} for d_f > 0.25 of CBN-18.

7.5. Co-sintering effects

In the previous chapter, the difference in the permittivity response of a co-sintered set of NNBT pellets and the simulations was discussed. The addition of a thin interface region, with a composition that was an average of the two pellets was shown to better model the experimental results. Due to the geometry of bulk pellets, this interface effect had only limited effect on the permittivity profile.

In commercial MLCC devices, the real layer thicknesses are significantly smaller. If the real thickness of the interface region remains consistent, then the relative thickness of this interface region will increase. Therefore, the interface region produced in a co-sintering a bilayer system may be considered as a distinct third layer.

To generate the experimental data, CBN-18 and SBN-65 were mixed as calcined powders, at the 18:82 volume ratio predicted to be optimised for a series system. The pellets were then pressed and sintered. Pellets were sintered with the dual conditions (1200°C, 4 hr and 1350°C, 2 hr; labelled dual), to maintain consistency with how the independent (single) materials were sintered.

These sintering conditions are designed to produce fully dense ceramics that are homogeneous. Therefore, it is likely that when the mixed samples were sintered with the dual sintering procedure, a significant amount of homogenisation would occur, as also seen in the NNBT mixed pellets in chapter 6. A short sinter (1350°C for 1 hr, labelled fast) was also investigated, in an attempt to limit chemical homogenisation between grains of the different TTB materials.

The XRD patterns of the two mixed materials are compared to their component materials in Figure 7.17. Both mixed samples indicate a single-phase material being formed, although there is slight peak broadness in the fast sinter, which may suggest a more heterogeneous compositional distribution. The lattice parameters are compared in Table 7.1, with only a slight difference between the fast and dual sintered mixed samples.

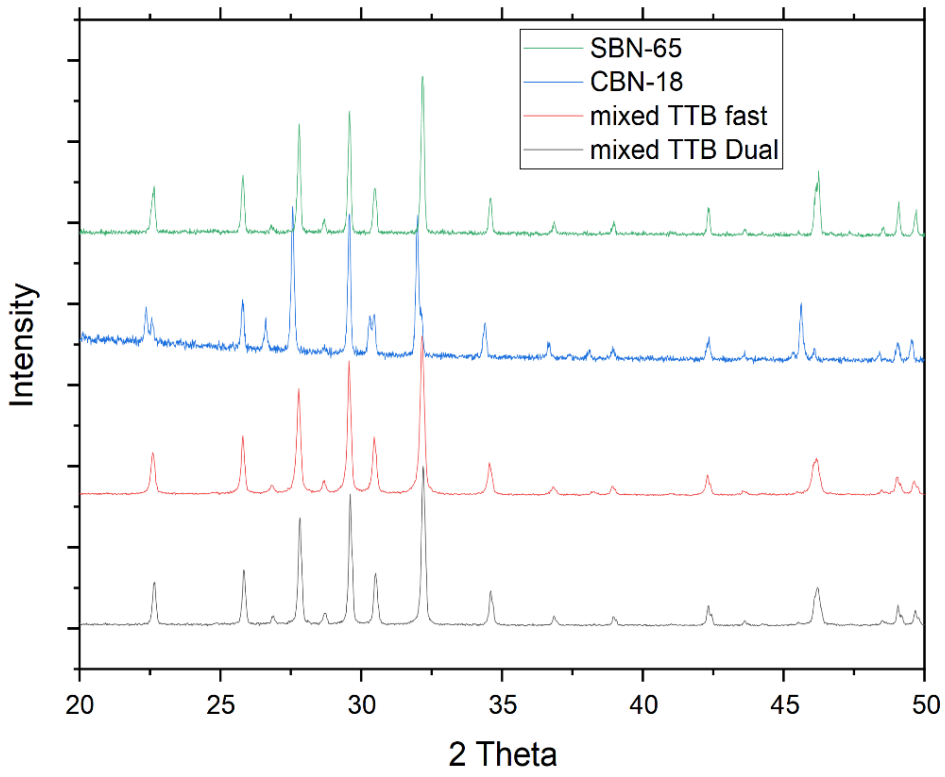

Figure 7.17 XRD patterns, 2 θ = 20° – 80°, comparing the SBN-65 and CBN-18 to the two mixed samples. The mixed TTB fast sample was sintered at 1350°C for 1 hour, whilst all others were sintered using the dual step procedure. The mixed samples were produced by mixing the CBN-18 and SBN-65 calcined powders, at a vol% 18:82 ratio respectively, using a pestle and mortar.

Table 7.1 Lattice parameters of individually sintered CBN-18 and SBN-65 materials and the resultant values when mixed as calcined powders.

Material	a_o (Å)	c_o (Å)	Volume (Å^3)
CBN18	12.4480(4)	3.9730(3)	615.63(9)
SBN65	12.4403(4)	3.9226(3)	607.07(8)
Mixed – Dual	12.4423(5)	3.9243(4)	607.53(11)
Mixed - Fast	12.4430(5)	3.9275(4)	608.10(11)

The permittivity and tan δ response of the mixed samples are shown in Figure 7.18, with comparison to their component materials. A single permittivity peak is observed for both the dual and fast sintered samples, with T_{max} values of 85 and 87°C, respectively. Although dense pellets (>90%) were achieved for all compositions, the addition of CBN-18 resulted in the mixed samples having a higher density than SBN-65. This additional density explains the increased permittivity magnitude in the mixed samples.

The tan δ response of the mixed samples has strong similarities to SBN-65, with a high tan δ loss at temperatures approaching T_{max}, related to a relaxor-type transition. Unlike SBN-65, both mixed samples produce a tan δ peak at ~ 240°C. This response is largest in the mixed fast sample, suggesting some localised regions that have not fully homogenised during the sintering processes.

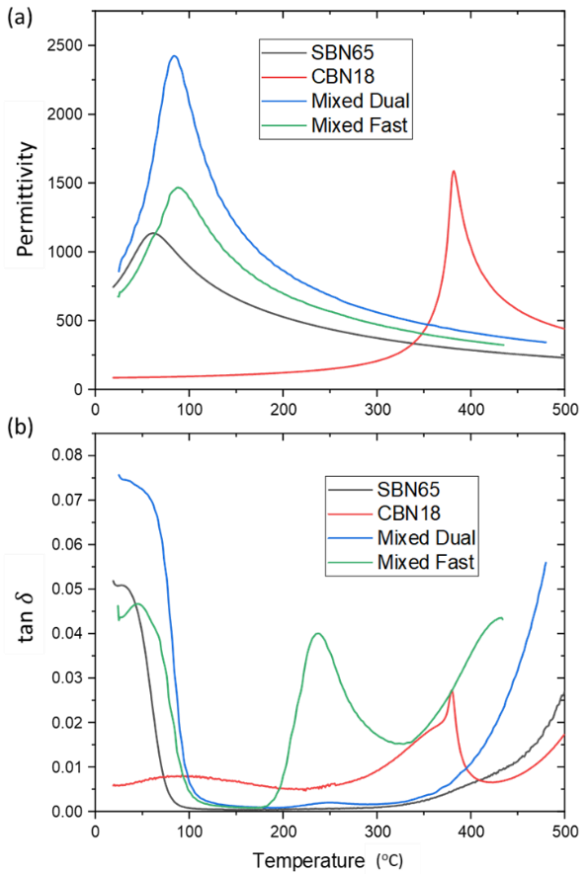

Figure 7.18 The dielectric properties of the mixed TTB samples, with the component materials for comparison. The permittivity (a) and tan δ (b) profiles, both measured at 100 kHz for all samples.

T_{max} and the unit cell volume of the mixed materials, compared to SBN-65 and CBN-18, are shown in Figure 7.19. Due to the mixed materials only containing 18% of CBN-18, the values are close to pure SBN-65, however, they are increased in line with the trend observed for the other TTB synthesised.

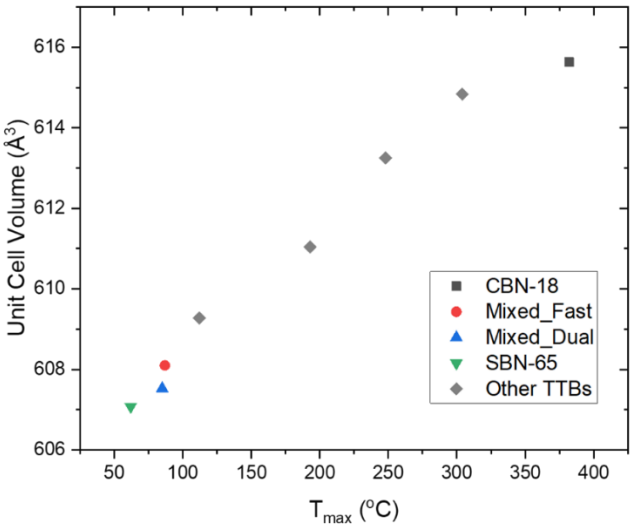

Figure 7.19 Unit cell volume of the TTB materials, and their relationship with T_{max} (°C). The mixed samples, which consist in 'green' form of SBN-65 and CBN-18, are in agreement with the trend.

7.6. Mixed systems compared to simulated profiles

The difference in permittivity response between the series and parallel simulations, and the mixed samples, are shown in Figure 7.20. Both simulation profiles have the same CBN-18:SBN-65 ratio of 18:82 used for the mixed samples. Neither of the simulations model the response observed for the mixed samples. The parallel model fits better at low temperature, however the permittivity peak associated with CBN-18 is not seen in mixed samples. The series and parallel simulations are the extremes of the possible composite responses but only if the components remain chemically independent. The significant divergence in the mixed responses demonstrate that co-sintering must be carefully considered, in terms of chemical diffusion producing permittivity responses not included in the simulation model.

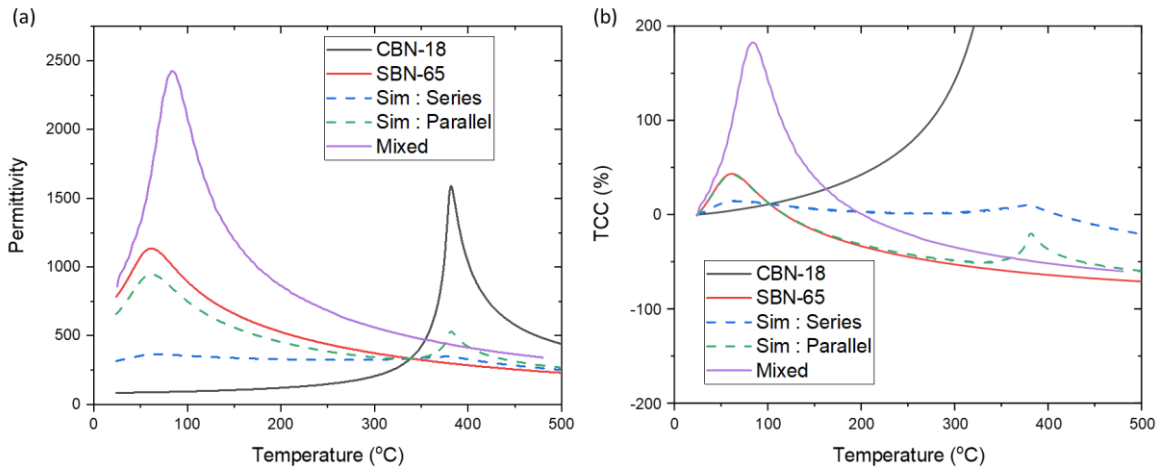

Figure 7.20 Comparison of the measured electrical properties of the mixed TTB samples, compared to the simulated profiles when the components are electrically connected either in series or parallel. (a) Permittivity and (b) TCC%. Dashed lines indicate simulated profiles.

7.7. Series Simulation with Interface

From the XRD data of the mixed pellets, co-sintering of CBN-18 and SBN-65 results in near complete interdiffusion. In a layered system, this interdiffusion will occur at the dielectric-dielectric layer interface. As seen in chapter 6, the incorporation of an interface layer into the simulation model can account for the permittivity response of co-sintered pellets of different NNBT compositions. At the length scale of ~3mm for the binary stack, the interface layer produced is relatively thin, and therefore has little impact on the layered system. The dielectric layers in MLCC devices are often less than 10 microns (<0.01 mm), and therefore a significant potential that the binary layer may homogenise to such an extent that it becomes a homogenous monolayer.

The interface layer was modelled as a 3rd material layer, using the Mixed Dual permittivity profile as the input. The full range of layer thicknesses, d_f = 0 to 1, was simulated for all 3 material layers.

Although all layer ratios were simulated, only those that meet TCC_{abs} < 50% are plotted in Figure 7.21. A colour code shows the regions of the ternary diagram that meet different TCC_{abs} criteria.

The CBN-18 and SBN-65 join of the ternary diagram is the binary model, without an interface layer being considered. This edge includes the same data as shown in the series plot in Figure 7.16, with the optimised 0.18:0.82 denoted by a * symbol. This ratio meets the R classification (±15%), shown with a dark blue data point.

The interface layer has a negative effect on the layered systems ability to stabilise TCC_{abs}. If the interface layer is d_f > 0.02, the R class can no longer be achieved. The S class is no longer met if the interface layer is > 0.36, and ±30% is not met above > 0.61. This destabilisation in TCC performance can also be seen with the decrease in layer ratios that meet each of the TCC_{abs} classifications. The R class is no longer achieved if $d_{interface}$ > 0.02. Similarly, the S and ±30% classifications cannot be achieved if $d_{interface}$ > 0.36 and $d_{interface}$ > 0.61, respectively.

The black dashed tie line in Figure 7.21 shows the layer ratios that maintain a 0.18:0.82 ratio for the CBN-18 and SBN-65 layers, regardless of the interface thickness. By $d_{interface}$ > 0.2, the optimised layer thicknesses deviate significantly from this ratio. The interface dependence means that the 0.18:0.82 layer ratio of CBN-18 and SBN-65, will probably not have the TCC_{abs} performance expected, when co-sintered. If the interface layer is greater than 24% of the binary system, then this starting ratio is no longer predicted to achieve the S (±22%) classification. Therefore, the CBN-18 and SBN-65 starting layer thicknesses must be altered, to account for the created interface layer.

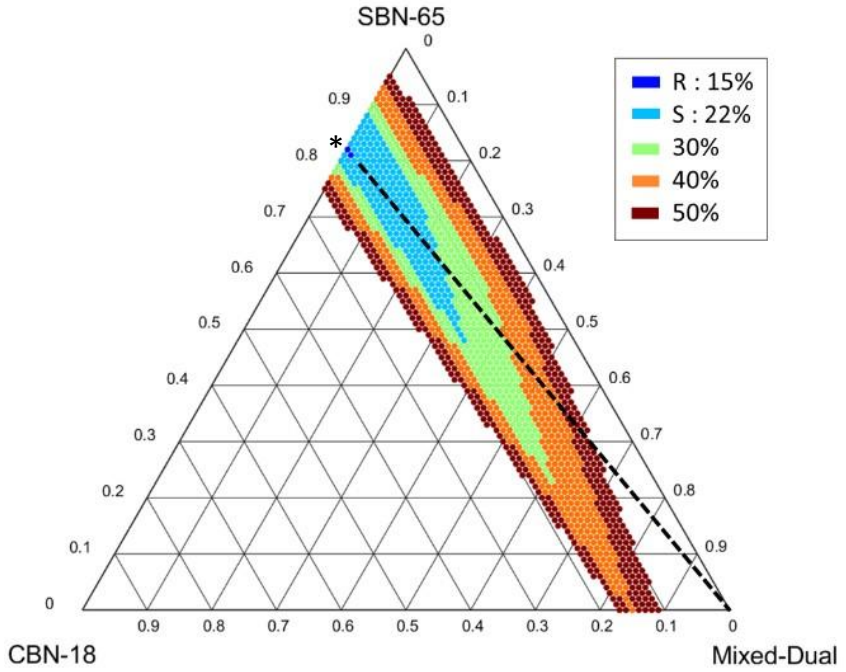

Figure 7.21 Ternary colourmap of CBN-18, SBN-65 and Mixed-Dual, showing the layer thickness ratios that achieve various TCC_{abs} values. The optimised ratio of CBN-18 to SBN-65 (0.18:0.82) is marked with the * symbol. The black dashed line shows the tie line that maintains this ratio, when an interface layer is considered.

The decrease in TCC_{abs} performance due to the interface layer is quantified in Figure 7.22 (a). This plots the 'valley floor' of the colourmap in Figure 7.21, at regular interface thickness intervals of 0.05. TCC_{abs} increases at a near linear rate with increased interface thickness until $d_{interface} = 0.85$. When $d_f > 0.85$, the system no longer optimises with an SBN-65 layer.

The relative thickness of the interface layer also affects the optimised layer thicknesses, as seen in (b) of Figure 7.22. The stacked bar chart represents the relative thickness of each component layer, and how these change with increased interface layer thickness. The left-hand side, where $d_{interface} = 0$, shows the system optimises as a thick SBN-65 layer (0.82) and a thin CBN-18 layer (0.18). As more interface layer is created, the system optimises to contain a thinner SBN-65 layer. The CBN-18 layer thickness remains relatively independent to the interface layer, until $d_{interface} > 0.85$.

This decrease in SBN-65 thickness demonstrates the optimised layer thicknesses are dependent on the amount of interdiffusion between the layers, as this would determine the thickness of the interface layer. This issue may be exasperated by the A-site vacancies that exist in CBN and SBN materials, as they are both 'unfilled' TTBs, which may allow A-site cation homogenisation.

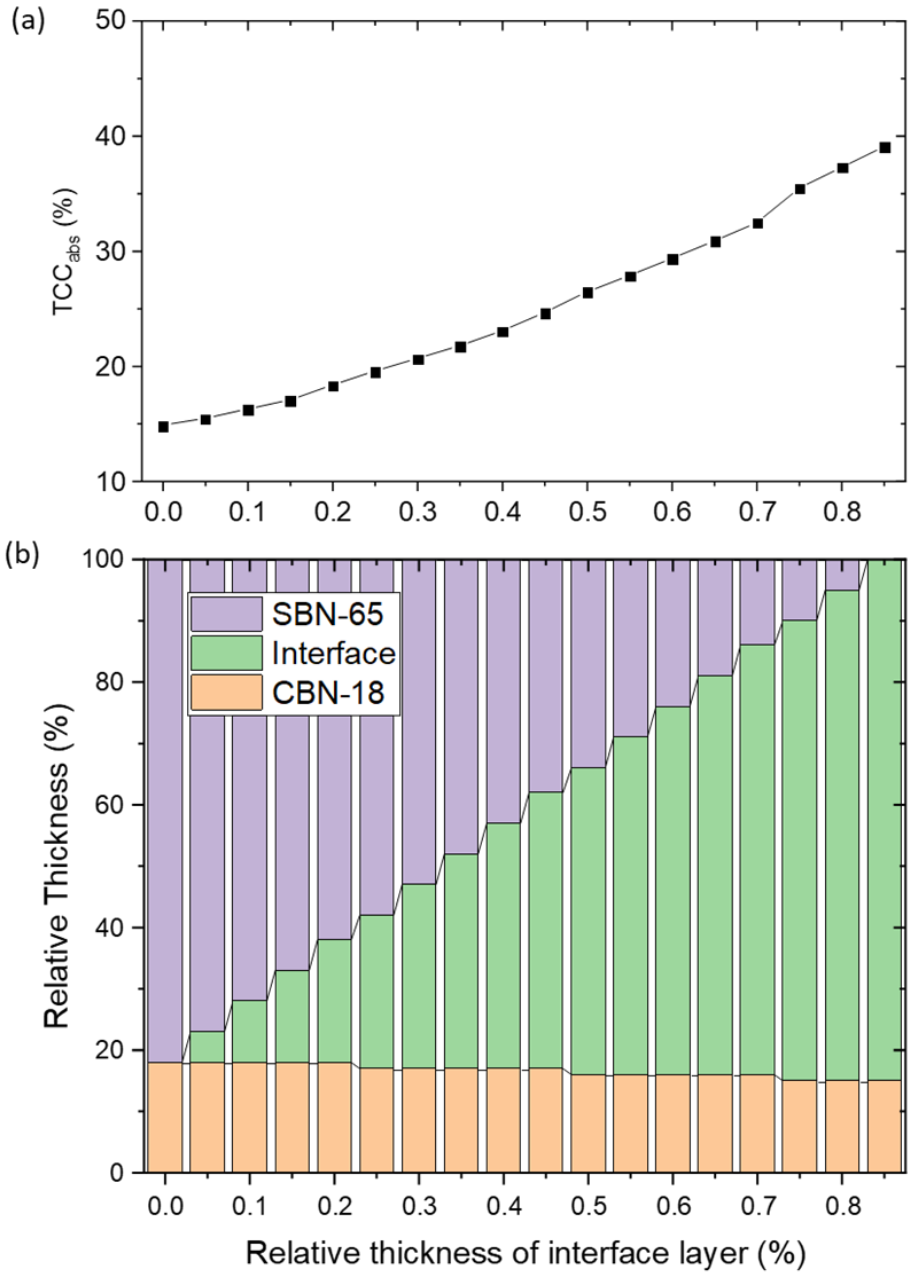

Figure 7.22 Plots showing the impact of the interface layer on the optimised layer ratio. (a) Increasing the relative thickness of the interface layer increases TCC_{abs} values of the system. (b) Dependence of the optimised layer thicknesses on the thickness of the interface layer.

7.8. Conclusions

In this chapter, materials of $(Ca_xSr_y,Ba_{1-x-y})Nb_2O_6$ were synthesised and characterised with the goal of targeting materials with a wide range of T_{max} values. Bulk ceramics were sintered in an identical manner, with all confirmed to have the Tetragonal Tungsten Bronze structure.

The bulk ceramic permittivity profiles of 6 materials were used as inputs into the Ternary Optimisation software. Using a temperature range of 25 to 400°C, the 20 different ternary combinations were simulated and ranked by their ability to optimise TCC_{abs}.

From these results, the binary system of CBN-18 and SBN-65 was further investigated. Pellets containing a mixture of these compositions prior to sintering underwent significant homogenisation during the sintering step.

In a co-sintered layer system, this interdiffusion is modelled as an interface layer. The results show this interface is likely to deteriorate the TCC_{abs} performance. It also complicates the optimised layer thicknesses of CBN-18 and SBN-65 to use, as this is dependent upon the level of interdiffusion that occurs during the co-sintering process.

7.9. Future Work

Based upon the XRD and permittivity profiles, the mixed samples undergo significant homogenisation during the sintering process. Due to COVID-19 restrictions, scanning electron microscopy (SEM) techniques could not be used to image the microstructure of the mixed samples. In the future, Electron microscopy should be used to image the microstructure of mixed samples. As seen in Figure 7.6, EDX imagery can be useful in mapping the uneven distribution of cations throughout the microstructure. With Quantitative electron microscopy (QEM) techniques, the distribution of the A-site cations would provide useful insight to the amount of homogenisation produced in the mixed samples.

In this work, a 0.18:0.82 ratio of CBN-18 to SBN-65 was used for the mixed samples. This SBN-65 dominant ratio may favour homogenisation due to the likelihood of CBN-18 grains being in contact with multiple SBN-65 grains at once. To explore this, mixed samples of different mixing ratios should be produced, sampling the possible ratios at equal intervals. In a permittivity response, a heterogeneous composite and a relaxor transition may produce similarly broadened peak shapes, so QEM could be used to distinguish these effects.

From the simulation results in this chapter, there is potential for high temperature permittivity stability when combining CBN-18 and SBN-65 materials as a layered system. Future work should co-sinter these materials, similar to the work performed in chapter 6. Using QEM techniques, the real interface thickness could then be obtained. The relative layer thicknesses produced experimentally could then be overlaid on the ternary diagram in Figure 7.21, to allow comparison with the simulation results. This can be used to assess the accuracy of the simulation results at different relative layer thicknesses of the two component materials and the interface region.

In other systems, an interface having a compositional gradient has been reported [15], so would not have a consistent permittivity response across the interface region. To model this, the interface needs to be subdivided into several layers. Using the permittivity responses obtained from the set of

mixed pellets, the QEM data can be used to match the cation composition to the nearest mixed ratio. The benefit of a more accurate model for the interface, which requires additional experimental data can then be investigated providing useful information and direction for the future development of layered systems.

In this work a high sintering temperature of 1350°C was used to ensure all TTB materials were fully densified. Future work could alter the sintering conditions with a focus on optimisation of the permittivity performance of the component materials. The minimal sintering conditions, plus the use of sintering aids such as glass, to fully densify the materials should also be investigated, again QEM being used to determine the microstructural differences produced.

Future work should investigate material combinations of different crystal structures that are chemically incompatible but could co-sinter to produce dense ceramics. Lattice mismatching may also reduce the magnitude of interdiffusion. Potentially certain cations, that 'fit' in one crystal structure but not the other, may also be used to make interdiffusion of these cations energetically unfavourable. This approach would also allow material systems that achieve $T_{max} < -50°C$, allowing the potential for sub ambient temperature TCC stabilisation whilst maintaining the high temperature stability seen in this chapter.

7.10. References:

[1] S. M. Ke, H. Q. Fan, H. T. Huang, H. L. W. Chan, and S. H. Yu, "Dielectric, ferroelectric properties, and grain growth of CaxBa1-xNb2O6 ceramics with tungsten-bronzes structure," (in English), Journal of Applied Physics, Article vol. 104, no. 2, p. 6, Jul 2008, Art no. 024101, doi: 10.1063/1.2956615.

[2] B. Kang and G.-T. Joo, "Dielectric Properties of SrxBa1-xNb2O6Ceramics and Single Crystals," Japanese Journal of Applied Physics, vol. 45, no. No. 8, pp. L245-L246, 2006, doi: 10.1143/jjap.45.l245.

[3] H. Chen, S. B. Guo, X. L. Dong, F. Cao, C. L. Mao, and G. S. Wang, "CaxSr0.3-xBa0.7Nb2O6 lead-free pyroelectric ceramics with high depoling temperature," (in English), Journal of Alloys and Compounds, Article vol. 695, pp. 2723-2729, Feb 2017, doi: 10.1016/j.jallcom.2016.11.192.

[4] A. M. Glass, "Investigation of the Electrical Properties of Sr1−xBaxNb2O6 with Special Reference to Pyroelectric Detection," Journal of Applied Physics, vol. 40, no. 12, pp. 4699-4713, 1969, doi: 10.1063/1.1657277.

[5] M. Esser, M. Burianek, D. Klimm, and M. Muhlberg, "Single crystal growth of the tetragonal tungsten bronze CaxBa1-xNb2O6 (x=0.28; CBN-28)," (in English), J. Cryst. Growth, Article vol. 240, no. 1-2, pp. 1-5, Apr 2002, Art no. Pii s0022-0248(02)00868-0, doi: 10.1016/s0022-0248(02)00868-0.

[6] M. Esser et al., "Optical characterization and crystal structure of the novel bronze type CaxBa1-xNb2O6 (x=0.28; CBN-28)," Crystal Research and Technology, vol. 38, no. 6, pp. 457-464, 2003, doi: 10.1002/crat.200310057.

[7] J. R. Carruthers and M. Grasso, "Phase Equilibria Relations in the Ternary System BaO-SrO-Nb[sub 2]O[sub 5]," Journal of The Electrochemical Society, vol. 117, no. 11, p. 1426, 1970, doi: 10.1149/1.2407336.

[8] S. Podlozhenov, H. A. Graetsch, J. Schneider, M. Ulex, M. Wöhlecke, and K. Betzler, "Structure of strontium barium niobate Sr x Ba1 − x Nb2O6 (SBN) in the composition range 0.32 ≤ x ≤ 0.82,"

Acta Crystallographica Section B Structural Science, vol. 62, no. 6, pp. 960-965, 2006, doi: 10.1107/s0108768106038869.
[9] S. S. Aamlid, S. M. Selbach, and T. Grande, "The Effect of Cation Disorder on Ferroelectric Properties of SrxBa1-xNb2O6 Tungsten Bronzes," (in English), Materials, Article vol. 12, no. 7, p. 11, Apr 2019, Art no. 1156, doi: 10.3390/ma12071156.
[10] N. S. Vandamme, A. E. Sutherland, L. Jones, K. Bridger, and S. R. Winzer, "Fabrication of optically transparent and electrooptic strontium barium niobate ceramics," (in English), Journal of the American Ceramic Society, Article vol. 74, no. 8, pp. 1785-1792, Aug 1991, doi: 10.1111/j.1151-2916.1991.tb07789.x.
[11] X. K. Han, L. L. Wei, Z. P. Yang, and T. Zhang, "Phase formation, dielectric and ferroelectric properties of CaxBa1-xNb2O6 ceramics," (in English), Ceram. Int., Article vol. 39, no. 5, pp. 4853-4860, Jul 2013, doi: 10.1016/j.ceramint.2012.11.078.
[12] C. S. Pandey, J. Schreuer, M. Burianek, and M. Muhlberg, "Relaxor behavior of CaxBa1-xNb2O6 (0.18 <= x <= 0.35) tuned by Ca/Ba ratio and investigated by resonant ultrasound spectroscopy," (in English), Physical Review B, Article vol. 87, no. 9, p. 7, Mar 2013, Art no. 094101, doi: 10.1103/PhysRevB.87.094101.
[13] M. Muehlberg et al., "Phase equilibria, crystal growth and characterization of the novel ferroelectric tungsten bronzes (CBN) and (CSBN)," J. Cryst. Growth, vol. 310, no. 7-9, pp. 2288-2294, 2008, doi: 10.1016/j.jcrysgro.2007.12.023.
[14] M. Burianek, B. Joschko, I. Kerkamm, T. Schoenbeck, D. Klimm, and M. Muehlberg, "Crystal growth and characterization of CaxBa1-xNb2O6 (CBN) in the composition range of 0.22 <= x(Ca) <= 0.35," (in English), J. Cryst. Growth, Article vol. 299, no. 2, pp. 413-417, Feb 2007, doi: 10.1016/j.jcrysgro.2006.10.269.
[15] T. M. Amaral, E. Antonelli, D. A. Ochoa, J. E. Garcia, and A. C. Hernandes, "Microstructural Features and Functional Properties of Bilayered BaTiO3/BaTi1-xZrxO3 Ceramics," (in English), Journal of the American Ceramic Society, Article vol. 98, no. 4, pp. 1169-1174, Apr 2015, doi: 10.1111/jace.13417.

8. Conclusions and Future Work

8.1. Conclusions

The focus of this work was to predict novel material combinations for MLCC applications that do not rely on optimising the volume fraction of core and shell microstructures currently required for BT-based materials [1, 2]. The goal of using this approach is to accelerate material research for MLCC applications, by decreasing the dependence of progression on iterative experimental research and make the process more resource efficient.

The initial work involved the development of a simulation package that could predict the permittivity response of a ternary layered ceramic systems. In doing so, this could identify the relative layer thicknesses required to optimise the TCC performance of series connected ceramic composites.

The permittivity-temperature profiles of dense ceramics of 9 NNBT solid solution materials were used as data inputs which individually had poor TCC performance. In less than 4 seconds on a standard laptop, the simulation code assessed the different ternary combinations possible. The results were outputted as graphs showing the performance of all the combinations, as well as those with the lowest TCC values.

The material combinations which were found to meet the X9P classification, (-55 to 200^{o}C with TCC_{abs} = ±10%), were experimentally verified via electrical measurements on series connected stacks of bulk ceramics [3]. This TCC performance, especially up to 200^{o}C, is superior to currently used BT-based materials [4, 5].

The 9 input materials used in this work have similar permittivity-temperature profiles to those reported in the literature for various ferroelectric materials [6], with a range of T_{max} values and permittivity-temperature-frequency profiles, e.g. from sharp peaks of classical ferroelectrics [7] through to broad peaks observed in relaxor [8] or CS materials [9].

The best performing material combinations followed these general rules: (a) the materials had significantly different T_{max} values, and (b) the range of T_{max} values aligned with the temperature range considered. For both binary and ternary layer systems, these rules resulted in the occurrence of successful combinations including a low T_{max} and a high T_{max} material.

In binary systems, the lack of a middle T_{max} material layer resulted in the middle temperatures having lower permittivity values, which resulted in this region having a negative TCC. This negative TCC region is difficult to rectify, and often limits the TCC_{abs} obtainable for binary systems.

In ternary systems, the permittivity response of the middle temperature range is supported by the middle T_{max} material. This additional peak minimises the negative TCC value, and thus allows a better TCC_{abs} value to be achieved.

The work reported binary systems that achieved the X9S classification (-55 to 200°C with TCC_{abs} = ±22%), whilst ternary systems achieved an X9P (-55 to 200°C with TCC_{abs} = ±10%) [3]. Although ternary systems have better TCC_{abs} performance, the complexity and cost of co-processing 3 material layers may limit commercial demand, with binary systems being a more affordable solution. Ternary layer systems would however be much more feasible in specialist/military/high performance equipment, as the TCC_{abs} performance is superior. Although the work focused on temperature ranges of standard Class 2 MLCCs, the layered approach would allow any temperature range to be optimised for, allowing the possibility of application specific MLCC devices being designed.

The original NNBT dataset was optimised to combine materials with significantly different NN contents. This may not be ideal for co-sintering, due to a mismatch in the required sintering conditions of each layer. Therefore, the NNBT literature was analysed, with 70NNBT and 87.5NNBT being selected due to their chemical similarity, whilst maintaining significantly differing T_{max} values. The binary system was simulated to achieve X8P (-55 to 150°C, TCC_{abs} = ±10%), with ε_{RT} = ~1250.

Although co-sintering of these materials was successful, the simulated permittivity-temperature profile had discrepancies when compared to the experimental results. The addition of a 3rd layer, to account for interdiffusion between the layers dramatically improved the fit of the simulation to the experimental results. The simulation predicted this interface region to have a thickness of ~ 134 µm, which was later found to match the ~125 µm obtained from SEM data on the co-sintered ceramics.

These findings imply that interdiffusion has a dramatic effect on the accuracy of the layered model, especially at the <10 µm thicknesses of dielectric layers in commercial MLCCs. In conventional solid state sintering approaches, glass additives [10] are often used to decrease the sintering temperature required to produce full dense ceramics, which may decrease the severity of interdiffusion occurring in layered systems. Approaches such as cold sintering [11] or spark plasma sintering (SPS) [12] offer alternatives to the solid state sintering used in this work, with benefits of lowering temperature or time.

Unless the interdiffusion can be restricted (i.e sintering at lower temperatures/times) or properly simulated at the atomic scale, the separation of chemically different dielectric layers with internal electrodes is likely to be necessary.

Finally, this work investigated the CSBN material system [13-15] to further increase the maximum temperature above that obtained with NNBT and BT based materials. 6 different CSBN materials were produced, with a T_{max} range from 59 to 364°C. The materials SBN-65 and CBN-18 were simulated to achieve a TCC_{abs} < ±22% for the temperature range of 25 to 400°C. The drawback of these TTB materials is their relatively low ε_{RT} values, with optimised binaries having ε_{RT} ~ 320. However, these results demonstrate the potential of non-BT materials as dielectric materials in MLCC devices, especially those requiring TCC stability at high temperatures.

8.2. Future Work

Although this work demonstrates the potential benefit of composite layers for future MLCC applications, there remains a number of research areas that require further investigation.

One aspect of future work would involve the production of prototype MLCCs. The tapecasting processing routes for MLCCs is significantly different to bulk ceramics which will influence the permittivity response of the materials. By generating a small set of MLCC samples, the permittivity-temperature profiles can be used as inputs for the simulation code. This data would then allow the permittivity-temperature profiles of binary and ternary layered prototype MLCCs to be directly compared to the simulation results. These MLCC prototypes would facilitate important technological aspects such as electric field dependency of the permittivity-temperature profiles as a function of dielectric layer thickness [16, 17] to be properly investigated, especially if layers of different thicknesses are combined in a single MLCC device.

Another opportunity for future work would be to look at broadening the types of materials combined. From the results of this study, it is clear a high T_{max} material is often necessary in achieving TCC performance at high temperatures. Although this work focused on combining materials of the same system, there is potential for BT-based layers to be combined with high T_{max} systems, such as CSBN. This approach would allow existing BT materials, which are common in X7R MLCCs, to have their classification extended to X9R and potentially beyond. This approach would therefore only result in the need to develop new high T_{max} materials, as $T < 125^{o}C$ are already well established based on existing BT-based materials.

Although this work focuses on combinations of material layers in series, the code is also capable of optimising layers combined in parallel. Future work could simulate circuits containing a mixture of both series and parallel material combinations to study how this influences TCC. This has the potential to combine the excellent TCC stability obtained when layers are connected in series with the higher ε_{RT} obtained from parallel combinations. This will further improve the overall capacitance and TCC performance of future composite MLCC devices.

8.3. References

[1] C. H. Kim, K. J. Park, Y. J. Yoon, M. H. Hong, J. O. Hong, and K. H. Hur, "Role of yttrium and magnesium in the formation of core-shell structure of BaTiO3 grains in MLCC," (in English), *J. Eur. Ceram. Soc.,* Article vol. 28, no. 6, pp. 1213-1219, 2008, doi: 10.1016/j.jeurceramsoc.2007.09.042.

[2] S.-C. Jeon, B.-K. Yoon, K.-H. Kim, and S.-J. L. Kang, "Effects of core/shell volumetric ratio on the dielectric-temperature behavior of BaTiO3," *Journal of Advanced Ceramics,* vol. 3, no. 1, pp. 76-82, 2014, doi: 10.1007/s40145-014-0096-y.

[3] G. Kerridge, D. C. Sinclair, and J. S. Dean, "Resource efficient exploration of ternary phase space to develop multi-layer ceramic capacitors," (in English), *Acta Materialia,* Article vol. 207, p. 10, Apr 2021, Art no. 116690, doi: 10.1016/j.actamat.2021.116690.

[4] H. Kishi, Y. Mizuno, and H. Chazono, "Base-metal electrode-multilayer ceramic capacitors: Past, present and future perspectives," (in English), *Jpn. J. Appl. Phys. Part 1 - Regul. Pap. Short Notes Rev. Pap.,* Review vol. 42, no. 1, pp. 1-15, Jan 2003, doi: 10.1143/jjap.42.1.

[5] Y. Sun, H. X. Liu, H. Hao, Z. Song, and S. J. Zhang, "Structure Property Relationship in BaTiO3-Na0.5Bi0.5TiO3-Nb2O5-NiO X8R System," (in English), *Journal of the American Ceramic Society,* Article vol. 98, no. 5, pp. 1574-1579, May 2015, doi: 10.1111/jace.13517.

[6] R. Whatmore, "Ferroelectric Materials," Springer International Publishing, 2017, pp. 1-1.

[7] C. Zhao, Y. Huang, and J. Wu, "Multifunctional barium titanate ceramics via chemical modification tuning phase structure," *InfoMat,* vol. 2, no. 6, pp. 1163-1190, 2020, doi: 10.1002/inf2.12147.

[8] A. Peliz-Barranco, F. Caldern-Piar, O. Garca-Zaldvar, and Y. Gonzlez-Abreu, "Relaxor Behaviour in Ferroelectric Ceramics," *Advances in Ferroelectrics*, InTech, 2012, dio: 10.5772/52149

[9] M. T. Buscaglia, M. Viviani, Z. Zhao, V. Buscaglia, and P. Nanni, "Synthesis of BaTiO3 core-shell particles and fabrication of dielectric ceramics with local graded structure," (in English), *Chem. Mat.,* Article vol. 18, no. 17, pp. 4002-4010, Aug 2006, doi: 10.1021/cm060403j.

[10] M. J. Pan and C. A. Randall, "A brief introduction to ceramic capacitors," *IEEE Electrical Insulation Magazine,* vol. 26, no. 3, pp. 44-50, 2010, doi: 10.1109/mei.2010.5482787.

[11] T. Sada, K. Tsuji, A. Ndayishimiye, Z. Fan, Y. Fujioka, and C. A. Randall, "Highly Reliable BaTiO 3 -Polyphenylene Oxide Nanocomposite Dielectrics via Cold Sintering," *Advanced Materials Interfaces,* vol. 8, no. 18, p. 2100963, 2021, doi: 10.1002/admi.202100963.

[12] M. Biesuz *et al.*, "Flash joining of conductive ceramics in a few seconds by flash spark plasma sintering," *J. Eur. Ceram. Soc.,* vol. 39, no. 15, pp. 4664-4672, 2019, doi: 10.1016/j.jeurceramsoc.2019.07.036.

[13] M. Muehlberg *et al.*, "Phase equilibria, crystal growth and characterization of the novel ferroelectric tungsten bronzes (CBN) and (CSBN)," *J. Cryst. Growth,* vol. 310, no. 7-9, pp. 2288-2294, 2008, doi: 10.1016/j.jcrysgro.2007.12.023.

[14] M. Burianek, B. Joschko, I. Kerkamm, T. Schoenbeck, D. Klimm, and M. Muehlberg, "Crystal growth and characterization of CaxBa1-xNb2O6 (CBN) in the composition range of 0.22 <= x(Ca) <= 0.35," (in English), *J. Cryst. Growth,* Article vol. 299, no. 2, pp. 413-417, Feb 2007, doi: 10.1016/j.jcrysgro.2006.10.269.

[15] B. H. Kang and G. T. Joo, "Dielectric properties of SrxBa1-xNb2O6 ceramics and single crystals," (in English), *Jpn. J. Appl. Phys. Part 2 - Lett. Express Lett.,* Article vol. 45, no. 8-11, pp. L245-L246, Mar 2006, doi: 10.1143/jjap.45.l245.

[16] K. M. Johnson, "Variation of Dielectric Constant with Voltage in Ferroelectrics and Its Application to Parametric Devices," *Journal of Applied Physics,* vol. 33, no. 9, pp. 2826-2831, 1962, doi: 10.1063/1.1702558.

[17] S. H. Yoon, M. Y. Kim, and D. Kim, "Correlation between tetragonality (c/a) and direct current (dc) bias characteristics of BaTiO3-based multi-layer ceramic capacitors (MLCC)," (in English), *Journal of Materials Chemistry C,* Article vol. 8, no. 27, pp. 9373-9381, Jul 2020, doi: 10.1039/d0tc02067b.